UNIVERSITY OF TECHNOLOGY, SYDNEY

Nondestructive Evaluation of Ferromagnetic Critical Water Pipes Using Pulsed Eddy Current Testing

by

Nalika Ulapane

A thesis submitted in partial fulfillment for the
degree of Doctor of Philosophy

in the
Faculty of Engineering and IT
Intelligent Mechatronic Systems Group

February 2016

Declaration of Authorship

I, Nalika Ulapane , declare that this thesis titled, 'Nondestructive Evaluation of Ferromagnetic Critical Water Pipes Using Pulsed Eddy Current Testing' and the work presented in it are my own. I confirm that:

- This work was done wholly or mainly while in candidature for a research degree at this University.
- Where any part of this thesis has previously been submitted for a degree or any other qualification at this University or any other institution, this has been clearly stated.
- Where I have consulted the published work of others, this is always clearly attributed.
- Where I have quoted from the work of others, the source is always given. With the exception of such quotations, this thesis is entirely my own work.
- I have acknowledged all main sources of help.
- Where the thesis is based on work done by myself jointly with others, I have made clear exactly what was done by others and what I have contributed myself.

Nalika Ulapane

28 January, 2016

UNIVERSITY OF TECHNOLOGY, SYDNEY

Abstract

Faculty of Engineering and IT
Intelligent Mechatronic Systems Group

Doctor of Philosophy

by Nalika Ulapane

Modern day maintenance of infrastructure demands significant attention to structural health monitoring. Assessment of surface condition alone is insufficient for health and strength assessment, creating the necessity to evaluate the integrity of subsurface regions through Nondestructive Evaluation (NDE). This thesis focuses on approaches to solving the problem of condition assessment of critical pipes, *i.e.*, large diameter high-pressure pipes owned and managed by water utilities to distribute consumable fresh water to customers, by developing techniques for representing the geometry of electrically conductive ferromagnetic materials via Pulsed Eddy Current (PEC) sensors.

The main contribution of this thesis is a novel detector coil voltage decay rate based PEC signal feature, the fundamental behavior of the feature is analytically described and experimentally validated. The feature has a convenient advantage in practical application since it is directly extractable from raw PEC signals and demonstrates significant invariance to sensor shape, size, and lift-off. The feature behavior is exploited in two estimation approaches, in situ measurements on pipes are performed and pipe wall thickness is inferred with uncertainty.

Firstly, an analytical approach to learning a function mapping the decay rate feature to test piece thickness with the aid of signals captured on calibration blocks is presented. The requirement of fabricating calibration blocks to have material properties matching those of pipes is extremely challenging. Thus, combining ultrasound measurements together with PEC is proposed to address material variations.

Secondly, a numerical NDE semi-parametric estimation approach is presented, PEC sensor signals are simulated taking into account measured electrical and magnetic properties of materials being tested. The thickness-feature function is learned probabilistically using Gaussian Process. Unlike in the analytical approach, the function is learned non-parametrically, therefore, variations and marginal nonlinearities are captured. The advantages over the analytical approach are demonstrated in terms of improved accuracy of inferred material thickness.

Finally, the resolution of commercial PEC sensors employed on pipes is identified as a limiting factor for structural integrity assessment. A numerical study on optimizing PEC sensor architecture to achieve higher resolution while maintaining sufficient penetration capability is carried out and a framework which can be used to perform 3D profiling by means of joint inference of thickness and lift-off is proposed.

Keywords: Analytical Modeling, Critical Pipes, Ferromagnetic, Finite Element Analysis, Gaussian Process, Inverse Eddy Current Problem, Machine Learning, NDE, NDT, Pulsed Eddy Current Signal

Acknowledgements

I would like to express my gratitude to a number of people who have helped me during my Ph.D. study. Firstly, I thank my principal supervisor Associate Professor Jaime Valls Miro for his supervision and support throughout the research. I would also like to thank my co-supervisors Associate Professor Sarath Kodagoda and Dr. Alen Alempijevic for closely following, assisting and supervising me in all aspects of the research while allocating time to review my work.

Secondly, I would like to thank Professors Gamini Dissanayake and Tomonari Furukawa for their valuable insight and advice. Their experience, broad scope of knowledge and effective feedback were immensely helpful in identifying best research methodologies.

Next, I would like to extend my gratitude to the whole Critical Pipes Project research team of University of Technology Sydney (UTS), which included Dr. Teresa Vidal Calleja, Dr. Brad Skinner, Dr. Aengus Martin, Dr. Lei Shi, Dr. Qiang Zhang, Mr. Freek De Bruijn, Mr. Buddhi Wijerathna, Mr. Raphael Falque, Mr. Daobilige Su and Ms. Liye Sun, for assisting me in various aspects. If not for their tireless efforts and support, this research would not have become a possibility.

I would also like to extend my gratitude towards Rock Solid Group©, the main technological provider for this research. Their appreciable collaboration, provision of sensors, data, and details of the sensor for modeling were a major key to research outcomes.

Special thanks should go to Prof. Besim Ben-Nissan and Dr. Gregory Heness for sharing knowledge on metallurgy in relation critical pipe materials, and Dr. Germanas Peleckis and Mr. Russell Nicholson for their assistance in providing access to laboratory measurement facilities.

Numerous workshops, laboratory facilities, work & storage spaces within and outside UTS; and tools, devices & equipment provided by different commercial and non-commercial providers were used for various purposes including, but not limited to activities such as cutting, machining, grinding, grit blasting, measuring etc. I am not able to mention by name, all the parties, and individuals who were involved in facilitating all such activities, but there is no reduction in the immensity of my gratitude towards everybody involved.

Last but not the least, my utmost gratitude goes to my parents, Mahesh & Ramya Ulapane and family for their love and care right throughout; all my previous educational institutions and their members for educating me to come thus far in academia; the staff of UTS

Graduate Research School for orientating me as a research student and smoothly managing my candidature & scholarships; the UTS Library for providing unrestricted access to literature; the staff of UTS Faculty of Engineering and Information Technology and many other departments for assisting me in various respects; and my colleagues & friends for always being with me to keep the spirits high and the energy flowing.

This thesis is an outcome from the Critical Pipes Project funded by Sydney Water Corporation, Water Research Foundation of the USA, Melbourne Water, Water Corporation (WA), UK Water Industry Research Ltd, South Australia Water Corporation, South East Water, Hunter Water Corporation, City West Water, Monash University, University of Technology Sydney and the University of Newcastle. The research partners are Monash University (lead), University of Technology Sydney and University of Newcastle.

Contents

List of Figures

List of Tables

Abbreviations

2.5D	Two and a half Dimensional
3D	Three Dimensional
EC	Eddy Current
EDM	Electrical Discharge Machining
FEA	Finite Element Analysis
GP	Gaussian Process
GT	Ground Truth
MFL	Magnetic Flux Leakage
NDE	Nondestructive Evaluation
PEC	Pulsed Eddy Current
PPMS	Physical Property Measurement System
RFT	Remote Field Testing
RMS	Root Mean Square
RSG	Rock Solid Group
SNR	Signal to Noise Ratio
SQUID	Superconducting Quantum Interference Device
UTS	University of Technology Sydney
XRF	X-Ray Fluorescence

Nomenclature

Symbol	**Quantity**
$\vec{A}$	Magnetic vector potential
$\vec{B}$	Magnetic flux density
$\vec{D}$	Displacement current
d	Thickness of the ferromagnetic material in meters
$\vec{E}$	Electric field intensity
f	Frequency
$f(\cdot)$	A scalar valued function
$\vec{H}$	Magnetic field intensity
$\vec{J}$	Electric current density
$K(\cdot,\cdot)$	Kernel
$n(t)$	Time varying noise
$P(\cdot)$	Probability
R	Correlation coefficient
$\Re^+$	Set of positive real numbers
S	Numerically simulated PEC signal from the 3D sensor model
S_{2D}	Numerically simulated PEC signal from the 2D axisymmetric sensor model
T	Absolute temperature
t	time
t_{th}	Threshold crossing time for lift-off quantification
$V(t)$	Noise free induced detector coil voltage in time domain
$V_e(t)$	Noisy induced detector coil voltage such that $V_e(t) = V(t) + n(t)$

X	Set of training inputs for GP
X^*	Set of testing inputs for GP
Y	Set of training targets for GP
$\beta(t)$	Decay rate in time domain
β_{max}	Decay rate feature for thickness quantification
ϵ_0	Permittivity of free space (8.854×10^{-12} F/m)
ϵ_{noise}	Uncertainty encapsulating noise
θ	Set of hyper-parameters for GP
μ	Permeability ($\mu_r\mu_0$)
μ_0	Permeability of free space ($4\pi \times 10^{-7}$ H/m)
μ_m	Mean function for GP
μ_m^*	GP estimate (mean of posterior distribution)
μ_r	Relative permeability
Σ	Covariance function for GP
Σ_{un}^*	Estimated uncertainty for GP estimates
σ	Electrical conductivity
Φ	Magnetic scalar potential

Glossary of Terms

Autonomous	Without human intervention.
Calibration Blocks	Cuboid shaped blocks fabricated from desired materials to known dimensions for the purpose of calibrating EC/PEC sensor readings.
Critical Pipes	Large diameter (usually $\geq$ 300mm) high pressure pipes owned and managed by water utilities to distribute consumable fresh water to customers.
Critical Pipe Materials	Materials usually used for manufacturing critical pipes (gray cast iron, ductile cast iron and mild steel).
Lift-off	Vertical distance between an EC/PEC sensor and the surface of the test piece being evaluated
Training Data	Data used in various areas of information science to discover potentially predictive relationships.

Chapter 1

Introduction

Modern day maintenance of civil infrastructure demands significant attention to structural health monitoring. The fact that assessment of surface condition alone being insufficient for health and strength assessment of most solid structures, creates the necessity to evaluate the integrity of subsurface regions. Though condition assessment via accessing subsurface regions using solid state sensors is not possible, and destructively reaching subsurface regions is not desired, state of the art sensors have been developed to enable Nondestructive Evaluation (NDE) by means of induced fields and reflected waves. Such NDE techniques have evolved over the past five decades and are widely being used in different industries at present for condition assessment of civil infrastructure [7].

This thesis focuses on approaches for solving the problem of acquiring and representing the geometry of electrically conductive ferromagnetic materials via Pulsed Eddy Current (PEC) sensor based NDE. The target application is condition assessment of critical pipes; *i.e.*, large diameter (usually ≥ 300 mm) high pressure pipes owned and managed by water utilities to distribute consumable fresh water to customers. Critical pipes are manufactured from gray cast iron, ductile cast iron and mild steels. Therefore, critical pipe materials are conductive and ferromagnetic in nature.

Analytical and numerical approaches are developed in the thesis for NDE via modeling PEC sensor interaction with conductive ferromagnetic materials in order to study, characterize and quantify effects of material geometry on sensor signals. The objective is to use sensor models to characterize relationships between signals and material geometry, and use the characterized relationships to interpret real world PEC signals for ferromagnetic material specific quantitative condition assessment purposes.

The thesis presents: (a) a novel PEC signal feature possessing a useful representative capability of test piece geometry, and analytically described fundamentals behind the feature's behavior; (b) an experimental+analytical approach which exploits the feature to perform NDE of critical pipes; (c) a numerical+probabilistic approach which exploits the feature to perform NDE of critical pipes; and (d) a study on optimizing sensor geometry to achieve higher resolution while maintaining measurement capabilities suitable for critical pipe assessment. NDE related outcomes of the thesis are evaluated by applying them for in situ critical pipe condition assessment (Fig. 1.1), and validating interpreted pipe conditions against destructively measured actuality. Though sensor modeling approaches presented in this thesis generalize, they are specifically evaluated through using them to model a commercial PEC sensor provided by Rock Solid Group© (RSG) (http://www.rocksolidgroup.com.au/).

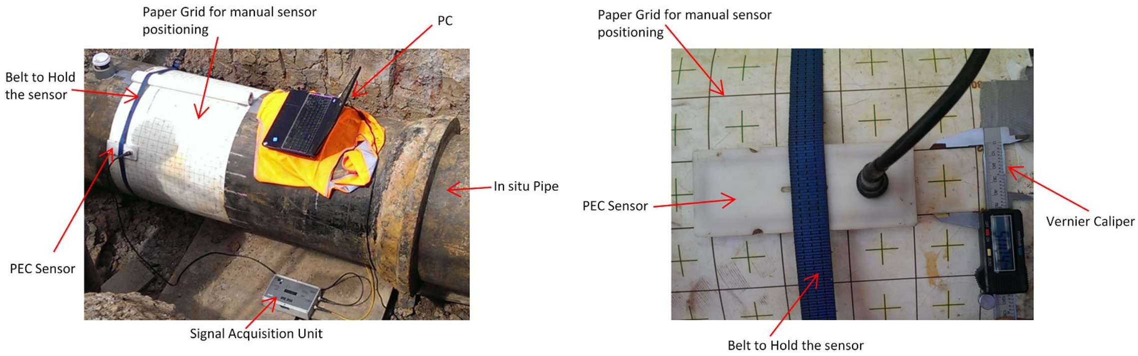

(a) (b)

FIGURE 1.1: PEC NDE: (a) PEC signal acquisition on an in situ critical pipe; (b) The commercial PEC sensor modeled in this thesis.

This chapter introduces the research work presented in the thesis. It commences with a background of the target application scenario of critical pipe evaluation and details key research issues. The remaining sections of this chapter describe the thesis scope and its main contributions and provide the outline of the remainder of the thesis.

1.1 Background

It is generally recognized worldwide that about 70% of the total asset base of urban water utilities consists of buried pipes [8]. Sydney Water (http://www.sydneywater.com.au/) has buried systems valued at over AU$15 billion and this is typical of large utilities.

Most major urban water utilities in Australia have extensive large, critical pressure main systems, parts of which have been in service up to a century or more [8–10]. Failure of critical pipes has significant impact on maintaining service levels to customers, loss of fire fighting supply, compromised safety, transport disruption and other social costs, as well as significant financial and reputational implications.

With further aging of this vital infrastructure, critical pipe failures will continue to occur. This will have very high and growing cost implications for the sustainability and effectiveness of water and wastewater services. This is a worldwide issue, with potential impacts of climate change on soil properties and moisture which lead to higher costs.

In Australia, the total replacement costs of the pipe network have been estimated to exceed AU$100 billion [10]. Over the next five years, the costs of urgently needed asset replacement are around AU$5 billion. Maintenance costs over the same period are estimated at some AU$2.5 billion [10]. Elsewhere, the USEPA estimates that the US public water sector will require US$335 billion of capital investment over the next 20 years to sustain essential service levels. Also, US studies indicate that the average cost per failure for large diameter pipes exceeds US$500,000 [10].

In response to these cost drivers, and to meet demands for reliable water supply services, water utilities have already made considerable efforts to control potential failures by applying existing, state-of-the-art methods for failure prediction, condition assessment and proactive pipe asset management technologies. The methods used have limited level of confidence which limits the ability to target renewal programs. It has been conservatively estimated that even a 30% improvement in the present state of the art, would reduce the high consequence events by 50% and total failure events by 30% resulting in potential savings of over AU$160 million over a 20 year period to the Australian Water industry [10]. With better prediction from condition assessment, expenditure can be delayed by

5 years and replacement costs reduced up to 20%, the projected savings over a 20 year period will exceed a further AU$300 million [10].

Water utilities urgently need better techniques for estimating the probability of failure of critical pipelines and for estimating their remaining life. The unavailability of such tools increases the risk of substantial funds being potentially misdirected through premature replacements. This could impact on future water service pricing. On the other hand, not undertaking timely replacement of pipes could lead to increasing number and frequency of failures with associated costs and disruption.

Corrosion and graphitization are the main causes which weaken the strength of aging critical pipes and cause them to fail eventually [8, 11]. Knowing the amount of non-compromised conductive ferromagnetic material remaining in pipe walls is therefore the key first step towards lifetime or failure prediction. Since corrosion and graphitization occur on inner and outer surfaces of pipe walls, healthy material often remain in subsurface regions which cannot be accessed directly. Causing any physical destruction to critical pipes even in the form of corrosion removal done to access the healthy material surface is undesired due to the risk of pipe bursts. Therefore, the amount of healthy material can only be evaluated nondestructively. Consequentially, many NDE techniques have emerged and grown in demand in the field of critical pipe condition assessment [12].

Due to the conductive and ferromagnetic nature of critical pipe materials, electromagnetic NDE techniques such as PEC (the focus of this thesis), Magnetic Flux Leakage (MFL) and Remote Field Testing (RFT) are widely used for critical pipe condition assessment [12]. Though these technologies are well established and provided commercially at present, the techniques used in practice have shortcomings. One issue is the requirement of sensor calibration to achieve quantitative interpretation of pipe condition [6, 13, 14]. Accurate calibration is challenging in the target application due to the difficulty of obtaining calibration materials having properties which satisfactorily match those of critical pipes. As a result of calibration errors, interpreted pipe conditions can be observed to deviate from reality in practice. Another issue is the requirement of time intensive manual labor to analyze signals individually to accomplish accurate interpretation. Although ferromagnetic material specific PEC signal processing techniques have been proposed [4, 13, 14], an autonomous framework which is readily usable with a commercial PEC tool is lacking. A system which models sensors taking into account unknown material properties and hence autonomously inferring pipe condition using NDE data, has the potential to greatly increase productivity of the process and the accuracy of results.

This thesis originated as a part of Activity 2 of the Advanced Condition Assessment & Pipe Failure Prediction Project (http://www.criticalpipes.com/), which is co-led by University of Technology Sydney (UTS). The project is strongly supported by Sydney Water and many Australian and international water utilities, condition assessment service providers and research institutions. This activity aims to advance knowledge and improve levels of confidence of direct methods for condition assessment using sensor modeling and advanced data interpretation techniques which have already been successfully employed in fields such as aerospace, cargo handling, undersea ecology, land vehicles and mining. The desired outcome of Activity 2 is a method of accurately predicting sensor readings for a given geometric description of a buried large critical pipe, and obtaining the best estimate of the pipe geometry from a set of measurements based on maximum likelihood principles. As a part of this activity, this thesis deals with PEC sensor specific modeling and data interpretation.

1.2 Motivation

PEC sensor signals are strictly dependent on the geometry and electrical and magnetic properties of the material being tested. Therefore, to ensure accurate assessment of geometric condition of a certain material, sensor readings require to be calibrated with respect to material geometry. Common industrial practice of PEC sensor calibration with respect to geometry involves using readings acquired on reference test pieces with known geometry and intrinsic material properties as close as possible to those of the actual material being evaluated. Such reference test pieces used for calibration are henceforth referred to as "calibration blocks" in this thesis.

Calibration blocks can be either fabricated or destructively extracted from the domain being evaluated. In the application of critical pipe evaluation however, destructive extraction is not possible due the physical damage it causes to the infrastructure. As a result, common industrial practice enables geometric calibration of critical pipe materials only by means of fabricated calibration blocks.

To fabricate calibration blocks which replicate the desired geometric sensitivity, precise intrinsic properties (specifically electrical conductivity and magnetic permeability) of the material to be evaluated have to be known. That enables fabricating calibration blocks having identical or at least very close, intrinsic properties to those of the material required to be tested. When it comes to pipe assessment however, precise intrinsic properties of pipe materials are unknown. Specifically, the pipes in focus of this thesis were manufactured and laid in the early 19th century where quality control methods were not widely enforced. Though measuring the necessary properties is a possibility, having the capability to manufacture a critical pipe material to have the exact measured intrinsic property values is highly unlikely. This is due to critical pipe materials being manufactured by casting and cooling, a process highly influential on intrinsic properties of the end product. Expecting a casting and cooling process to repeat itself identically, so that the exact properties of a previously manufactured material sample is replicated, is highly ambitious. Further, fabricating tailored calibration blocks on each condition assessment undertaken is undesired due to the cost, time and labor requirement constraints.

Usual practice followed by commercial PEC service providers to avoid the aforementioned constraints is performing one off fabrication of sets of calibration blocks. Such a method is reasonable for materials which can be guaranteed to have fairly precise intrinsic properties and narrow margins of variation. In light of critical pipe materials however, that is not the case. For critical pipe materials which include gray cast iron, ductile cast iron and mild steel, electrical conductivity and magnetic permeability values can vary approximately up to ±20% from the expected mean [15]. Reasons behind such a variation are the high degree of inhomogeneity in the materials itself, and the nonlinearity attributed with intrinsic properties [15]. Therefore, electrical and magnetic properties of critical pipe material specific calibration blocks could deviate within ±20% from those of pipes. Such discrepancies between calibration and measurement adversely affect the measuring technique by offsetting interpreted geometric condition from reality.

Another issue related to the NDE techniques, especially the commercially provided ones, is the requirement of time intensive manual labor to analyze signals individually to accomplish accurate interpretation. The lack of efficient algorithms to autonomously interpret data negatively impact service providers by hampering their delivery speed of results. Although ferromagnetic material specific PEC signal processing techniques have been proposed [4, 13, 14], autonomous data interpretation frameworks which are readily usable with commercial PEC tools to make them more efficient are not common.

Developing methods of taking into account measured electrical and magnetic properties of materials and artificially generating NDE signals via computational means to eliminate the requirement of calibration blocks are clearly warranted. Approaches which use calibration data to learn relationships between signal features and material geometry are also necessary to enable efficient and autonomous interpretation of signals.

1.3 Scope

The thesis specifically aims to develop PEC based advanced NDE approaches suitable for critical pipe condition assessment. Developed approaches are intended to overcome the issues related to calibration and requirement of manual data interpretation, in addition to being able to accurately predict pipe condition with confidence bounds. Two approaches are developed with the objective to learn functions which map PEC signal features to test piece geometry and use the learned functions to interpret PEC data acquired from on site measurements to predict geometric condition of in situ critical pipes.

It should be noted that designing a novel PEC sensor architecture to produce more accurate measurement capabilities is beyond the scope of this research. The objective is to rather use a standard PEC sensor architecture which is used by RSG, the commercial PEC service provider partnering with this research, and to propose approaches to better interpret the data. Therefore, the scope of this thesis is limited to the “detector coil” based PEC sensor architecture, which is the one used by RSG. All Eddy Current (EC) and PEC sensors operate by a coil (exciter coil) being excited by a time varying current which induces eddy currents in the test piece, and using a receiver/detector to capture the resultant time varying magnetic field. Since the influence of eddy currents induced in the test piece are contained in the resultant magnetic field, the signal induced by the detected field can be used to characterize different properties of the test piece. Though all EC and PEC sensor architectures have an exciter coil in common, the sensor architectures differ based on the type of detector used [1].

The detector coil based PEC sensor architecture is known to have superior sensitivity to geometric properties of conductive ferromagnetic materials over other architectures [1], thereby making it the most suitable architecture for the target application. Subject to the capabilities of the used architecture, pipe geometry is evaluated and presented in the form of average wall thickness remaining under the detector coil. When a condition assessment is done, the thickness estimates are presented as a 2.5D thickness map which uses pipe axial and circumferential positions as x and y coordinates respectively to represent the location of each thickness estimate. Hence the scope of assessed pipe condition is limited to average wall thickness under the detector coil.

The target application of this thesis is critical pipe assessment, aged critical pipes are found in either of the three critical pipe materials: gray cast iron, ductile cast iron or mild steel [8, 9, 11]. Thus, all NDE related developments are experimented on in situ pipes made of critical pipe materials. However, the proposed approaches generalize for condition assessment of any electrically conductive and ferromagnetic material.

A novel PEC signal feature, the “detector coil voltage decay rate” is introduced in this thesis. Existence of a functional behavior between the feature and conductive ferromagnetic material thickness is theoretically proved and experimentally verified. Suitability of the feature for critical pipe condition assessment is demonstrated.

The thesis presents two NDE approaches based on the “detector coil voltage decay rate” signal feature. First, an analytical approach which requires experimental calibration and secondly a probabilistic approach which uses numerically modeled data for learning. In the first approach, calibration data are obtained from calibration blocks and a function between thickness and a signal feature is analytically derived using calibration data. This function is eventually used to interpret NDE signals to predict thickness of in situ critical pipes. Accuracy of the pipe conditions interpreted by the approach is quantitatively evaluated. The method requires the aid of calibration blocks, or alternatively as proposed in this thesis, ultrasound measurements performed on pipe sections. Consequentially, the requirement of the probabilistic approach based on numerical modeling is proposed to eliminate the requirement of calibration and to capture nonlinearities. The second approach deals with experimentally measuring intrinsic electrical and magnetic properties of pipe materials, using the measured properties to numerically simulate PEC signals using a Finite Element Analysis (FEA) [16, 17] model and probabilistically learning the thickness-feature function. Gaussian Process (GP) [18] is used as the probabilistic approach to learn the nonlinear function since it yields the useful information of uncertainty for inferences performed. The hence learned function is used for in situ critical pipe assessment, the performance of the second approach is also evaluated.

Due to the fact that the PEC sensor architecture used for this work can measure only the average thickness which generalizes to a region underneath the sensor, sensor resolution is primarily limited by the sensor size. This limitation in resolution prevents identification and quantification of fine defects, identified as an additional research challenge. In the view of the constraints on altering the existing design, this thesis presents an FEA based study on optimizing the PEC senor geometry to achieve better resolution while maintaining penetration and measurement capabilities required for in situ critical pipe assessment. In addition to increasing resolution, the thesis presents a framework applicable for 3D profiling by means of concurrent inference of material thickness and lift-off, the vertical distance between the sensor and the conducting material surface.

The thesis thus presents the theoretical fundamentals behind the detector coil voltage decay rate signal feature, a numerical study focused on optimizing sensor geometry to achieve better resolution facilitate 3D profiling capability and presents the critical pipe NDE approaches implemented as frameworks so that they generalize to any detector coil based PEC sensor.

1.4 Contributions

The contributions of this thesis are:

1. Introduction of a novel PEC signal feature based on the detector coil voltage decay rate as a feature capable of thickness discrimination of conductive ferromagnetic materials and the validation of the feature's monotonic functional behavior with thickness [19]. Fundamentals behind the feature's behavior are analytically described and experimentally validated, and suitability for critical pipe assessment is established.
2. An analytical approach to parametrically learn the thickness-feature function and use it for PEC NDE of critical pipes [19]. Function parameters are estimated for critical pipe materials via experiments performed on calibration blocks and the function's performance on in situ critical pipe assessment is evaluated. The practical difficulty of obtaining calibration blocks which have properties matching those of critical pipe materials substantiates the need for an alternative calibration method based on two sensing modalities; a method of calibrating by means of PEC and ultrasound measurements is proposed [19].
3. A critical pipe NDE approach which takes into account measured electrical and magnetic properties of critical pipe materials to simulate PEC sensor responses using FEA, and non-parametrically learns the thickness-feature function using the decay rate feature extracted from simulated sensor responses. Simulation is done using a validated FEA model [6] tailored to represent the commercial PEC sensor used for this work. Measured electrical and magnetic properties of critical pipe materials are incorporated with properties of the sensor, and the sensor's interaction with the material being tested is numerically modeled [6]. The modeling technique presented generalizes to model any EC/PEC sensor's interaction with a conductive material. Learning the thickness-feature function is done probabilistically using GP and the performance on in situ critical pipe assessment is evaluated against ground truth after destructive testing. Non-parametric probabilistic learning demonstrates increased accuracy over the analytical approach due to being able to learn and model local nonlinearities present in the thickness-feature function.

4. Low resolution associated with the commercial PEC sensor used for this work is identified as an additional limitation. A simulation study is carried out to optimize the sensor geometry with the objective of achieving better resolution while maintaining the desired penetration capability suitable for critical pipe assessment. The study also suggests a framework applicable for 3D profiling by quantifying material thickness and sensor lift-off concurrently.

1.5 Publications

The following peer reviewed research papers were either published during candidature or were being reviewed at the time of completion of this thesis. Some publications are not directly related to the work of the thesis, however, techniques presented in such publications are adapted and incorporated within the thesis. Notations 'J' and 'C' refer to journal articles and conference papers respectively.

1.5.1 Directly Related Publications

J1. Jaime Valls Miro, Jeya Rajalingam, Teresa Vidal-Calleja, Freek de Bruijn, Roger Wood, Dammika Vitanage, **Nalika Ulapane**, Buddhi Wijerathna, and Daoblige Su, "A live test-bed for the advancement of condition assessment and failure prediction research on critical pipes," Water Asset Management International, ISSN Print: 1814- 5434, ISSN Online: 1814-5442, 10(2):03-08, 2014.

J2. **Nalika Ulapane**, Alen Alempijevic, Jaime Valls Miro, Teresa Vidal Calleja, "Non-destructive evaluation of ferromagnetic material thickness using Pulsed Eddy Current sensor detector coil voltage decay rate," NDT & E International, 2014, Under Review.

C1. **N. Ulapane**, A. Alempijevic, T. Vidal-Calleja, J. V. Miro, J. Rudd, and M. Roubal, "Gaussian process for interpreting pulsed eddy current signals for ferromagnetic pipe profiling," in Proceedings of the 9^{th} IEEE International Conference on Industrial Electronics & Applications (ICIEA), pp. 1762-1767, 2014.

1.5.2 Indirectly Related Publications

J3. **Nalika Ulapane**, Sunil Abeyratne, Prabath Binduhewa, Chamari Dhanapala, Shyama Wickramasinghe, Nimal Rathnayake, "A Simple Software Application for Simulating Commercially Available Solar Panels," International Journal of Soft Computing And Software Engineering (JSCSE), e-ISSN: 2251-7545, Vol.2,No.5, pp. 48-68, 2012

C2. **Nalika N.B. Ulapane** and Sunil G. Abeyratne, "Gaussian process for learning solar panel maximum power point characteristics as functions of environmental conditions," in Proceedings of the 9th IEEE International Conference on Industrial Electronics & Applications (ICIEA), pp. 1756-1761, 2014.

C3. Daobilige Su, **Nalika Ulapane** and Buddhi Wijerathna, "An acoustic sensor based novel method for 2D localization of a robot in a structured environment," in Proceedings of the 10th IEEE International Conference on Industrial Electronics & Applications (ICIEA), 2015, in press.

1.6 Thesis Layout

The thesis is structured so the first two chapters outline the research and provide background for the thesis. Chapter 3 introduces the detector coil voltage decay rate as a PEC signal feature suitable to evaluate conductive ferromagnetic material thickness and presents the decay rate based analytical approach for NDE of critical pipes. The requirement of accurate calibration in this approach leads to the realization why the numerical approach proposed in Chapter 4 is required. Chapter 4 presents the decay rate based numerical sensor modeling technique and the probabilistic thickness-feature function learning approach for NDE of critical pipes. Chapter 5 presents the study on optimizing sensor geometry to increase resolution and enable 3D profiling. Conclusions are presented in Chapter 6. The detailed outline of each chapter follows:

Chapter 2 contains a review of related work in the field of PEC sensing. The chapter presents PEC sensor operating principles, sensor architectures and applications. Further, the chapter investigates PEC signal features used in practice and their applications. PEC sensor modeling techniques are subsequently investigated and the chapter concludes by reviewing already published knowledge on the influence of sensor geometry on measurement capabilities.

Chapter 3 introduces the detector coil voltage decay rate as a PEC signal feature suitable for conductive ferromagnetic material thickness discrimination. Analytical derivations result in a parametric function which maps the feature value to thickness. The functional behavior of the feature is demonstrated for pipe materials using experimental PEC signals obtained from calibration blocks. Some important low dependencies associated with the decay rate feature are hypothesized and experimentally validated. These low dependencies on certain factors make the feature immune to some practical anomalies encountered during performing in situ measurements. Since the target application is critical pipe evaluation, and the fact that pipe walls are curved unlike calibration blocks, the effect of test piece curvature on the feature is numerically studied using FEA determining a curvature range which does not impact significantly on the feature. The decay rate based analytical approach for NDE of critical pipes is also presented. Readings on calibration blocks are used to estimate parameters of the thickness-feature function for different pipe materials. The learned function is then used for wall thickness estimation of in situ critical pipes and the accuracy of results is demonstrated. To avoid requirement of calibration, an alternative method is introduced to estimate thickness by using ultrasound measurements for scaling. The chapter concludes by characterizing sensor noise and identifying the requirement of calibration as a practical difficulty which has to be adhered with when executing the proposed approach in addition to the limitation of the approach not being able to accurately model local nonlinearities present in the thickness-feature function.

Chapter 4 presents the numerical and probabilistic approach for NDE of critical pipes. Methods followed for measuring electrical and magnetic properties of in situ critical pipe materials are discussed. The development of the FEA model of the commercial PEC sensor used for this work is presented. The model is validated by comparing the simulations with experimental results obtained from a range of calibration blocks. Decay rate feature values are extracted from simulated sensor signals and are used as training data to non-parametrically learn the thickness-feature function using the probabilistic technique of GP. The hence learned function is validated on wall thickness estimation of in situ critical pipes using feature values extracted from on site NDE measurements. This approach proves a slight superiority over the analytical approach due to being able to learn local nonlinearities in the thickness feature-function.

Chapter 5 identifies the low resolution associated with the commercial PEC sensor used for this work as an additional limitation. An FEA based simulation study is carried out to optimize the sensor geometry with the objective of achieving better resolution while maintaining the penetration capability required for critical pipe assessment. The chapter concludes by presenting a framework usable for 3D profiling by means of concurrently inferring material thickness and sensor lift-off.

Chapter 6 summarizes the research work presented in this thesis followed by a discussion on limitations of the decay rate feature, implemented NDE approaches and the sensor optimization study. Conclusions are drawn with regards to this research and avenues for future work are proposed.

Chapter 2

Review of Related Work

There are numerous challenges in developing an NDE approach which takes into account measured intrinsic properties of a material, models sensor signals to learn functions between signal features and material geometry, and eventually use the function to autonomously interpret signals acquired form on site NDE measurements to predict test piece geometric condition. Since the target application is clearly defined to be critical pipe wall thickness evaluation and the scope is limited to using PEC sensors, the main research challenges involved are: (a) Identifying a suitable sensor architecture; (b) Sensor modeling; and (c) Identifying thickness discriminative signal features.

PEC technique is a category of EC inspection techniques and the justification behind selecting the PEC technique for the target application over other EC techniques has to be clearly understood. This chapter therefore begins by reviewing the available EC inspection techniques and their capabilities and limitations so that the reason behind choosing the PEC technique is clarified.

Though there are a few different PEC sensor architectures, the detector coil based architecture is the one used for the work of this thesis. This architecture had to be incorporated mainly due to the commercial sensor partnering with this work being based on it. However, this architecture is also the most suitable and the most commonly used one for ferromagnetic material thickness quantification. After reviewing EC inspection techniques, this chapter reviews the PEC sensor architectures to help understand the suitability of the detector coil based architecture for the target application of this thesis.

Subsequently, existing work on PEC based ferromagnetic material thickness quantification are reviewed. This mainly highlights application specific signal noise suppression and thickness discriminative feature extraction techniques which have been previously proposed. Suitable noise suppression techniques presented in literature are adapted and used for signal processing in this thesis. However, the review on thickness discriminative features helps to realize their characteristics which make them not ideal for the target application of critical pipe evaluation. This brings to the realization about why the newly proposed PEC signal feature in this thesis, the "detector coil voltage decay rate" is required.

Finally, the chapter reviews previous studies on the influence of sensor geometry on measuring capabilities. This thesis eventually builds on that knowledge to study the possibility of increasing PEC sensor resolution with respect to the target application. The chapter concludes with a summary of findings so that the research gaps this thesis attempts to fill become clear.

2.1 EC Inspection Techniques

EC inspection techniques can mainly be classified into (a) single frequency EC techniques and (b) multi-frequency EC techniques [1]. The conventional EC techniques fall into the single frequency EC class whereas PEC falls into the multi-frequency class [1]. However, due to its quick excitation and small excitation time, the PEC technique stands out from the class of multi-frequency techniques. Therefore, the single frequency EC technique, the multi-frequency EC technique and the PEC technique are addressed separately in subsections 2.1.2, 2.1.3 and 2.1.4 respectively. Remote Field Eddy Current Testing (RFT) is another important derivative of EC inspection [1, 20]. RFT is very useful when inspecting large test pieces such as water, oil and gas pipelines due to its sensor architecture and the operating mechanism which enables it to examine large areas in a short space of time [1, 20]. However, RFT is not considered as a separate EC technique in this review since its operating principle is based on single frequency and multi-frequency EC principles despite the sensor architecture being different. Therefore, RFT technique is not addressed in length in this review.

The operating principle of all EC techniques is the same and before elaborating on different EC inspection techniques, EC sensor operating principles are briefly explained in subsection 2.1.1 while formula based detailed theoretical descriptions are provided in Chapters 3 and 4.

2.1.1 Principle of EC Inspection

The principle of eddy current inspection is based on the interaction between a magnetic field source and a test material. This interaction induces eddy currents in the test piece and the presence of cracks or other imperfections can be detected by monitoring changes in the eddy current flow [21]. According to Ampere's law, when a time varying current passes through a conductor, a resulting time varying magnetic field is generated around it. When such a conductor is placed adjacent to another conducting material, eddy currents are induced in the conducting material in accordance with Faraday's and Lenz's laws. The eddy currents propagate in circular paths and eddy current densities are sensitive to properties of the conductive material in which the eddy currents are flowing. Some examples of these properties are: material conductivity, material composition, magnetic permeability, stress and strain, temperature, material volume and flaws in the material [1]. Thus, if the variations occurring in the induced eddy currents are sensed and quantified, it is possible to estimate the aforesaid material properties [1].

2.1.2 Conventional (Single Frequency) EC Inspection

The single frequency conventional eddy current inspection technique is the most preliminary of all the EC techniques and was the first EC testing method to be evolved more than half a century ago [1, 22]. When coil probes are used, this technique is usually operated as per Fig. 2.1. A single exciter coil is placed above a test piece and the coil is excited by a sinusoidal input with a certain frequency. The excited coil would have defined impedance when standing alone. However, when it is placed above a test piece, eddy currents are induced in the test piece and this causes a change in the impedance of the coil due to magnetic field interaction. The impedance change is affected by the eddy currents inducing a reverse electromotive force on the coil. This change in impedance can then be plotted on a normalized impedance plane modeled to extract properties of the test piece [1, 22–25].

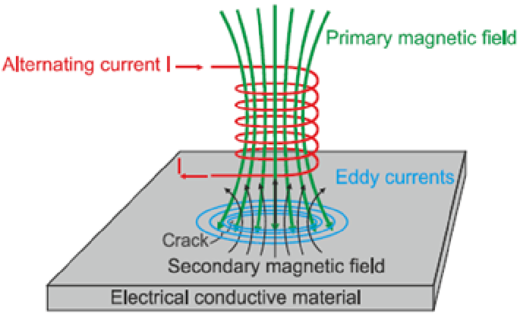

FIGURE 2.1: Basic setup of conventional EC inspection (Adapted from [1]).

A major drawback in the conventional EC inspection technique is the skin effect limitation [1]. It is known that the depth of penetration of the eddy currents is inversely proportional to the square roots of: (a) Electrical conductivity of the material; (b) Magnetic permeability of the material; and (c) The frequency of the excitation voltage. Since critical pipe materials are conductive and ferromagnetic, they usually have high conductivity and permeability values. Therefore, for a given frequency, eddy current penetration depth in these materials will be lower than a nonmagnetic material having similar conductivity. As a result, the conventional EC technique is typically used for crack/defect identification in nonmagnetic materials [23–25], in applications such as aircraft inspection [23, 24]. Furthermore, it is known that despite this technique being capable of assessing geometric condition of nonmagnetic materials, it does not have the same capability when assessing ferromagnetic materials [1]. The reason for this is the sensor's sensitivity to test piece geometry being overshadowed by its sensitivity to material permeability due to the permeability of ferromagnetic materials being high. Therefore, the conventional EC technique can be used to easily discriminate ferromagnetic materials from nonmagnetic materials [1] and it can be effectively used for quantifying material properties such as magnetic permeability as done in [26]. However, the sensor's sensitivity to the geometry of ferromagnetic materials is minimal and as a result, the conventional EC technique is not suitable for the target application of critical pipe assessment.

Multi-frequency techniques were developed to overcome the skin effect limitation associated with the conventional technique.

2.1.3 Multi-Frequency EC Inspection

Multi frequency techniques use a combination of several excitation signals with several frequencies; different frequencies penetrate different depths and provide information about different locations on the test piece [1]. Therefore, the multi-frequency technique can handle the skin effect limitation better than the conventional technique while being able to provide more information at different depths [1].

Given the inverse relationship between eddy current penetration depth and frequency, it can be hypothesized that higher penetration depth can be achieved by exciting with lower frequencies, and therefore, a multi-frequency technique can assess any depth of any material including ones having ferromagnetic properties. Though achieving higher penetration in such a way is fundamentally possible, a hence achieved penetration is hardly usable for condition assessment due to the reason detailed henceforth. Nondestructive condition assessment of electrically conductive materials when using electromagnetic sensors can be done only by reading the magnetic field resulting from excitation fields interacting with the test piece. Such a resultant magnetic field has the frequency of the excitation signal and the field can be read by measuring a current or a voltage induced by it. Since induction follows Faraday's law, the magnitude of induced fields are proportional to the rate of change of magnetic flux, *i.e.*, the frequency of the magnetic filed. Consequentially, lower frequencies will result in lower induced fields which can be difficult to measure, despite they cause eddy currents to penetrate deeper. As a result, using multiple excitation frequencies, or simply using lower excitation frequencies is a not an ideal option for conductive ferromagnetic material inspection. Therefore, multi-frequency techniques too are generally used for assessing nonmagnetic materials [27–29]. Although the multi-frequency technique too in its usual form is not suitable for geometric condition assessment of ferromagnetic materials, exploiting it in the form of the PEC variant produces some salient properties which are greatly advantageous and create the desired geometric sensitivity when interacting with ferromagnetic materials.

2.1.4 PEC Inspection

The main difference of the PEC technique is the sensor being excited by a voltage or a current pulse as opposed to being excited by a set of frequencies as in multi-frequency techniques. This technique stands out as the most versatile and modern counterpart of EC techniques at present [1].

PEC technique has proven itself to be able to easily overcome the skin effect and produce detectable magnetic field variations at the same time due to the salient characteristics of its pulsed excitation. It has therefore commonly been used for geometric condition assessment of ferromagnetic materials in the recent past [2–4, 6, 13, 14, 19, 20, 30–33].

Rising and falling edges of the pulsed excitation can be theoretically described by a Heaviside step function. The Fourier transform of the Heaviside function is known to be $\delta(f) + \frac{1}{i2\pi f}$ where $i = \sqrt{-1}$, f denotes frequency and $\delta(f)$ denotes the unit impulse function of f. This result clearly suggests that the power of low frequencies can be very high. A power of that magnitude may not be achievable by exciting with a single low frequency due to the limitations of excitation circuitry. However, a pulse enables having such desired high powers in the low frequency range while enabling a wide frequency spectrum to be contained within the magnetic field. The PEC technique can therefore achieve admirable penetration capability. It can also produce reasonable magnitudes for the resultant magnetic field since the power of low frequencies are very high, while high frequencies too exist with low powers. As a result, this technique has significant versatility over the other EC techniques and therefore is used for condition assessment of a wide variety of materials including ones having ferromagnetic properties [1]. Consequentially, the PEC technique can be identified as the most suitable EC technique for the target application of this thesis, *i.e.*, thickness estimation of critical pipe materials which are electrically conductive and ferromagnetic. Commonly used PEC sensor architectures are described in the following section.

2.2 Commonly Used PEC Sensor Architectures

All EC/PEC sensor architectures have in common a solenoid exciter coil for excitation [1]. However, PEC sensor architectures when taken collectively, use separate sensors to detect the magnetic filed and therefore differ from the conventional EC sensor architecture which uses the exciter coil alone (Fig. 2.1) to measure the impedance change. PEC sensor architectures can be classified based on the type of detector used. Typically used detectors are solenoid coils, superconducting quantum interference devices (SQUIDs) and Hall-effect and magnetoresistive sensors [1]. With respect to the target application of conductive ferromagnetic material inspection, this chapter classifies PEC sensor architectures into the two categories: (a) Detector coil based architecture; and (b) Non-Detector coil based architecture. The former category simply refers to sensors which use solenoid coils as detectors to sense the magnetic field whereas the latter includes sensors which incorporate the rest of the sensing devices, *i.e.*, SQUIDs, Hall-effect sensors and magnetoresistive sensors.

2.2.1 Detector Coil Based PEC Sensor Architecture

The detector coil based architecture simply uses a solenoid coil to detect the magnetic field via sensing the induced voltage or current across the coil. This is easily the most commonly used architecture for thickness estimation of ferromagnetic materials [2–4, 6, 14, 19, 30, 31]. Desirable thickness discriminative capability possessed by the signals produced by this architecture is the major reason for the common use. This architecture can hence be considered suitable for critical pipe assessment and this thesis deals explicitly with this architecture due to the sensor partnering with this work (Fig. 1.1) is of the typical detector coil based architecture. The cross-sectional view of the configuration of this architecture is shown in Fig. 2.2. A limitation of this architecture is the low resolution since a coil which has a considerable size is used as the detector. Therefore, this architecture has limited sensitivity to fine and isolated defects, but can detect an averaged representation of the material thickness or volume remaining under the footprint of the sensor [34].

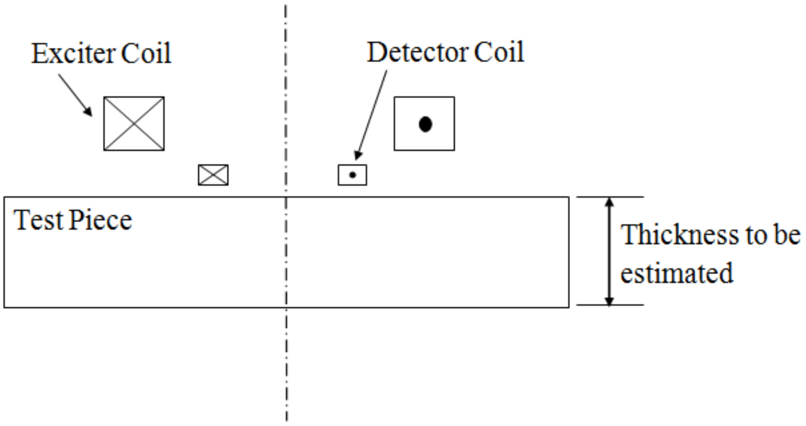

FIGURE 2.2: Cross-sectional view of the typical detector coil based PEC sensor architecture used for ferromagnetic material thickness estimation.

This architecture has coils whose axis is perpendicular to the surface of the test piece. These probes can be either air-core coils or ferrite-core coils. Ferrites have high permeability and the initial coil impedance is higher than that of the air-core coils. Air-cored coils are the ones typically used for ferromagnetic material assessment [2–4, 6, 14, 19, 30, 31, 35]. This architecture is generally suitable for evaluating flat surfaces [1], but this is also used on large diameter pipes [6, 19, 31] as shown in Fig. 1.1 and 2.3 since curvature of large pipes is low relative to the sensor size. Center axis of the cylindrical pipe shown in Fig. 2.3 is perpendicular to the page.

Coils are occasionally arranged in different configurations to obtain variations of this architecture such as Encircling coil probes, Horseshoe-shaped coil probes, Double-function probes, Separate-function probes, Absolute-Mode probes and Differential-Mode probes [1]. These variations are mostly used for nonmagnetic material inspection and RFT sensors used for pipe inspection [20]. Therefore these variations are not of direct relevance to the work of this thesis and are not discussed in detail.

It is known that this architecture is very sensitive to lift-off (vertical distance between an EC/PEC sensor and the surface of the test piece) and tilt [1]. Therefore, it is ideally suited to assess the thickness of flat surfaces by placing the sensor as parallel as possible to the surface. However, when assessing critical pipes, such surface conditions cannot be expected due to the nonmagnetic substances such as rust and graphite being present between the sensor and the ferromagnetic material. As a result, using this architecture for

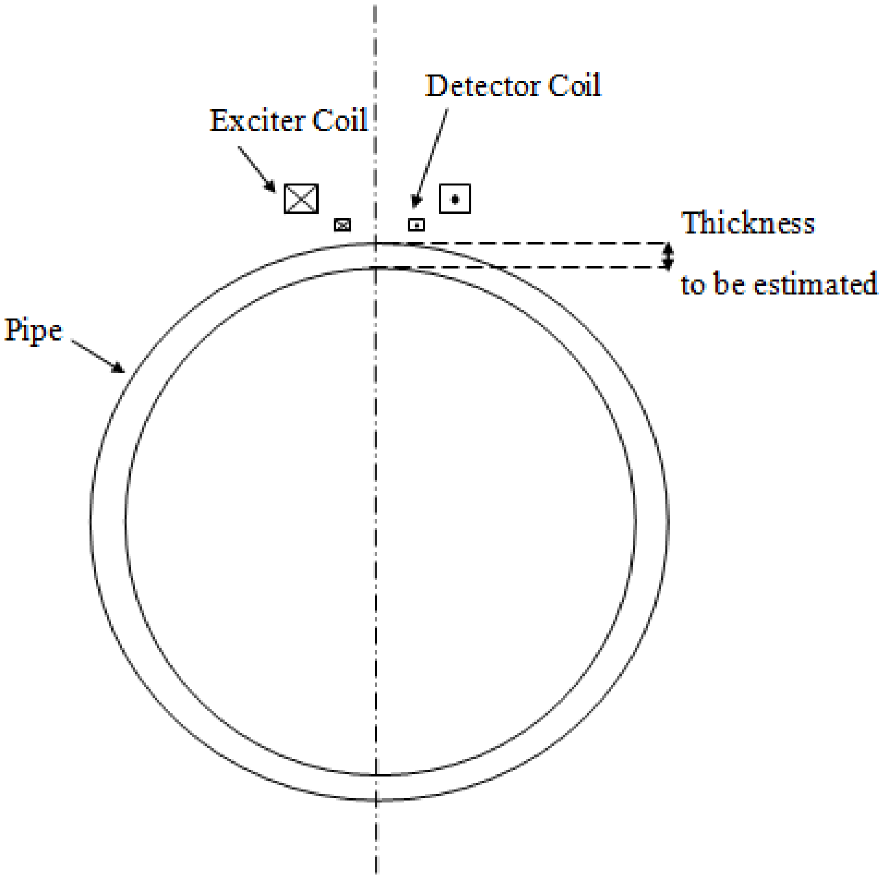

Figure 2.3: Cross-sectional view of the typical detector coil based PEC sensor architecture used for pipe thickness assessment (The figure is not drawn to scale).

critical pipe evaluation with the use of existing signal processing and feature extraction techniques is not straightforward. To address the issue, this thesis proposes the “detector coil voltage decay rate” as a signal feature relevant to this architecture since it exhibits desirably reasonable insensitivity to lift-off as shown in the chapters to follow.

2.2.2 Non-Detector Coil Based PEC Sensor Architecture

The non-detector coil based architecture uses magnetic sensors such as SQUIDs, Hall-effect sensors and magnetoresistive sensors to detect the magnetic field instead of the detector coil in the previous architecture [1]. This architecture is not commonly used for ferromagnetic material assessment, however, it has been used on a few occasions with limited applicability [13, 32, 33]. Most commonly this architecture is used for thickness estimation [36], defect detection [37] and achieving lift-off invariance [38, 39] in relation to nonmagnetic materials. An advantage of this architecture is the use of small magnetic sensors instead of large detector coils enabling it to achieve higher resolution than the detector coil based architecture.

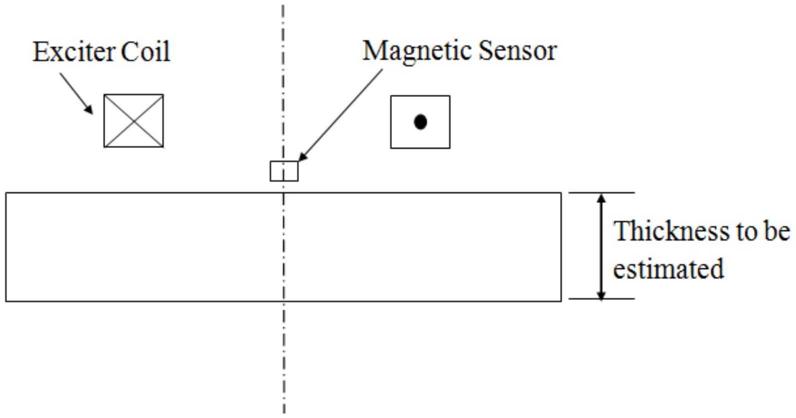

FIGURE 2.4: Cross-sectional view of the typical non-detector coil based PEC sensor architecture.

A magnetoresistive sensor has been used in [13] to assess carbon steel pipe wall thicknesses up to 10 mm. Reference [33] has presented a way of using a Hall-effect sensor supported by a ferrite core to evaluate stainless steel thicknesses up to 5 mm. Using magnetization to improve the sensitivity of a sensor is proposed in [32] to detect and quantify subsurface defects in ferromagnetic steels. It is hence evident that when this architecture is used to assess ferromagnetic materials, it has been mostly applied on low thickness steels. The objective of this thesis however, is not only to assess steels, but also to assess gray and ductile cast irons having thicknesses up to 30 mm. Work which suggest the usability of this architecture on nonlinear and inhomogeneous ferromagnetic materials such as cast irons having high thicknesses is rare and consequentially this architecture is not preferred for the work of this thesis.

2.3 PEC Based Ferromagnetic Material Thickness Quantification

Since the rationale behind selecting the PEC inspection technique and the detector coil based architecture for the target application of this thesis have been clarified , this section focuses on reviewing previous PEC related work in conductive ferromagnetic material thickness estimation and highlighting application specific signal noise suppression and thickness discriminative feature extraction techniques.

2.3.1 Application Specific Noise Suppression Techniques

PEC signals are time varying induced voltages or currents in the detector due to the net magnetic field resulting from excitation and electromagnetic interaction with the test piece. Signals resulting from excitations used in practice are usually small in magnitude and do not exceed the millivolt scale irrespective of the type of detector. Given the small magnitude of signals, they are highly susceptible to noise [40]. Therefore, appropriate signal conditioning, noise suppression and amplification are essential to acquire signals in the quality suitable for extracting discriminative features to perform condition assessment.

Signal conditioning done in hardware is no different from any standard signal acquisition device as long as minimal distortion is introduced. Amplification and filtering are usually done before sampling and storing the signals. Operational amplifier based amplification [41] and active filtering [42] techniques are used as in any common low voltage electronic system. The thesis [40] has presented the complete design and implementation steps of a PEC system. In [40], a second order Sallen and Key [43] low pass filter is used and amplification is done using an instrumentation amplifier [44] before digital sampling. The hardware signal conditioning methods are not fixed by any means and there is freedom to use any filtering [42] and amplification [41] mechanism depending on the desired signal quality expected at the input of the sampling stage, however, minimal distortion is desired.

Digital sampling networks are known to introduce noises which are unique to the sampling circuitry, and therefore software based signal noise suppression is required to further cleanse the signals [40]. When it comes to software based noise suppression, there are a few unique techniques which are used on PEC signals [40]. Some tailor made methods for signals captured using detector coils have been researched and published as well [2, 3].

As in hardware filtering, the desired feature in software based filtering techniques used on PEC signals is introducing minimal distortion since preserving the original shape of signals is essential to derive relationships between test piece geometry and signal features. Therefore, software implemented counterparts of commonly used filtering techniques such as Chebyshev, Butterworth and Bessel [45, 46], are not generally used due to their tendency to introduce distortion. Instead, techniques such as acquiring multiple signals and averaging, Mean filtering and Gaussian filtering are used [40].

Averaging multiple signals which are synchronized is a useful distortion free noise suppression technique and is used in the digital signal processing stage of the commercial PEC signal acquisition unit (Fig. 1.1) used in this thesis. Mean and Gaussian filters have been examined only on signals acquired by means of magnetic sensors (e.g. Hall-effect) as done in [40] and therefore not used for this work where signals are acquired by means of a detector coil. On the contrary, the techniques proposed in [2] and [3] are applied explicitly on detector coil based signals and are more relevant to this thesis.

Reference [2] introduces a noise suppression method which improves the signal to noise ratio (SNR) up to about 40 dB. Improvement of signal discriminative capability resulted by filtering can clearly be seen in Fig. 2.5. The signals have been acquired for different thicknesses of steel using a step wedge Q235 steel plate at a constant lift-off of 20 mm. Steps included in the noise suppression method are:

1. Recording multiple PEC signals and calculating the averaged PEC signal.
2. Performing double logarithmic transform of the averaged PEC signal (refers to expressing both signal voltage and time in logarithmic scale).
3. Processing the signal from step(2) by median filtering.
4. Performing an invert signal transformation to Cartesian domain (optional).

As mentioned before, signals of [2] are detector coil based and are very similar to the signals worked with in this thesis, and recording multiple signals and averaging is done in the digital signal processing stage of the PEC signal capturing unit used in this thesis. However, averaging alone is insufficient to obtain desired signal quality. That is why [2] has proposed using a median filter to further suppress the noise. As seen by the results, median filtering can be considered to be very effective in suppressing detector coil based

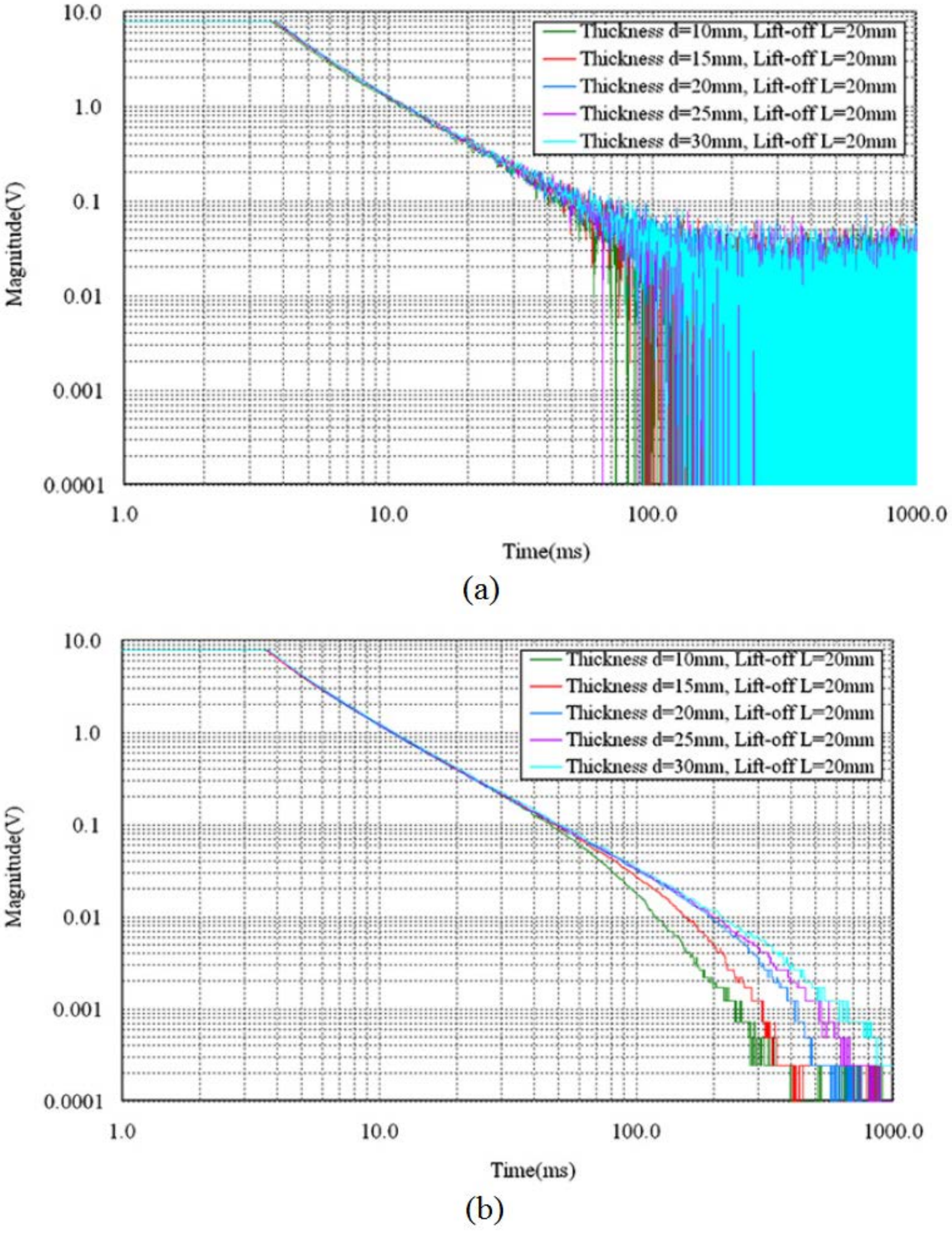

FIGURE 2.5: Detector coil based PEC signals processed in [2], acquired on Q235 steel: (a) Signals before filtering; (b) Signals after filtering

PEC signal noise. However, median filters too may introduce distortion if the filter order is not properly selected [47] and therefore is not employed for signal processing in this thesis.

Reference [3] introduces a distortion free noise suppression technique based on numerical cumulative integration. Fig. 2.6 shows signals processed in [3] and the signals have been acquired on different thicknesses of Q235 steel.

The time domain PEC signal (voltage induced in the detector coil) is integrated over time and an analytical model is fitted by approximating the cumulative integration of noise (average over time) to zero. Certain estimated analytical model parameters exhibit functional behavior usable to quantify thickness of ferromagnetic plates. This noise suppression technique is highly desirable for PEC signal processing since it does not introduce distortion and therefore was considered incorporable for the work of this thesis. The approach of approximating average of noise to zero is exploited in this thesis to fit a straight line to the late stage of the induced detector coil voltage to extract the “detector coil voltage decay rate” signal feature. Hence, the procedure followed in this thesis to extract the proposed feature uses the fundamental of approximating average noise to zero as done in [3]. Advantages and disadvantages of the noise suppression techniques in relation to the target application of this thesis are summarized in Table 2.1.

2.3.2 Thickness Discriminative Feature Extraction Techniques

Traditional PEC signal features used for metal test piece property and defect quantification can be classified as: time domain signal features [14, 39], frequency spectrum features [33, 48, 49], principal components [50, 51] and integral features [52]. Among those works related to traditional features, [14] is related to ferromagnetic materials and [33] and [48] are related to evaluating stainless steel thicknesses up to 5 mm. The rest have all been evaluated on non-ferromagnetic materials with non-detector coil based sensors, therefore, they are not directly related to the this thesis.

References [33] and [48] use Hall-effect sensors to evaluate thickness of stainless steel by using features of the power spectral density to discriminate thickness. However, thickness sensitivity has been evaluated only up to 5 mm. Since the signals are acquired using Hall-effect sensors and not detector coils, the feature extraction methods are not directly incorporable with this thesis. Further, the features have not been evaluated on higher thicknesses and other ferromagnetic magnetic materials such as gray and ductile cast

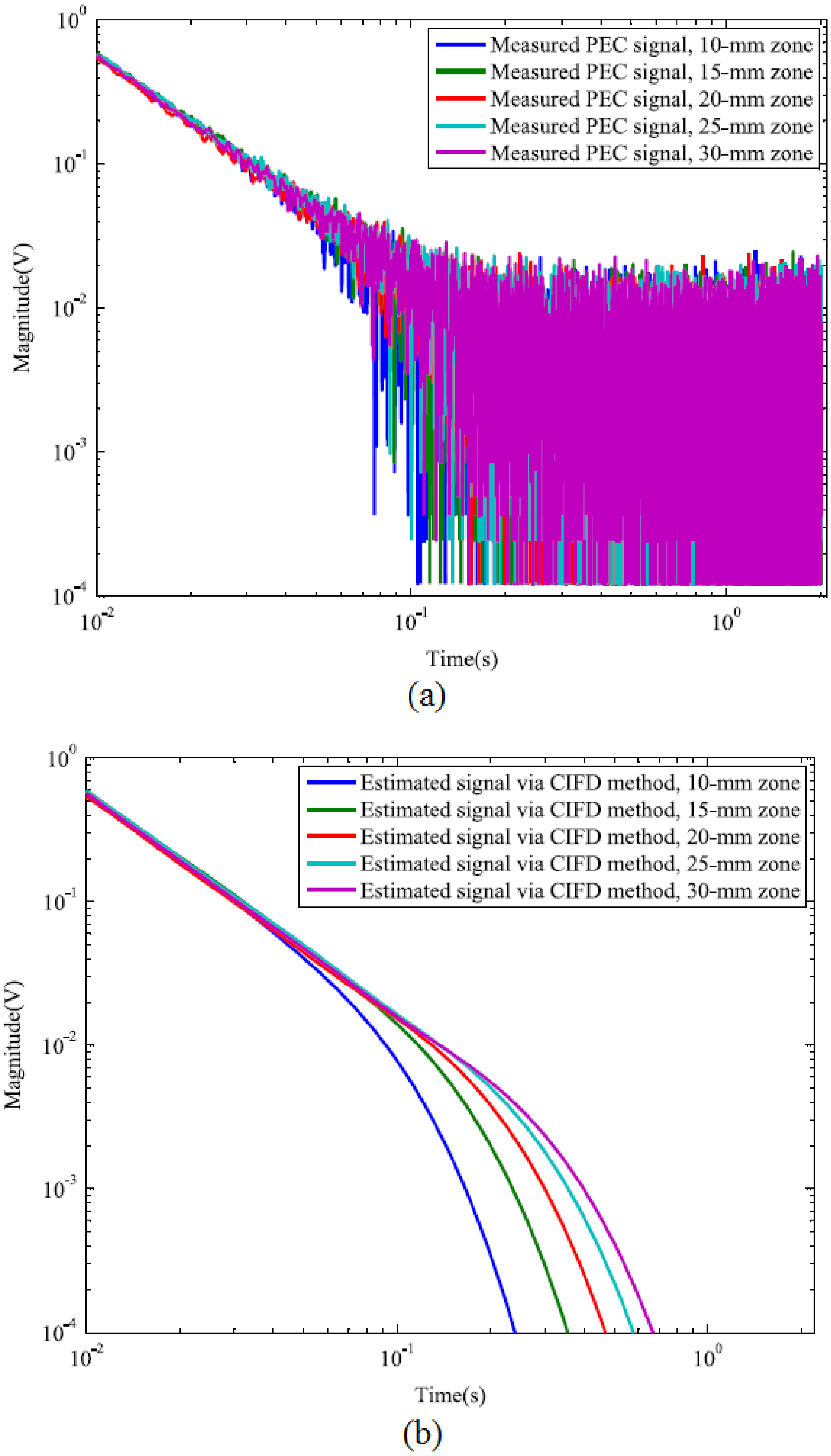

FIGURE 2.6: Detector coil based PEC signals processed in [3], acquired on Q235 steel: (a) Signals before processing; (b) Signals after processing

Table 2.1: Summary of advantages and disadvantages of the application specific signal noise suppression techniques in relation to the target application of this thesis.

Technique	Advantages	Disadvantages	Used in this thesis?
Hardware filtering [40]	Useful as the first stage of filtering.	Requires complex hardware, likely to introduce high distortion if not properly designed.	Yes (Embedded within the commercial kit)
Averaging multiple signals [2, 40]	Digitally implementable, distortion free.	Requires synchronization.	Yes (Embedded within the commercial kit)
Mean filtering [40]	Digitally implementable.	Tested on non-detector coil based signals, may introduce distortion if the window width is not properly selected	No
Gaussian filtering [40]	Digitally implementable.	Tested on non-detector coil based signals, may introduce distortion if the window width is not properly selected	No
Median filtering [2]	Digitally implementable.	May introduce distortion if the filter order is not properly selected	No
Analytical model fitting [3]	Digitally implementable, distortion free.	Minimal, requires determining the analytical model which describes the underlying noise free signal	Yes

irons, which are materials of interest for this thesis. Therefore, the feature extraction methods proposed in [33] and [48] are not incorporated in this thesis.

The detector coil based architecture is used in [14] with the main purpose of finding an efficient and easy-to-use signal feature for the assessment of ferromagnetic pipe wall thinning. Analytical modeling for a detector coil based PEC probe placed over an insulated piping system is performed and its result is verified by experimental test. Two commonly used time-related features, the peak value and the time-to-peak, are found in the differential signal obtained by subtracting the test signal from a reference signal. The time-to-peak is found to be superior to the peak value due to its linear variation with wall thickness.

Influences of various conditions in practical testing on the PEC signal are investigated. Results show that the time-to-peak is independent of the insulation thickness and the probe lift-off. Robustness of time-to-peak to probe configuration is also validated by employing three probes of different dimensions and structures. To determine the linear range of time-to-peak with amount of wall thinning, differential signals based on different reference thicknesses are examined. However, results show that the time-to-peak only keeps linear for relative wall thinning less than 60%, which is a drawback and therefore this feature extraction technique is not used in this thesis. Despite that the technique could still be useful for calibration purposes in periodical in-service inspection of insulated pipelines.

Publications [20] and [32] focus on defect identification in ferromagnetic materials. In [20], a remote field eddy current sensor (RFT) has been energized by a PEC excitation to detect axisymmetric surface slot defects on ferromagnetic tubes by examining the variations of the induced detector coil voltage features. However, since the RFT sensing technique is used and the fact that the focus is on defect detection, this work cannot be coupled with this thesis. Using magnetization to improve the sensitivity of the time domain reference subtracted PEC difference signal features was proposed in [32] to detect and quantify subsurface defects in ferromagnetic steels. Although the features used in [20] and [32] are effective on defects, their effectiveness on ferromagnetic material thickness quantification has not been examined, as a result those feature extraction techniques are not incorporated in this thesis.

Several analytical methods which are directly related to ferromagnetic material thickness quantification have been proposed [4, 36, 53]. Such methods are the most closely related ones to the focus of this thesis. References [36] and [53] follow similar approaches in modeling Hall-effect sensor readings and PEC difference signals respectively, when used on non-ferromagnetic materials. In the context of ferromagnetic materials however, sensitivity of those sensing techniques to thickness have not been evaluated and consequently, those techniques are not made use of in this thesis.

Recent work [3] and [4] have proposed methods of fitting analytical models for detector coil based PEC sensor signals. Those publications exhibit the appreciable thickness sensitivity of the induced detector coil voltage to ferromagnetic material thickness. Thickness sensitivity up to 25 to 30 mm have been achieved for steel. Having sensitivity up to about 30 mm is greatly desired for critical pipe evaluation. The gray cast iron pipes which are evaluated in this thesis have maximum thicknesses up to 30 mm [9]. Therefore, the analytical model for PEC detector coil voltage used in [3] and [4] is exploited in this thesis. The "detector coil voltage decay rate" signal feature proposed in this thesis is derived starting from that analytical model.

In [4] where the analytical model was first published, a detector coil based PEC sensor placed above a conductive ferromagnetic plate is modeled as an infinite set of mutually coupled coils. That analysis yields an analytical model in the form of an infinite summation of exponentials, to the induced detector coil voltage (PEC signal). This analytical model is then fitted to experimentally captured PEC signals by estimating model parameters [3, 4]. Some model parameters exhibit monotonic variation with thickness up to about 30 mm. It is suggested that such model parameters may be used for in situ ferromagnetic material condition assessment purposes such as critical pipe assessment. However, [3] and [4] have not developed and validated complete frameworks on in situ pipes. Therefore, the objective of this thesis has not been accomplished in those works. This thesis hence builds upon the theoretical models used in [3] and [4] to propose a novel PEC signal feature which shows some low dependence to lift-off, sensor shape, and size; and use the feature to learn a thickness-feature function, and use the learned function to estimate wall thickness of in situ critical water pipes.

A similar analytical model for the detector coil based PEC architecture has been proposed in [54] and it has been used to simultaneously quantify material properties and thickness of carbon steel by fitting to PEC data and estimating model parameters [35]. However, that model is defined for concentric circular sensors, hence cannot be used with non-circular sensors; and that approach requires the lift-off to be accurately known. In critical pipe related applications, pipe surfaces are not always clean and the healthy ferromagnetic material is often covered by corrosion and graphitization layers. Therefore, knowing an accurate measure of lift-off is not always possible. Therefore, although the model parameter estimation methods do perform well in thickness assessment of flat plates at constant and supposedly known lift-offs, they do comprise vulnerabilities in relation to the particular application of in situ critical pipe evaluation. That is why the "detector coil voltage decay rate" feature introduced in this thesis is required since it demonstrates low dependence on lift-off, and some other factors which makes the feature immune to practical challenges encountered during in situ critical pipe wall thickness assessment. Consequentially, this thesis brings novelty by introducing a PEC signal feature having a significant lift-off invariance which is suitable for in situ critical pipe assessment. Aspects associated with previously proposed feature extraction techniques which limit their applicability for the work of this thesis are summarized in Table 2.2.

TABLE 2.2: Aspects associated with previously proposed feature extraction techniques which limit their applicability for the work of this thesis.

References	Technique	Limiting Aspects
[33, 48]	Power spectral density features.	Analysis done only on stainless steel, thickness sensitivity reported up to 5 mm, study based on Hall-effect sensors.
[14]	Features of the time domain difference signal.	Limited applicability, linearity observed for relative wall thinning less than 60%.
[20, 32]	Features of the detector coil voltage.	Focused on defect identification, possibility of thickness discrimination not reported.
[36, 53]	Analytical modeling of Hall device readings and difference signals.	Tested only on non-ferromagnetic materials
[3, 4, 35, 54]	Analytical model parameter estimation.	Lift-off insensitivity not demonstrated, have not been evaluated on in situ ferromagnetic pipes.

2.4 Effect of PEC Sensor Geometry on Measurement Capabilities

Resolution of the detector coil based PEC sensor architecture is limited by the size of the detector coil, and in general, the size of the sensor. In simple terms, larger the sensor, larger the region impacted by the magnetic field will be, and consequently, the interpreted condition will be an averaged representation of a large region of the test piece [34]. Though the resolution can be increased by reducing the size, that limits the spread of the magnetic field and results in not being able to assess thick material since the eddy current penetration depth will be lower. Theoretically, it can be argued that increasing the strength of excitation will compromise the reduction of magnetic field spread caused by the reduction of size. But then again, the amount of increase allowable to the excitation is limited by the available electronic circuitry and related hardware. Therefore, for a given strength of excitation, achieving deep penetration can usually be done at the cost of sacrificing resolution [40].

Studies on the effect of PEC sensor geometry on measurement capabilities are rare. The doctoral thesis [40] presents a fairly comprehensive FEA based numerical study on the influence of shielding, including and excluding a ferrite core and the size of the excitation coil on eddy current penetration and lateral spread caused by a Hall-effect based PEC sensor. There is no exact analytical technique to determine the most effective design and sensor size [40]. The study has found that shielding has a tendency to increase penetration depth while reducing the lateral spread, which are desirable characteristics. Including a core has the tendency to further reduce the lateral spread which is desirable again, but that will also reduce the penetration depth which is undesired. In addition, the influence of the geometry of the excitation coil has also been studied. The findings are:

1. The larger the internal radius, the deeper the penetration and the larger the lateral spread of eddy currents.
2. The larger the outer radius, the deeper the penetration and the larger the lateral spread of eddy currents.
3. The smaller the height, the deeper the penetration and the larger the lateral spread of eddy currents.

Though [40] has presented important knowledge on the effect of the excitation coil geometry on the spread of eddy currents, the study is limited to non-ferromagnetic materials. Further, the effect of sensor geometry on the sensitivity of thickness discriminative signal features based on the detector coil architecture has not been studied.

Since a study on ferromagnetic materials has not been done in [40], this thesis brings forth a detailed numerical study (using FEA) to aid understanding the influence of detector coil based sensor geometry on the thickness discriminative capability of the “detector coil voltage decay rate” signal feature. The objective is to find how the sensor resolution can be increased so that the detection of fine and isolated flaws on ferromagnetic materials becomes viable.

2.5 Conclusions

This chapter reviewed the various EC inspection techniques and clarified the necessity of the PEC technique for geometric condition assessment of conductive ferromagnetic materials. Various PEC sensor architectures were then reviewed and the use of the detector coil based architecture for the target application of this thesis was justified. Application specific signal conditioning and noise suppression techniques were reviewed while discussing the importance of distortion free signal processing. The distortion free noise suppression methods of fitting analytical models to noisy signals by approximating the average noise to be zero was identified as the method suitable for the target application of this thesis. Existing ferromagnetic material thickness discriminative feature extraction techniques were reviewed eventually. The fact that the influence of lift-off on proposed features not being studied and quantified was identified as a limitation in the usability of the available feature extraction techniques in complex scenarios like critical pipe evaluation. Therefore, the requirement of the novel signal feature introduced in this thesis is warranted. Finally, existing knowledge on the influence of sensor geometry on measurement capabilities was reviewed. Previous studies were found to be limited to effects on eddy current penetration depth and lateral flow in non-ferromagnetic materials. Therefore, room for analyzing the impact on the sensitivity of thickness discriminative signal features for ferromagnetic materials and the effect of sensor geometry on measurement was identified.

Chapter 3

Detector Coil Voltage Decay Rate as a Thickness Discriminative PEC Signal Feature

This chapter introduces the detector coil voltage decay rate as a thickness discriminative PEC signal feature suitable for condition assessment of conductive ferromagnetic materials. Analytical derivation of a parametric function which maps the feature value to thickness is presented. Functional behavior between thickness and the feature is demonstrated for pipe materials using decay rate values extracted from PEC signals experimentally obtained using calibration blocks. Some unique low dependencies associated with the decay rate feature are identified and experimentally verified. These low dependencies make the feature immune to certain practical challenges encountered during in situ application such as having to investigate via non conducting and non magnetic coatings and undesired lift-off being present in the form of irremovable dirt deposits on pipe surfaces. The low dependencies are exploited in the work of Chapter 5. Since the target application is critical pipe evaluation, and the fact that pipe walls are curved unlike calibration blocks, the effect of test piece curvature on the decay rate feature is studied using FEA. The study presented within this chapter is tailored for the PEC sensor used in this thesis and gray cast iron as the material being tested. However, the analysis method generalizes and can be used to evaluate any PEC sensor architecture on any material by incorporating required sensor and material properties. On confirming the feature's validity on large diameter pipe structures, the analytically derived thickness-feature function is used to estimate wall thickness of in situ critical pipes. Finally, performance of the decay rate feature when used for in situ critical pipe NDE via the analytical approach is evaluated. Requirement of calibration blocks is identified as a limitation in this NDE approach. Therefore, a method exploiting ultrasounds is introduced to directly transform feature values to thickness without the use of calibration blocks. The chapter concludes by discussing the performance, nonlinearities and limitations associated with the analytical approach for critical pipe NDE and characterizes sensor noise to be used in the following chapter.

3.1 Analytical Derivation of the Functional Behavior between Thickness and the Decay Rate Feature

A detector coil based PEC sensor placed above a conducting test piece, when not affected by external sources of noise, can be modeled in circuit theory as a setup composed of infinitely many mutually coupled coils [4]. Fig. 3.1 shows how [4] models a circular PEC sensor placed above a conducting ferromagnetic plate as a set of mutually coupled coils.

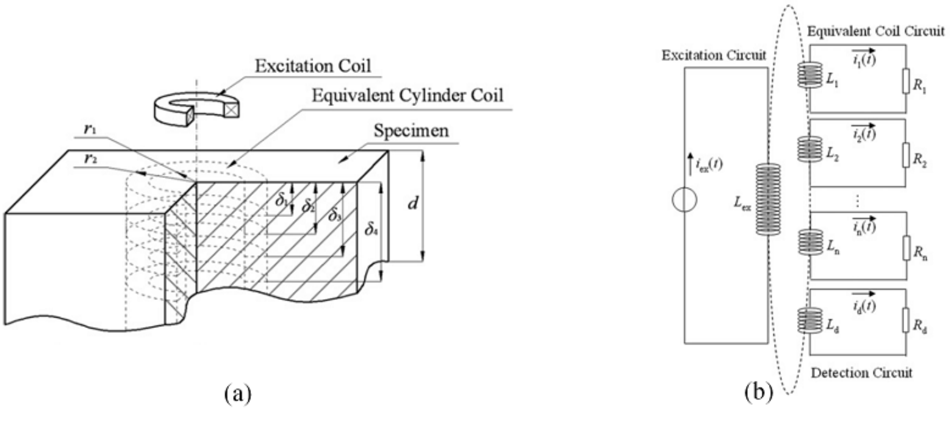

Figure 3.1: Mutually coupled coil architecture for PEC sensor modeling: (a) Mutually coupled coil model; (b) equivalent circuit model for pulsed eddy current testing system. (adapted from [4]).

As done in [4], by applying Kirchhoff's laws to every current carrying coil in the model considering coil resistances (denoted by R terms), self inductances (denoted by L terms)

$$
\begin{array}{l}
i_{ex}(t) = Au(t) \\
M_{1ex}\frac{di_{ex}(t)}{dt} - L_1\frac{di_1(t)}{dt} + M_{12}\frac{di_2(t)}{dt} + M_{13}\frac{di_3(t)}{dt} \cdots + M_{1n}\frac{di_n(t)}{dt} + M_{1d}\frac{di_d}{dt} - R_1 i_1(t) = 0 \\
M_{2ex}\frac{di_{ex}(t)}{dt} - M_{21}\frac{di_1(t)}{dt} - L_2\frac{di_2(t)}{dt} + M_{23}\frac{di_3(t)}{dt} \cdots + M_{2n}\frac{di_n(t)}{dt} + M_{2d}\frac{di_d}{dt} - R_2 i_2(t) = 0 \\
M_{3ex}\frac{di_{ex}(t)}{dt} - M_{31}\frac{di_1(t)}{dt} - M_{32}\frac{di_2(t)}{dt} - L_3\frac{di_3(t)}{dt} \cdots + M_{3n}\frac{di_n(t)}{dt} + M_{3d}\frac{di_d}{dt} - R_3 i_3(t) = 0 \\
\qquad\qquad\qquad\qquad\vdots \\
M_{(n-1)ex}\frac{di_{ex}(t)}{dt} - M_{(n-1)1}\frac{di_1(t)}{dt} - M_{(n-1)2}\frac{di_2(t)}{dt} \cdots - L_{n-1}\frac{di_{n-1}(t)}{dt} + M_{(n-1)n}\frac{di_n(t)}{dt} + M_{(n-1)d}\frac{di_d}{dt} - R_{n-1} i_{n-1}(t) = 0 \\
M_{nex}\frac{di_{ex}(t)}{dt} - M_{n1}\frac{di_1(t)}{dt} - M_{n2}\frac{di_2(t)}{dt} \cdots - M_{n(n-1)}\frac{di_{n-1}(t)}{dt} - L_n\frac{di_n(t)}{dt} + M_{nd}\frac{di_d}{dt} - R_n i_n(t) = 0 \\
M_{dex}\frac{di_{ex}(t)}{dt} - M_{d1}\frac{di_1(t)}{dt} - M_{d2}\frac{di_2(t)}{dt} \cdots - M_{d(n-1)}\frac{di_{n-1}(t)}{dt} - M_{dn}\frac{di_n(t)}{dt} - L_d\frac{di_d(t)}{dt} - R_d i_d(t) = 0
\end{array}
$$

FIGURE 3.2: Simultaneous differential equations governing the mutually coupled coil model (adapted from [4]).

and mutual inductances (denoted by M terms), the set of simultaneously solvable differential equations shown in Fig.3.2 can be derived for a pulsed current excitation $Au(t)$, where A denotes amplitude and $u(t)$ denotes the Heaviside step function. Solving the set of equations yields an expression consisting of an infinite summation of exponents and an infinite summation of sinusoidal oscillations for the induced detector coil voltage. Considering the practical circumstance where the signal is conditioned by amplifiers and filters, the oscillations can be ignored and the analytical model in Eq. 3.1 which represents the decaying part of a PEC induced detector coil voltage can be derived [4].

$$V(t) = \sum_{i=1}^{\infty} b_i \exp(-c_i t) \tag{3.1}$$

Terms b_i and c_i in Eq. 3.1 are constants which contain the properties of the sensor setup and the test piece. The condition $c_i > 0$ holds for all i [4]. By means of linear and homogeneous representation of magnetic permeability μ and electrical conductivity σ, the diffusion time constant of eddy currents induced in a ferromagnetic plate of thickness d is defined as $\mu\sigma d^2/\pi^2$ [30]. Steps for deriving this expression for the time constant is provided in Appendix D. This is the largest time constant appearing in an exponential term within the infinite summation of Eq. 3.1, in return the corresponding exponential term becomes dominant in the late stage of the signal (the stage of the signal immediately before the eddy currents decay towards zero) [30]. In this thesis, the dominant term is isolated and

$V(t)$ is rewritten as

$$V(t) = b_1 \exp\left(\frac{-\pi^2 t}{\mu\sigma d^2}\right) + \sum_{i=2}^{\infty} b_i \exp(-c_i t). \tag{3.2}$$

The intention is to obtain the time derivative of $V(t)$ to express the decay rate. Before differentiating, $V(t)$ is expressed in natural logarithmic form in this thesis.

$$\ln[V(t)] = \ln\left[b_1 \exp\left(\frac{-\pi^2 t}{\mu\sigma d^2}\right) + \sum_{i=2}^{\infty} b_i \exp(-c_i t)\right] \tag{3.3}$$

This logarithmic representation is necessary to obtain a direct proportionality between the thickness in the form of $1/d^2$ and the decay rate in addition to the exponential relationship which already exists. The later stage of a noise free PEC signal in the form of $V(t)$ becomes a positive valued decreasing convex function of time which can be characterized by a summation of exponential decays as Eq. 3.1 suggests. If the logarithm of this region is considered, $\ln[V(t)]$ also becomes a decreasing function, typically a convex one. Though decrease of $\ln[V(t)]$ is obvious, confirming convexity or concavity is not straightforward, however to check that in theory the second derivative of $\ln V[t]$ should be considered. $V'(t)$ and $V''(t)$ denote the first and second time derivatives of $V(t)$ respectively.

$$\frac{\mathrm{d}^2 \ln[V(t)]}{\mathrm{d}t^2} = \frac{V(t)V''(t) - [V'(t)]^2}{[V(t)]^2} \tag{3.4}$$

According to principles of convex functions [55–57], a positive second derivative confirms convexity and a negative one ensures concavity. Therefore,

$$V(t)V''(t) > [V'(t)]^2 \tag{3.5}$$

is the sole condition which needs to be satisfied for $\ln[V(t)]$ to be convex for a prescribed period of time. Parameters of Eq. 3.1 can be estimated as done in [4] for a given PEC signal and be used to check the condition in Eq. 3.5 to verify convexity. Alternatively, this can easily be identified by studying signals plotted against time as in Fig. 3.5. $\ln[V(t)]$ for materials considered in this paper are convex. Since this behavior is common to many ferromagnetic and non-ferromagnetic materials, convexity in the late stages of $\ln[V(t)]$ is usually the norm. However, existence of concavity is not impossible although rare. Differentiating Eq. 3.3 yields Eq. 3.6 which is a negative valued function since $\ln[V(t)]$ is decreasing with time in its decaying part.

$$\frac{\mathrm{d}\ln[V(t)]}{\mathrm{d}t} = -\frac{\dfrac{b_1\pi^2}{\mu\sigma d^2}\exp\left(\dfrac{-\pi^2 t}{\mu\sigma d^2}\right) + \displaystyle\sum_{i=2}^{\infty} b_i c_i \exp(-c_i t)}{b_1 \exp\left(\dfrac{-\pi^2 t}{\mu\sigma d^2}\right) + \displaystyle\sum_{i=2}^{\infty} b_i \exp(-c_i t)}. \tag{3.6}$$

By grouping exponential terms, the absolute value of the decay rate can be expressed as

$$\left|\frac{\mathrm{d}\ln[V(t)]}{\mathrm{d}t}\right| = \frac{\pi^2}{\mu\sigma d^2}\left\{\frac{1+\displaystyle\sum_{i=2}^{\infty}\frac{b_i}{b_1}\left[\frac{c_i}{\pi^2/(\mu\sigma d^2)}\right]\exp\left[\left(\frac{\pi^2}{\mu\sigma d^2}-c_i\right)t\right]}{1+\displaystyle\sum_{i=2}^{\infty}\frac{b_i}{b_1}\exp\left[\left(\frac{\pi^2}{\mu\sigma d^2}-c_i\right)t\right]}\right\}. \tag{3.7}$$

Since $\mu\sigma d^2/\pi^2$ is the largest time constant and $c_i > \pi^2/(\mu\sigma d^2)$ holds for all i, we express the main relationship used for our work, the reciprocal of the absolute value of the decay rate as

$$\beta(t) = \left|\frac{\mathrm{d}t}{\mathrm{d}\ln[V(t)]}\right| = \frac{\mu\sigma d^2}{\pi^2}\left\{\frac{1+\displaystyle\sum_{i=2}^{\infty}\frac{b_i}{b_1}\exp\left[-\left(c_i-\frac{\pi^2}{\mu\sigma d^2}\right)t\right]}{1+\displaystyle\sum_{i=2}^{\infty}\frac{b_i}{b_1}\left[\frac{c_i}{\pi^2/(\mu\sigma d^2)}\right]\exp\left[-\left(c_i-\frac{\pi^2}{\mu\sigma d^2}\right)t\right]}\right\}. \tag{3.8}$$

The absolute value of the decay rate thus characterizes the whole decaying part of a PEC induced detector coil voltage in the absence of noise. Since the relationship in Eq. 3.8 is composed of exponential terms, it is differentiable with respect to time. Given the typical convex decrease of the noise free logarithmic PEC signal (Fig. 3.5 shows noisy experimental signals), its derivative will be a negative valued increasing function of time. Therefore, the absolute decay rate will be a positive valued decreasing function. This causes $\beta(t)$, the reciprocal of the absolute decay rate to be a positive valued monotonically increasing function of time. It can thus be concluded that for a given thickness d of a material having properties μ and σ, the relationship for $\beta(t)$ is a monotonically increasing function of time which reaches a maximum of $\mu\sigma d^2/\pi^2$ as t reaches infinity for materials producing convex $\ln[V(t)]$ signals. If $\ln[V(t)]$ becomes a concave decreasing function by any chance for a rare material, $\beta(t)$ will be a monotonically decreasing function which will reach a minimum of $\mu\sigma d^2/\pi^2$. This is a useful attribute of the decay rate when used for thickness quantification as demonstrated later in the chapter.

Monotonic increase for the case of this thesis suggests that $\beta(\infty) = \dfrac{\mu\sigma d^2}{\pi^2}$ (by applying $t \to \infty$ in Eq. 3.8), will be an ideal signal feature for thickness discrimination since it is directly proportional to the square of thickness. Under practical circumstances $t = \infty$ cannot be achieved since the signal will enter noise bounds of sensor sampling circuitry. Obtaining decay rates at the late stage (just before the signals enter the noise bound) is possible in practical applications. Therefore, the decay rate at late stages can be characterized by the approximation $\beta(t) \approx \dfrac{\mu\sigma d^2}{\pi^2}$. We therefore use β_{max}, the maximum achievable value of $\beta(t)$ of convex $\ln[V(t)]$ before the signals enter the noise margin as the discriminative signal feature for thickness quantification. If a concave $\ln[V(t)]$ is encountered, the feature will be the same, but should be defined as the minimum achievable value of $\beta(t)$, *i.e.*, $\beta_{min} \approx \dfrac{\mu\sigma d^2}{\pi^2}$.

Since the derived relationship was in the form of $\beta_{max} \approx \dfrac{\mu\sigma d^2}{\pi^2}$, in order to obtain direct proportionality between $\ln\beta_{max}$ and $\ln d$, it was opted to further model the relationship as $\ln\beta_{max} \approx 2\ln d + c$ where $c \approx \ln\left(\dfrac{\mu\sigma}{\pi^2}\right)$ is a constant. This approach allows to generalize the relationship by introducing a scalar offset c that encompasses the material properties μ and σ. Thus, the decay rate feature and the linear form of the thickness-feature function introduced in thesis can be expressed respectively as

$$\beta_{max} \approx \frac{\mu\sigma d^2}{\pi^2} \tag{3.9}$$

and

$$\ln\beta_{max} \approx 2\ln d + c \tag{3.10}$$

where

$$c \approx \ln\left(\frac{\mu\sigma}{\pi^2}\right). \tag{3.11}$$

To apply the thickness-feature function to perform condition assessment in the form of estimating thickness, c is the only parameter that requires to be estimated from material specimens. The parameter c for a particular material can be in practice estimated in several different ways. Firstly, particles of the specimen can be fed through SQUID or PPMS devices to measure electrical and magnetic properties. Alternatively, c can be estimated from a known thicknesses with a minimum of one calibration signal. Estimating c is further discussed in the remainder of this chapter.

3.2 Experimental Validation of the Behavior of the Decay Rate Feature

This section presents the experimental procedures followed and the validation of the linear thickness-feature function and the monotonic variation of the decay rate with time.

3.2.1 PEC Sensing Unit Used in this Thesis

All experiments including on site NDE related to this thesis were performed using the HSK 300 commercial PEC signal capturing unit provided by Rock Solid Group©. Fig. 3.3 shows the unit and available sensors.

PEC sensors from different sizes are available as shown in Fig. 3.3 (b). However, under obligatory requirements the 50 mm PEC sensor marked in Fig. 3.3 (b) was incorporated with this research. The 50 mm sensor is composed of a single exciter coil and a single detector coil. The exciter coil is rectangular in shape with a width of 50 mm and the detector coil takes the shape of a square whose side length is 50 mm. Coils are concentric, air cored and are made of copper. Subject to a nondisclosure agreement, publishing sensitive information about the sensor such as number of coil turns, wire radius and impedances is not possible. Such information is not critically important for this work and the technical contributions of this thesis is general for the detector coil based PEC sensor architecture irrespective of fine details.

Sensor excitation and capturing detected signals is done by the signal capturing unit. The sensor is excited by a periodic voltage pulse. Pulses generally take the shape of a Heaviside step function and it was agreed to not to publicize sensitive information such as pulse amplitude, rise time, duty ratio and frequency. All rising and falling edges of pulses induce time varying detector coil signals making the operating principle of this system no different from that of any other PEC setup. Detector coil signals are amplified and interfaced with a digital sampling network. Multiple signals are captured by the sampling network and are averaged to reduce noise. Averaged signals are sent to a PC via a USB interface to be visualized and saved. The typical shape of an averaged signal (detector coil voltage) produced by the unit is shown in Fig. 3.4.

3.2.2 Obtaining PEC Signals from Calibration Blocks made of Critical Pipe Materials

Experimental validation was initially done on calibration blocks made of ferromagnetic pipe materials where the signal acquisition was done in a laboratory setting. Calibration blocks are simply cuboid shapes manufactured to a fixed length and width but different

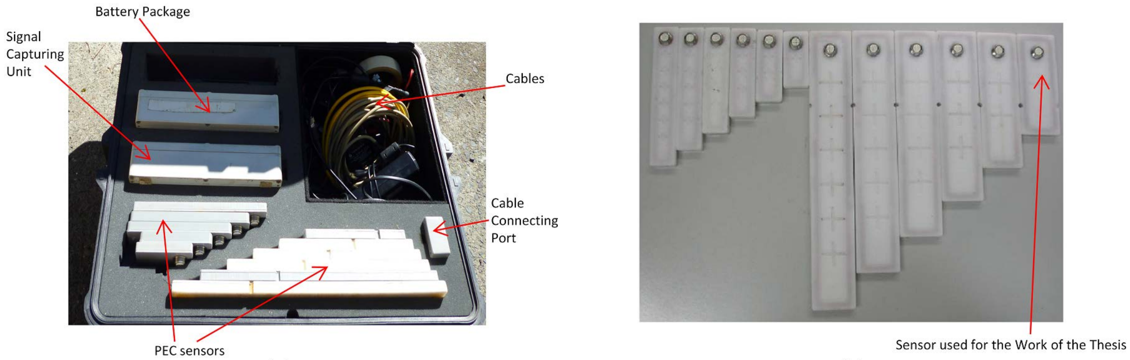

(a) (b)

Figure 3.3: PEC sensing unit used for the work of this thesis: (a) HSK 300 commercial PEC signal capturing unit; (b) 50 mm sensor used for this work (adapted from [5]).

heights (thicknesses). It was found through numerical simulations that edge effect associated with PEC measurements [1] can be minimized by placing the sensor at the center of calibration blocks which are significantly larger than the sensor. With respect to the particular sensor used in this work, simulations showed minimal edge effect when calibration block length and width were made equal to three times the sensor length and width respectively. Though calibration data from a single ferromagnetic material is sufficient to model the thickness-feature relationship, for completeness and to validate the generalization of the model, calibration data were obtained on gray cast iron, ductile cast iron and mild steel calibration blocks. The detailed thickness breakdown of all the blocks from which calibration data were acquired is provided in Table 3.1. Despite perfect linearity suggested by theory in Section 3.1, it should be noted that linearity is lost at very low and very high thicknesses due to practical limitations associated with the penetration capability of the sensor. Reasons for these nonlinearities are described later in Section. 3.6. Due to theses nonlinearities, only the thicknesses indicated in black in Table 3.1 are used to model the linear thickness-feature function while the low and high thicknesses marked in red are avoided. Three raw PEC measurements were taken on each block to capture system noise. Commonly encountered critical pipe wall thicknesses are available [58–60].

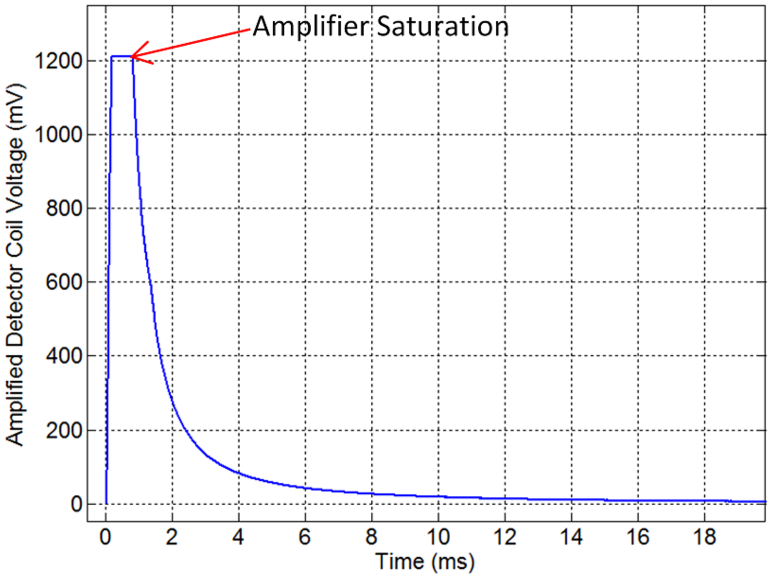

Figure 3.4: Typical shape of a PEC signal produced by the HSK 300 unit (Captured on a 30 mm thick gray cast iron calibration block).

TABLE 3.1: Ferromagnetic material calibration block thicknesses.

Material	Thicknesses (mm)
Mild Steel	1, 2, 3, 4, ..., 12, 13, 14, 15
Ductile Cast Iron	1, 2, 3, 5, 6, 8, ..., 18, 20, 22, 24, 27
Gray Cast Iron	1, 2, 3, 4, ..., 10, 12, ..., 22, 25, 30, 35

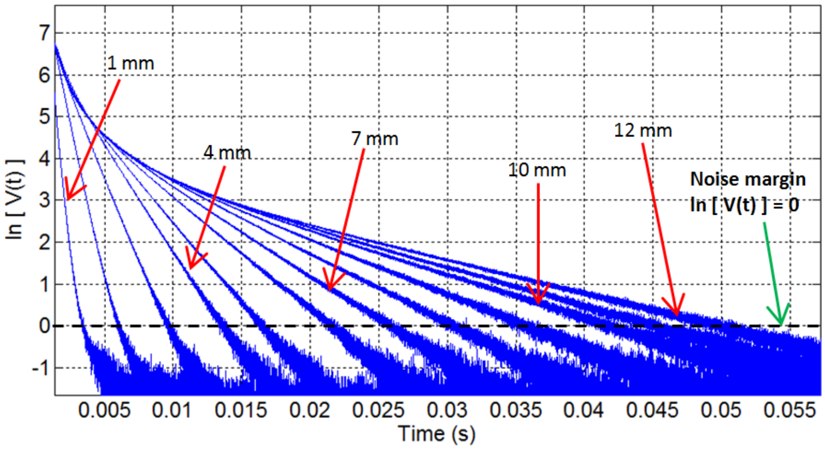

FIGURE 3.5: Decaying part of raw PEC signals for Mild Steel

Fig. 3.5 shows the set of PEC signals obtained for mild steel with the considered noise margin of $V(t) = 1$ mV marked. The y-axis of Fig. 3.5 represents $\ln V(t)$ instead of $V(t)$ as in Fig. 3.4 since the decay rate feature proposed in this chapter is incorporated with the logarithmic scale.

3.2.3 Experimental Validation of $\beta(t)$ Monotonicity

Presented in Fig. 3.6 is the time variation of mild steel related $\beta(t)$ computed using the signals in Fig. 3.5. Since the signals are sampled for a period within the millisecond range and the sampling interval of the signal acquisition setup is 10 μs, there are a few thousand samples for a signal. Time variation of $\beta(t)$ for each signal was calculated by fitting a straight line to a moving window containing 100 samples centered at each sample of the signal before entering the noise margin. Least square fitting of straight lines was performed since it encompasses the effective noise suppression technique of zero approximation of noise which was discussed in Subsection 2.3.1 and in [3]. It is evident in Fig. 3.6, that computing decay rates has been stopped at different times for different thicknesses. These stopping times correspond to the instances in Fig. 3.5 at which the signals cross the noise margin.

Theoretical observations made in Section 3.1 regarding the behavior of $\beta(t)$ through Eq. 3.8 can be summarized into two main properties.

- $\beta(t)$ monotonically increases with t for a given d of a particular material and asymptotically reaches a maximum as t tends towards ∞.
- though $t = \infty$ is not achievable, $\beta(t)$ at later stages will be sensitive to d and will monotonically increase with d^2 for a given material ($\beta(t) \approx \frac{\mu\sigma d^2}{\pi^2}$).

Curves in Fig. 3.6 can be considered as experimental evidence which support the validity of the above properties. The monotonic increase of $\beta(t)$ with time is evident for all the thicknesses (prior to entering the noise region at late stages of signal). The behavior suggests that the derivative of $\beta(t)$ is positive and is decreasing over time which indicates that $\beta(t)$ tends to an asymptotic maximum as t becomes large. These experimental observations are in agreement with the theoretically identified property of the relationship. Fig. 3.6 also shows that β_{max}, the feature used for thickness characterization in this work,

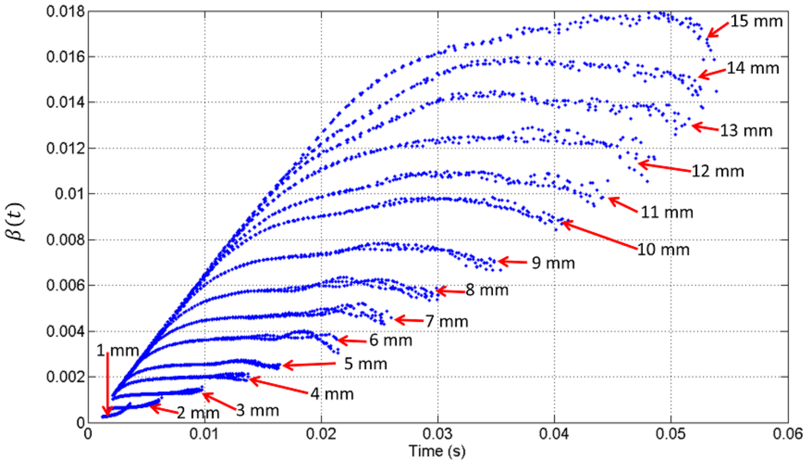

FIGURE 3.6: Behavior of decay rate β against time for different thicknesses of Mild Steel.

is monotonically increasing with d. This validates the second property, β_{max} directly represents $\beta(t)$ at late stages. Behaviors that are quantitatively different, but qualitatively identical to those of Fig. 3.5 and 3.6 were observed for ductile and gray cast irons as well.

3.2.4 Extracting β_{max} from Experimental PEC Signals

Derivations in Section 3.1 introduced the thickness discriminative PEC signal feature $\lim_{t\to\infty} \beta(t) = \beta_{max} \approx \dfrac{\mu\sigma d^2}{\pi^2}$. Hence, $\beta(t)$ which represents the gradient of $\ln[V(t)]$, becomes time invariant as t becomes large. Consequentially, $\ln[V(t)]$ should behave as a straight line. This behavior can be seen in Fig. 3.5 with the presence of noise when $\ln[V(t)]$ is less than about 2 for the whole mild steel thickness range. A similar behavior was observed for the other two critical pipe materials gray and ductile cast iron as well as shown in Fig. 3.7 and 3.8. Theoretically, this behavior should prevail until t becomes very large (*i.e.*, ∞). However, in practice, as the signals enter the noise margin of the sampling circuitry, the time within which a signal remains sensible is limited.

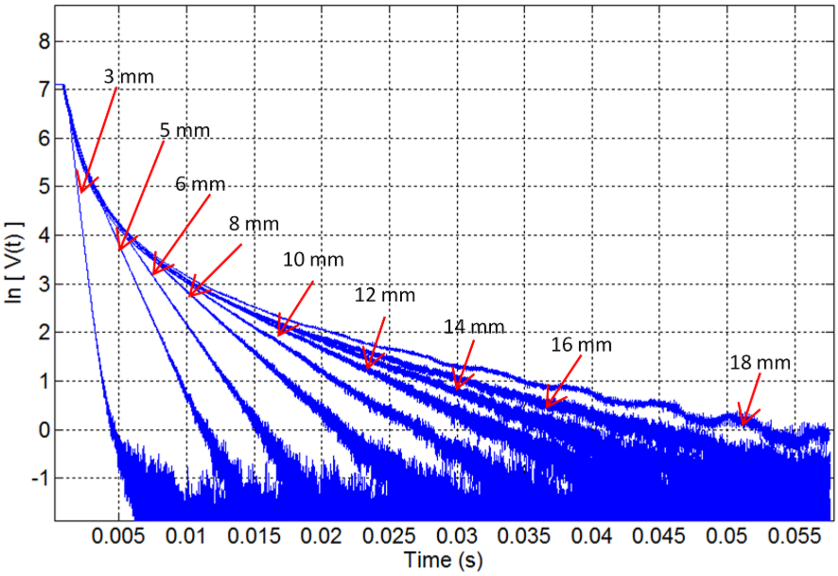

FIGURE 3.7: Decaying part of raw PEC signals for Ductile Cast Iron.

It can be observed from Fig. 3.5 that the noise contamination increases significantly when $\ln[V(t)] < 0$. That lured to the selection of $\ln[V(t)] = 0$ as the noise margin threshold for the sensor used in this work given the behavior was common for all three critical pipe

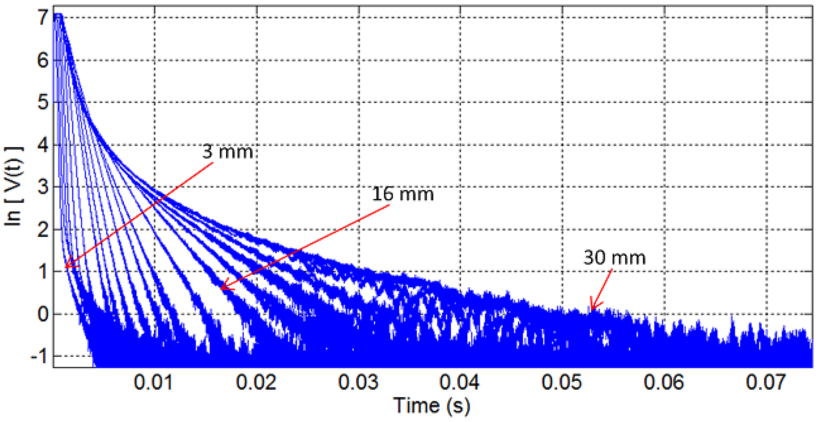

FIGURE 3.8: Decaying part of raw PEC signals for Gray Cast Iron.

materials. Therefore, extraction of the β_{max} feature for all critical pipe materials was done in this thesis by making use of the linear region $0 < \ln[V(t)] < 2$ which was common to all pipe materials. When coming to practical application, it is infeasible to theoretically impose a global quantitative fixation on the region adequate to extract the feature. In practice, this region will vary for different materials and sensors, and should be identified by studying experimentally captured or numerically simulated signals. For the particular sensor used in this thesis, $0 < \ln[V(t)] < 2$ is a reasonable region for critical pipe materials. Although the region $0 < \ln[V(t)] < 2$ is selected for this work as an effective range for feature extraction, selecting $\ln[V(t)] = 0$ and $\ln[V(t)] = 2$ as the noisy and upper margins is by no means compulsory; signals can be visually inspected and a linear region where $\beta(t)$ remains fairly constant as in Fig. 3.9 for the whole, or a great extent of the full thickness range that will be measured, can be selected. In quantitative sense with respect to this work, a region of two units in the log voltage axis having a minimal absolute mean of the second derivative can be used as an appropriate region. A range of two units in the log voltage scale is selected to encompass an adequate amount of data points to fit a straight line. The reduction of $\beta(t)$ very late in the signals in both Fig. 3.6 and 3.9 after remaining constant is due to noise as signals enter the noisy region. A slight variation in gradient that could occur as a signal enters the noise margin is shown in Fig. 3.10.

Since $V(t)$ expressed in Section 3.1 is the PEC signal in the absence of noise, an experimentally captured signal $V_e(t)$ should be expressed as $V(t) + n(t)$ where $n(t)$ is the time varying noise. To extract the decay rate feature ($\beta(t) = \left|\frac{\mathrm{d}t}{\mathrm{d}\ln[V(t)]}\right|$) from experimental

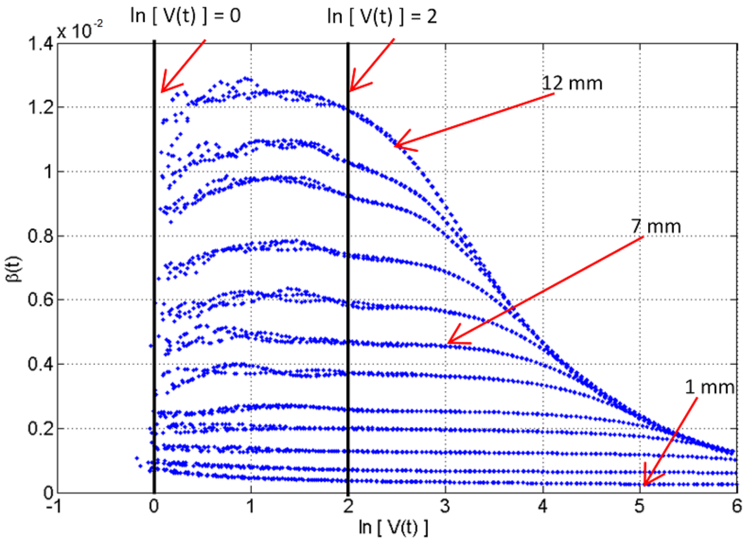

Figure 3.9: Behavior of $\beta(t)$ against $\ln[V(t)]$ of Mild Steel thicknesses from 1 mm to 12 mm, linearity observable between $\ln[V(t)] = 0$ and $\ln[V(t)] = 2$.

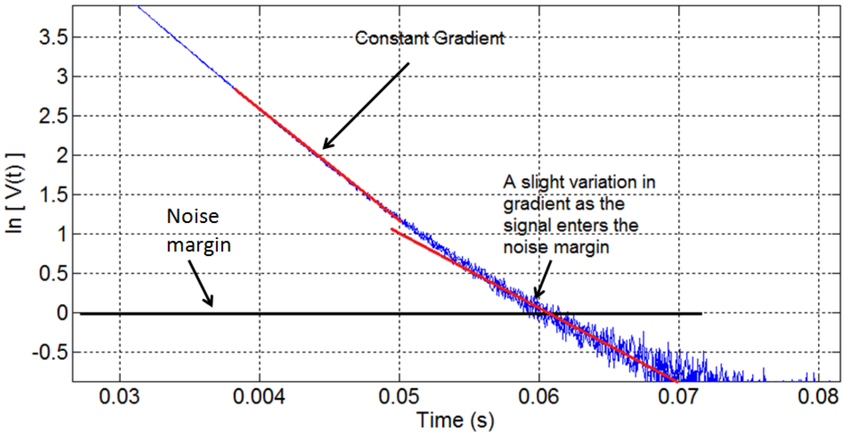

Figure 3.10: Slight change in gradient as a signal enters the noise margin.

signals, the $\ln[V(t)]$ component should be isolated. This can be done as shown below,

$$V_e(t) = V(t) + n(t)$$

$$\ln\left[V_e(t)\right] = \ln\left[V(t) + n(t)\right]$$

$$\ln\left[V_e(t)\right] = \ln\left[V(t)\right] + \ln\left[1 + \frac{n(t)}{V(t)}\right]$$

$$\ln\left[V_e(t)\right] = \ln\left[V(t)\right] + \epsilon_n(t), \tag{3.12}$$

where $\epsilon_n(t) = \ln\left[1 + \dfrac{n(t)}{V(t)}\right] \approx 0$ since $n(t) << V(t)$ before the experimental signal enters the noise margin (*i.e.*, $\ln[V_e(t)] = 0$).

As mentioned before, $\ln[V(t)]$ varies as a straight line for the region of interest $0 < \ln[V(t)] < 2$ for PEC signals captured on a pipe material. The fundamental reason for this can be recalled as $\beta(t) = \left|\dfrac{\mathrm{d}t}{\mathrm{d}\ln[V(t)]}\right| \approx \dfrac{\mu\sigma d^2}{\pi^2}$ being constant, or time invariant at later stages of the signal (*i.e.*, t becomes large) for a given thickness of a particular material, and hence the signal taken in the form of $\ln[V(t)]$ behaving as a straight line. Therefore, the $\ln[V(t)]$ component of an experimental signal can be expressed as a linear model $\ln[V(t)] = mt + k$ where m is the gradient and k is the intercept. The required β_{max} feature is contained in m since β_{max} is a representation of the gradient of $\ln[V(t)]$ at later stages (*i.e.*, just before signals enter the noise margin). By estimating m, β_{max} can be computed as $\beta_{max} = -\dfrac{1}{|m|}$.

Estimating m can be done by expressing $\ln[V_e(t)]$ with the aid of the linear model as $\ln[V_e(t)] = mt + k + \epsilon_n(t)$ and applying the principle followed for noise suppression in [3]. As discussed in Subsection 2.3.1, [3] suggests that a distortion free noiseless signal can be obtained from noisy experimental signals by approximating the average of noise to zero. If this fundamental is applied to the noisy model $\ln[V_e(t)] = mt + k + \epsilon_n(t)$ to estimate m and k by minimizing the power of noise, that simply becomes a case of fitting a straight line to noisy data using linear least squares. Therefore, m for an experimental signal can be estimated using the matrix $M = (A^TA)^{-1}A^TV$ [61] where,

$$M = \begin{bmatrix} m & k \end{bmatrix}^T$$

$$V = \begin{bmatrix} \ln[V_e(t_1)] & \ln[V_e(t_2)] & \dots & \ln[V_e(t_n)] \end{bmatrix}^T$$

and

$$A = \begin{bmatrix} t_1 & t_2 & \dots & t_n \\ 1 & 1 & \dots & 1 \end{bmatrix}^T$$

for n being the number of samples captured by the sampling network within the range $0 < \ln[V_e(t)] < 2$. A linear model fitted to the range $0 < \ln[V_e(t)] < 2$ of a noisy signal captured on gray cast iron (thickness = 14 mm) is shown in Fig. 3.11. Corresponding feature value is $\beta_{max} = 1/374.42 = 0.00267$.

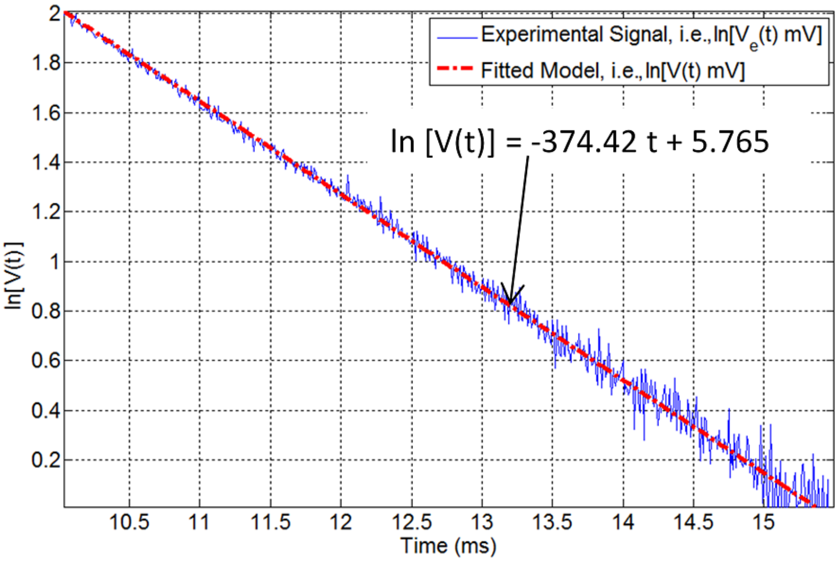

FIGURE 3.11: A fitted linear model to a noisy signal captured on gray cast iron.

3.2.5 Experimental Validation of the Existence of the Linear Thickness-Feature Function

Existence of the thickness-feature function was experimentally validated after capturing PEC signals on calibration block thicknesses given in Table 3.1 and extracting the β_{max} feature following the method presented in Subsection 3.2.4. To achieve linearity, the function was modeled in the form of $\ln \beta_{max} = 2 \ln d + c$ where $c = \ln \dfrac{\mu\sigma}{\pi^2}$ as elaborated in Section 3.1. Fig. 3.12 resulted when $\ln \beta_{max}$ values were plotted against $\ln d$ values for all measurements taken on all three pipe materials. Three readings were obtained on each thickness of each material to characterize sensor noise and $\ln \beta_{max}$ from all those readings are shown in Fig. 3.12. Noise in this case is partially caused by manual errors resulting from unintentional sensor movement including lift-off and tilt occurring while scanning. In addition to that, the whole sensor setup does not have electromagnetic shielding making the signal susceptible to noise induced by external electromagnetic sources including power lines. Random noise including quantization errors is also introduced by the signal sampling circuitry. Due to the logarithmic scale, the noise appears to be minimal in Fig. 3.12.

However, noise is more visible if β_{max} itself is considered and a noise characterization for gray cast iron is done in Section 3.7 in order to be used in Chapter 4 for numerical sensor modeling.

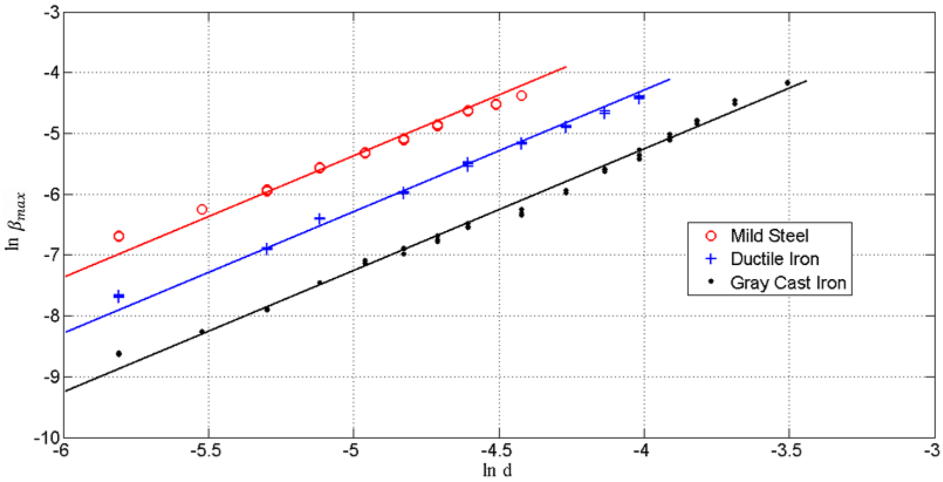

FIGURE 3.12: Linear relationship between $\ln \beta_{max}$ and $\ln d$ for different ferromagnetic materials.

Linearity is observable in Fig. 3.12 for all three critical pipe materials. Hence this can be taken as experimental evidence of the thickness-feature relationship derived in Section 3.1. Once calibration signals are available, c is the sole parameter which is required to be estimated to use the $\ln \beta_{max} = 2 \ln d + c$ model to estimate unknown thicknesses. c for a particular material can simply be estimated by taking the mean of $\ln \beta_{max} - 2 \ln d$ values resulting from known calibration thicknesses. Availability of multiple calibration signals will help in capturing effects of noise, but estimation may be done with a minimum of one calibration signal taken on a known thickness. The procedure followed for model estimation in this chapter is explained in Subsection 3.4.1.

Table 3.2 shows the estimated c values for all three pipe materials along with Root Mean Square (RMS) errors of the fitted straight lines. Estimation of c provides the additional capability of estimating the $\mu\sigma$ multiplication of a material. This can be considered advantageous since a limited but useful indication of electromagnetic properties of a material can be derived in the form of $\mu\sigma$ from this method. It can be seen that $\mu\sigma$ values increase in the respective order of gray cast iron, ductile cast iron and mild steel. This observation aligns with the fact that the iron content of those materials increasing sequentially [15].

Therefore, useful conclusions such as the conductivity and permeability of those materials increasing sequentially can be made. Further, capability of estimating $\mu\sigma$ will be helpful when the requirement for material identification prevails. For instance, if there are two aged pipes laid nearly a century ago and their materials are unknown, simply quantifying c values of the two pipes with the aid of calibration signals performed on machined test sections having known thickness, will enable verifying their materials. The proposed thickness-feature relationship is thus useful for both thickness quantification and material property identification.

TABLE 3.2: Parameters of fitted straight lines for $\ln \beta_{max}$ vs $\ln d$ variation of different materials.

Material	c	RMS Error	$\mu\sigma$
Gray Cast Iron	2.7473	0.1109	153.973
Ductile Cast Iron	3.7143	0.09819	404.940
Mild Steel	4.6330	0.1324	1014.829

3.2.6 Sensitivity Analysis of β_{max}

Since the $\beta_{max} \approx \frac{\mu\sigma d^2}{\pi^2}$ approximation for the feature is only dependent on thickness and material properties, the low dependencies listed below can be hypothesized given sufficient penetration capability prevails. In theory, if β_{max} is obtained at $t = \infty$, these low dependencies could be considered as independences since $\lim_{t\to\infty} \beta(t) = \frac{\mu\sigma d^2}{\pi^2}$ according to Eq. 3.8. However, achieving $t = \infty$ is not possible in practice and β_{max} is obtained at a finite time where $\beta(t)$ exhibits a constant gradient. It could be observed through numerical simulations that the variation of the gradient is minimal at the time period succeeding the interval where β_{max} is captured from experimental signals. Therefore, the value captured from the constant gradient region of experimental signals before they enter the noise margin can be considered as a close approximation to the theoretical value occurring at $t = \infty$. For example, values in Table 5.2 appearing later in the thesis can be considered as evidence supporting the above statement since they result from an exercise which compares simulated β_{max} values captured at a finite time against theoretical values (calculated as $\beta_{max} = \frac{\mu\sigma d^2}{\pi^2}$) occurring at $t = \infty$. Considering the practical case however, theoretical independences occurring at $t = \infty$ are considered as practical low dependencies (*i.e.*, variation of 15% or less with respect to a reference value of β_{max} acquired at 0 mm lift-off) in this subsection and are listed below.

1. When there is sufficient penetration capability, β_{max} is lowly dependent on sensor lift-off.
2. When there is sufficient penetration capability, β_{max} is lowly dependent on sensor size.
3. When there is sufficient penetration capability, β_{max} is lowly dependent on sensor shape.

Low dependence on lift-off and sensor size were experimentally verified using available rectangular sensors. Low dependence on shape was verified numerically and is discussed in Chapter 5. These low dependencies proved to be useful for the work of Chapter 5 and are exploited in a framework proposed to concurrently infer thickness and lift-off.

3.2.6.1 Low Dependence on Sensor Lift-off

According to the approximation $\beta_{max} \approx \dfrac{\mu\sigma d^2}{\pi^2}$, the feature exhibiting low dependence (low sensitivity) to sensor lift-off was hypothesized given the prevalence of sufficient penetration capability. This hypothesis was experimentally tested by capturing β_{max} values on calibration blocks using the rectangular sensor by varying lift-off by increments of 2 mm. The result in Fig. 3.13 was observed and the zoomed views of low (5 to 12 mm) and high (14 to 25 mm) thicknesses are provided in Fig. 3.14 and 3.15 respectively. As per the many quantified pipe wall thickness maps provided in Appendices A and B, it can be concluded that encountering thicknesses of 30 mm or more on aged in situ gray cast iron critical pipe walls is extremely rare. The mean of maximum estimated thickness values across all gray cast iron pipe segments examined within this thesis was approximately 26 mm. Therefore the effect of lift-off was not tested beyond the thickness of 25 mm from available calibration blocks.

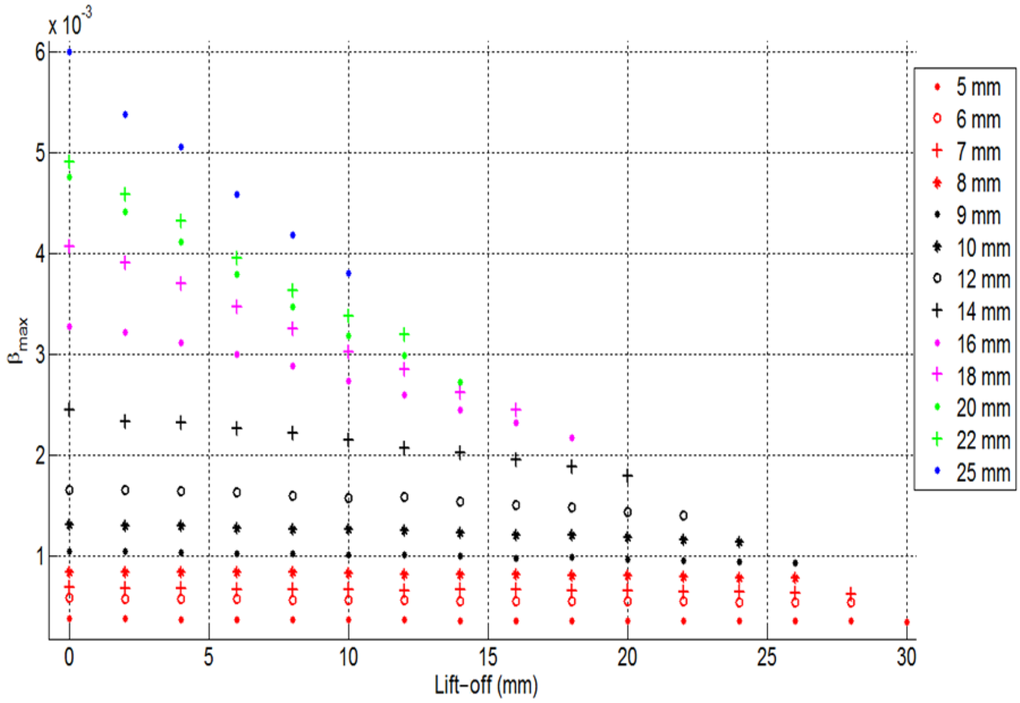

FIGURE 3.13: Low dependence on sensor lift-off.

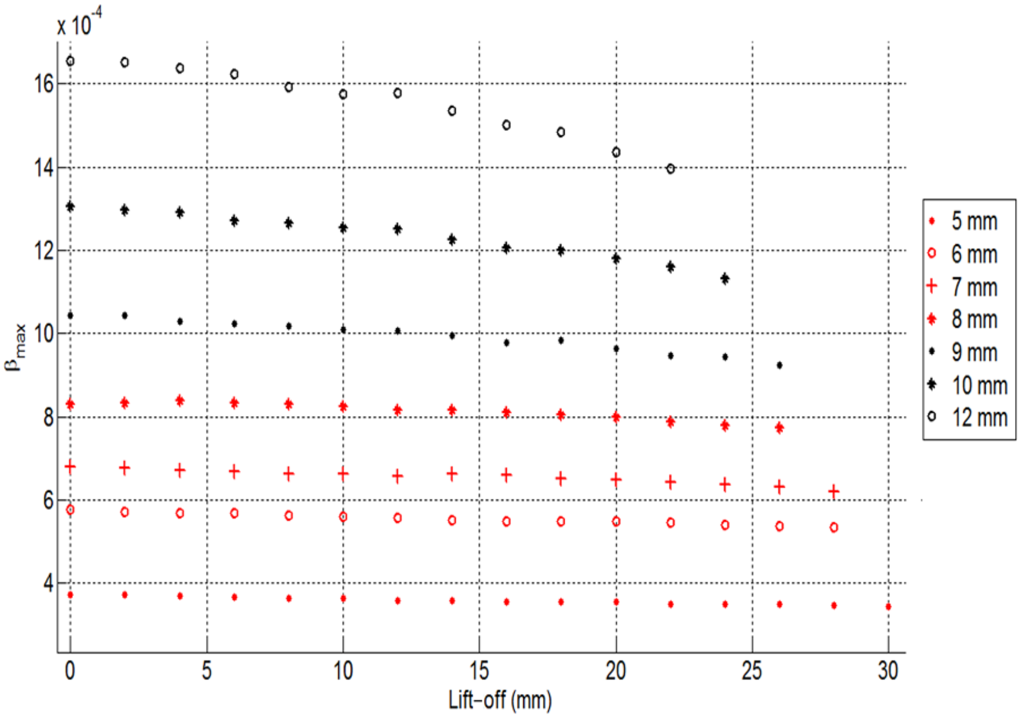

FIGURE 3.14: Low dependence on sensor lift-off (Low Thicknesses).

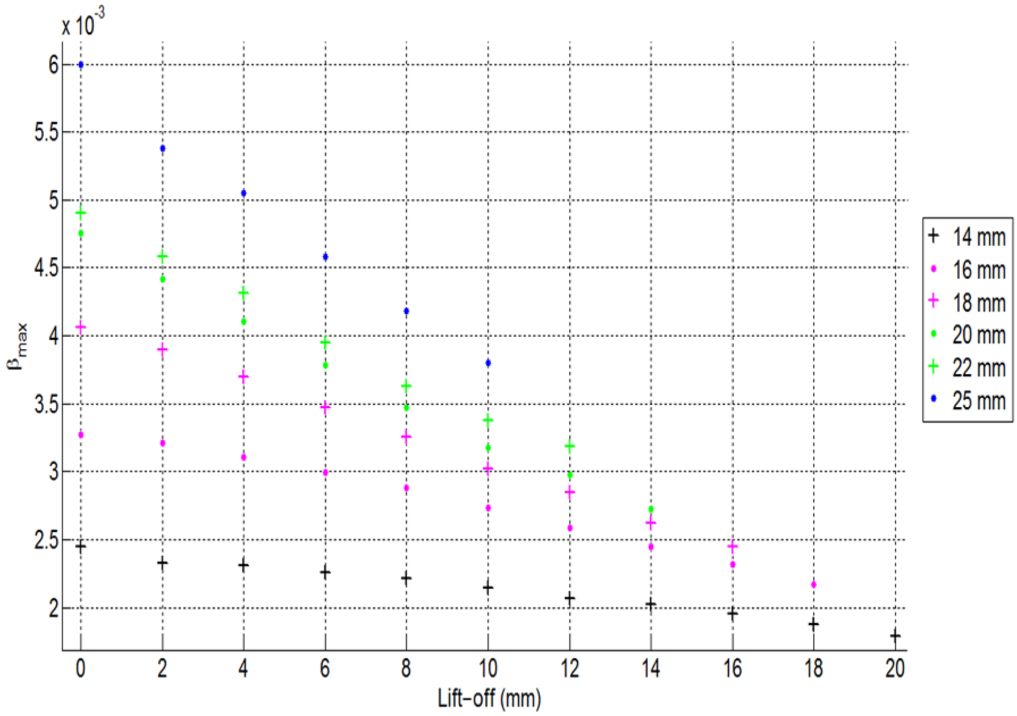

FIGURE 3.15: Low dependence on sensor lift-off (High Thicknesses).

A considerable degree of low sensitivity to lift-off can be observed in Fig. 3.13. Low sensitivity in this case is quantitatively defined to be less than 15% variation of β_{max} with respect to the value at 0 mm lift-off for a particular thickness. According to Fig. 3.14, a great degree of invariance (*i.e.*, less that 5% variation) can be observed for thicknesses 8 mm and less. Slight variation (*i.e.*, 5 to 15% variation) can be observed for 9 mm to 12 mm at higher lift-offs. Lift-off dependence is greater (*i.e.*, variation greater than 15%) for higher thicknesses as can be seen from Fig. 3.15 and for a selected thickness, the dependence increases with lift-off. These observations can be explained with the light of eddy current penetration capability. For a given excitation, a PEC sensor should have a fixed eddy current penetration depth for a given material at 0 mm lift-off. Since the excitation magnetic fields remain constant depending on the fixed excitation, the field strengths reaching into the material should decrease as the lift-off increases causing reduction in eddy current penetration depth withing the material. If the sensor is designed to marginally achieve maximum penetration depth at 0 mm lift-off for higher thicknesses, effect of lift-off will impact high thickness β_{max} values since the reduction of penetration depth due to lift-off in those thicknesses is obvious. On the contrary, feature values from lower thicknesses do not have such a significant effect since magnetic fields may still be sufficient despite lift-off to achieve full penetration into the low thickness which results in almost perfect lift-off invariance for a larger lift-off range.

Observations from the above experiment confirm that β_{max} is lowly dependent on lift-off given the prevalence of sufficient penetration capability. However, if the excitation marginally achieves full penetration in higher thicknesses at 0 mm lift-off, the lift-off effect on high thickness β_{max} values will be more prominent since lift-off directly reduces the distance which the excitation field can penetrate into thick material substrates. If a certain PEC sensor's excitation strength is fixed, similar to the case encountered in this work, the excitation's penetration capability can easily be tested through simulations similar to those done in Chapters 4 and 5. Alternatively, enabling a variable excitation in hardware is a greatly acceptable practical solution to achieve greater penetration capability and lift-off invariance.

Though the β_{max} feature experiences low dependence on lift-off, the actual PEC signal for a fixed thickness varies with lift-off as shown in Fig. 3.16. Decaying part of the signal exhibits a leftward shift with lift-off increase implicating a signal attenuation attributed to reduction of excitation magnetic field strength penetrating the material caused by the increase of distance between the sensor and the material in the form of lift-off. This signal shift which occurs while β_{max} variation remains low is exploited in Section 5.6 for concurrent inference of thickness and lift-off to enable 3D profiling. Since this subsection elaborated the low dependence of β_{max} thus far, Fig. 3.17 exhibits how the low dependence propagates to $\ln \beta_{max}$ as well in the same manner.

3.2.6.2 Low Dependence on Sensor Size

As per the approximation $\beta_{max} \approx \dfrac{\mu\sigma d^2}{\pi^2}$, the feature exhibiting low dependence to sensor size can be hypothesized given the prevalence of sufficient penetration capability. This hypothesis was experimentally tested by exciting the larger and smaller PEC sensors shown in Fig. 3.18 with identical excitation voltages (varying the excitation was not possible with the electronics of the excitation circuit provided by the manufacturer), and evaluating the β_{max} values obtained on gray cast iron calibration blocks. The result in Fig. 3.19 could

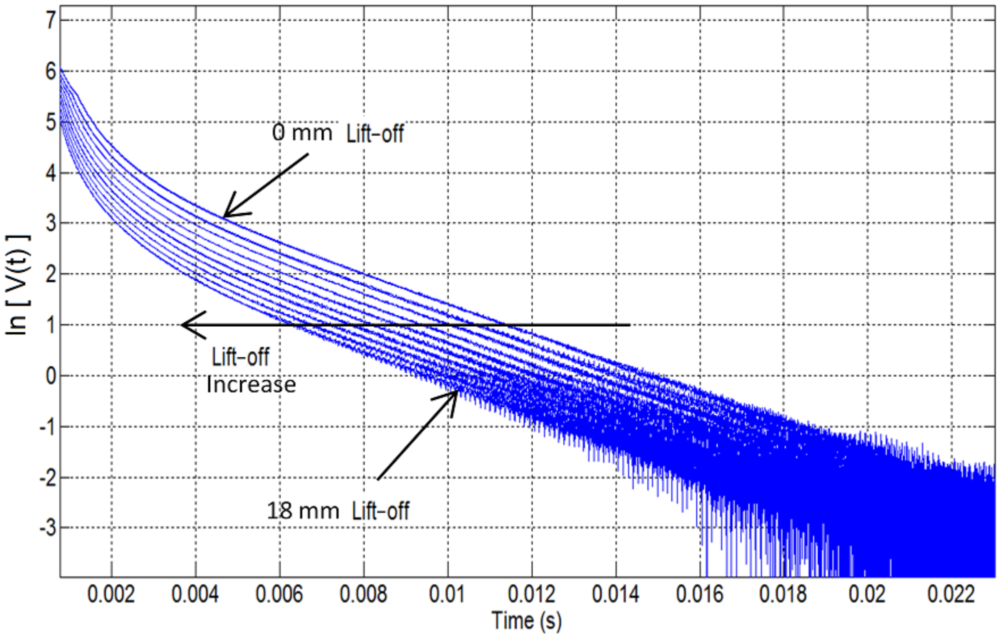

FIGURE 3.16: Impact of lift-off on the PEC signal for a fixed material thickness (Captured on a gray cast iron calibration block, 16 mm thickness).

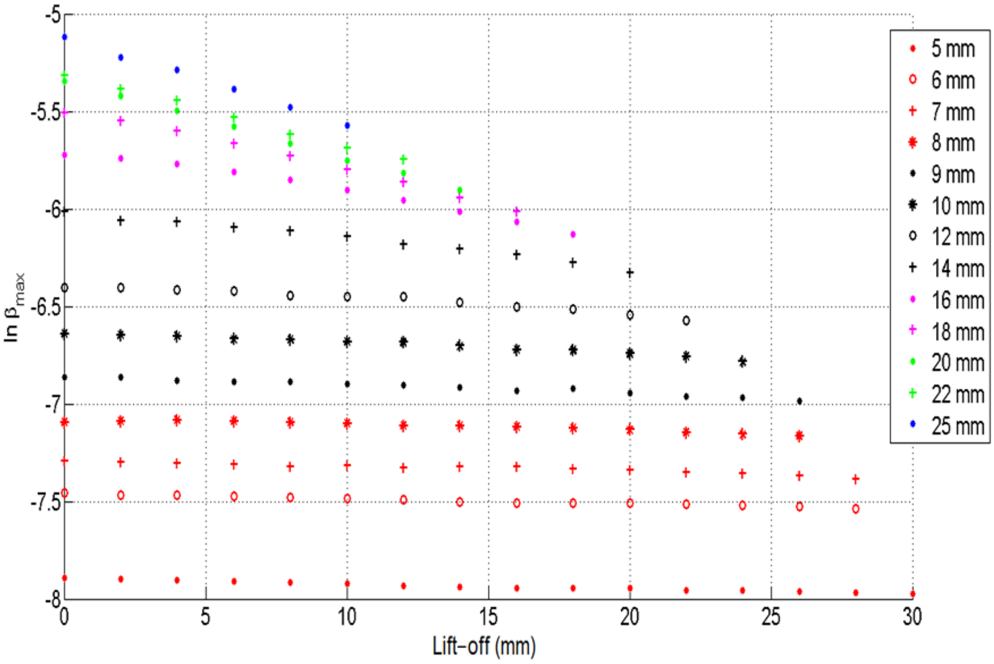

FIGURE 3.17: Low dependence on sensor lift-off when the feature is considered in the form of $\ln \beta_{max}$.

be observed for the variation of $\ln \beta_{max}$ against $\ln d$ and Fig. 3.20 shows the absolute differences in the feature values produced by the two sensors against $\ln d$.

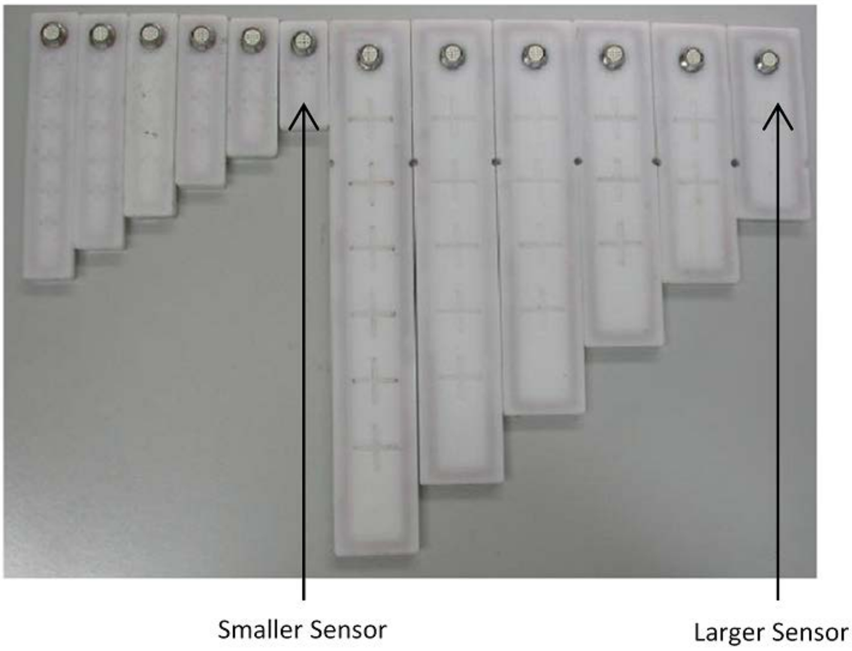

FIGURE 3.18: The two different PEC sensor sizes used for the experiment.

According to Fig. 3.19 and 3.20 it can be seen that the two sensor sizes produce almost identical feature values for low to moderate thicknesses, and the smaller sensor loses thickness sensitivity in the higher thickness region and produces nearly constant feature values for different thicknesses in that region. This observation confirms the feature shows low sensitivity to sensor size as expected. Further, the smaller sensor should have lower penetration capability than the larger sensor for a fixed excitation as per the findings of [40] and that explains the loss of sensitivity in the higher thickness region. The small sensor producing almost the same feature value for different thicknesses in that region can be linked to the induced eddy currents penetrating to a constant depth despite thickness increase.

Shown in Fig. 3.21 are two PEC signals obtained on the same calibration block (gray cast iron, 10 mm thickness), from the two sensor sizes to visualize how the actual signals look. Signals from the smaller sensor always exhibit a leftward shift for all thicknesses

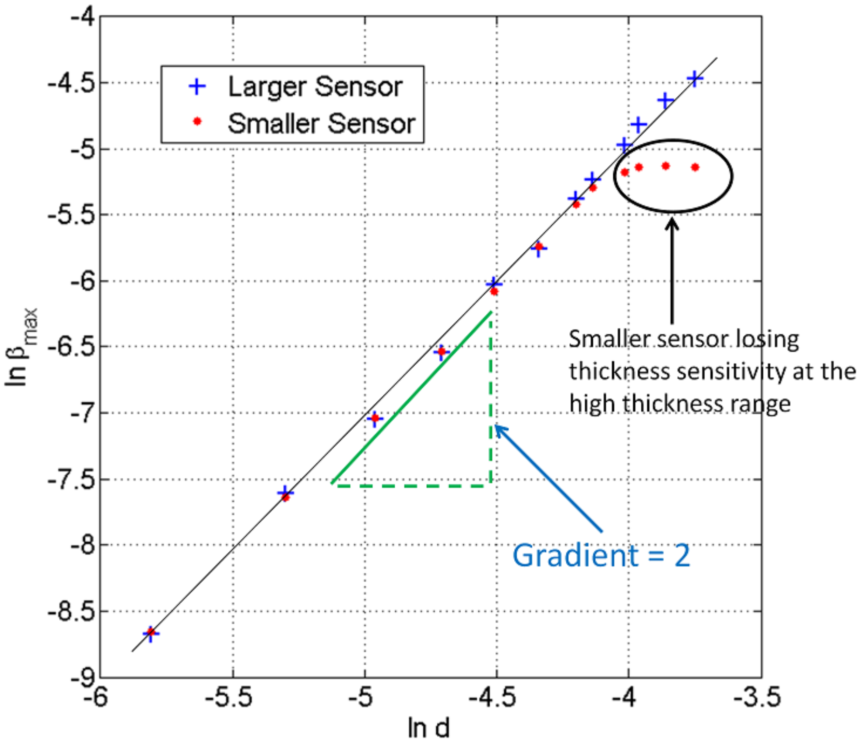

FIGURE 3.19: Variation of $\ln \beta_{max}$ values of two PEC sensor sizes against $\ln d$ for different thicknesses of gray cast iron.

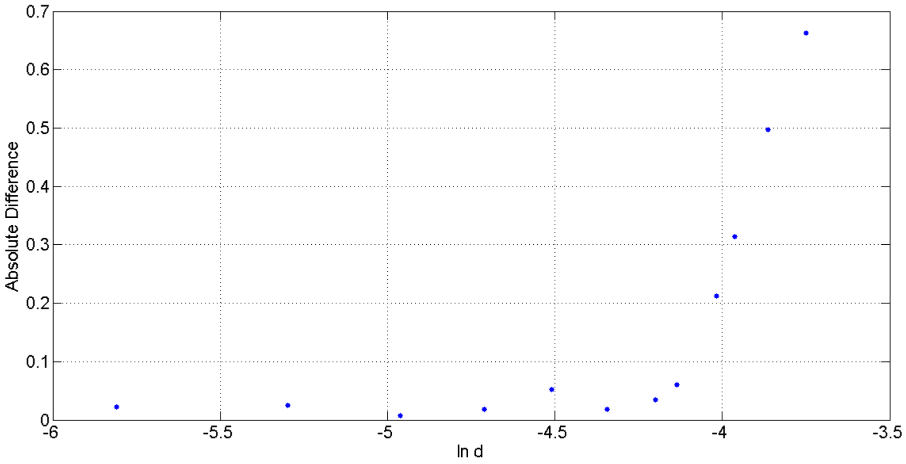

FIGURE 3.20: Variation of absolute difference of feature values produced by the two sensor sizes against $\ln d$.

implying an amplitude decrease in the induced detector coil voltage. This is attributed to the potential divider effect applying to the constant excitation voltage since the source has a finite output impedance while the smaller sensor has a lower excitation coil wire length resulting in lower resistance than in the larger sensor.

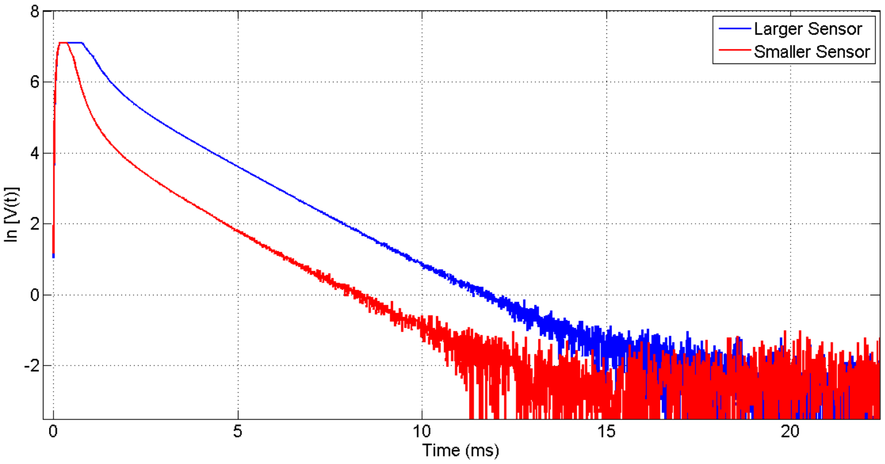

Figure 3.21: Two sample curves produced by the two sensor sizes on a 10 mm gray cast iron calibration block.

Based on the observations of Fig. 3.19, 3.20 and 3.21, it can be concluded that the β_{max} feature shows low sensitivity to sensor size when there is sufficient penetration capability. The observations also confirm that for a fixed excitation, a smaller sensor size will have a lower penetration capability, resulting in loss of thickness sensitivity for higher thicknesses.

3.3 FEA Validation of Invariance of β_{max} for Cylindrical Structures

Though the relationship for $\beta(t)$ was derived for conducting plates for simplicity, the intention was to use the decay rate as a signal feature for thickness quantification of cylindrical structures, large diameter in-situ pipes. It could be hypothesized that the plate approximation is reasonable given the pipes investigated are of radius R greater than 250 mm while the sensor width used w is 50 mm in the direction perpendicular to the pipe axis, thus the surfaces would exhibit low curvature.

Verification of this hypothesis was performed through finite element analysis (FEA) on a gray cast iron specimen extracted from one of the pipe segments considered in this work.

The FEA model was developed using COMSOL Multiphysics® [62] and it takes the sensor properties (physical dimensions, inherent properties and excitation signal characteristics) and test piece properties (physical dimensions, electrical and magnetic properties) as inputs and solves the magnetic vector potential equation to produce the sensor response. Development of the sensor model is discussed in detail in Chapter 4. For accurate simulation of material being tested, high precision magnetization curves and electrical conductivity were obtained using a Quantum Design Physical Property Measurement System (PPMS-9T) [63, 64]. The 3D simulation model and FEA results against measurements obtained using the PEC sensor are shown in Figures 3.22 and 3.23 and were also reported as a part of [6].

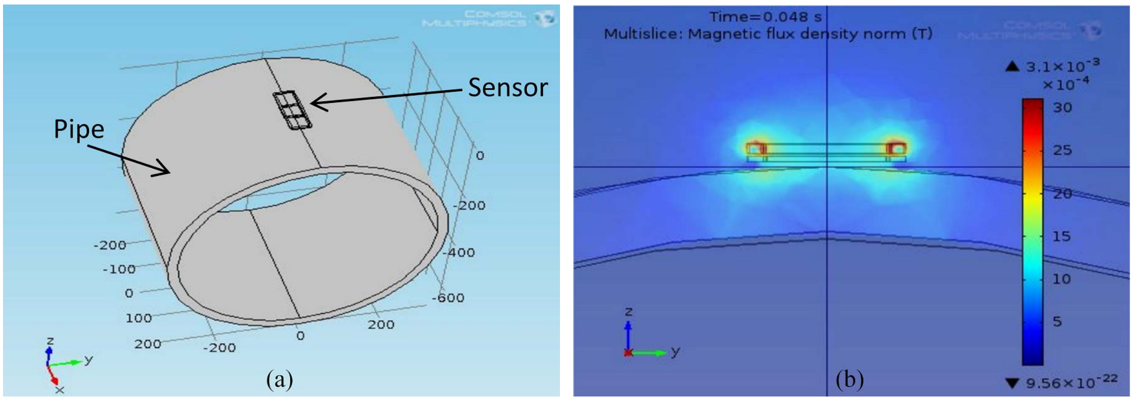

Figure 3.22: Numerical PEC sensor simulation model: (a) 3D model of the sensor and pipe, (b) Cross-section showing induced fields.

In order to validate the invariance of the sensor signal to curvature of the cylindrical structure, the hypothesis tested is that for a given PEC sensor width w perpendicular to the pipe axis, there exists a range $w/R < k$ where $k \in \mathbb{R}^{+}$, such that the variation of β_{max} due to the curvature of the test piece remains insignificant. It was noted that k depends on electromagnetic properties of the material being tested, sensor architecture and excitation signal characteristics. For practical quantification, the range of interest was defined to be where the curvature dependent variation of β_{max} for any thickness of interest is less that 1% from the flat plate reference. From the analysis reported in Fig. 3.24, the pipe radii which satisfy $w/R < 0.25$ produce β_{max} variations less than 1% for the used sensor. Given the minimum radius of the pipes scanned in this work was 250 mm, the maximum w/R value encountered was 0.2 ($w = 50$ mm and $R = 250$ mm), thus the approximation of large diameter pipe surfaces as flat plates holds for practical purposes. Therefore, it can

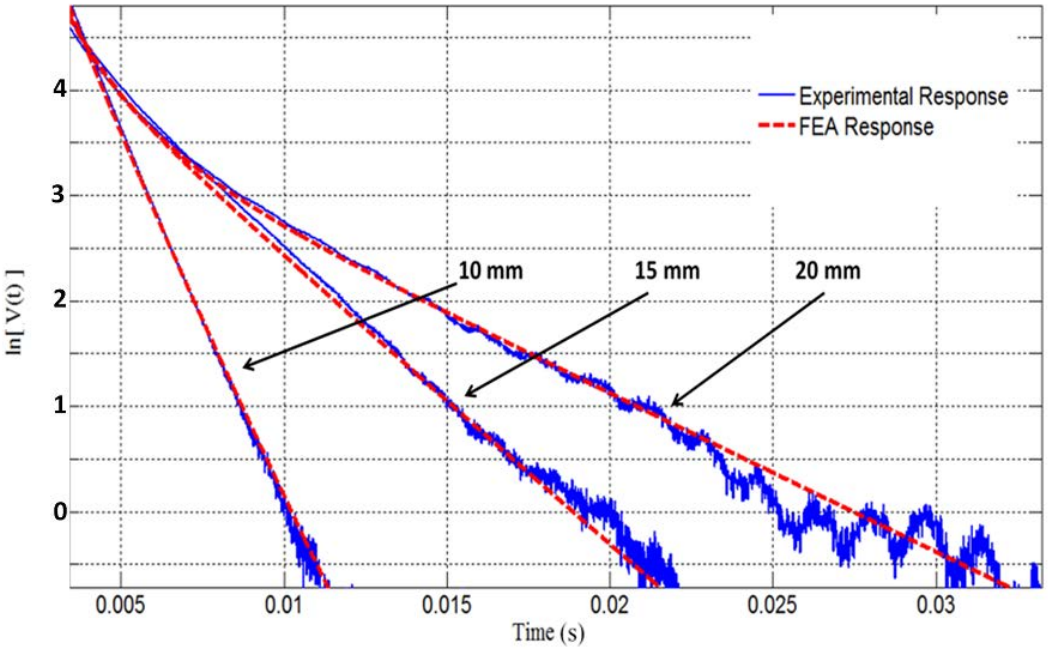

FIGURE 3.23: Simulated sensor responses against unfiltered experimental signals for a range of gray cast iron thicknesses.

be concluded that the β_{max} feature is useful for quantifying thickness of large diameter critical pipes under the flat plate approximation given the sensor is of appropriate size.

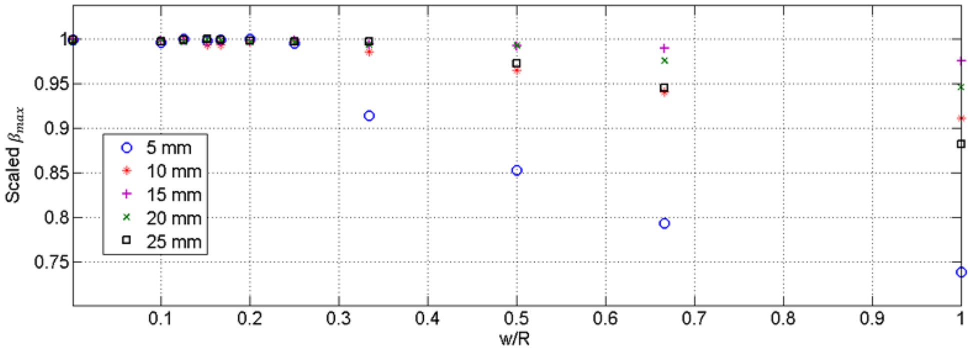

FIGURE 3.24: Effect of curvature on β_{max} for different thicknesses of gray cast iron.

Depending on the target application of the thesis, the study presented within this section is tailored for the PEC sensor used for this work and gray cast iron as the material being tested. However, the analysis method is generic and can be used to evaluate any

PEC sensor architecture on any material by incorporating required sensor and material properties.

3.4 Analytical NDE Framework Based On Experimentally captured Calibration Signals

The framework consists of the two steps of analytical model estimation (Fig. 3.25) and the model being used for critical pipe NDE (Fig. 3.26), each step is elaborated in turn.

3.4.1 Analytical Model Estimation

Model estimation procedure is depicted in Fig. 3.25. As presented in Section 3.2, given the availability, signals should be acquired on calibration blocks having matching electrical and magnetic properties to those of the pipe to be evaluated. Feature extraction procedure should be carried out to extract β_{max} values corresponding to available calibration thicknesses. Once features are extracted, they should exhibit the characteristic of varying linearly with $\ln d$ as shown in Fig. 3.25. Model estimation can be achieved by computing the y-axis intercept c of the line $\ln \beta_{max} = 2 \ln d + c$ fitted to the linear scatter. c is the sole parameter which describes the whole model and by estimating c, the model can be used to estimate unknown thicknesses as explained in Subsection 3.4.2.

As mentioned is Subsection 3.2.5, three signals were captured on each calibration block to characterize noise and all data were used for parameter estimation. The minimum thickness used for all materials for parameter estimation was 4 mm. Though data for 1, 2 and 3 mm thicknesses were available, they were not used for parameter estimation partially due to the nonlinearity observed in that thickness region, and due to the chances of such low thicknesses prevailing on functioning in situ pipes being highly unlikely. Similar to the low thickness end, a nonlinearity was observed in the very high thickness end as well (above 30 mm for gray cast iron, above 16 mm for ductile cast iron and above 12 mm for mild steel). Therefore, the linear thickness-feature function for each material was estimated only by considering the linear range (shown in Fig. 3.12) while excluding the nonlinear regions observed in the very low and very high thickness ranges. The reasons behind these local nonlinearities are explained in Section 3.6 and the method of capturing those nonlinearities is explained in Chapter 4.

3.4.2 Using the Analytical Model for Critical Pipe NDE

Steps included in using the estimated model to quantify critical pipe wall thickness is pictorially described in Fig. 3.26. First, signals should be acquired by scanning the pipe wall exterior. For the work of this thesis, the full circumference of 1 m long pipe segments were scanned. Sensor positioning was done with the aid of a thin plastic grid having 50 mm × 50 mm squares marked upon wrapped around the pipe as shown in Fig. 1.1. Aligning the center of the PEC sensor with the centers of the squares was done to achieve precise positioning. Appendix C provides further details about the on site pipe scanning protocol followed during experiments and how the produce 2.5D thickness maps relate to

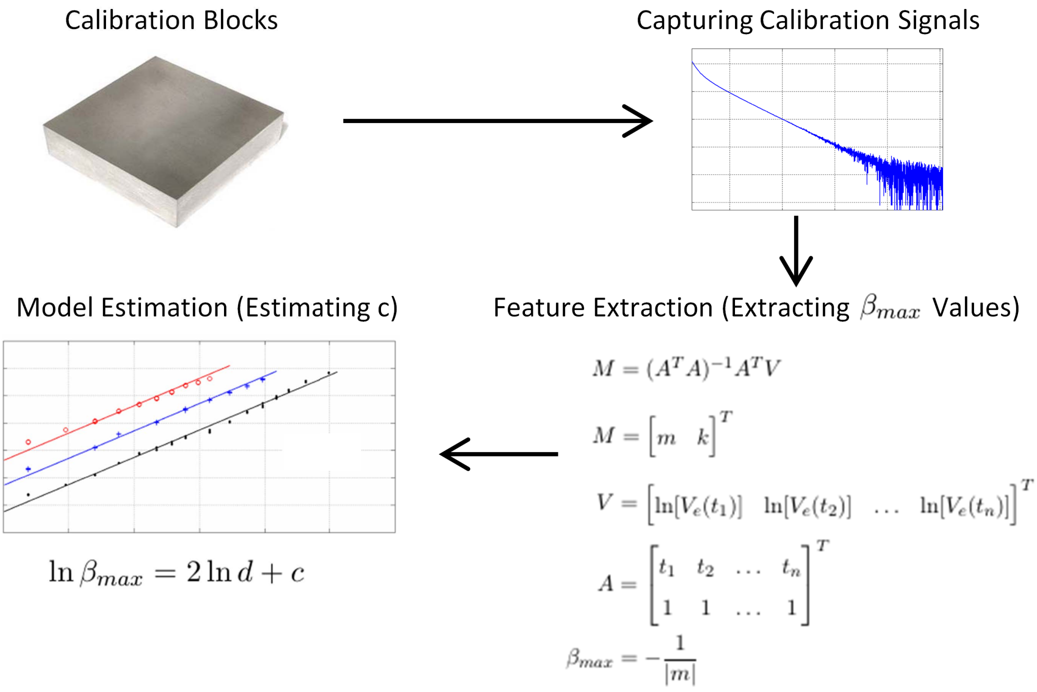

FIGURE 3.25: Analytical model estimation.

the actual locality of pipes. Since $\beta_{max} \approx \frac{\mu\sigma d^2}{\pi^2}$ is used for thickness quantification, the process is immune to many practical obstacles present during in situ scanning such as lift-off caused by the thickness of the paper grid (a few micrometers), dirt deposits on the pipe surface, rust and graphitization; and unintentional sensor tilt. Following signal acquisition, β_{max} feature values should be extracted by following the usual feature extraction method. Once feature values are computed, unknown thickness values (d) of each sensor location can be calculated using the expression $d = \exp\left(\frac{\ln\beta_{max} - c}{2}\right)$. Inferred thickness values of a pipe segment are presented as a 2.5D thickness map as shown in Fig. 3.26. x-axis of the thickness map provides the axial position in mm while the y-axis provides the circumferential position in degrees. Color bar on the right of the map can be used as a legend to visually identify wall condition. Since the detector coil is a square with a 50 mm side length, the thickness map contains values at the center of every 50 mm × 50 mm square. As detector coil based PEC sensors produce domain measurements and not point measurements, the thickness value in each square should be considered as the average of pipe wall thickness corresponding to the area covered by the square.

3.4.3 Validation

Validation of the analytical NDE approach was done by comparing produced pipe wall thickness maps against the actual amount of ferromagnetic material remaining in evaluated pipe walls. The actual thickness of ferromagnetic material remaining in pipe walls is henceforth known as the ground truth (GT). Procedure followed to obtain the GT is elaborated in Fig. 3.27. After performing PEC scanning, pipe segments were exhumed and grit blasted to remove rust and graphitization. The cleaned pipes were scanned with a 3D laser scanner to obtain high resolution 3D point clouds. A tailored ray tracing algorithm [65] was executed on the pint clouds to extract high resolution (0.8 mm) 2.5D thickness maps. These high resolution maps were down sampled via averaging to obtain GT maps having a resolution which match that of the PEC sensor. Validation was done by quantitatively comparing the thickness maps produced by the NDE approach against the aligned GT maps. Results of the quantitative comparison and remarks are presented in Subsection 3.4.4.

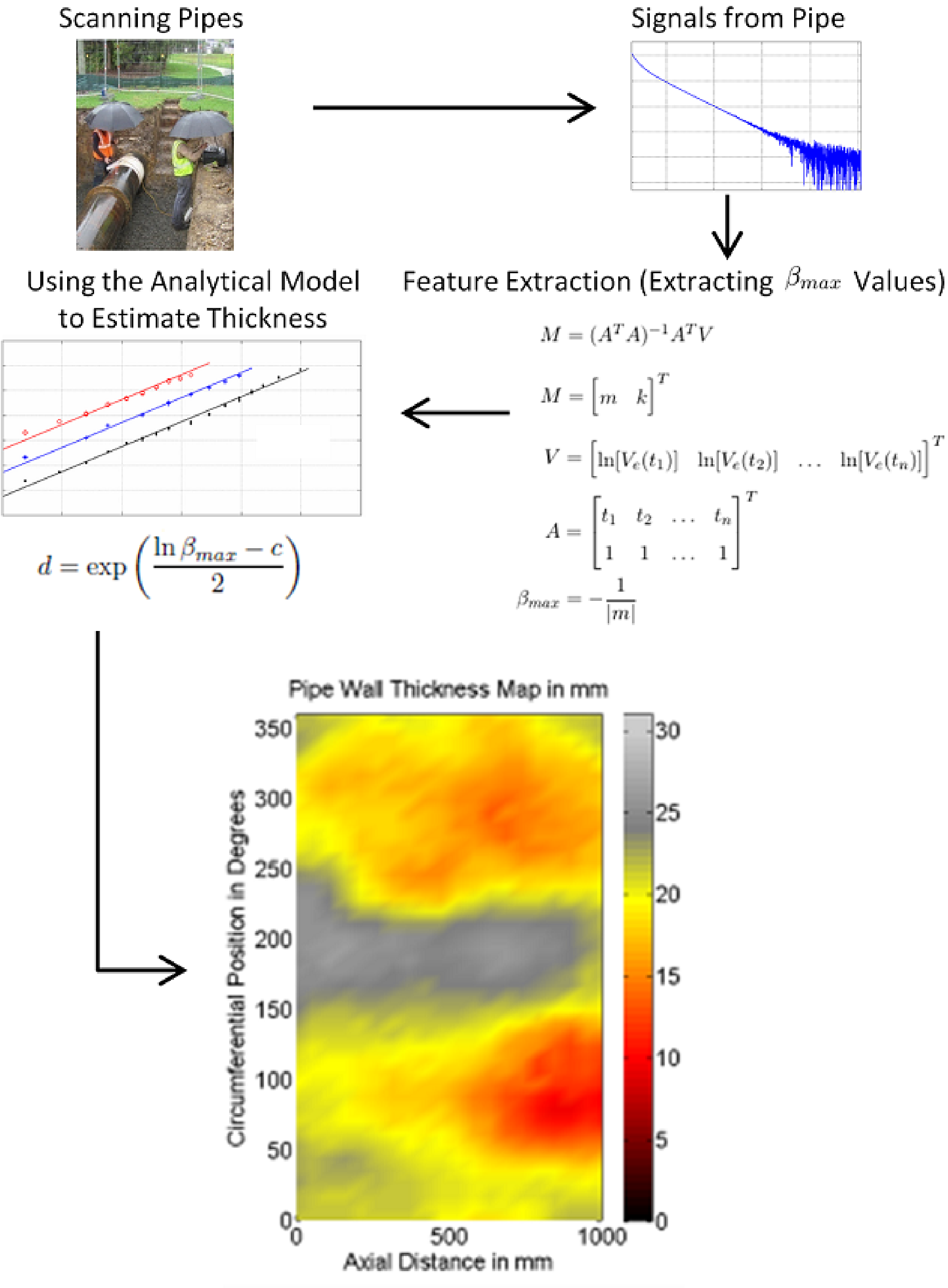

FIGURE 3.26: Analytical model being used for critical pipe NDE.

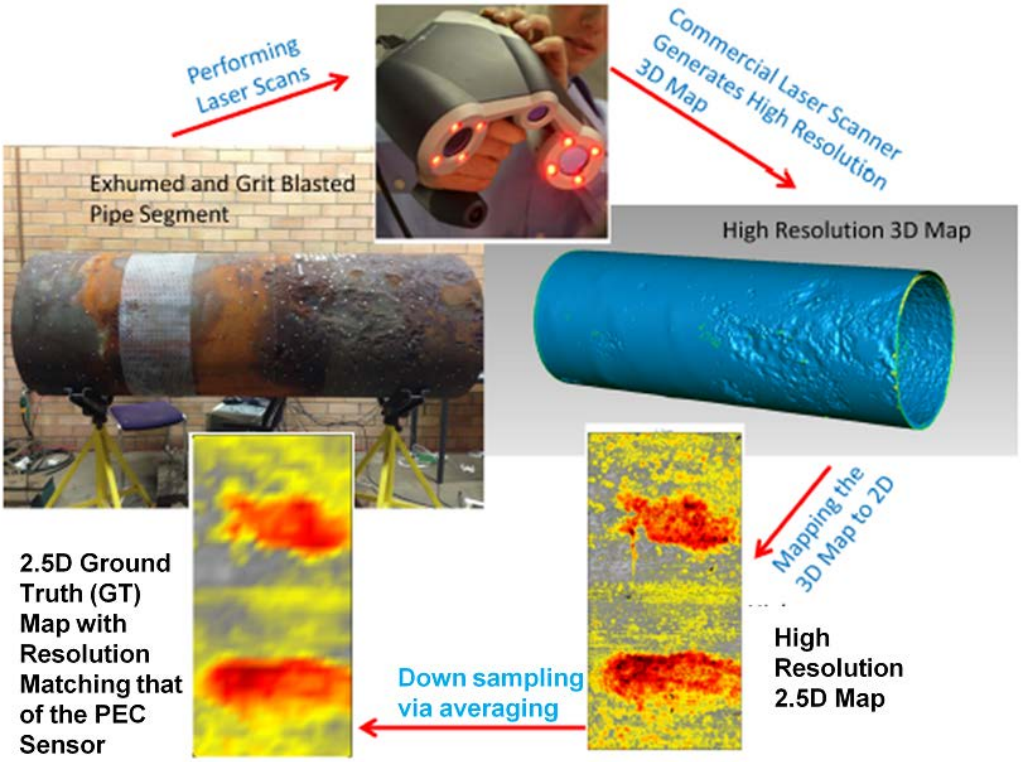

FIGURE 3.27: Obtaining ground truth (GT).

3.4.4 Results

Data from in-situ pipes were obtained by scanning full circumference of several in situ gray and ductile cast iron pipe segments in collaboration with Sydney Water, the local water utility [9]. Steel pipes were not available to be scanned at the time of experiments. Fig. 3.28 and 3.29 show the interpreted pipe wall thickness maps of two 1 m long gray cast iron pipe segments along with their ground truth (GT). The level of agreement between the interpretations and GT is graphically exhibited in Fig. 3.30, an ideal curve taking the form of $y = x$ is noted and the interpretation against GT appears as scatter. The scatter follows the trend of the graph with quantifiable deviations. These deviations are errors in the interpretations and their absolute values can be considered as a representation of accuracy. Several statistical parameters of the absolute errors were therefore quantified and are presented in Table 3.3. A mean percentage accuracy of over 90% was observed for gray cast iron. Similarly, a 1 m long ductile cast iron pipe segment was tested and results are presented in Fig. 3.31 and 3.32 while the statistical error analysis results are given in

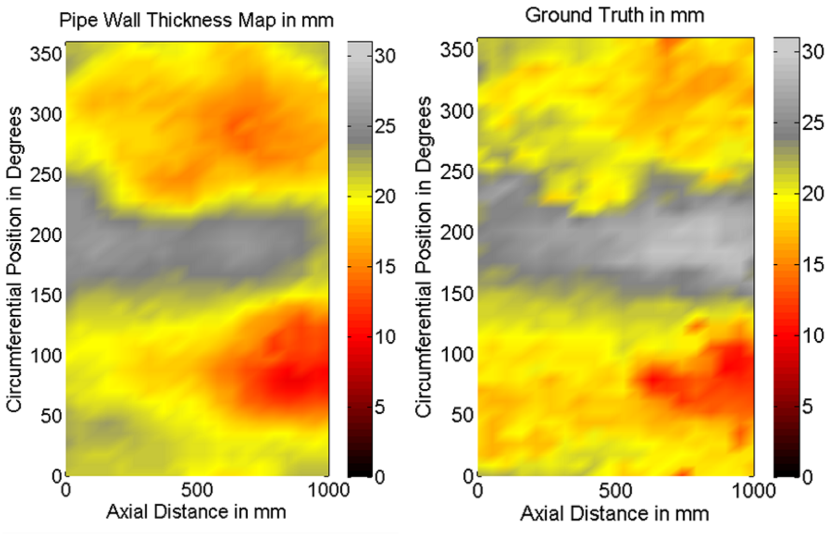

FIGURE 3.28: Interpreted thickness map and GT for the first Gray Cast Iron pipe segment.

Table 3.4. Achieved mean percentage accuracy was over 94%. Since all interpreted thicknesses showed the property $|\text{Interpretation} - \text{GT}| < \text{GT}$, the mean percentage accuracies in Tables 3.3 and 3.4 were obtained by computing $\left(1 - \frac{|\text{Interpretation} - \text{GT}|}{\text{GT}}\right) \times 100\%$ for each individual interpretation and then calculating their mean.

3.4.5 Limitations of the Analytical NDE Approach

The main limitation of the analytical approach is the requirement of proper calibration and the possibility of calibration errors due to material property mismatches leading to

TABLE 3.3: Statistics of absolute error between interpreted pipe wall thickness maps and ground truth for Gray Cast Iron pipe segments.

Statistical Parameter	Value
RMS Error	2.42 mm
Mean Absolute Error	2.00 mm
Standard Deviation of Absolute Error	1.37 mm
Maximum Absolute Error	7.06 mm
Mean Percentage Accuracy	90.3%

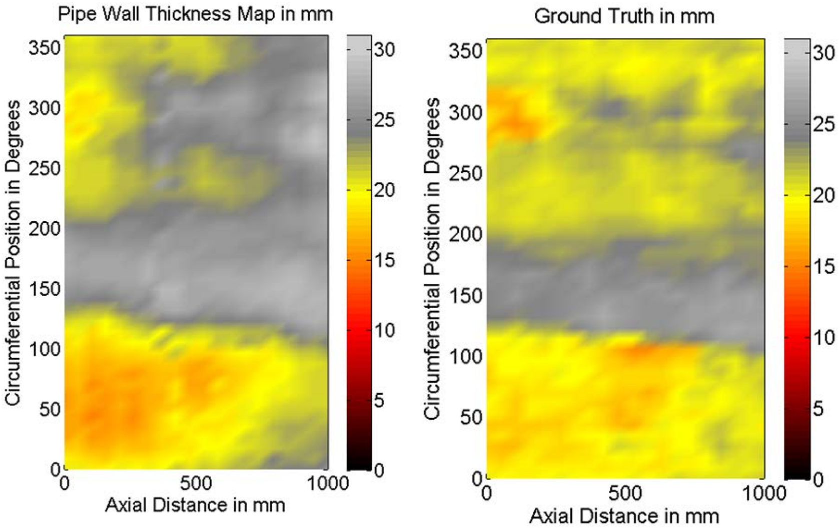

FIGURE 3.29: Interpreted thickness map and GT for the second Gray Cast Iron pipe segment.

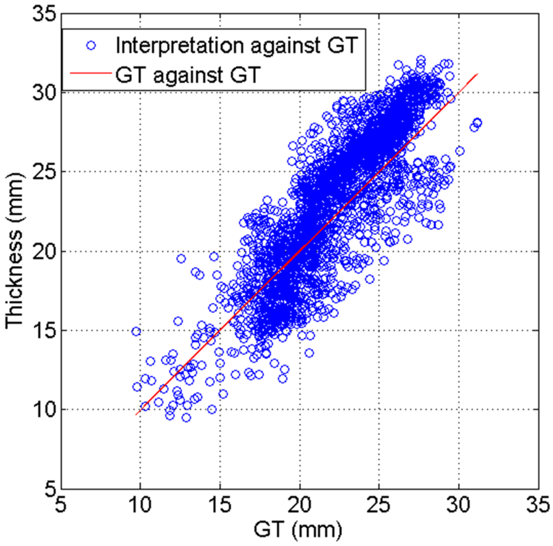

FIGURE 3.30: Variation of interpretations along with GT for the Gray Cast Iron pipe segments.

errors in interpreted thicknesses. In addition, fabricating calibration blocks is costly and time consuming. If the models are learned from a certain set of calibration blocks, the material properties embedded within c will be unique to pipes having similar properties. In reality, even in pipes made of the same material (say gray cast iron for instance),

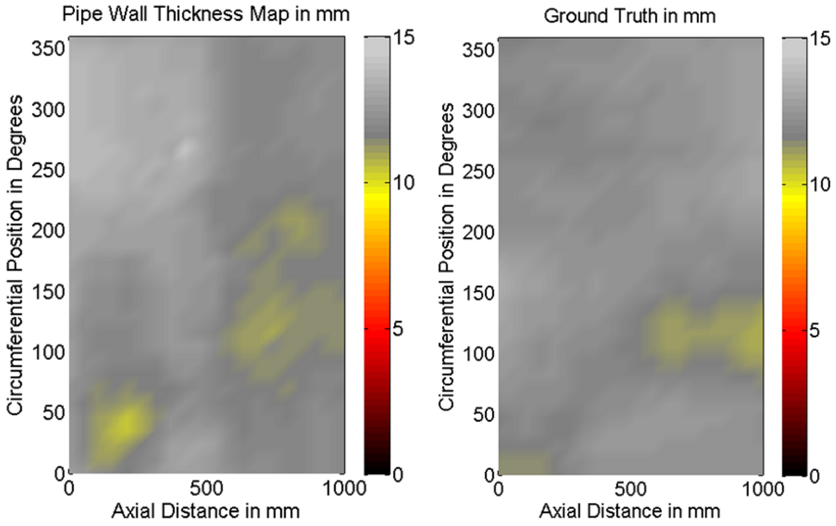

FIGURE 3.31: Interpreted thickness map and GT for the Ductile Cast Iron pipe segment.

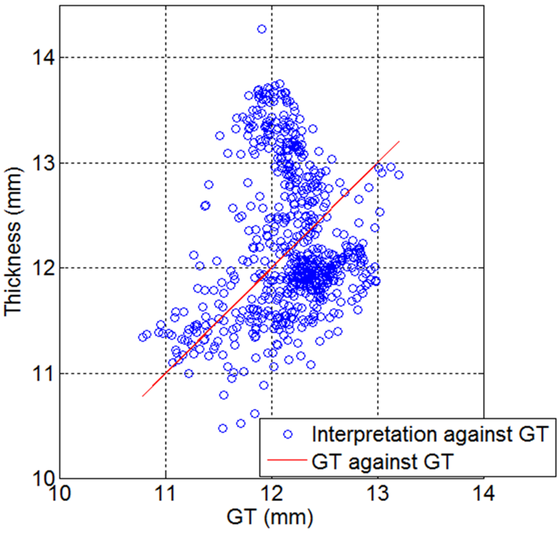

FIGURE 3.32: Variation of interpretations along with GT for the Ductile Cast Iron pipe segment.

material properties may change from one pipe to another depending on the way they were manufactured and previous electromagnetic interactions they have been subjected to. In such instances, a model learned from one set of calibration blocks may not be sufficiently universal for thickness quantification of all pipes of the same material. This challenge may be tackled by calibrating the c value using $c = (\ln \beta_{max} - 2 \ln d)$ when desired

Table 3.4: Statistics of absolute error between interpreted pipe wall thickness map and ground truth for the Ductile Cast Iron pipe segment.

Statistical Parameter	Value
RMS Error	0.755 mm
Mean Absolute Error	0.616 mm
Standard Deviation of Absolute Error	0.438 mm
Maximum Absolute Error	2.359 mm
Mean Percentage Accuracy	94.93%

using one or a few known thicknesses on a pipe. Performing destructive testing to obtain calibrations thicknesses on in situ pipes by cutting out samples large enough for the PEC sensor is not feasible. However, using techniques such as ultrasounds is a feasible option after cleaning the pipe surface on suitable locations to expose healthy metal and achieve sufficient connectivity as shown in Fig. 3.33. Alternatively, extracting tiny samples and using SQUID or PPMS devices to precisely measure electrical and magnetic properties and numerically simulating the decay rates as per Section 3.3 for calibration is viable. To overcome the limitation of calibration errors, Section 3.5 presents a practically applicable method of scaling based on ultrasound measurements.

3.5 Scaling Based Alternative Thickness Quantification Method for Critical Pipe NDE

The possibility of using ultrasound measurements to calculate c and estimate the full thickness map of a 1 m long gray cast iron pipe segment was examined in this work. Accuracy of ultrasound measurements too are subjective to calibration, however sound velocities in different materials are available in literature (*e.g.*, http://www.olympus-ims.com/en/ndt-tutorials/thickness-gage/appendices-velocities/). More accurate calibration can be performed on small specimens having known thickness extracted from the material to be evaluated.

Since $\ln \beta_{max}$ is linearly related to thickness expressed in the form of $\ln d$ as per the result $\ln \beta_{max} = 2 \ln d + c$, the $\ln \beta_{max}$ values corresponding to a pipe segment were plotted as per Fig. 3.34 and a region containing high $\ln \beta_{max}$ values was identified. The size of the identified high feature value region was set to 10 cm×10 cm. 16 ultrasound measurements were performed in the region using a direct contact ultrasound probe whose diameter was 2.5 cm. The square was cleaned well before performing ultrasound measurements to achieve good connectivity. Each ultrasound based thicknesses was estimated using the kernel fitting method proposed in [66], and an average thickness was calculated for the square. Similarly, an average $\ln \beta_{max}$ value was also calculated for the square using the PEC signals. The average thickness and average $\ln \beta_{max}$ values were 25.1301 mm and -4.688 respectively. c for the evaluated pipe segment was obtained using $c = \ln \beta_{max} - 2 \ln d$. The c value was found to be 2.6794. The hence calculated c was then used in the transformation $d = \exp\left(\frac{\ln \beta_{max} - c}{2}\right)$ to estimate the full thickness map. Results are shown in Fig. 3.35 and Fig. 3.36. Table 3.5 shows the error statistics, the percentage accuracy was over 94%, which was slightly better than 92% for the same pipe section when thickness was estimated using $c = 2.7473$, which is the value resulting from calibration blocks. Therefore, the approach can be considered a practically effective method to reduce the errors caused by material property discrepancies between calibration and testing.

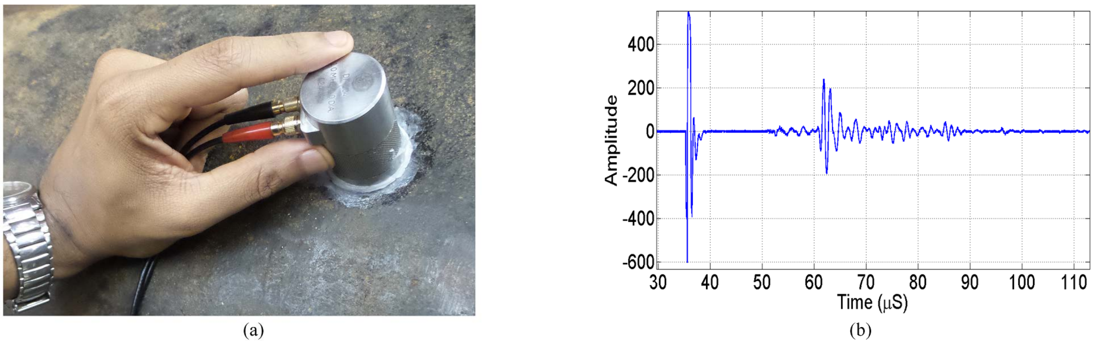

(a) (b)

FIGURE 3.33: Measuring pipe wall thickness using ultrasounds after cleaning the surface: (a) Ultrasound probe on pipe, (b) An ultrasound waveform.

3.6 Local Nonlinearities Present in the Thickness-Feature Function

Though the thickness-feature function considered in this work ($\ln \beta_{max} = 2 \ln d + c$) suggests linearity for all thicknesses in theory, due to practical limitations, the linearity is

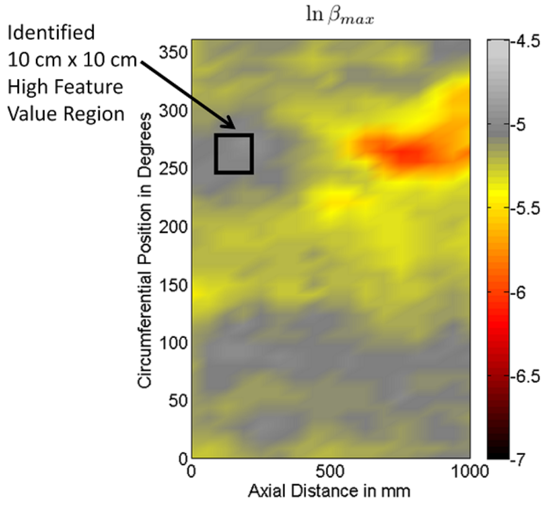

FIGURE 3.34: Plot of $\ln \beta_{max}$ values for data obtained on a gray cast iron pipe segment.

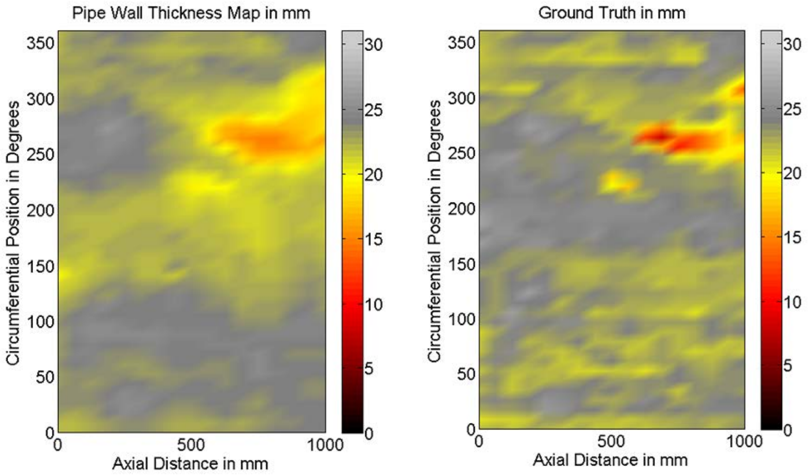

FIGURE 3.35: Interpreted thickness map (by estimating c using ultrasounds) and GT for a Gray Cast Iron pipe segment.

TABLE 3.5: Statistics of absolute error between interpreted pipe wall thickness map (by estimating c using ultrasounds) and ground truth for a Gray Cast Iron pipe segment.

Statistical Parameter	Value
RMS Error	1.62 mm
Mean Absolute Error	1.25 mm
Standard Deviation of Absolute Error	1.02 mm
Maximum Absolute Error	7.41 mm
Mean Percentage Accuracy	94.39%

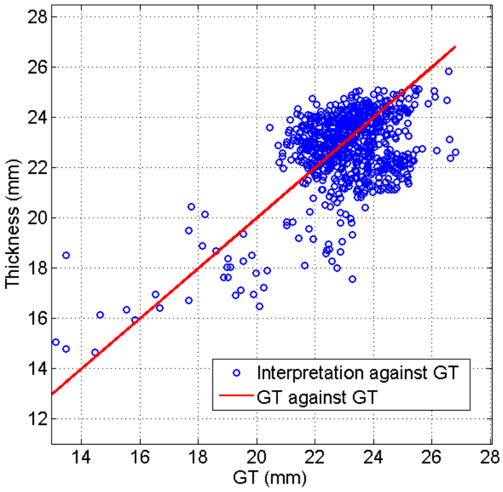

FIGURE 3.36: Variation of interpretations (by estimating c using ultrasounds) along with GT for a Gray Cast Iron pipe segment.

lost at very low and very high thickness ends as mentioned in Subsection 3.4.1. Fig. 3.37 elaborates the loss of linearity for the material of gray cast iron. Similar nonlinearity was observed on other pipe materials too and this behavior is general to ferromagnetic materials, but the nonlinear regions are specific for a given PEC sensor. The figure shows noisy readings, *i.e.*, 3 repeated readings on each thickness, for calibration blocks of thickness 1, 2, ..., 10, 12, ..., 22, 25, 30 and 35 mm. The linear region can be identified to be from 4 mm to 30 mm. Feature values for 1, 2 and 3 mm, and the feature value for 35 mm seem to exist beyond the linear range. More precisely, linear or nonlinear regions can be identified by plotting c values for each individual measurement against $\ln d$ and identifying a region where c exhibits an insignificant variation as shown in Fig. 3.38. In quantitative sense, this can be considered as a region where there is more than 0.95 correlation between $\ln \beta_{max}$ and $\ln d$. Loss of linearity occurs purely due to practical limitations prevailing in the measurement system, and the linear thickness-feature function is incapable of capturing this nonlinearity and therefore, this is a limitation which has to be adhered when executing.

Loss of linearity at the high thickness end is not greatly visible in the figure but was observed more vividly with a smaller sensor in Fig. 3.20. This is attributed to the sensor not having a strong enough excitation to penetrate a 35 mm gray cast iron thickness, or any large enough thickness of any other ferromagnetic material. This limitation is to be expected in any practical sensor and this can be avoided to an extent by increasing the

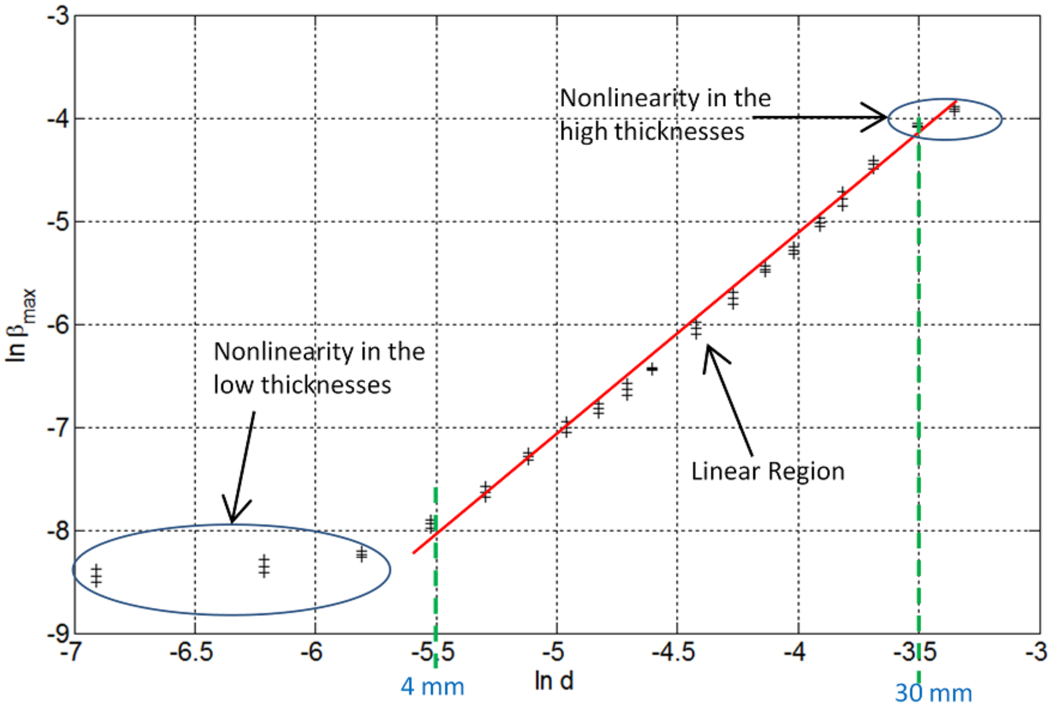

FIGURE 3.37: Nonlinearity in the thickness-feature function in the low and high thickness ends for gray cast iron.

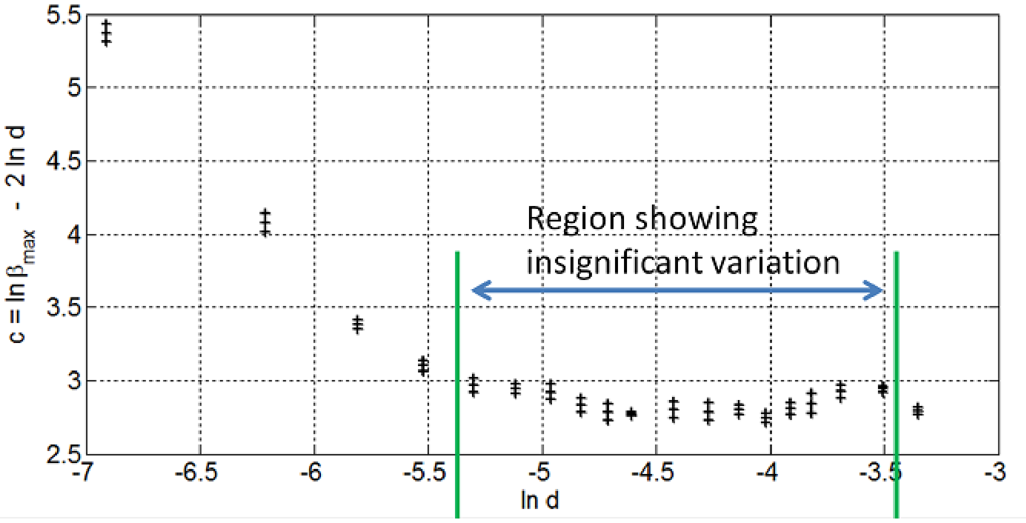

FIGURE 3.38: Variation of c of each measurement against $\ln d$ for gray cast iron.

excitation strength. It can thus be concluded that the linearity prevails only within the thickness range which the excitation is strong enough to penetrate, and the linearity is lost when the thickness is beyond the sensor's penetration capability.

Nonlinearity in the low thickness end is attributed to the signal entering the noise margin before it attains its constant gradient. This practical limitation forces the β_{max} feature to be extracted at an undesired time and consequentially the extracted value is not in accordance with the $\beta_{max} \approx \dfrac{\mu\sigma d^2}{\pi^2}$ approximation.

In the light of the critical pipe specific target application of this thesis, the role played by these nonlinearities is not very significant since for instance when assessing gray cast iron pipes, the maximum expected thickness is around 30 mm, and the chances of having thicknesses less than say 5 mm, is highly unlikely. Therefore, the analytical approach is still suitable for the target application, however, a method having the capability to model these nonlinearities will be an additional asset.

With the observations thus far, it is evident that these nonlinearities are specific to materials, sensor geometry and excitation strength. Therefore, redesigning sensors to suit different thickness ranges may be an option to avoid the nonlinearities and enable using the linear thickness-feature function to assess all desired thicknesses. Alternatively, the complexity and cost of having to redesign the sensor can be avoided by using alternative methods to learn the thickness-feature function while capturing nonlinearity. That is where GP based machine learning adds value and it is used in Chapter 4 since it can learn the nonlinear thickness-feature function along with uncertainty.

The logarithmic thickness-feature function consists of both linear and nonlinear regions as can be seen in Fig. 3.37. However, if the function between d and β_{max} is considered, the function is by default nonlinear and becomes much smoother as shown in Fig. 3.39. The function between d and β_{max} is considered as the nonlinear form of the thickness-feature function in this thesis. Noise is more visible in this case due to the absence of attenuation caused by the logarithmic scale. Given the smoothness and functional behavior, the function between d and β_{max} shown in Fig. 3.39 is learned non-parametrically using GP in Chapter 4 by using numerically simulated feature values as training data, and the learned function is used for critical pipe NDE. Sensor noise quantification to aid numerical modeling in Chapter 4 is done in Section 3.7.

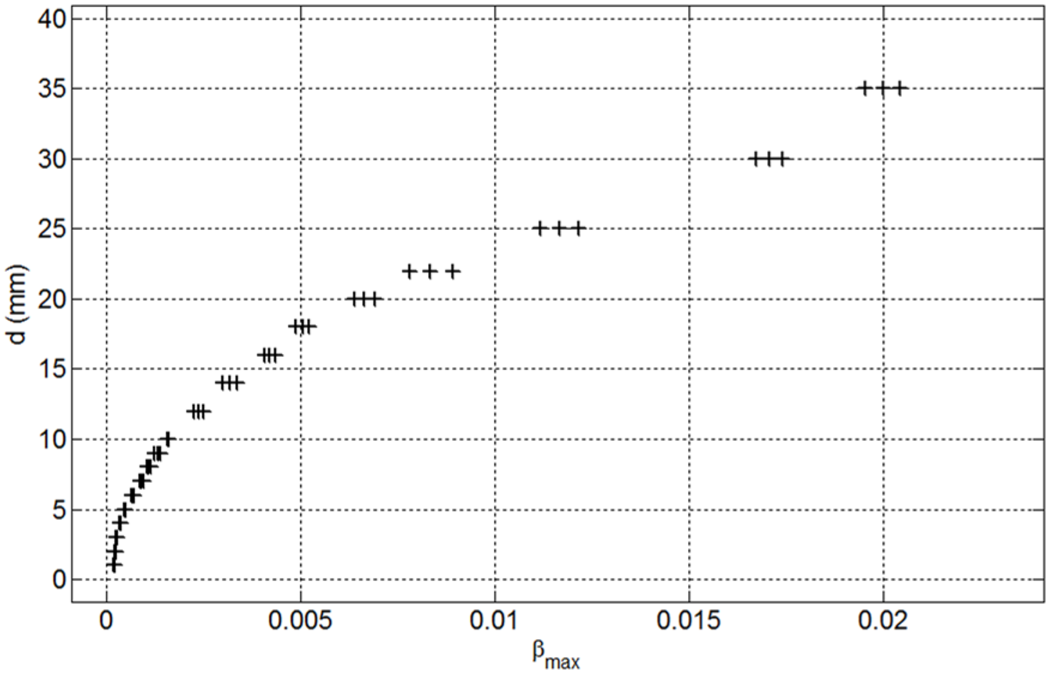

FIGURE 3.39: Nonlinear variation of d against β_{max}.

3.7 Sensor Noise Characterization

For a numerical sensor model to be realistic, the noise characteristic prevailing in the actual measurement setup should be incorporated. Chapter 4 numerically models the rectangular PEC sensor's interaction with gray cast iron. To aid that modeling exercise, this section characterizes the noise levels of the sensor for different gray cast iron thicknesses with the aid of calibration blocks.

As mentioned earlier in this chapter, three measurements were performed on each calibration block of each material. Noise characterization for gray cast iron was done with measurements obtained on 1, 2, ..., 10, 12, ..., 22, 25, 30 and 35 mm thicknesses. Characterization was done by calculating β_{max} for each measurement and computing the mean and standard deviation of β_{max} for each thickness. Assuming the noise is Gaussian, the $\pm 2\times$standard deviation bound of β_{max} for each thickness is considered as the noise margin of the sensor. Table. 3.6 provides the results and Fig. 3.40 graphically depicts the noise characteristic. This noise characterization method can be generalized to any PEC

TABLE 3.6: Noise characteristic of the PEC sensor used for in situ applications when used on gray cast iron.

Thickness (mm)	Mean of β_{max}	±2×standard deviation of β_{max}
1	0.000216	2.81×10^{-5}
2	0.000236	3.12×10^{-5}
3	0.000265	1.64×10^{-5}
4	0.000356	2.84×10^{-5}
5	0.000486	5.11×10^{-5}
6	0.000685	4.45×10^{-5}
7	0.000911	1.03×10^{-4}
8	0.001088	1.03×10^{-4}
9	0.001314	1.56×10^{-4}
10	0.001601	4.08×10^{-5}
12	0.002369	2.88×10^{-4}
14	0.003176	4.07×10^{-4}
16	0.004212	2.56×10^{-4}
18	0.005052	3.37×10^{-4}
20	0.006632	5.50×10^{-4}
22	0.008321	1.19×10^{-3}
25	0.011654	1.03×10^{-3}
30	0.017055	6.82×10^{-4}
35	0.019989	9.18×10^{-4}

sensor and material in relation to the β_{max} feature. The characterized noise bounds are incorporated in Chapter 4 for numerical sensor modeling.

3.8 Conclusions

The main objective of this chapter was to introduce the detector coil voltage decay rate as a ferromagnetic material specific thickness discriminative PEC signal feature. Analytical derivation of an expression for the decay rate $\beta(t)$ was presented. Hence a simplistic approximation for the feature in the form of $\beta_{max} \approx \frac{\mu\sigma d^2}{\pi^2}$ was obtained and by using it, a parametric linear relationship between thickness and the feature value in the form of $\ln \beta_{max} = 2 \ln d + c$ where $c = \frac{\mu\sigma}{\pi^2}$ was derived. The relationship behaves as a function which maps feature values to thickness and the parameter c fully specifies the specificness of the function towards a particular material and therefore, the function can be used for NDE in the form of thickness estimation when c has already been estimated.

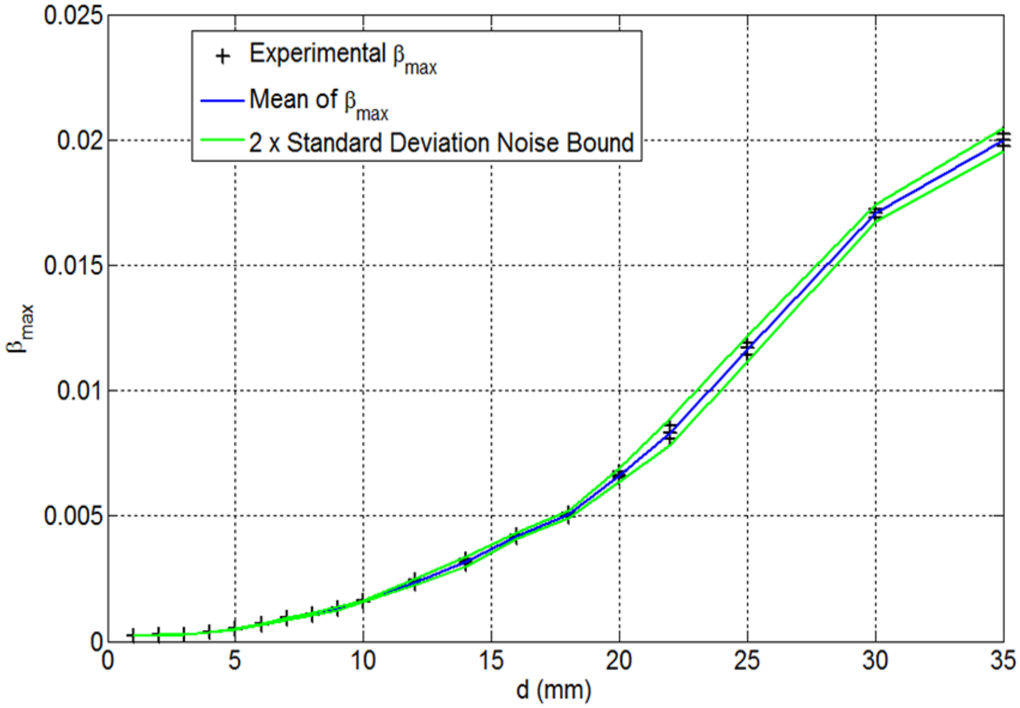

FIGURE 3.40: Graphical depiction of sensor noise characteristic when used on gray cast iron.

Two methods are proposed in the chapter to estimate c where the first method uses calibration blocks and the second uses ultrasound measurements. Once calibration signals are captured and the feature values are obtained, they can be used to fit a straight line through which the parameter c is estimated as the y-axis intercept. The main limitation in this approach is its susceptibility to calibration errors caused by material property discrepancies. In addition to fabricating calibration blocks being costly and time consuming, producing blocks which have material properties which precisely match those of pipe materials is practically infeasible. Therefore, the incidence of material property mismatches between calibration and testing is likely and such discrepancies result in errors in thickness estimates. To overcome the challenge with material properties, an alternative method of scaling the feature values using ultrasound measurements to directly produce thickness is proposed. Although this method is practically applicable, requirement of identifying smooth regions suitable for ultrasound measurements and cleaning the pipe surface to obtain sufficient coupling is challenging to perform in situ. Thus, despite the analytical approach proposed in this chapter being effective on in situ critical pipe NDE, the approach encompasses the aforementioned challenges and limitations. Nevertheless, applicability of the framework on in situ critical pipe assessment is justified by the percentage accuracy of over 90% when comparing interpreted results with reality. In addition to results provided within this chapter, this claim is supported further by the analytical approach based thickness maps and error statistics for a number of gray cast iron pipes evaluated throughout the course of this research, provided in Appendix A.

Fitting a straight line to estimate c in order to specify the thickness-feature function can be done by avoiding the very low and very high thicknesses. Due to practical limitations of the sensor, nonlinearities are observed in the low and high thickness ends and the analytical approach is limited by not being able to model those nonlinearities without making alterations to the sensor itself. Nonlinearity in the high thickness end is caused due to the excitation not being strong enough to penetrate the high thicknesses while the nonlinearity in the low thickness end is caused due to the signal entering the noise margin before it attains constant gradient. When considering the challenges associated with the analytical approach in terms of calibration and nonlinearities, a more effective approach to overcome those challenges would be to measure precise electrical and magnetic properties of pipe materials and learn nonlinear thickness-feature functions based on numerically modeled sensor responses which incorporate measured material properties. An NDE approach operating hence is proposed in Chapter 4 and a sensor noise characterization was done at the end of this chapter to aid the numerical sensor modeling approach proposed in Chapter 4.

Chapter 4

Approach for Numerical and Probabilistic Sensor Modeling

This chapter introduces a numerical and probabilistic sensor modeling approach for critical pipe NDE via inferencing pipe wall thickness. The objective of the proposed approach is to overcome the calibration requirements and the practical difficulties associated with executing the analytical approach presented in Chapter 3. Elimination of calibration requirements is accomplished by measuring electrical and magnetic properties of pipe materials and incorporating them in a numerical sensor simulation model to produce calibration signals as opposed to using calibration blocks as done in the analytical approach.

The detector coil voltage decay rate is used as the thickness discriminative signal feature in this approach as well, however, the learning process of the thickness-feature function is probabilistic unlike in the previous approach where the parametric function was analytically derived and a model was fitted through parameter estimation. Decay rate values extracted from simulated sensor signals are used to non-parametrically learn the thickness-feature function using Gaussian Process (GP) based probabilistic machine learning. The hence learned function is used to probabilistically infer pipe wall thickness using feature values extracted from signals captured through in situ measurements. Unlike in the analytical approach, since the function is learned non-parametrically, subtle variations and local nonlinearities are captured through this approach. This aspect is an advantage over the analytical approach and consequentially, an improvement in the accuracy of inferred results is demonstrated in the chapter.

Two different forms of the eddy current problem, *i.e.*, the forward problem [67–69] and the inverse problem [70–72] are solved in practice. Solving the forward problem can be described as the process of computing the sensor signal when the test piece properties are known whereas the solving the inverse problem is the process of computing test piece properties when the signal is known. Technically, it is the inverse problem which has to be solved to accomplish condition assessment since the requirement is to predict the geometry of the test piece through a set of measured signals. However, solving the inverse problem is not straightforward in many cases, especially in scenarios similar to the target application of this thesis due to ill conditions of the inverse problem. This chapter therefore adapts the approach of numerically solving the forward problem using Finite Element Analysis (FEA) to predict signals in order to learn the thickness-feature function, and probabilistically solving the inverse problem using measured signals. The learned function is exploited to probabilistically infer the test piece property of pipe wall thickness by taking β_{max} feature values extracted from in situ measurements as inputs and hence, the inverse problem is solved.

In this chapter, the approach is broken down into the four sections: (a) Measuring electrical and magnetic properties of pipe materials; (b) Numerically modeling the PEC sensor; (c) Non-parametric learning of the thickness-feature function using GP; and (d) Probabilistic inference of pipe wall thickness. The chapter unfolds by sequentially describing the four sections. Conclusion of the chapter includes a discussion about the implications of results along with a comparison of accuracies produced by the analytical and probabilistic thickness estimation methods.

4.1 Measuring Electrical and Magnetic Properties of Pipe Materials

The procedure for measuring electrical and magnetic properties of critical pipe materials is presented in Fig. 4.1. When done in situ, high thickness regions are required to be

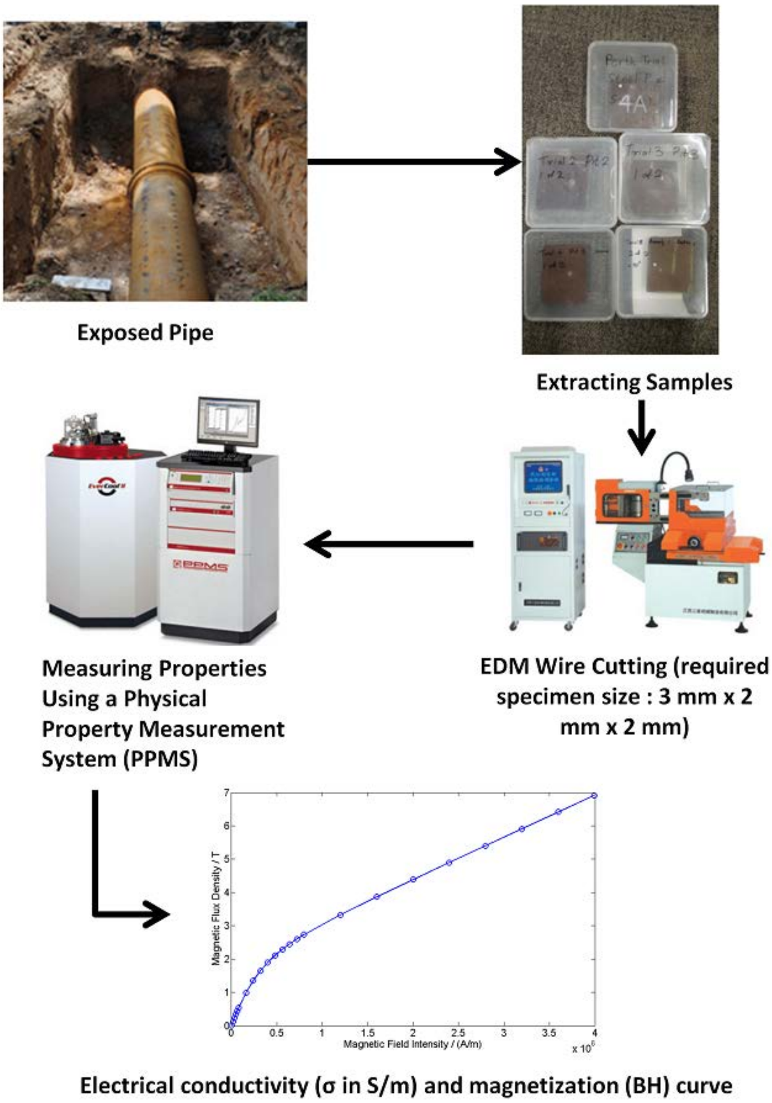

FIGURE 4.1: Steps for measuring electrical and magnetic properties of critical pipe materials. (Images adapted from http://www.diytrade.com/ and http://www.qdusa.com/)

qualitatively identified first since that enables extracting samples from those regions while causing minimal physical destruction to the structural integrity of pipes. This can be done by performing PEC scans first and visualizing the β_{max} values since they are proportional to the thickness of remaining ferromagnetic material. Usual mechanical cutting tools can be used for this process and extracting relatively large samples is necessary in order to avoid heating the interior of samples from which specimens of size 3 mm × 2 mm × 2 mm are eventually cut using an Electric Discharge Machining (EDM) wire cutter [73, 74]. The key when wire cutting specimens is to pay strict consideration towards minimizing heating by using cooling liquids since heat may adversely affect electrical and magnetic properties which are intended to be measured. Alternatively, filing the specimens too is an option with the capability of controlling heating given a significant availability of time and manual labor. A machine cut sample obtained from a gray cast iron pipe along with two wire cut test specimens of different sizes extracted from that sample are shown in Fig. 4.2. The original sample in this experimental case was deliberately made to have about 10 cm × 10 cm surface area as can be seen in Fig. 4.2 to enable extracting multiple specimens if required. Obtaining samples of such size causes significant partial destruction to in situ pipe walls, in actual practice therefore, the original sample can be much smaller if only one specimen is intended to be extracted as long as adequate cooling liquid is used to avoid over heating while machine cutting.

To model the PEC sensor interaction with pipe materials, it is required to measure: (a) Electrical conductivity (σ) in S/m; and (b) Magnetization curve (B-H loop) at a desired temperature (measurements done in room temperature were suitable for the work of this thesis). As done in this research, the state of the art mechanism for measuring such intrinsic physical properties is using a Physical Property Measurement System (PPMS) [75, 76]. Cutting specimens of size 3 mm × 2 mm × 2 mm was necessary to allow optimal fitting into the specimen holders and performing accurate measurements. Using powder particles

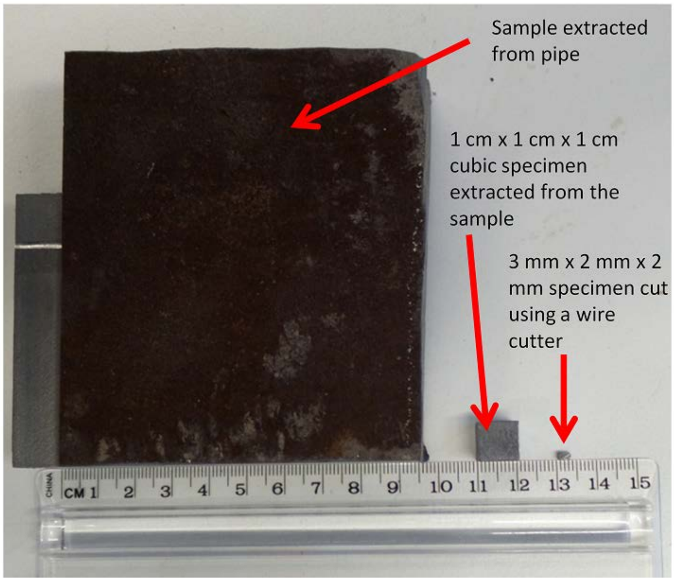

Figure 4.2: Extracted specimens for testing material properties.

instead of solid specimens is also possible with a PPMS to measure magnetization curves although not recommended due to the chances of powder being contaminated by foreign materials as a result of the process of extraction. Since such contaminations are likely to affect the accuracy of measurements, best practices were followed during this research by performing measurements on solid specimens. A magnetization curve measured in the form of magnetic flux density variation against magnetic field intensity from a specimen extracted from a gray cast iron pipe segment is shown in Fig. 4.3. Measuring up to a magnetic field intensity as high as the value shown in the figure is usually not necessary for PEC sensor modeling in the absence of externally applied strong magnetic fields, since field values resulting from PEC sensors alone are relatively low. Getting an idea about the produced field magnitudes and measuring only the low magnetic field range at a high sampling rate best suits the purpose.

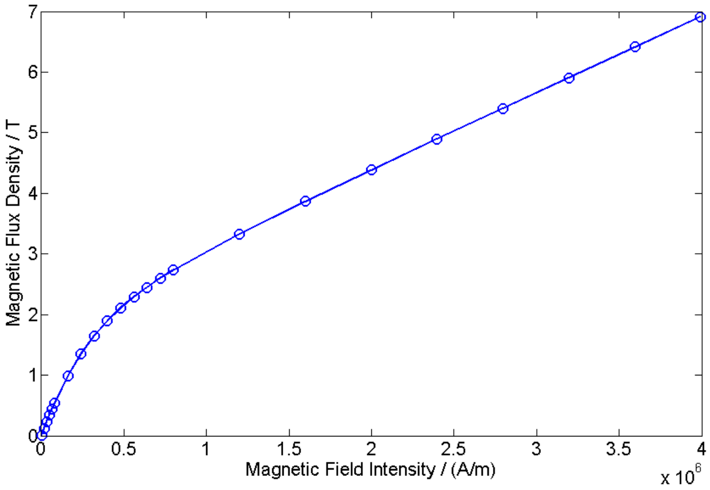

Figure 4.3: A magnetization curve measured from a specimen taken from a gray cast iron pipe segment.

Four Probe Method [77, 78] is used by the PPMS to perform resistivity measurements. An alternative method based on X-ray fluorescence (XRF) devices was experimented as well to calculate a range for electrical conductivity of pipe materials. State of the art portable XRF devices [79, 80] are available for in situ applications at present as shown in Fig. 4.4 and these devices can be used to analyze emission characteristics of materials to nondestructively determine a material's composition. Despite subtle variations, all examined pipe materials were composed of about 93 % Fe, 3 % C, 2 % Si in mass percentages and the rest included elements such as P, Mn, S, Ti and Cr. Pipe surfaces require to be cleaned to remove rust and graphitization in order to expose ferromagnetic material to enable X-rays to make contact to determine correct composition. Physical properties including electrical conductivity of elements and certain composite materials are known and are available in standard texts [15, 81] and online resources (http://www.periodictable.com/), these properties were used to apply the rule of mixtures [82, 83] to calculate a range for effective electrical conductivity of the composite material. Since this method allows only gaining a basic idea through a range for conductivity, the four probe facility available with the PPMS was used to measure the actual value.

An advantage prevails with the PPMS since the temperature dependence of conductivity can easily be characterized. Conductivity of gray cast iron pipe material was measured against temperature and the variation is plotted in Fig. 4.5. Since pipes exist in natural environment and are not subject to drastic temperature variations while in operation, temperature was not incorporated for numerical modeling. Therefore, $\sigma = 5.9 \times 10^5$ S/m, was used for modeling since it is the conductivity observed at a temperature of 300 K, *i.e.*, a close value to room temperature. However, the temperature coefficient $\alpha_\sigma = -643.956$ S/(m.K) of the pipe material's conductivity could be calculated through the experiment and the equation to model the conductivity σ_T in A/m, at a given temperature T in K, in terms of α_σ and conductivity $\sigma_{273} = 6.04358675 \times 10^5$ S/m at absolute zero (*i.e.*, $T_{273} \approx 273$ K), can be given as

$$\sigma_T \approx \sigma_{273} + \alpha_\sigma (T - T_{273}). \tag{4.1}$$

In the light of the target application of condition assessment of critical pipes, it should be noted that at times the exact material of aged in situ pipes may not be on record with water utilities. For instance, a utility will be certain that a particular pipe is made of some type of cast iron, but they may be unaware about the exact type (*i.e.*, whether a pipe is made of gray cast iron, or ductile cast iron for example). In such instances, the process of extracting specimens done in this work can aid to easily identify the type of cast iron through microscopic inspection since accurate discrimination via on site visual inspection or composition checks is difficult. Since some pipes were encountered within this research

FIGURE 4.4: In situ application of an XRF device for material analysis. (Image from http://www.electronicproducts.com/)

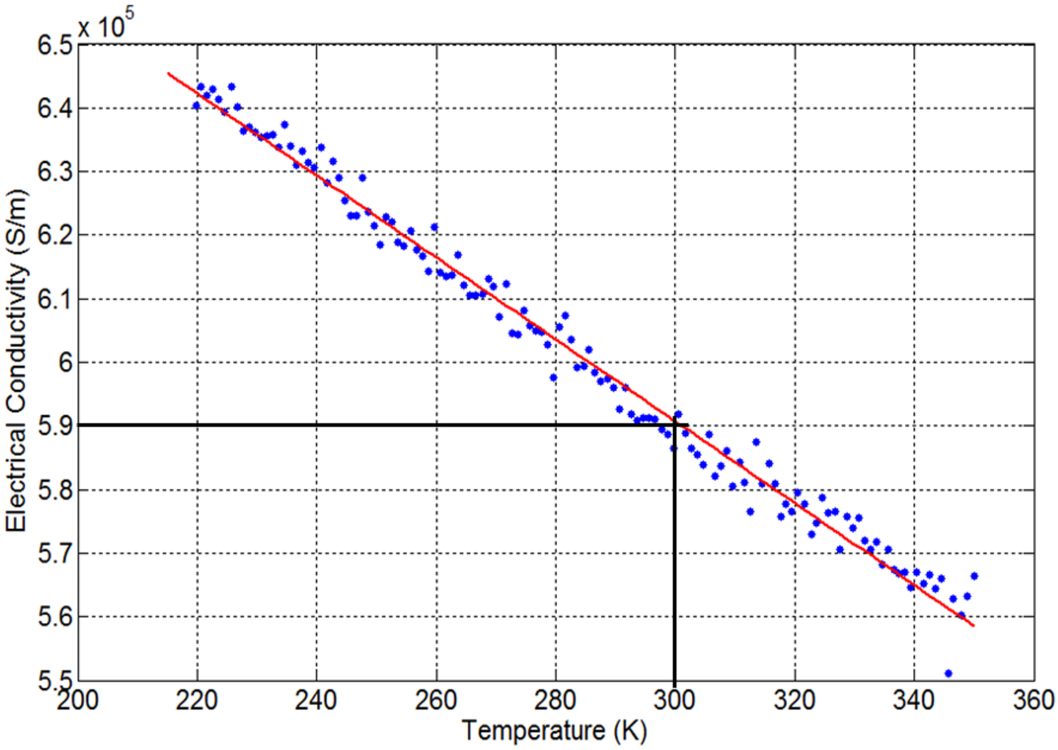

FIGURE 4.5: Temperature variation of electrical conductivity of gray cast iron pipe material (measured using Four Probe Method (PPMS)).

where the water utilities were not aware about the exact type of cast iron, specimens were extracted and microscopically examined. The difference in the grain structure between gray and ductile cast irons could easily be observed through this process as evident in Fig. 4.6 and this can be identified as a secondary advantage of extracting specimens since it enables confirmation of material, given that information is important for both water utilities and NDE service providers.


(a) (b)

Figure 4.6: Microscopic view of micro-structures of cast irons: (a) Gray cast iron; (b) Nodular or Ductile cast iron.

Once the required electrical and magnetic properties are measured, it is possible to model the PEC sensor's interaction with pipe materials as explained in Section 4.2. Measured conductivity and magnetization curve of gray cast iron were used in the numerical model.

4.2 Numerically Modeling the PEC Sensor

Numerical modeling in this section refers to numerically solving the mathematical model of the PEC sensor setup derived using Maxwell's equations. The procedure followed to numerically model sensor responses for gray cast iron is shown in Fig. 4.7. Modeling was done using Finite Element Analysis (FEA) [16, 17] and the commercial FEA package COMSOL Multiphysics® [62, 84]. Measured electrical and magnetic properties of pipe materials and the geometric and physical properties of the PEC sensor are taken as inputs by the model and numerically solves the magnetic vector potential [85–87] based equations via time stepping FEA [88, 89] to calculate the time varying PEC signal. Governing equations of the underlying physics are derived in the subsequent section.

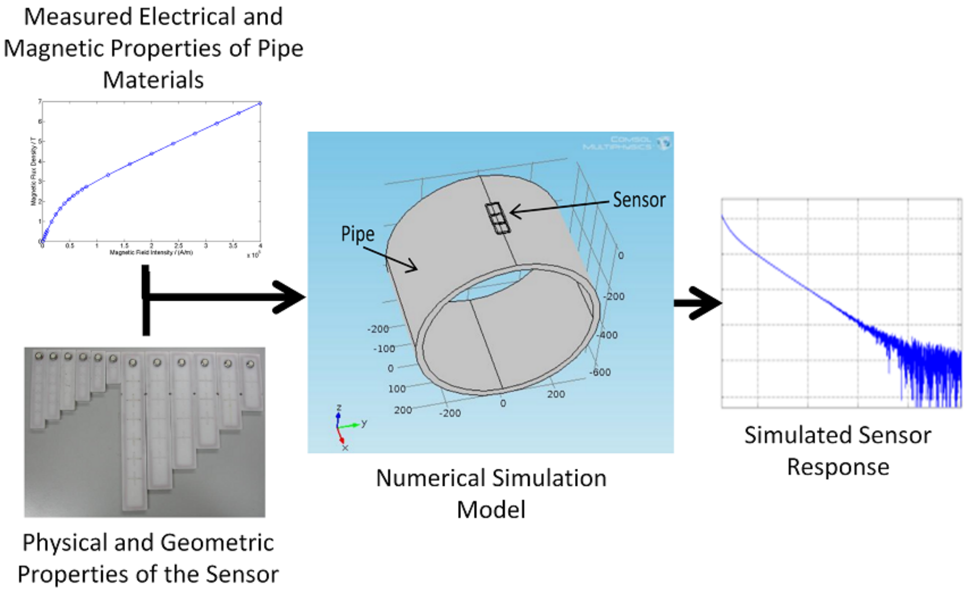

Figure 4.7: Procedure followed to numerically simulate sensor signals.

4.2.1 Governing Equations of the Numerical Model

Maxwell's equations [90–92] which describe the relationships between electric and magnetic fields can be identified as the series of laws which govern electromagnetic phenomena. Equations describe Ampere's, Faraday's and Gauss's laws in both differential and integral forms [92, 93].

Ampere's law in differential form is given in Eq. 4.2 and it states that a circulating magnetic field $\vec{H}$ is produced by an electric current density $\vec{J}$. The notation $(\nabla\times)$ is the curl operator and $\vec{D}$ denotes the displacement current.

$$\nabla \times \vec{H} = \vec{J} + \frac{\partial \vec{D}}{\partial t} \tag{4.2}$$

Integral form of Ampere's law expressed in Eq. 4.3 states that a current flowing through a surface produces a circulating magnetic field $\vec{H}$ around that surface.

$$\oint_c \vec{H}.\mathrm{d}l = \int_s \left(\vec{J} + \frac{\partial \vec{D}}{\partial t} \right) .\mathrm{d}s \tag{4.3}$$

For the quasi-static case where $\sigma >> \omega\epsilon_0$, $\omega = 2\pi f$ for frequency f and $\epsilon_0 = 8.854 \times 10^{-12}$ F/m is the permittivity of free space, the displacement current $\vec{D}$ is neglected. Therefore Ampere's law can be simplified to $\nabla \times \vec{H} = \vec{J}$ and $\oint_c \vec{H}.\mathrm{d}l = \int_s \vec{J}.\mathrm{d}s$.

Differential form of Faraday's law shown in Eq. 4.4 states that a changing magnetic flux density $\vec{B}$ produces a circulating electric field intensity $\vec{E}$.

$$\nabla \times \vec{E} = -\frac{\partial \vec{B}}{\partial t} \tag{4.4}$$

Integral form of Faraday's law in Eq. 4.5 states that a changing magnetic flux density through a surface induces a circulating electromotive force (emf) on the boundary of that surface. Currents induced by a changing magnetic flux oppose the change in flux according to Lenz's law [94, 95] and is signified by the negative sign.

$$\oint_c \vec{E}.\mathrm{d}l = -\frac{\partial}{\partial t} \int_s \vec{B}.\mathrm{d}s \tag{4.5}$$

Gauss's law for magnetic fields when expressed in differential form as shown in Eq. 4.6 states that the divergence of the magnetic flux density $\vec{B}$ at any point is zero.

$$\nabla.\vec{B} = 0 \tag{4.6}$$

Integral form of Gauss's law shown in Eq. 4.7 states that the net magnetic flux density passing out of a surface is zero.

$$\int_s \vec{B}.\mathrm{d}s = 0 \tag{4.7}$$

In addition to Maxwell's equations, the following constitutive relationships are also used for modeling. Terms μ_0, μ_r and σ are permeability of free space (*i.e.*, $\mu_0 = 4\pi \times 10^{-7}$ H/m), relative permeability and electrical conductivity respectively.

$$\vec{B} = \mu_0 \mu_r \vec{H} = \mu \vec{H} \tag{4.8}$$

$$\vec{J} = \sigma \vec{E} \tag{4.9}$$

Since Eq. 4.8 and 4.9 are used, measuring electrical and magnetic and properties become critically important for numerical modeling. μ_r is constant for linear materials, but it is nonlinear for most ferromagnetic materials like those of critical pipes and permeability becomes a function of magnetic field as shown in Eq. 4.10. The importance of measuring the B-H curve which is a function in the form of $||\vec{B}|| = f(||\vec{H}||)$ can hence be realized.

$$\mu(||\vec{H}||) = \frac{\partial ||\vec{B}||}{\partial ||\vec{H}||}. \tag{4.10}$$

It is also known that the magnetic flux density $\vec{B}$ can be expressed in terms of magnetic vector potential $\vec{A}$ as in

$$\vec{B} = \nabla \times \vec{A}. \tag{4.11}$$

Substituting the result in Eq. 4.11 in Eq. 4.4 yields

$$\nabla \times \vec{E} = -\frac{\partial}{\partial t} \nabla \times \vec{A} = -\nabla \times \frac{\partial \vec{A}}{\partial t}. \tag{4.12}$$

Solving Eq. 4.12 expresses $\vec{E}$ as

$$\vec{E} = -\frac{\partial \vec{A}}{\partial t} - \nabla \Phi \tag{4.13}$$

where Φ is the applied magnetic scalar potential [96–98] since the curl of the gradient of any scaler field is always the zero vector (*i.e.*, $\nabla \times (\nabla\Phi) = \vec{0}$) [99–101]. Multiplying both sides of Eq. 4.13 by σ yields

$$\sigma\vec{E} = -\sigma\frac{\partial\vec{A}}{\partial t} - \sigma\nabla\Phi. \tag{4.14}$$

Here, $\vec{J_s} = -\sigma\nabla\Phi$ can be considered as an externally applied source current and hence Eq. 4.14 can be rewritten as

$$\sigma\vec{E} = -\sigma\frac{\partial\vec{A}}{\partial t} + \vec{J_s}. \tag{4.15}$$

Right hand side of Eq. 4.15 expresses the total current density $\vec{J} = \vec{J_{ind}} + \vec{J_s}$ where $\vec{J_{ind}} = -\sigma\frac{\partial\vec{A}}{\partial t}$ is the induced current density. Consequentially, Eq. 4.15 becomes the same as Eq. 4.9 and this enables combining Eq. 4.15 and Eq. 4.2 for the quasi-static case by eliminating the common $\vec{J}$. This results in

$$\nabla \times \vec{H} = -\sigma\frac{\partial\vec{A}}{\partial t} + \vec{J_s}. \tag{4.16}$$

By substituting for $\vec{H}$ in Eq. 4.16 using Eq. 4.8, and expressing $\vec{B}$ in terms of magnetic vector potential as in Eq. 4.11, Eq. 4.16 can be rewritten as

$$\nabla \times \vec{B} = \nabla \times (\nabla \times \vec{A}) = -\mu\sigma\frac{\partial\vec{A}}{\partial t} + \mu\vec{J_s}. \tag{4.17}$$

Since curl of a curl of any vector can be expressed as $\nabla \times (\nabla \times \vec{A}) = \nabla(\nabla.\vec{A}) - \nabla^2\vec{A}$ [99–101], Eq. 4.17 can be expanded as

$$\nabla(\nabla.\vec{A}) - \nabla^2\vec{A} = -\mu\sigma\frac{\partial\vec{A}}{\partial t} + \mu\vec{J_s}. \tag{4.18}$$

By using the Coulomb gauge, $\nabla.\vec{A} = 0$, on Eq. 4.18 and manipulating we get

$$\nabla^2 \vec{A} - \mu\sigma \frac{\partial \vec{A}}{\partial t} = -\mu \vec{J}_s. \tag{4.19}$$

Eq. 4.19 is the expression for the magnetic vector potential for a location within the modeled domain and thus it becomes the numerically solvable governing equation for the PEC setup considered in this thesis. Subsection 4.2.2 details the development of the model.

4.2.2 Developing the Numerical Model

Finite Element Analysis (FEA) [16, 17, 102] is commonly used for solving many multi-physics problems including ones involving electromagnetic phenomena such as the eddy current problem [86, 103, 104]. In this chapter, the model is developed using the commercially available COMSOL Multiphysics®[62, 84, 105] FEA simulation package. Other software packages such as ANSYS [106–108] and CIVA [109–111] have also been used in literature to solve eddy current related problems. Since this chapter proposes an approach of numerically solving the forward problem to predict signals and probabilistically solving the inverse problem with the aid of predicted and measured signals to infer pipe wall thickness, the purpose of the developed numerical model is to cater the requirement of solving the forward problem by taking into account actual physical properties of critical pipe materials. Since the formulated problem does not yield closed form solutions and is governed by the nonlinear form of Eq. 4.19, solving requires to be done numerically which is why the versatile technique of FEA is used in this work.

The numerical model takes electrical and magnetic properties of the test piece, geometry of the test piece, geometric and physical properties of the PEC sensor and excitation signal characteristics as inputs, and produces the time varying sensor signal for a given test piece as the output. In COMSOL, the model can be geometrically constructed and the governing equations of each domain can be defined. Once the model is constructed, meshing requires to be done before solving since FEA is used. Meshing is the process of spatial segmentation of the model to provide discrete nodes at which FEA will calculate fields in order to compute the necessary solution. The ground rule is, the finer the mesh, the more accurate the solution will be. However, a fine mesh also increases the computation time. Therefore, since the required signal is the voltage induced in the detector coil, a finer mesh was set to the detector coil and the adjacent region while the regions further away from the sensor were left coarse. Several trial and error simulations were run to ensure mesh independence and convergence of the solution. Fig. 4.8, 4.9 and 4.10 show the developed geometric model, meshed geometry and induced fields respectively.

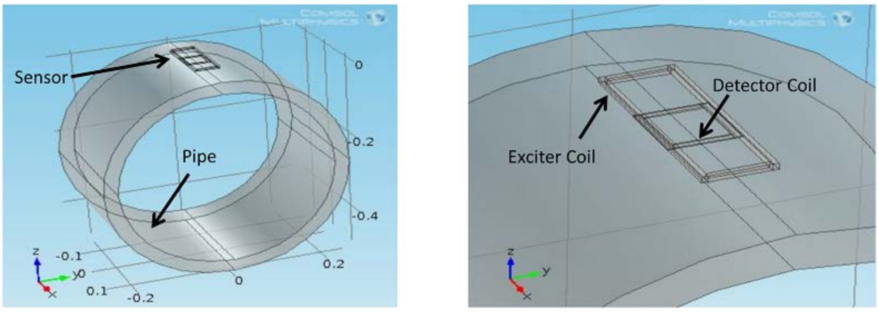

(a) (b)

FIGURE 4.8: Developed FEA model: (a) Complete model; (b) Zoomed view of the sensor.

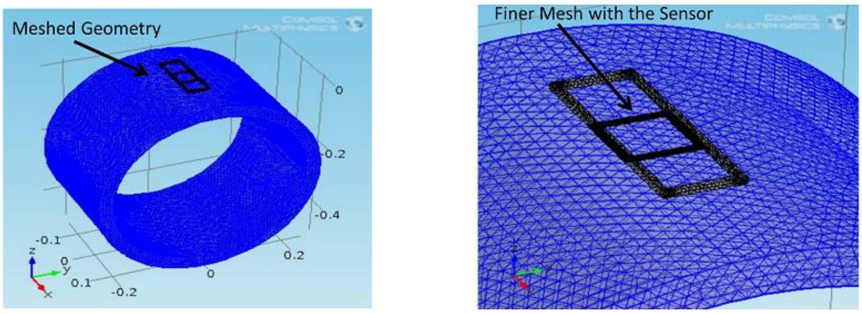

(a) (b)

FIGURE 4.9: Meshed FEA model: (a) Complete model; (b) Fine mesh of the sensor.

To describe the model as a function which produces PEC signals as the output, it is important to explicitly identify the variables required for modeling. Numerical values of the input variables are not provided in this thesis to prevent revealing sensitive information which remain as the intellectual property of the PEC service provider. However, a symbolic representation of the model as a function relating the input variables to the PEC signal is provided.

The output of the FEA model is the time varying PEC signal $\ln V(t)$ itself and the flexibility of obtaining it in the form of $\ln V(t)$ or $V(t)$ is prevalent. Assuming the output is

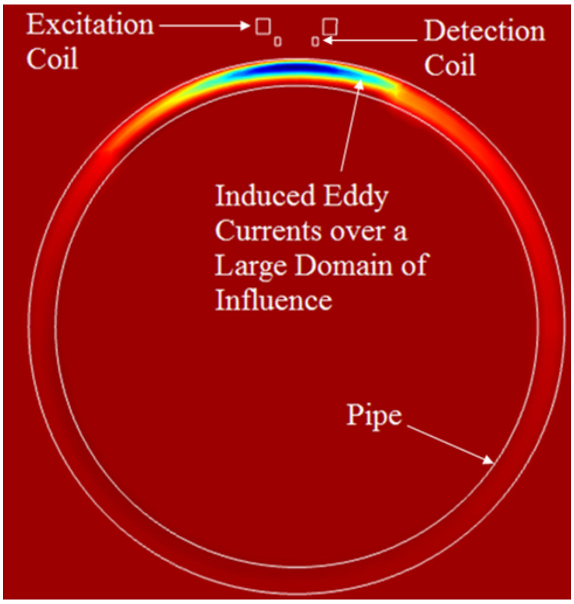

Figure 4.10: Cross-sectional view of the numerical model showing the eddy current induction phenomenon (Adapted from [6]).

obtained in the form of $\ln V(t)$, the output is expressed as $S = \ln V(t)$ in this section for notational simplicity.

One of the important sets of input variables is the set of test piece properties. The test piece in this case is the pipe and therefore the required input variables in terms of geometry are pipe radius r and wall thickness d. In terms of intrinsic material properties, measured electrical conductivity σ and magnetic permeability μ are required. But since pipe materials are ferromagnetic and consist nonlinear magnetic properties, obtaining a constant μ is not possible and as a result, the measured magnetization curve (B-H curve) in the form of $||\vec{B}|| = f(||\vec{H}||)$ is required.

The sensor excitation voltage essentially takes the shape of a Heaviside step function since PEC technique is employed. Due to the decay rate signal feature used for thickness quantification appearing in the later stages of the signal, capturing the excitation signal's influence on the early stages of the detector signal is not of critical importance for this work. An ideal step function is therefore used to excite the simulated sensor since the rise time of the excitation signal has no significant impact of the predominantly thickness dependent decay rate feature $\beta_{max} \approx \dfrac{\mu\sigma d^2}{\pi^2}$. Excitation parameters required for modeling are the output impedance of the source Z_{so}, pulse amplitude V_{amp}, pulse frequency f_p and the duty ratio $D\%$.

Required geometric properties of the exciter and detector coils are shown in Fig. 4.11 and 4.12, and apart from them, the following parameters are required for modeling: (a) number of excitation coil turns n_e; (b) number of detector coil turns n_d; (c) electrical conductivity of the exciter coil σ_e; (d) electrical conductivity of the detector coil σ_d; (e) magnetic permeability of the exciter coil μ_e; (f) magnetic permeability of the detector coil μ_d; and (g) load impedance connected to the detector coil Z_{dl}. Both exciter and detector coils were made of copper and the standard conductivity and permeability values of copper [112, 113] were used. The impedance Z_{dl} is the load which the detector coil signal is measured across and this impedance can be measured. Finally, the geometric properties of the sensor shown in Fig. 4.11 and 4.12 are required. Quadrilaterals in the plan view of Fig. 4.11 are rectangular while those of the plan view of Fig. 4.12 are square. Table 4.1 provides a summary of the parameters required for modeling.

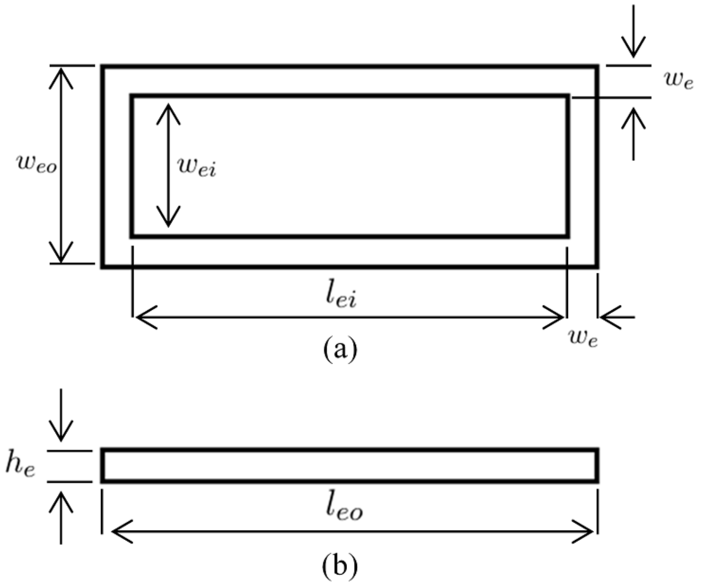

FIGURE 4.11: Geometric properties of the excitation coil: (a) Plan view; (b) Side view.

The numerical model can thus be expressed as a function f_{num} which maps the parameters required to the output logarithmic PEC signal S as shown in

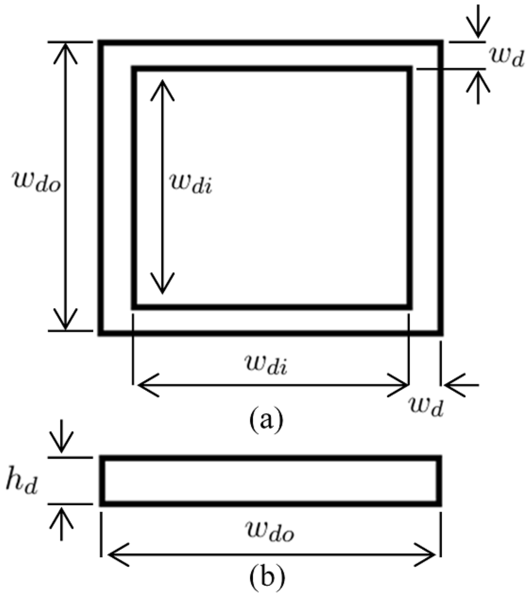

Figure 4.12: Geometric properties of the detector coil: (a) Plan view; (b) Side view.

$$S = f_{num}(r, d, \sigma, \mu, Z_{so}, V_{amp}, f_p, D\%, n_e, n_d, \sigma_e, \sigma_d, \mu_e, \mu_d, Z_{dl}, w_{eo}, w_{ei}, l_{eo}, l_{ei}, w_e, h_e, w_{do}, w_{di}, w_d, h_d, t). \tag{4.20}$$

where t denotes time. Extraction of the β_{max} feature from a signal S produced by the numerical model for learning the thickness-feature function is done by capturing the maximum as shown in Eq. 4.21 before the signal enters the noise margin.

$$\beta_{max} = \max\left(\left|\frac{\partial S}{\partial t}\right|^{-1}\right) \tag{4.21}$$

4.2.3 Results Produced by the Numerical Model

Shown in Fig. 4.13 are some simulated sensor signals and corresponding experimental signals for gray cast iron. The default model produces signals with only numerical noise and no experimental noise unless added artificially. Noise characterization done in Section 3.7 shows an average standard deviation of 1.645×10^{-4} for β_{max} for gray cast iron when considering all thicknesses. The default model with no added noise shows appreciable

Table 4.1: Parameters required for simulation.

Symbol	Description
r	Pipe radius
d	Pipe wall thickness
σ	Electrical conductivity of pipe material
μ	Nonlinear magnetic permeability of pipe material
Z_{so}	Output impedance of the source
V_{amp}	Excitation voltage pulse amplitude
f_p	Excitation pulse frequency
$D\%$	Duty ratio of the excitation pulse
n_e	Number of excitation coil turns
n_d	Number of detector coil turns
σ_e	Electrical conductivity of the exciter coil
σ_d	Electrical conductivity of the detector coil
μ_e	Magnetic permeability of the exciter coil
μ_d	Magnetic permeability of the detector coil
Z_{dl}	Load impedance connected to the detector coil
w_{eo}	External width of the exciter coil
w_{ei}	Internal width of the exciter coil
l_{eo}	External length of the exciter coil
l_{ei}	Internal length of the exciter coil
w_e	Exciter coil domain width
h_e	Exciter coil domain height
w_{do}	External width of the detector coil
w_{di}	Internal width of the detector coil
w_d	Detector coil domain width
h_d	Detector coil domain height

convergence and solution repeatability by exhibiting an average noise of less than 10^{-8} for β_{max} on gray cast iron when tested with multiple simulations of the same calibration block thicknesses used for noise characterization in Section 3.7. Therefore, the mean value of experimental β_{max} for each thickness of gray cast iron was compared with mean of simulated β_{max} for each thickness and the agreement in Fig. 4.14 was observed. As Fig. 4.15 indicates, the level of agreement between the numerical model and experiments could be quantified in terms of a correlation coefficient [114–116] of $R = 0.999437$. The mathematical formula used to calculate the correlation coefficient is given in Eq. 4.22 where u and v signify two data vectors of which the correlation is computed. u_i and v_i denote the i th element of the vectors u and v respectively, and n is the number of elements

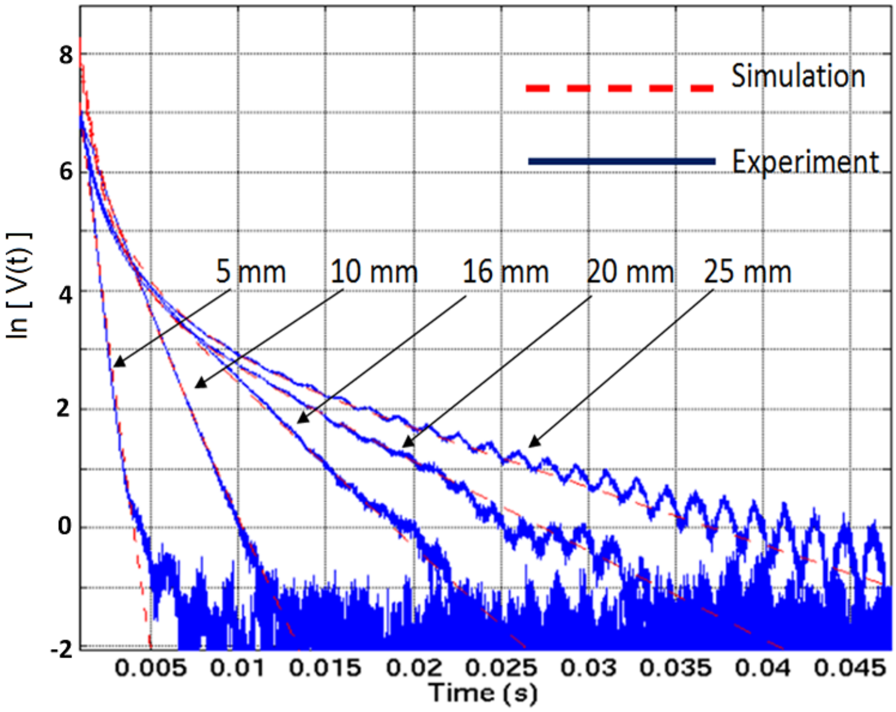

FIGURE 4.13: Numerically simulated PEC signals along with experiments (gray cast iron).

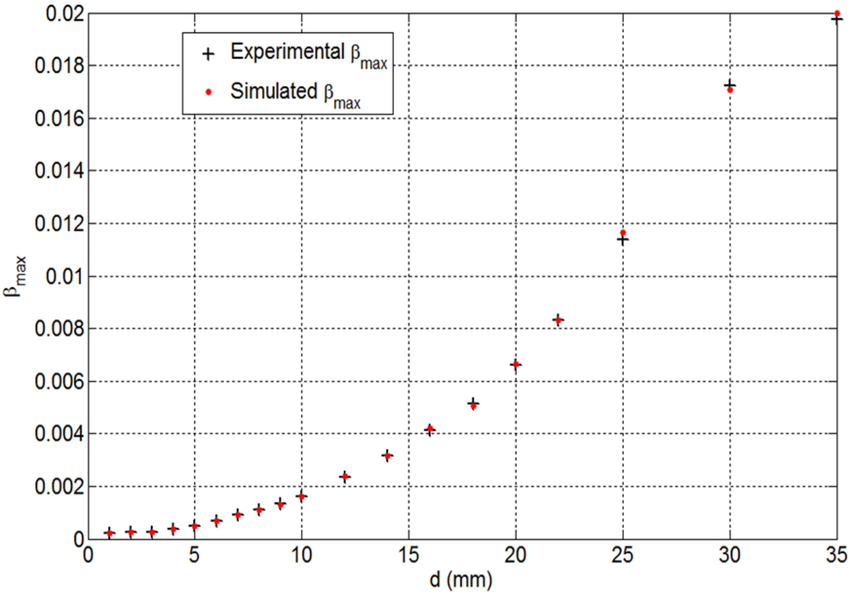

FIGURE 4.14: Feature values (β_{max}) vs thickness (d), agreement between simulation and experiments.

contained in each vector.

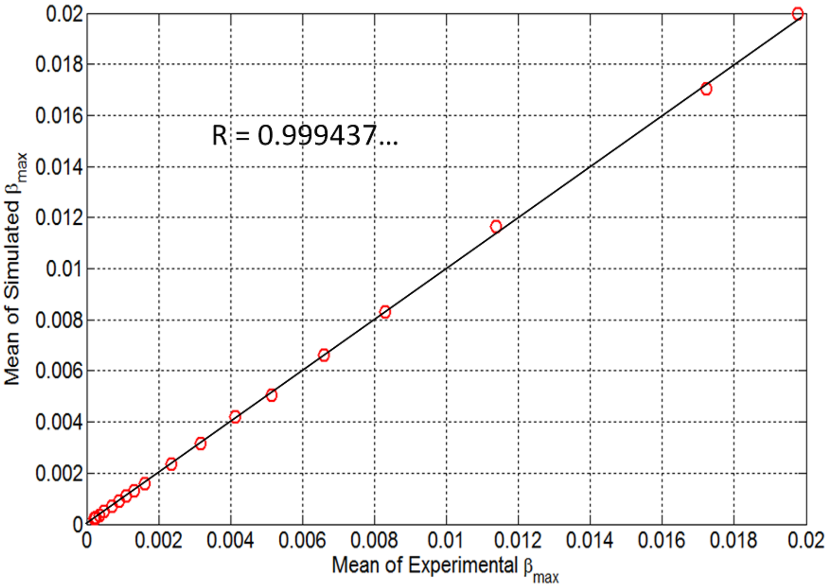

FIGURE 4.15: Correlation between the numerical simulation model and experiments.

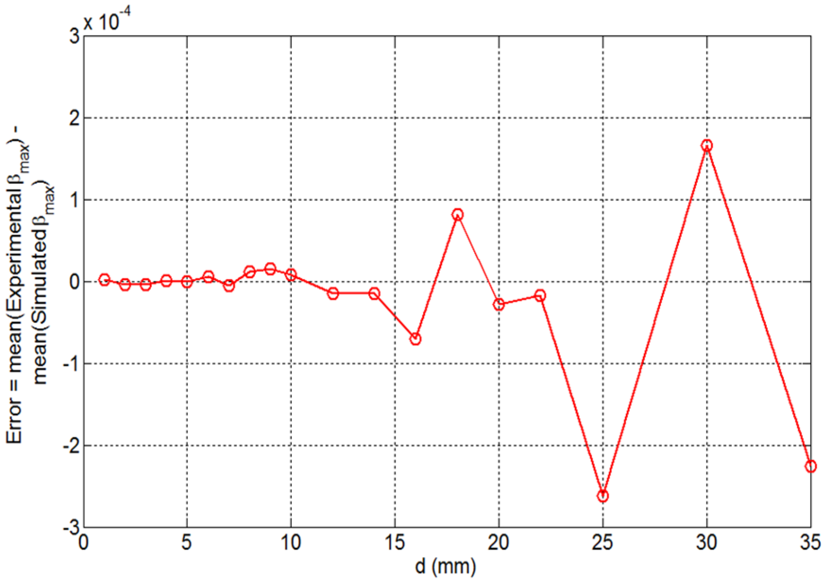

FIGURE 4.16: Error between model and experiments against thickness.

$$R_{u,v} = \frac{n\sum_{i=1}^{n} u_i v_i - \sum_{i=1}^{n} u_i \sum_{i=1}^{n} v_i}{\sqrt{\left[n\sum_{i=1}^{n} u_i^2 - \left(\sum_{i=1}^{n} u_i\right)^2\right]\left[n\sum_{i=1}^{n} v_i^2 - \left(\sum_{i=1}^{n} v_i\right)^2\right]}} \tag{4.22}$$

A significant pattern in the error, *i.e.*, the difference between experimental β_{max} and simulated β_{max} could not be observed as shown in Fig. 4.16 which shows the variation of error against gray cast iron thickness in mm, therefore, the error between simulation and experiments can be concluded to be arbitrary. The correlation coefficient R taking a value very close to one (*i.e.*, $R = 0.999437$) implies strong correlation between simulated signals and reality. According to these observations, the validity of the numerical model was sufficiently conclusive and therefore, β_{max} values extracted from numerically simulated signals were used to probabilistically learn the thickness-feature function as explained in Section 4.3.

It should be noted that the thickness-feature function is learned between d and β_{max} in this chapter to capture nonlinearities, therefore the comparison of β_{max} values is sufficient. However, for the sake of completeness, Fig. 4.17 shows the agreement between $\ln \beta_{max}$ values as well. A correlation coefficient of $R = 0.999597$ was evident for $\ln \beta_{max}$ values as shown in Fig. 4.18. This value is slightly greater than what was achieved for β_{max} and this increase could be attributed to the logarithmic scale transformation. Similar to β_{max} values, errors between experimental and simulated $\ln \beta_{max}$ values was random as well as shown in Fig. 4.19.

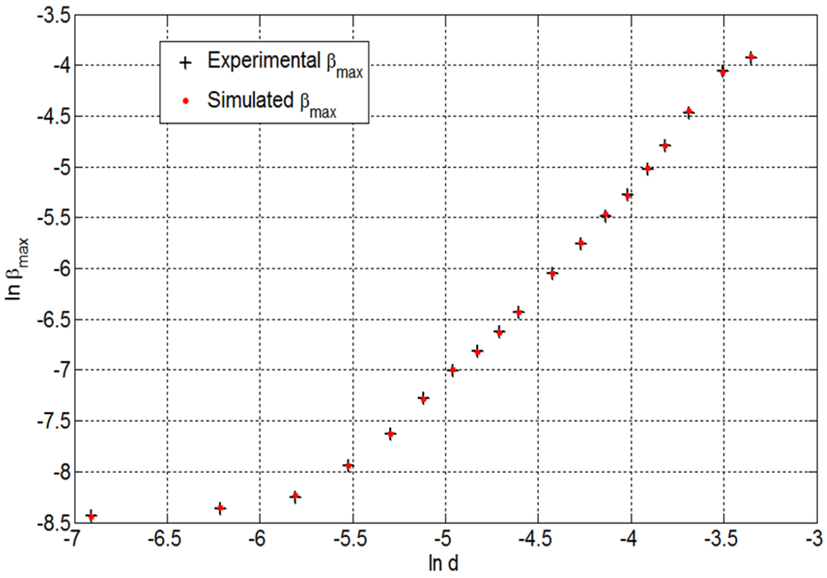

FIGURE 4.17: Feature values ($\ln \beta_{max}$) vs thickness ($\ln d$), agreement between simulation and experiments.

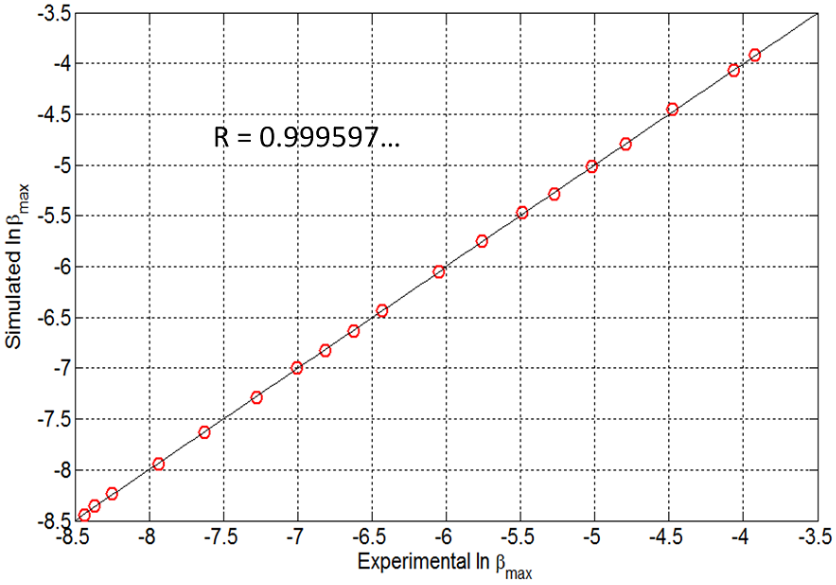

FIGURE 4.18: Correlation between the numerical simulation model and experiments in terms of means of $\ln \beta_{max}$.

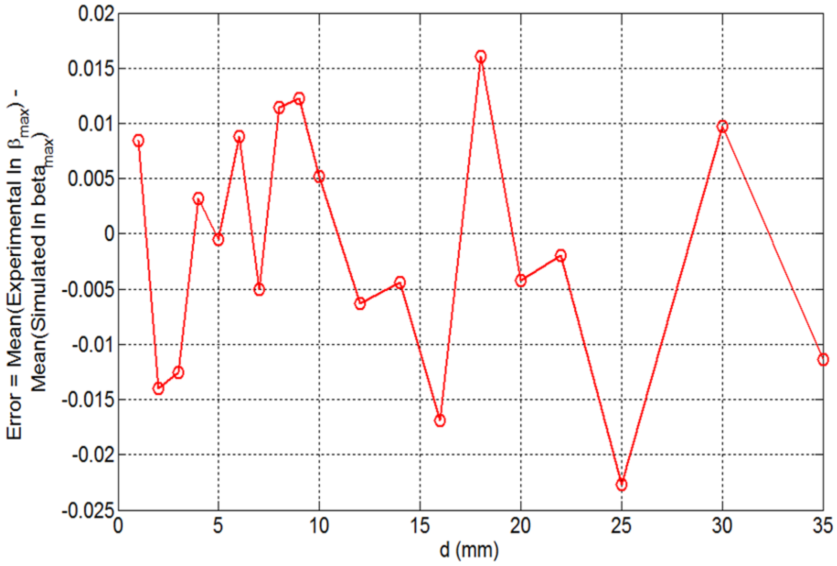

FIGURE 4.19: Error between model and experiments against thickness for $\ln \beta_{max}$.

4.3 Non-Parametric Learning of the Thickness-Feature Function Using GP

The proposed methodology to non-parametrically learn the thickness-feature function using GP is presented in Fig. 4.20.

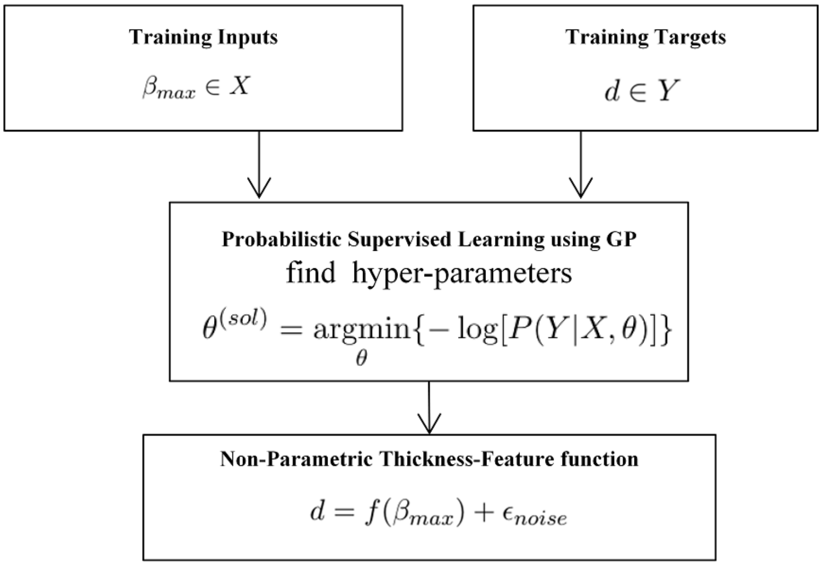

FIGURE 4.20: Non-parametric learning of the thickness-feature function using GP.

Estimating thickness d from PEC sensor signal features β_{max} can be formulated as a non-linear regression problem. Gaussian Process models are a powerful tool to solve such regression problems. GPs [18, 117, 118] can be thought of as a Gaussian prior over the function space mapping inputs x and outputs $f(x)$. It is completely specified by its mean function $\mu_m = \mathrm{E}[f(x)]$ and the covariance function $\Sigma = \mathrm{E}[(f(x) - \mu_m)(f(x)^T - \mu_m^T)]$ [18].

In the light of this thesis, let $[X\ Y]$ be the training data set drawn by the noisy process $d^{(i)} = f(\beta_{max}^{(i)}) + \epsilon_{noise}^{(i)}$, where $X = [\beta_{max}^{(1)}, \beta_{max}^{(2)}, ..., \beta_{max}^{(i)}, ..., \beta_{max}^{(n)}]^T$ be the vector of training inputs which in particular to the thesis correspond to the features extracted from the numerically simulated PEC signals and $Y = [d^{(1)}, d^{(2)}, ..., d^{(i)}, ..., d^{(n)}]^T$ be the vector of training labels, which are the corresponding cast iron thicknesses in mm. A Gaussian Process estimates posterior distributions over functions f from the training data $[X\ Y]$. Although the functions are infinitely dimensional, the GP model is used to infer, or predict, function values at a finite testing set of prediction points $X^* = [\beta_{max}^{*(1)}, \beta_{max}^{*(2)}, ..., \beta_{max}^{*(i)}, ..., \beta_{max}^{*(n1)}]^T$.

To apply a GP framework to this regression problem, one must first select a kernel $K(X, X)$ whose elements are given by $k_{i,j} = k(x_i, x_j)$. This specifies the kind of functions that are expected, before any data have been seen. Technically, the kernel places a prior likelihood on all possible functions. After evaluating a number of commonly used kernels, the squared exponential kernel was chosen for this work. It is defined as

$$k(x_i, x_j) = \alpha^2 \exp\left[-\frac{||x_i - x_j||^2}{2l^2}\right], \tag{4.23}$$

where α and l represent its hyper-parameters and together with sensor noise variance σ_n are learned from the training data $[X, Y]$. Since any given x_i dealt in this work takes the form $x_i = \beta_{max}^{(i)} \in \Re^+$, the vector norm appearing withing the exponential term of Eq.4.23 can be simplified to yield the form given in Eq. 4.24 [119], consequentially, the form in Eq. 4.24 was used in this work.

$$k(x_i, x_j) = \alpha^2 \exp\left[-\frac{(x_i - x_j)^2}{2l^2}\right] \tag{4.24}$$

The GP model was trained by minimizing the negative log marginal likelihood in Eq. 4.25 with respect to $\theta = [\alpha, l, \sigma_n]^T$.

$$-\log P(Y|X, \theta) = \frac{1}{2}Y^T\Sigma^{-1}Y + \frac{1}{2}\log|\Sigma| + \frac{n}{2}\log(2\pi) \tag{4.25}$$

The covariance function Σ is given by

$$\Sigma = K(X, X) + \sigma_n^2 I\,. \tag{4.26}$$

where I is the corresponding identity matrix.

Minimization was done using conjugate gradients [120–122] and since Σ is a symmetric, positive definite matrix, inversion and calculating the determinant was done using Cholesky decomposition [122–124] to achieve computational efficiency. To maintain consistency with calibration blocks and noise characterization of Chapter 3, training data were produced through FEA simulation of thicknesses 1, 2, ..., 10, 12, ..., 22, 25, 30 and 35 mm for gray cast iron. This resulted in 19 training data points, *i.e.*, one β_{max} value for one thickness. However, the training data is intended to be used to learn the nonlinear function between d in mm and β_{max} and the purpose of this is to infer critical pipe wall thickness (d^*) from

β^*_{max} values extracted from experimentally captured PEC signals on in situ pipes. Experimental PEC measurement setup encompasses noise, and since a GP prediction produces uncertainty associated with each inference, it is important that the function learned from simulated data captures realistic noise. However, since the numerical model is ideal, the 19 simulated signals do not carry noise which is matchable with reality. Therefore, if the thickness-feature function is learned only with β_{max} values corresponding to those 19 signals, the function would not learn the noise existing in reality. This may result in errors in prediction in addition to producing unrealistic uncertainties associated with predictions. To avoid this, the $\pm 2\times$ standard deviation noise margins of β_{max} on each available gray cast iron thickness, which were quantified in Section 3.7, were introduced to the simulated β_{max} values. Thus, the number of training β_{max} values was tripled from 19 to 57. Out of 57, 19 were simulated β_{max} values coming directly from the numerical model. Another 19 were created by subtracting the $2\times$ standard deviation margin from the simulated set. Similarly, the last 19 were created by adding the $2\times$Standard Deviation margin to the vector of simulated β_{max} values. By doing so, three β_{max} values were created for each training thickness. Fig. 4.21 shows the full set of training data (simulated β_{max} values with added noise) and the figure also shows the shape of the nonlinear thickness-feature function which is intended to be learned. Moreover, the figure shows how the artificially introduced noise on simulated β_{max} values manages to envelope the experimental β_{max} values.

As a result of conjugate gradients being used to minimize the negative log marginal likelihood, in theory, reaching the global minimum is not guaranteed since different initial values may lead to different solutions depending on existent local minimums. Therefore, following many trial and error tests, a solution stable for a considerable span of initial conditions was found for the training data set shown in Fig. 4.21. The solution was

$$\theta^{(sol)} = \underset{\theta}{\operatorname{argmin}}\{-\log[P(Y|X,\theta)]\} = [39.2, 0.0112, 0.9631]^T, \tag{4.27}$$

where

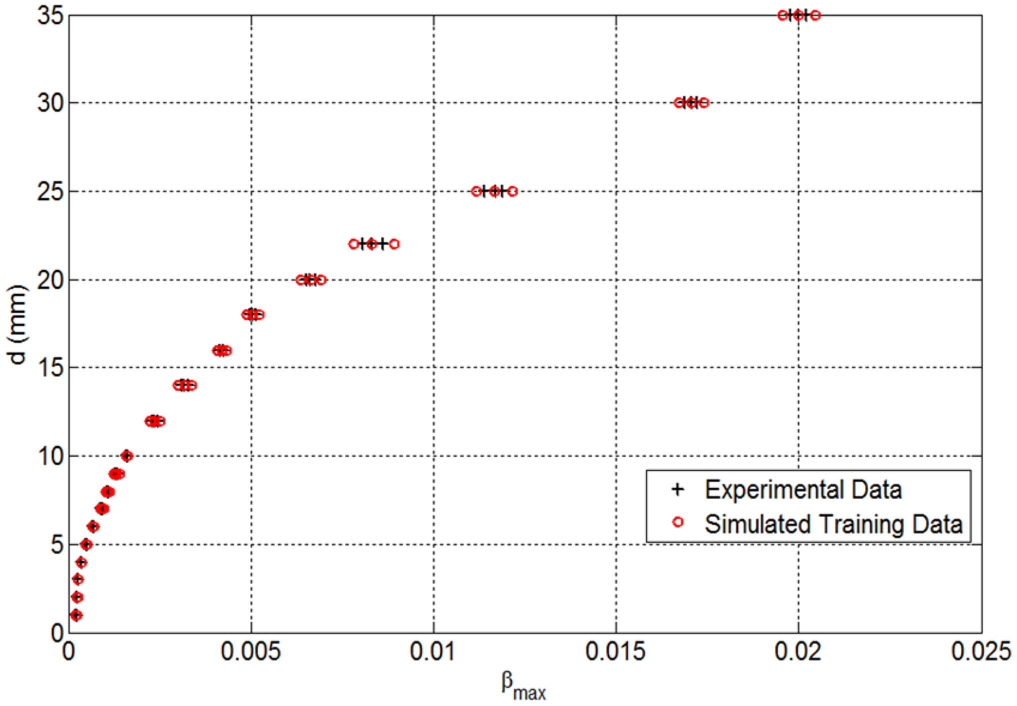

FIGURE 4.21: Nonlinear thickness-feature function, *i.e.*, d vs β_{max} intended to be learned using GP, as described by simulated training data and experimental data.

$$-\log[P(Y|X,\theta^{(sol)})] = 41.08864..., \tag{4.28}$$

which results from initial values $\theta^{(ini)} = [\alpha^{(ini)}, l^{(ini)}, \sigma_n^{(ini)}]^T$ roughly spanned by

$$\forall\alpha^{(ini)} \in \{\alpha^{(ini)} : 0.1 \leq \alpha^{(ini)} \leq 50\}$$

$$\forall l^{(ini)} \in \{l^{(ini)} : 0.01 \leq l^{(ini)} \leq 3\}$$

$$\forall\sigma_n^{(ini)} \in \{\sigma_n^{(ini)} : 0.1 \leq \sigma_n^{(ini)} \leq 3\}$$

.

There is no guarantee of this being the global minimum, but less superiority was observed in solutions resulting from a large number of initial value combinations chosen from outside the spanning limits. Therefore, $\theta^{(sol)}$ was selected as the optimum set of hyper-parameters for the GP model. A convergence plot of the negative log marginal likelihood obtained while optimizing hyper-parameters is shown in Fig. 4.22. Initial condition used for this case was $\theta^{(ini)} = [50, 0.7, 2]^T$ which is within the aforementioned span. The solution was obtained in 21 iterations and 58 function evaluations. The trend shown in Fig. 4.22 was common to tested combinations of initial values chosen from within the span though the number of iterations and function evaluations varied.

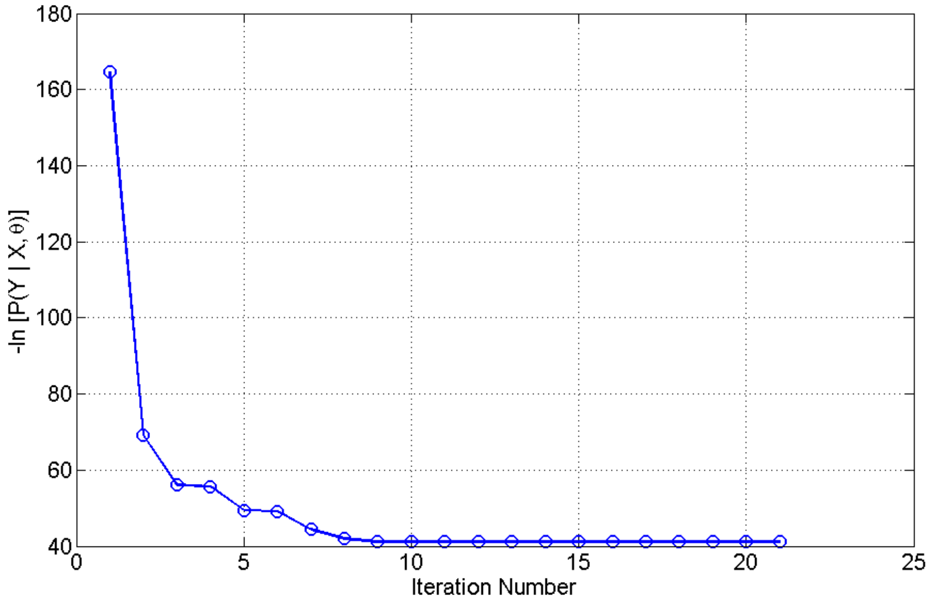

Figure 4.22: Variation of negative log marginal likelihood against iteration number while optimizing GP model hyper-parameters starting from the initial condition $\theta^{(ini)} = [50, 0.7, 2]^T$.

Once the hyper-parameters of the GP model are learned from the training set $[X, Y]$, they can be used to infer unknown thickness from a testing dataset $X^* = [\beta^{*(1)}_{max}, \beta^{*(2)}_{max}, ..., \beta^{*(i)}_{max}, ..., \beta^{*(n1)}_{max}]^T$ as explained in Section 4.4.

4.4 Probabilistic Inference of Pipe Wall Thickness

The combination of the training data and the kernel induces not only the most likely state, but also a full posterior probability distribution. The basic GP regression equations are given by

$$\mu_m^* = K(X^*, X)\{K(X, X) + \sigma_n^2 I\}^{-1} Y \tag{4.29}$$

$$\Sigma_{un}^* = K(X^*, X^*) + \sigma_n^2 I - K(X^*, X)\{K(X, X) + \sigma_n^2 I\}^{-1} K(X, X^*) \tag{4.30}$$

where I is the corresponding identity matrix.

The expected pipe wall thicknesses (d^*) for the testing input vector X^* (*i.e.*, β_{max}^* values extracted from in situ measurements) will therefore be given by the mean of the posterior distribution μ_m^* and the associated uncertainty will be given by the covariance Σ_{un}^*. Fig. 4.23 graphically elaborates the procedure for using the GP model for critical pipe wall thickness inference.

Before using the learned function for condition assessment of critical pipes, the function's performance was visualized to verify how the nonlinearities are captured. Inferred thicknesses were plotted with uncertainty with the aid of a continuous vector of testing inputs β_{max}^* as shown in Fig. 4.24 and 4.25. The figures also display the training data and experimental data corresponding to the training targets. Fig. 4.24 exhibits a reasonable capture of the nonlinearity in the low thickness range, *i.e.*, $d \leq 5$ mm, while Fig. 4.25 shows how higher thicknesses are modeled. Since the figures elaborate reasonable learning of local nonlinearities and shows reasonable uncertainty bounds which encapsulate experimental data, the GP model was deemed suitable for the critical pipe NDE. β_{max}^* values extracted from signals captured on in situ gray cast iron pipes were fed into the learned model and pipe wall thicknesses and uncertainties were estimated using Eq. 4.29 and Eq. 4.30 respectively.

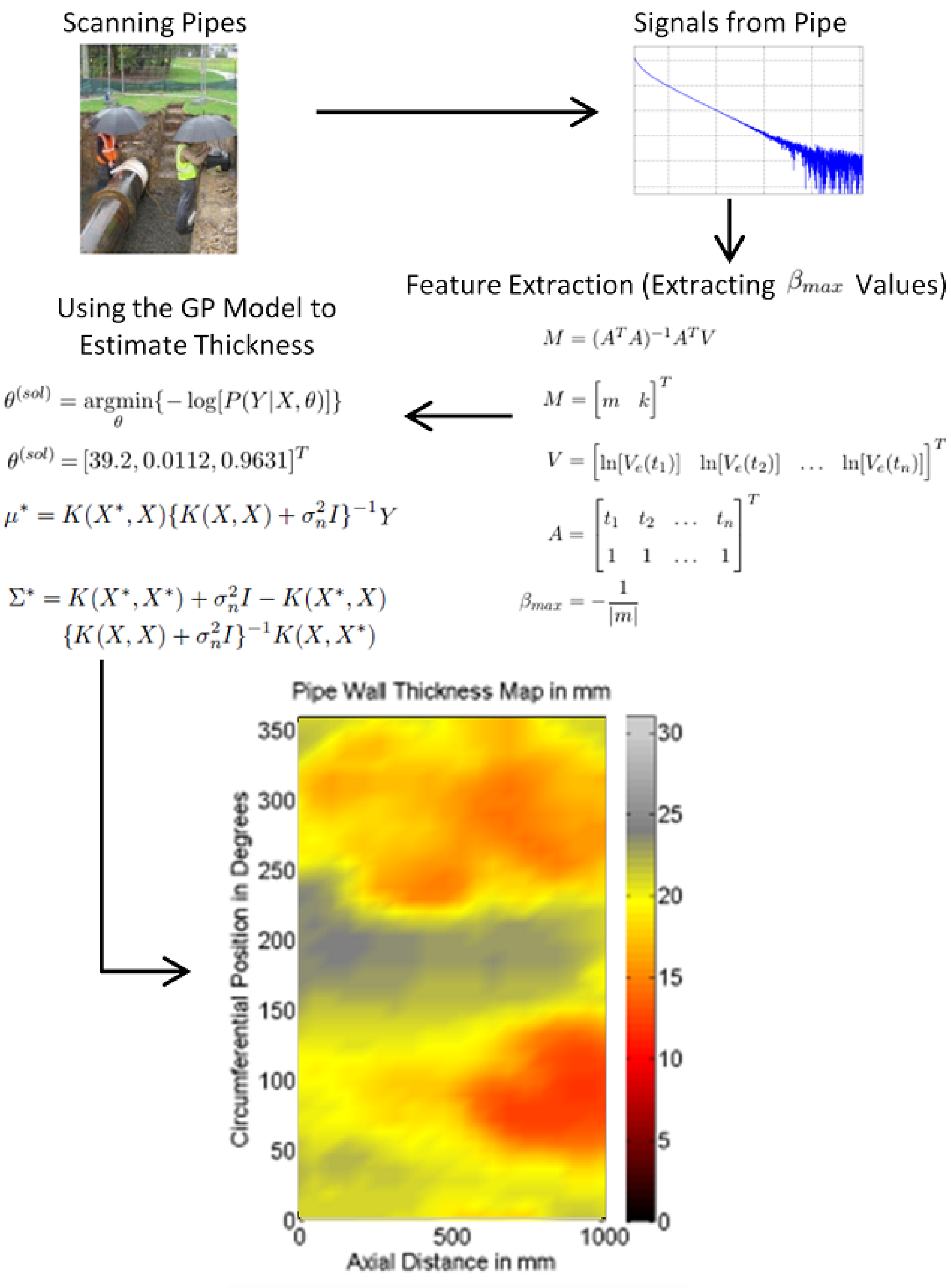

FIGURE 4.23: GP model being used for critical pipe NDE.

Two plots comparing GP inferred thickness maps against the GT are given in Fig. 4.26 and 4.27. For the ease of comparison the same pipe sections shown in Fig. 3.28 and 3.29

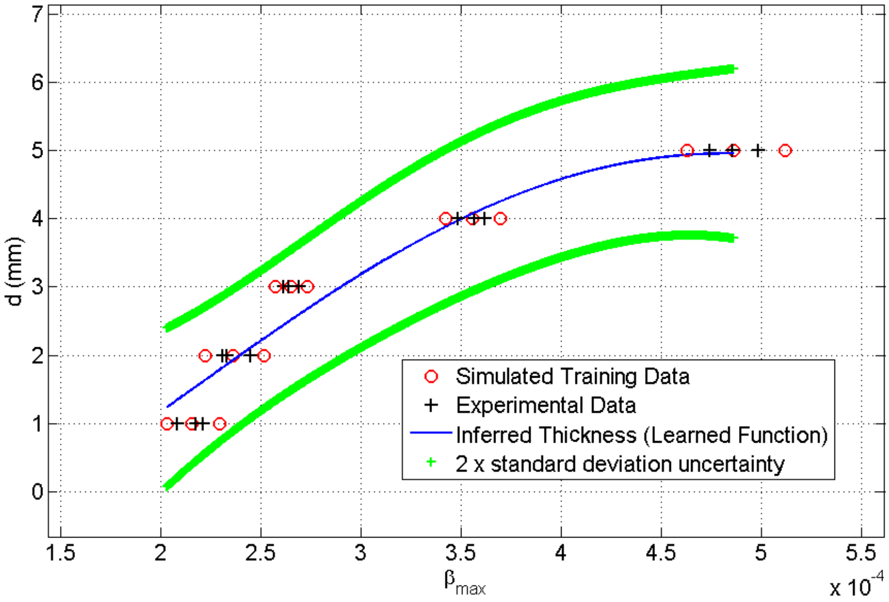

FIGURE 4.24: The GP model: Capturing nonlinearity in the low thickness range ($d \leq 5$ mm).

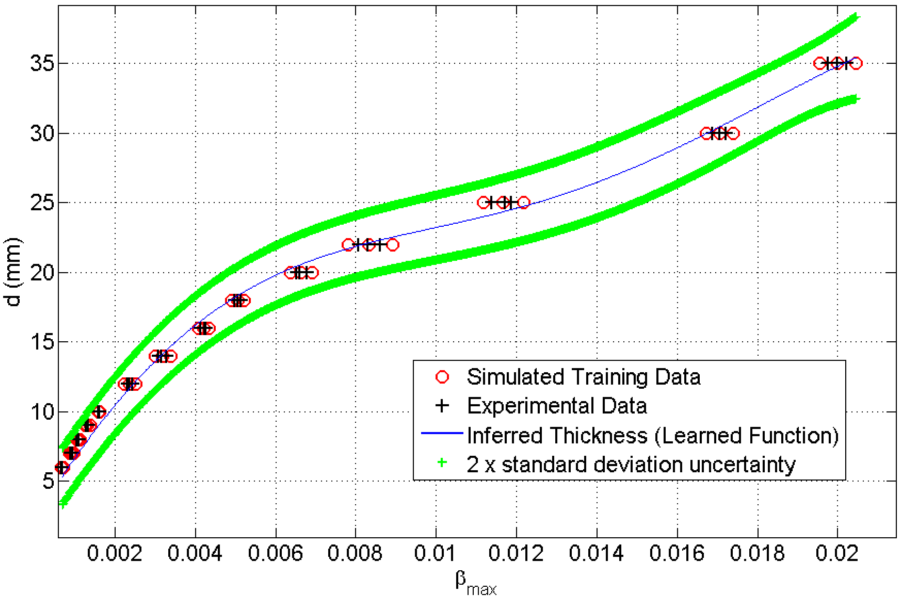

FIGURE 4.25: The GP model: Capturing nonlinearity for higher thicknesses ($d > 5$ mm)

in Chapter 3 were selected. The figures qualitatively suggest that the GP inferences are very similar in value to the analytically calculated values. Fig. 4.28 provides the GT as a scatter plot along with the inference and 2 × standard deviation uncertainties plotted

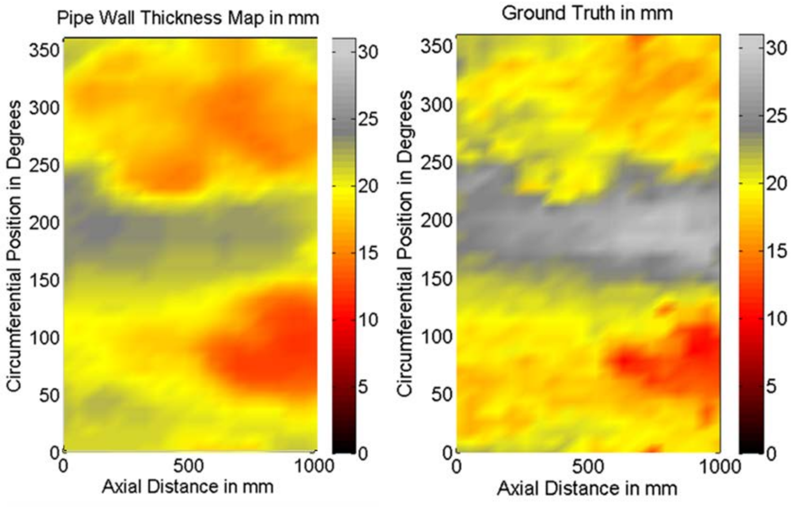

Figure 4.26: GP interpreted thickness map and GT for the first Gray Cast Iron pipe segment.

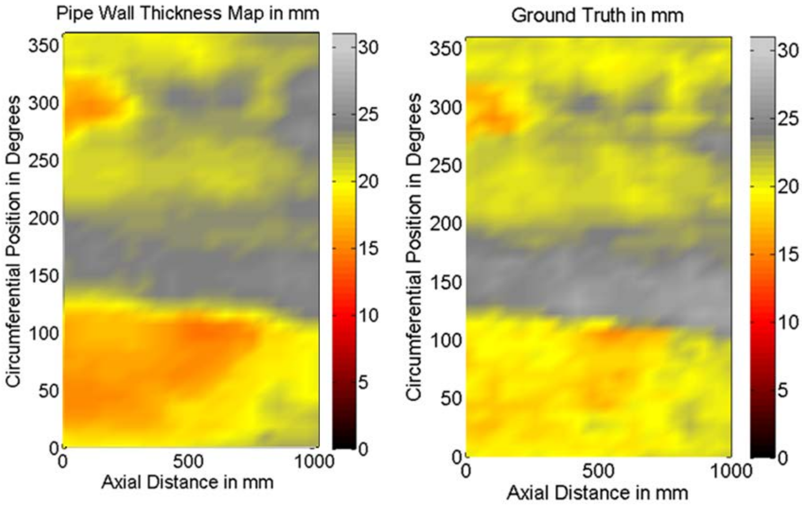

Figure 4.27: GP interpreted thickness map and GT for the second Gray Cast Iron pipe segment.

as lines when the results for the two pipe segments are considered collectively. It can be seen that the inference is fairly centered within the GT and the majority of the deviations between inference and GT are less than or equal to the uncertainty, which is a desirable property. Collective error statistics for the two pipe segments are presented in Table 4.2.

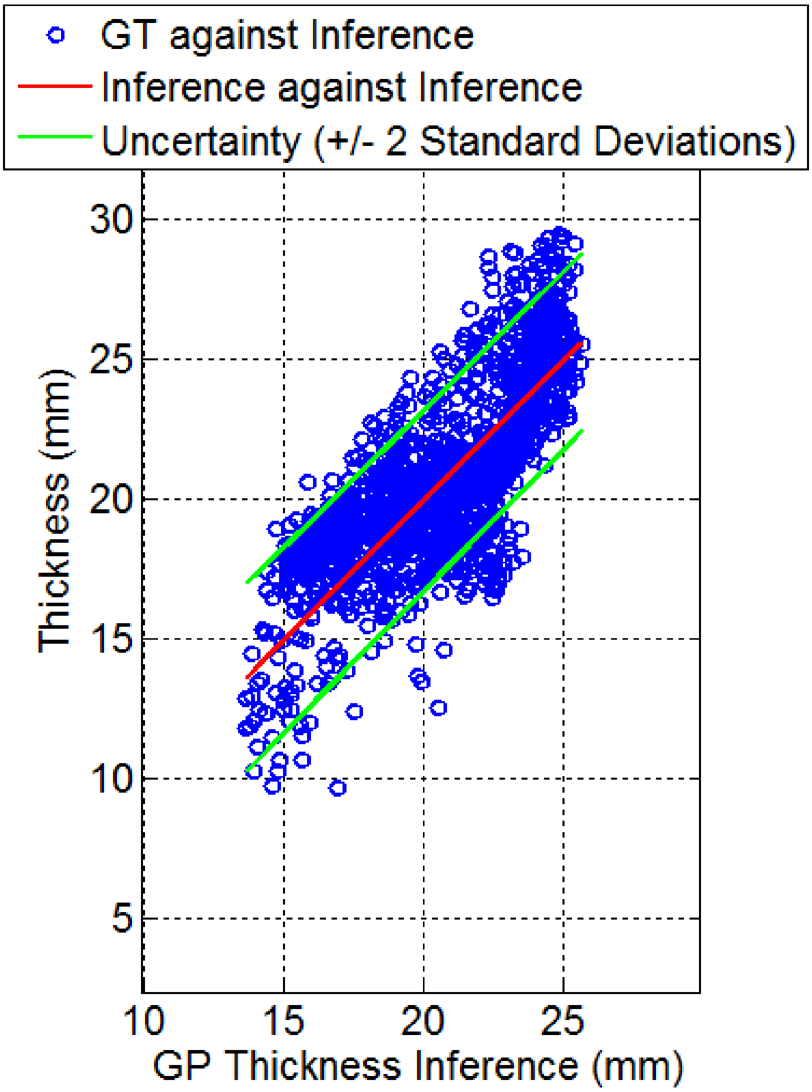

FIGURE 4.28: Variation of GP interpretations and uncertainty along with GT for the Gray Cast Iron pipe segments.

The average 2 × standard deviation uncertainty for the inferred thicknesses was 3.23 mm with a low variance of 0.00157 mm^2.

Table 4.2: Statistics of absolute error between interpreted pipe wall thickness and ground truth for Gray Cast Iron pipe segments.

Statistical Parameter	Value
RMS Error	2.049 mm
Mean Absolute Error	1.608 mm
Standard Deviation of Absolute Error	1.270 mm
Maximum Absolute Error	7.901 mm
Mean Percentage Accuracy	91.96%

4.5 Comparison of GP Interpreted Results with the Analytical Approach

Error statistics shown in Table 4.3 and 4.4 between interpreted thicknesses and GT were calculated for both analytical and numerical approaches and compared. It was evident from this comparison that the numerical simulation and probabilistic inference based approach increased the accuracy of inferred thicknesses when comparing with the analytical approach. The capability of capturing and modeling actual material properties and non-linearities in the thicknesses-feature function can be identified as the possible causes for this improvement. With respect to the two gray cast iron pipe segments considered in both Chapter 3 and 4, the improvement can be quantitatively expressed via error statistics presented in Table 4.3. An increment of overall percentage accuracy up to almost 92% from 90% was achieved by using the numerical approach along with reductions in RMS and mean absolute errors.

Table 4.3: Comparison of absolute error statistics between analytical and numerical approaches.

Statistical Parameter	Analytical Approach	Numerical Approach
RMS Error	2.42 mm	2.05 mm
Mean Absolute Error	2.00 mm	1.61 mm
Standard Deviation of Absolute Error	1.37 mm	1.27 mm
Maximum Absolute Error	7.06 mm	7.90 mm
Mean Percentage Accuracy	90.3%	91.96 %

In addition to the two pipe segments discussed above, thickness maps and error statistics of all evaluated gray cast iron pipe segments are presented in Appendices A (analytical approach) and B (numerical approach). Considering all the evaluated sections, improvement in accuracy associated with the numerical approach can be confirmed further as shown in Table 4.4. As can be seen in that table, the overall percentage accuracy was observed to increase from approximately 90% to 92% while the RMS and mean absolute errors decreased. It can therefore be concluded that the probabilistic inference based on numerical simulations has a small, but noticeable positive impact on the accuracy of interpreted thicknesses over the analytical approach. Since the additional information of uncertainty is given along with thickness through GP inference, the probabilistic method is more advantageous over the analytical method for sensor fusion purposes to achieve even higher accuracy. For example, a method of improving the thickness estimates by fusing results produced by the proposed approach with localized defect information captured by another sensor is proposed in [125]. The numerical NDE approach presented in this chapter can thus be concluded to be suitable for condition assessment of critical pipes and suitable for sensor fusion applications. Though the approach has been evaluated on gray cast iron with the use of a rectangular PEC sensor due to the industrial requirements associated with this research, the sensor modeling and thickness inference methods are generic to any PEC sensor architecture and material, as long as sensor and material properties are given.

TABLE 4.4: Comparison of absolute error statistics between analytical and numerical approaches (using all evaluated pipe segments).

Statistical Parameter	Analytical Approach	Numerical Approach
RMS Error	2.69 mm	2.05 mm
Mean Absolute Error	2.14 mm	1.62 mm
Standard Deviation of Absolute Error	1.52 mm	1.197 mm
Maximum Absolute Error	10.65 mm	8.66 mm
Mean Percentage Accuracy	89.8%	92.4 %

4.6 Conclusions

This chapter introduced a critical pipe NDE approach based on numerical PEC sensor modeling and probabilistic inference of pipe wall thickness. The objective of the proposed approach was to overcome the experimental calibration requirement and the practical difficulties associated with executing the analytical approach presented in Chapter 3. Elimination of experimental calibration was accomplished by measuring electrical and magnetic properties of pipe materials and incorporating them in a numerical sensor simulation model to produce calibration signals as opposed to performing measurements on calibration blocks as done in the analytical approach.

Electrical conductivity and magnetization curve are the material properties required for numerical modeling and the procedure followed for measuring them was extracting specimens and using them in a PPMS. The alternative method for estimating a range for electrical conductivity by finding material composition with the aid of an XRF device and applying rule of mixtures was experimented. However, since the XRF method produces a range while the PPMS can measure the exact value, the XRF measurement based method becomes redundant in this application although it may still be useful in instances where only nondestructive approximation of conductivity is required, or for a case where a PPMS or a four probe conductivity measurement apparatus is unavailable.

Once electrical and magnetic properties are measured, they can be incorporated to numerically model the PEC sensor interaction with materials. The objective of numerical simulation was to simulate PEC signals given an arbitrary PEC senor architecture and facilitate a mechanism of replacing the procedure of experimentally obtaining calibration data using calibration blocks. Intended operation of the model was to produce PEC signals as the output when sensor and material properties are provided as inputs. As the first step of developing the model, the equation governing the EC phenomenon was derived starting from Maxwell's equations. Since analytically deriving a closed form solution for the PEC signal from the magnetic vector potential based governing equation is complicated, an FEA numerical simulation model was developed using COMSOL Multiphysics® commercial software package to obtain the solution numerically. Outputs of the FEA model corresponding to the rectangular sensor addressed in this thesis showed acceptable agreement with experimental signals as shown in this chapter. Therefore, the numerical model was chosen as a convenient option to replace calibration blocks and a generic method which has flexibility to model given sensor architectures and materials having different intrinsic properties.

The numerical model was used to simulate calibration signals for gray cast iron and the gradient feature values (β_{max}) were extracted to learn the thickness-feature function. Unlike modeling the function as a straight line as done in Chapter 3, it was intended to non-parametrically learn the function in order to capture any plausible nonlinearities which could exist in reality, with the objective of achieving higher accuracy for pipe wall thickness estimates than in the analytical NDE approach. Before learning the function, agreement between simulated β_{max} values and experimental values was evaluated in this chapter. On observing reasonable agreement, the thickness-feature function was learned using GP with simulated β_{max} values used for training. Optimization based learning process was detailed and the resulting hyper-parameters were presented.

Applying the GP model for critical pipe NDE was done by probabilistically inferring pipe wall thickness using PEC signals captured by scanning in situ pipes. An extended evaluation of results was done using all scanned pipe sections (results presented in Appendices A and B) and an overall percentage accuracy of over 92% was observed when comparing against ground truth. This implicated a 2% increase in accuracy when comparing with the analytical approach along with reduction in RMS and mean absolute errors. Therefore, the probabilistic thickness inference method can be concluded to have an improvement in accuracy than the analytical approach. A main reason for the increase in accuracy can be identified as the possibility of the GP method to learn local nonlinearities of the thickness-feature function as apposed to the analytical method which models the function as a perfect straight line. A second cause for increased accuracy can be attributed to numerical sensor modeling, as it uses pipe material properties which enables reducing calibration errors caused by material property mismatches which generally occur when using calibration blocks.

In addition to increased accuracy, the capability of providing uncertainty information for inferred thicknesses is a significant advantage in GP inference. This information assists sensor fusion applications as done in [125] in relation to the sensor addressed in this thesis, to obtain more accurate interpretations of pipe condition. Therefore, the NDE approach proposed in this chapter which numerically solves the forward eddy current problem and probabilistically solves the inverse eddy current problem can be concluded to be an effective tool for critical pipe health monitoring.

Chapter 5

Towards 3D Profiling in Critical Pipe NDE

For a given PEC excitation strength and a number of coil turns, it is known that the maximum achievable eddy current penetration depth in a material being tested is proportional to the size of the exciter coil [40]. With respect to rectangular coils, size can be specified by internal and external lengths and widths of coil domains while for circular sensors, size can be specified by internal and external radii of the same. Hence the relationship between exciter coil size and penetration depth is monotonic, *i.e.*, larger the exciter coil, deeper the penetration. As a result, since penetrating up to 30 mm in ferromagnetic materials is required for critical pipe NDE at the focus of this thesis, the PEC sensor being used inevitably requires to be sufficiently large for a finite excitation strength. However, when the sensor is large, the lateral spread of the magnetic field also increases which results in the lateral domain of influence of the sensor being large. Consequentially, PEC sensors suitable for critical pipe evaluation are generally low in resolution for practically manageable excitations and the detector is perceiving an averaged effect of the actuality of remaining material within the domain of influence [34]. Therefore, when using commercial PEC sensors capable of critical pipe assessment [5, 34], it is difficult to detect anomalies such as pitting which are localized to areas smaller than the sensor footprint. This limitation existing in current practice highlights the need for research aimed towards increasing PEC sensor resolution for the applications of PEC in general.

The objective of this chapter is to investigate the capability of increasing PEC sensor resolution while maintaining adequate penetration depth to suit the application of critical pipe NDE. Reducing the sensor size is the obvious method of increasing resolution and it is also the focus of this chapter. As discussed in Chapter 2, a previous study [40] which investigates the effect of the geometry of a circular PEC sensor on the penetration capability in non-ferromagnetic materials has identified several aspects on the nature of eddy currents induced in the material being tested.

1. The larger the internal radius of the excitation coil, the deeper the penetration and the larger the lateral spread.
2. The larger the outer radius of the excitation coil, the deeper the penetration and the larger the lateral spread.
3. The smaller the height of the excitation coil, the deeper the penetration and the larger the lateral spread.

Based on the above findings, it can be ascertained that though increased resolution can be achieved through a smaller sensor, that limits the spread of the magnetic field and results in not being able to assess thick material since the eddy current penetration depth will be lower [40]. However, it may be possible to compensate the reduction of magnetic field spread by increasing the excitation strength. However, the amount of increase allowable to the excitation is limited by the available electronic circuitry and related hardware. Therefore, this chapter investigates the possibility of increasing resolution by reducing sensor size and compromising the magnetic field spread by increasing excitation strength within constrained limits.

Similar to the non-ferromagnetic material and non detector coil based PEC sensor related study in [40], this chapter brings forth a ferromagnetic material specific numerical study (using FEA) to aid understanding the influence of the geometry and properties of the detector coil based PEC sensor architecture on the thickness discriminative capability of the decay rate (β_{max}) signal feature throughout a thickness range adequate from critical pipe assessment. As this chapter investigates general improvements to the sensor design, a circular sensor model is selected for simplicity. Findings about size and properties of the sensor generalize to both rectangular and circular sensors while modeling circular sensors is much simpler. To derive association with the application of critical pipe assessment, gray cast iron is used as the material being tested within this study.

Subsection 3.2.6 hypothesized an important low dependence of β_{max} on sensor shape, a validation of this hypothesis is performed in simulation. Low dependencies on lift-off and sensor size identified in Subsection 3.2.6 are exploited in this chapter to propose a framework usable for 3D profiling of ferromagnetic materials by means of concurrent inference of thickness and lift-off and the performance of the framework is demonstrated using FEA simulation.

5.1 FEA Model Used for the Study

For computational efficiency and simplicity of analysis, a 2D axisymmetric model of a circular PEC sensor was developed and used for the study. Since this thesis focuses on detector coil based sensor architecture, same scope was mandated for this study and the model was made to be detector coil based. Gray cast iron is used as the ferromagnetic pipe material in this model, and the study, to draw relationship to critical pipe assessment, or to ferromagnetic materials in general.

5.1.1 Developing the Model

Fig. 5.1 shows the 2D axisymmetric sensor model developed using COMSOL Multiphysics ® while Table 5.1 provides the input parameters required for modeling. Unlike the numerical model of Chapter 4 which uses a voltage pulse for excitation, this model uses a current pulse in the form of a perfect Heaviside step function. It was noted in this exercise that a current excitation enables faster simulation than a voltage excitation in COMSOL. In the practical scenario, the excitation coil current has a non zero rise time. However, that is not the case in this study since the current is a perfect step function. Though one might therefore argue that this analysis is unrealistic with respect to the practical circumstance, it should be noted that this study is interested only in the late stage of the signal. Since the effect of the rising edge dies down after several time constants [30], the rising edge does not have any significant impact on the β_{max} signal feature focused in this study, as it is extracted from the very late stages of the signal just before entering the noise margin. Therefore, using a step current excitation is a valid exercise when considering computational efficiency. To coincide with feature extraction from experimental signals,

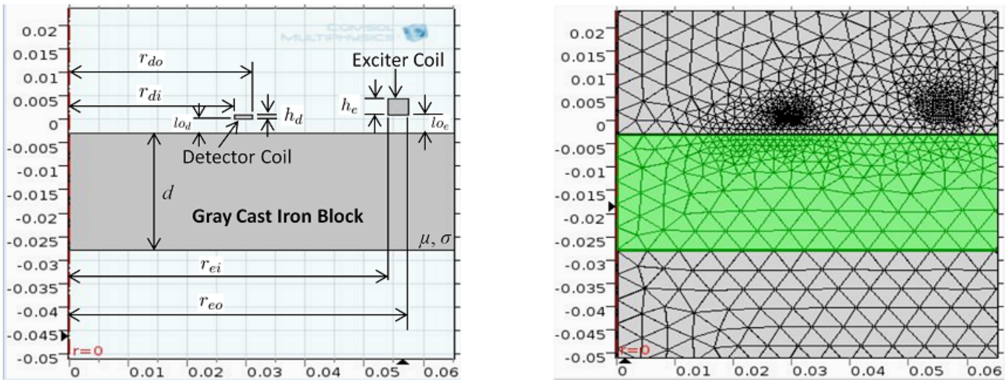

(a) (b)

FIGURE 5.1: 2D Axisymmetric FEA model developed for the study: (a) 2D axisymmetric model; (b) Meshed model.

TABLE 5.1: Parameters required for simulation.

Symbol	Description
r_{di}	Inner radius of detector coil domain
r_{do}	Outer radius of detector coil domain
h_d	Height of detector coil domain
lo_d	Vertical offset of the detector coil
n_d	Number of detector coil turns
σ_d	Electrical conductivity of the detector coil
μ_d	Magnetic permeability of the detector coil
r_{ei}	Inner radius of exciter coil
r_{eo}	Outer radius of exciter coil
h_e	Height of exciter coil domain
lo_e	Vertical offset of the exciter coil
n_e	Number of excitation coil turns
σ_e	Electrical conductivity of the exciter coil
μ_e	Magnetic permeability of the exciter coil
d	Plate thickness
σ	Electrical conductivity of pipe material
μ	Nonlinear magnetic permeability of pipe material
I_e	Amplitude or the excitation current pulse
Z_{dl}	Load impedance connected to the detector coil

$\ln V[t] = 0$ and $0 < \ln V(t) < 2$ are considered as the noise margin and the region for capturing β_{max} respectively as shown in Fig. 5.5. Thickness of flat plates is modeled in this study since simulating curved surfaces like pipes in an axisymmetric environment does not replicate desired reality. If developing circular sensors for pipe evaluation by incorporating knowledge gained from this study, the method described in Section 3.3 can be followed to confirm the test piece curvature range for which the flat plate approximation is valid.

Similar to the model in Chapter 4, this model takes the inputs described in Table 5.1 and outputs the time domain logarithmic PEC signal S_{2D} as expressed in Eq. 5.1. The usual β_{max} signal feature is extracted for analysis as shown in Eq. 5.2 before the signal enters the noise margin.

$$S_{2D} = f_{num2D}(r_{di}, r_{do}, h_d, lo_d, n_d, \sigma_d, \mu_d, r_{ei}, r_{eo}, h_e, lo_e, n_e, \sigma_e, \mu_e, d, \mu, \sigma, Z_{dl}, I_e, t) \quad (5.1)$$

$$\beta_{max} = \max\left(\left|\frac{\partial S_{2D}}{\partial t}\right|^{-1}\right) \quad (5.2)$$

5.1.2 Theoretical Verification of the Model

To enable numerical study, the developed model was initially theoretically validated. The parameters of the base model described in Section 5.2 were used for verification by incorporating a hypothetical material having a relative permeability of 50 and an electrical conductivity of 1.5×10^6 S/m. Based on the assumed conductivity and permeability values, theoretical β_{max} values can be calculated using $\beta_{max} \approx \frac{\mu\sigma d^2}{\pi^2}$ for different thicknesses. Theoretical β_{max} values were calculated for thickness 5, 10, 15, 20 and 25 mm and those thicknesses were simulated using the numerical model to obtain time domain signals. β_{max} values were obtained from the simulated signals as well and were compared with the theoretical values to check the model validity. Results are shown in Table 5.2 and Fig. 5.2, and reasonable agreement was observed with an RMS error of 0.0271 and a mean percentage accuracy of 99.6%. Mean percentage accuracy in this instance was calculated by quantifying the percentage accuracy for each thickness using $\left(1 - \dfrac{|\text{theoretical} \ln \beta_{max} - \text{numerical} \ln \beta_{max}|}{|\text{theoretical} \ln \beta_{max}|}\right) \times 100$ since the condition $|\text{theoretical} \ln \beta_{max} - \text{numerical} \ln \beta_{max}| < |\text{theoretical} \ln \beta_{max}|$ prevailed for all thicknesses, and averaging them. Fig. 5.3 shows the low magnitude of the error between simulation and theory for each thickness value taken in mm. Fig. 5.4 shows the plot between simulated and theoretical $\ln \beta_{max}$ values and it produces a correlation coefficient of 0.99983 calculated using Eq. 4.22, which implies a highly significant agreement between theory and the model. Fig. 5.5 shows the simulated signals for all the thicknesses while Fig. 5.6 shows the spread of induced eddy current at a particular time instance inside a plate of 25 mm thickness.

The results thus exhibit acceptable agreement with theory and suggests sufficient model validity and accuracy to be incorporated in a numerical study. Section 5.2 formulates the problem which is intended to be solved through the numerical study in order to identify how sensor resolution can be increased.

TABLE 5.2: Agreement between the 2D axisymmetric model and theory, theoretical and simulated $\ln \beta_{max}$ values for different thicknesses.

Thickness	Theoretical $\ln \beta_{max}$	Simulated $\ln \beta_{max}$
5 mm	-8.340	-8.337
10 mm	-6.954	-6.971
15 mm	-6.143	-6.135
20 mm	-5.568	-5.512
25 mm	-5.121	-5.108

5.2 Problem Formulation for Increasing Sensor Resolution

The problem of increasing sensor resolution is solved using the base model described in Subsection 5.2.1.

5.2.1 The Base Model

The base model is the FEA simulation model shown in Fig. 5.1 designed with model parameter values provided in Table 5.3. It represents a circular PEC sensor with concentric

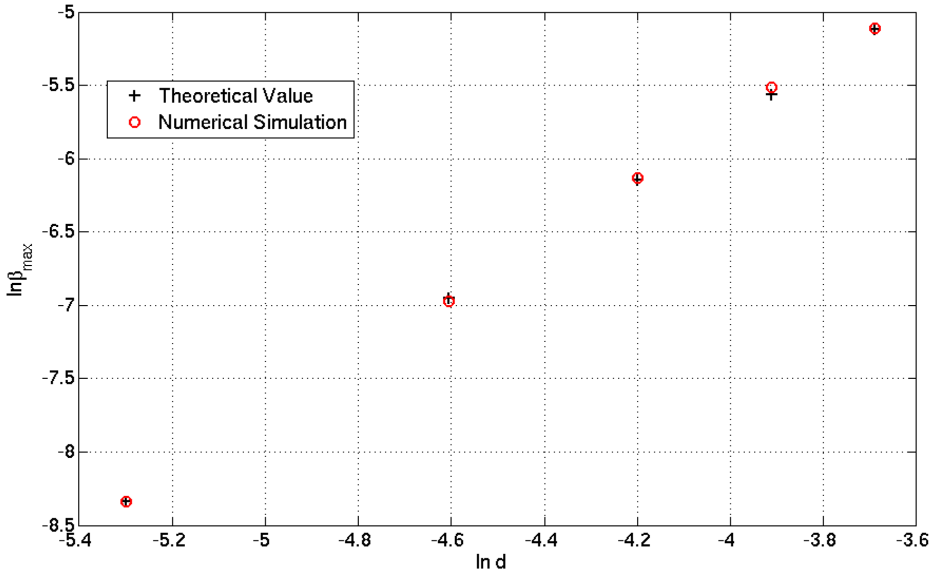

FIGURE 5.2: Feature values ($\ln \beta_{max}$) vs thickness ($\ln d$), agreement between simulation and theory.

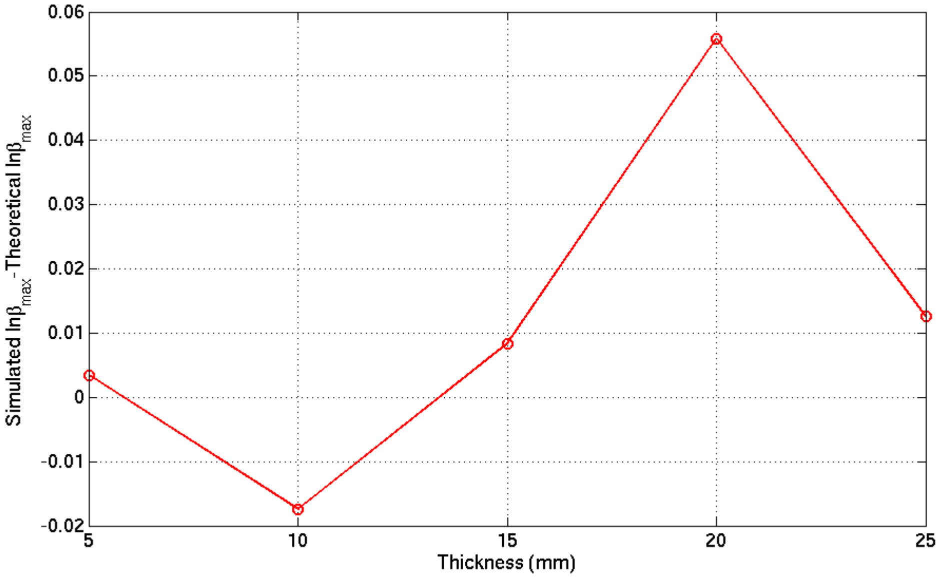

FIGURE 5.3: Error between simulation and theory against thickness.

coils.

Though the study is specific to gray cast iron to draw connection with critical pipe assessment, the study generalizes and can be repeated for any material by providing necessary electrical and magnetic properties. Coils of the sensor were assumed to be wound of copper

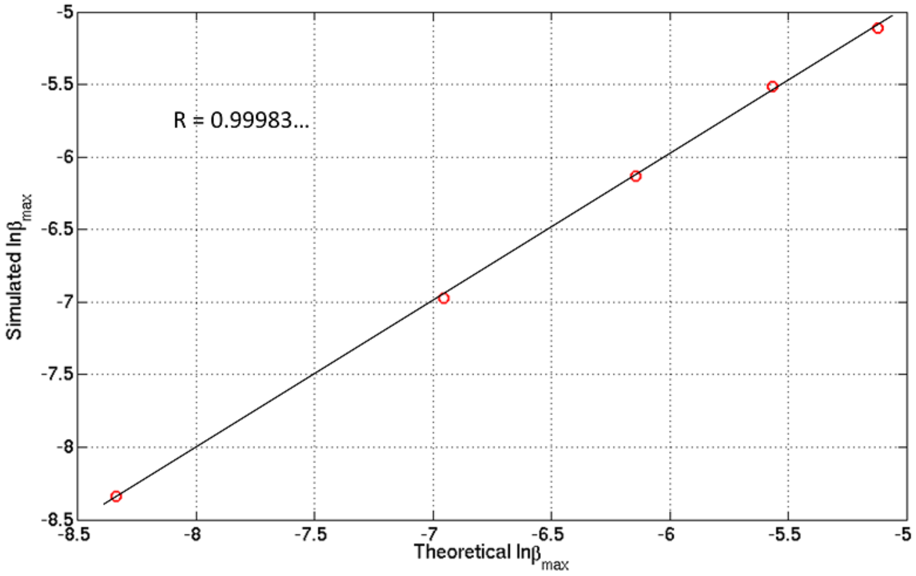

FIGURE 5.4: Correlation between the numerical simulation model and theory.

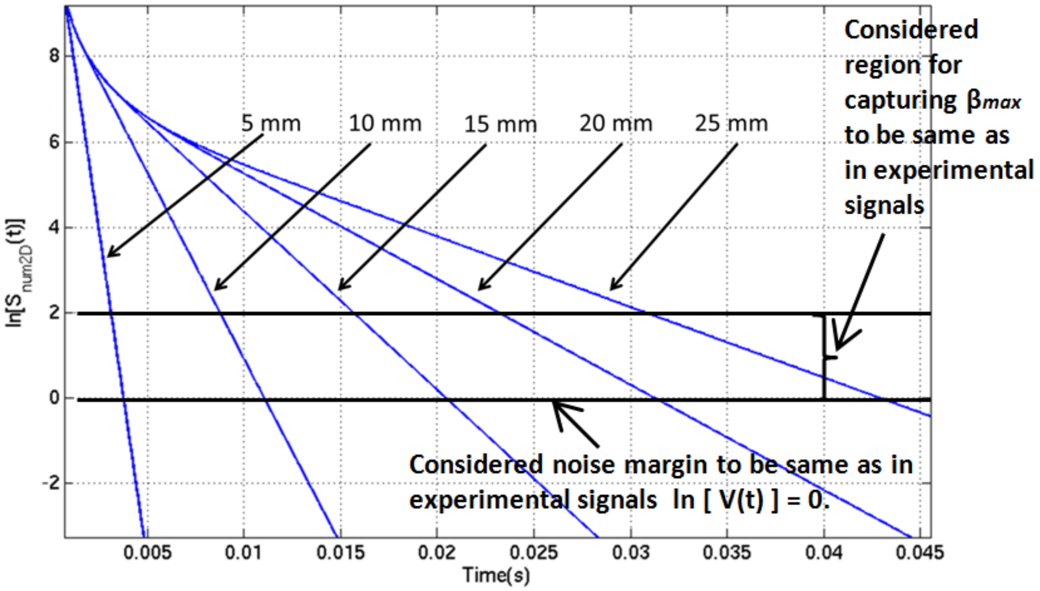

FIGURE 5.5: Numerically simulated signals by the 2D axisymmetric model for different thicknesses.

wires and therefore standard electrical conductivity and relative permeability of copper were used. The exciter coil was assumed to be wound of an AWG 32 wire while the detector coil was wound of an AWG 40 wire. Radii and heights of coil domains were set to be sufficient to accommodate the turn numbers specified in the table. As evident in the table, the assumed excitation was an ideal current pulse (Heaviside step) having a 50 mA

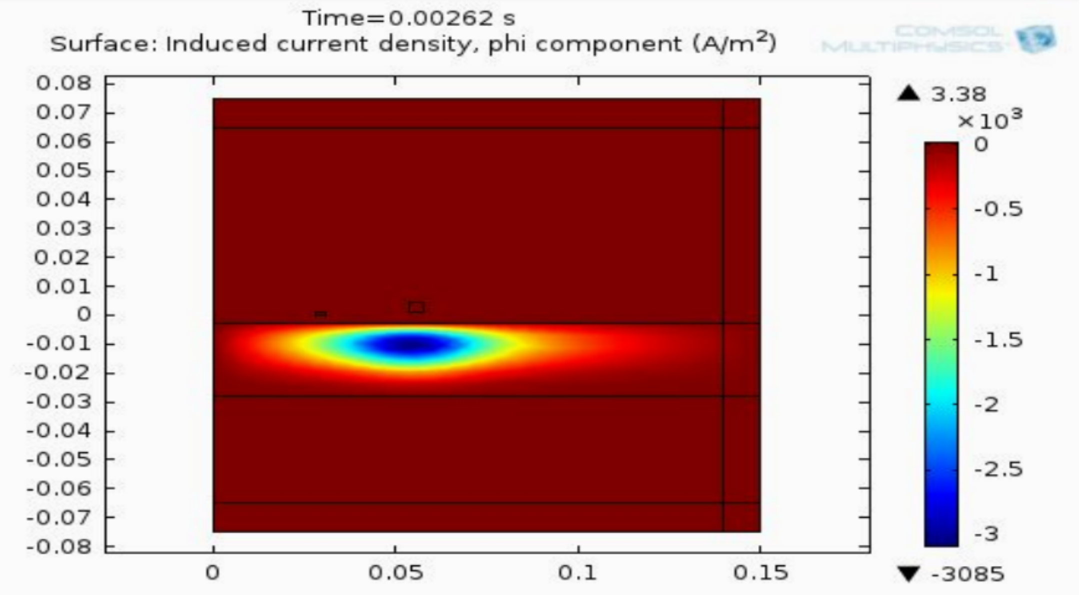

FIGURE 5.6: Induced eddy current density in a 25 mm thick plate displayed by the 2D axisymmetric model at a certain time instance.

TABLE 5.3: Parameters required for simulation.

Parameter	Value
r_{di}	30 mm
r_{do}	34 mm
h_d	0.1 mm
lo_d	4 mm
n_d	50
σ_d	5.998×10^7 S/m (Copper)
μ_d	μ_0 (Copper)
r_{ei}	60 mm
r_{eo}	65.1 mm
h_e	5.1 mm
lo_e	5 mm
n_e	625
σ_e	5.998×10^7 S/m (Copper)
μ_e	μ_0 (Copper)
d	30 mm
σ	5.9×10^5 S/m (Gray Cast Iron)
μ	BH Curve (Gray Cast Iron, Fig. 4.3)
I_e	50 mA
Z_{dl}	50 Ω

amplitude. Assuming an ideal current pulse for excitation is reasonable since the rising edge does not impact the β_{max} feature considered for this study since the signal feature is extracted well after the signal rise is completed. Subsection 5.2.2 describes the problem intended to be solved.

5.2.2 Procedure for Increasing Resolution

A PEC sensor usually has a domain of influence larger than its footprint. The domain of influence is the region in which eddy currents are induced due to the excitation field and Fig. 5.6 is an example which shows the domain of influence of the circular PEC sensor considered in this chapter. When the domain of influence is large, the thickness detected by the sensor usually becomes an averaged result of the actuality of the ferromagnetic material remaining within the domain of influence [34]. This in return reduces the resolution of a PEC sensor since the sensor becomes sensitive to a large volume domain impacted by eddy currents. Therefore, the target is to investigate how the sensor resolution can be increased, or more specifically, how the domain of influence can be reduced, by using the base model as the guide. During the process of increasing resolution, the low dependence of β_{max} on sensor shape, hypothesized in Subsection 3.2.6 is verified. Validating this hypothesis is important to establish generality of the knowledge gained from the circular sensor model in this chapter. The other low dependencies are used to propose a framework to perform 3D profiling by concurrently inferring thickness and lift-off.

The steps required to be followed in chronological order to solve the problem of achieving increased resolution and facilitating 3D profiling are listed below.

1. Validate the hypothesis of β_{max} being lowly dependent on sensor shape given the prevalence of sufficient penetration capability.
2. Quantify the domain of influence of the base model.
3. Perform a two fold study of reducing sensor size and increasing excitation to achieve reduced lateral domain of influence while maintaining sufficient thickness detection capability.

4. Propose a framework for 3D profiling of the material being testing by concurrently inferring thickness and lift-off by exploiting the verified low dependencies of β_{max}.

Section 5.3 investigates and confirms the low dependence exhibited by β_{max} on sensor shape while assessing ferromagnetic materials.

5.3 Low Dependence of β_{max} on Sensor Shape

Similar to the previously validated low dependence on lift-off and sensor size, low dependence on sensor shape was hypothesized for the condition that sufficient penetration capability remains despite sensor shape, and this hypothesis is tested in simulation in this section.

Previous chapters investigated a commercial rectangular PEC sensor and a 3D numerical model for the sensor was developed and validated in Chapter 4. The parameters of the base model discussed in this chapter, despite being circular provide a penetration capability nor less than that of the rectangular sensor. Therefore, given the prevalence of sufficient penetration capability, the hypothesis states that β_{max} values should exhibit low dependence to sensor shape, examined in the scope of this subsection as rectangular and circular shapes. This hypothesis was tested by comparing β_{max} values produced by the base model for gray cast iron against experimental values produced by the rectangular sensor. Fig. 5.7 shows an example how the base model impacts the signal when comparing with the signal from the rectangular sensor and Table 5.4 provides $\ln \beta_{max}$ values for different thicknesses obtained from both shapes.

TABLE 5.4: Shape dependence of $\ln \beta_{max}$ values.

Thickness	Rectangular Sensor ($\ln \beta_{max}$)	Base Model $\ln \beta_{max}$
5 mm	-7.722	-7.735
10 mm	-6.553	-6.615
15 mm	-5.930	-6.002
20 mm	-5.254	-5.304
25 mm	-4.801	-4.871

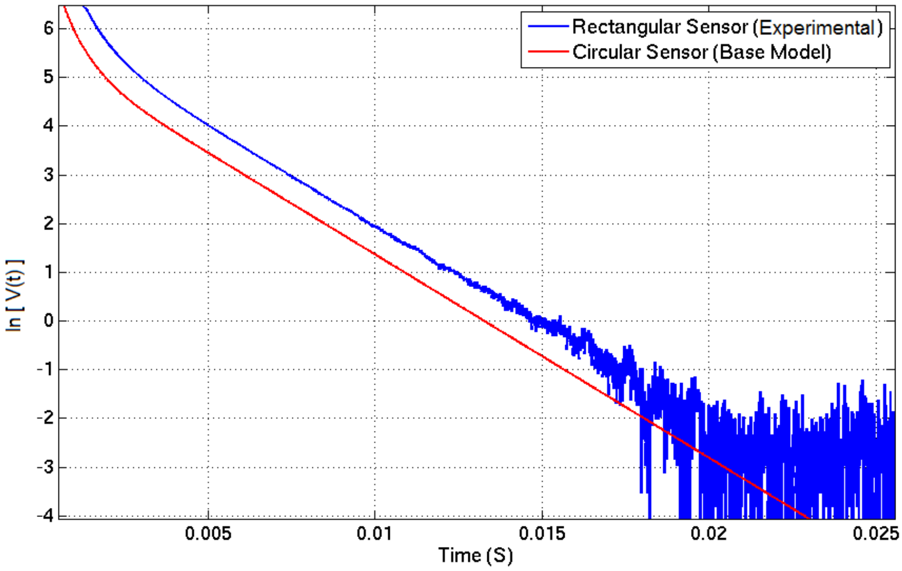

Figure 5.7: Example for the impact of circular shape on the signal when comparing with the signal captured from the rectangular sensor (captured on a gray cast iron calibration block, 16 mm thickness).

According to the results of Fig. 5.7 and Table 5.4, it can be concluded that the β_{max} feature is lowly dependent on sensor shape when there is sufficient penetration capability. However, the actual signal may vary differently for different sensor shapes and sensor properties such as excitation strength and number of coil turns. An example signal variation caused by the difference in shape and properties between the rectangular sensor and the base model is exhibited in Fig. 5.7.

5.4 Finding the Domain of Influence of the Base Model

Finding the domain of influence was done in two steps: (a) Verifying penetration capability; (b) Finding lateral (horizontal) domain of influence.

5.4.1 Verifying Penetration Capability

Desired penetration capability for this exercise is 30 mm on gray cast iron. To check the penetration capability of the base model, simulations were run by varying material thickness (d) while keeping all other parameters fixed at the values provided in Table 5.3. d was varied from 5 mm to 55 mm in steps of 5 mm and Fig. 5.8 shows the extent to which $\ln \beta_{max}$ remains linear with $\ln d$. From the figure, it can be seen that the base model shows the linear characteristic up to 30 mm and exhibits the nonlinear characteristic beyond. Lower thickness range is not paid attention to here since the objective of this chapter is to have sufficiently large enough penetration depth while increasing sensor resolution. The behavior shown in Fig. 5.8 is attributed to the 50 mA excitation current not being strong enough to induce eddy currents of sufficient intensity to show linearity in gray cast iron depths greater than 30 mm. It can thus be concluded that the base model just achieves the desired penetration capability of 30 mm on gray cast iron, but experiences loss of linearity thereafter. This implicates that the vertical domain of influence of the base model in terms of penetration depth exhibiting linear characteristic is about 30 mm.

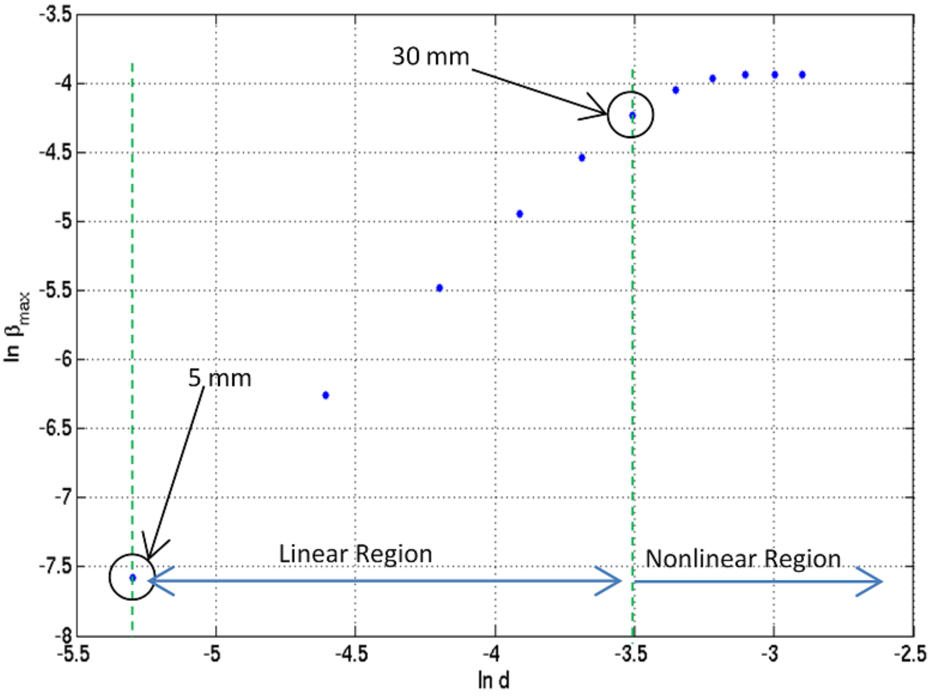

FIGURE 5.8: Vertical domain of influence (penetration depth) of the base model.

5.4.2 Finding Lateral (Horizontal) Domain of Influence

The modified base model shown in Fig. 5.9 was used to find the lateral domain of influence. For a fixed d, w was increased from 10 mm until β_{max} exhibited significant independence on w. When β_{max} becomes independent of w, that confirms that w has exceeded the lateral domain of influence of the sensor incorporated in the base model. Dependence of β_{max} on w was checked for d values: 5, 10, 15, 20, 25 and 30 mm and the result is shown in Fig. 5.10.

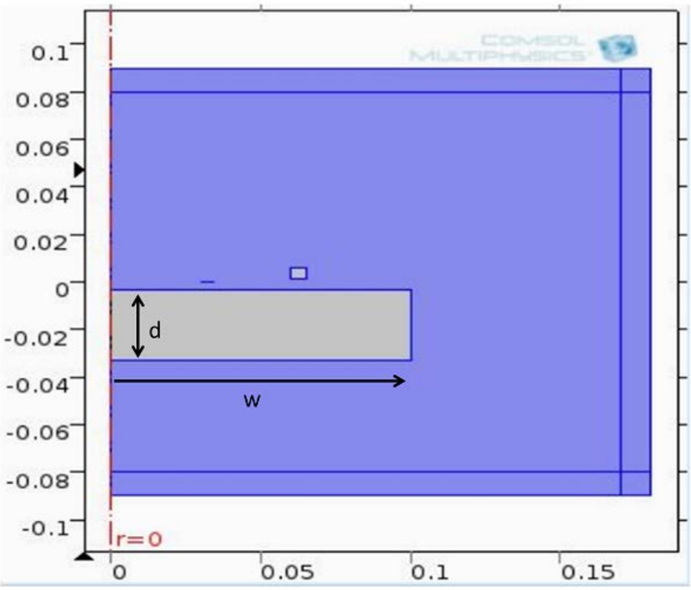

FIGURE 5.9: Simulation model to investigate lateral domain of influence.

After recording an array of β_{max} values for a single thickness, the array was divided by the maximum of the array in order to scale β_{max} values to have a maximum of 1 for ease of comparison. Lowest scaled β_{max} values for all thicknesses can be seen when w is minimal. That is attributed to having little metal volume under the sensor and it can be seen how β_{max} values increase with the increase of metal in proportion to w. At higher w values, it can be seen that β_{max} variation is insignificant. Therefore, the lateral domain of influence of the sensor was identified as the region where w contributes in a scaled β_{max} reduction of over 1% from maximum. This quantification suggested a lateral domain of influence of $w < 120$ mm. The effect of this margin is fairly visible in the figure and the domain of influence remained the same for all thicknesses. Inner and outer radii of the excitation coil is 60 and 65.1 mm respectively, and it was observed that the domain of influence

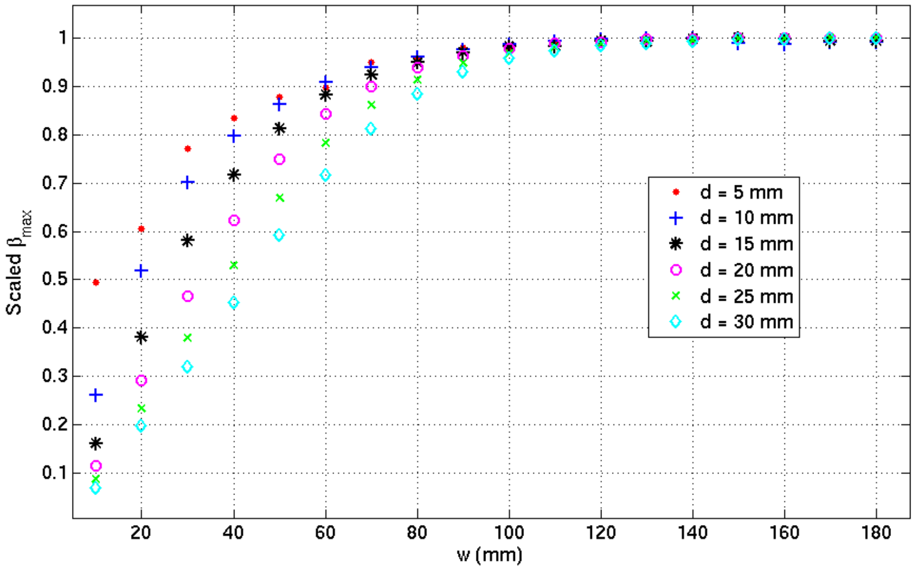

Figure 5.10: Lateral domain of influence.

was almost double the inner radius. This indicates the sensor footprint creates space for improving resolution as done in Section 5.5.

5.5 Increasing Sensor Resolution (Reducing the Domain of Influence)

To increase resolution, the study performs an iterative decrease of sensor size and an increase of excitation strength. As mentioned in Subsection 5.2.2, the inner radii of both exciter and detector coils were reduced by 50% to make the sensor smaller. Coil domain widths and heights were kept constant in order to accommodate same number of turns of AWG 32 and AWG 40 wires as specified in the base model. Intention of reducing size was to reduce the lateral domain of influence and achieve increased resolution in return. However, measurement capability up to $d = 30$ mm was desired. Simulations were run by increasing d from 5 mm to 35 mm with reduced coil radii while other base model parameters were kept constant. Due to reduction of wire length as a result of reduced coil size, excitation coil resistance decreased to 67 Ω in the small sensor from the original value of 128 Ω which existed in the base model. Observed result is shown in Fig. 5.11 in blue, the straight line in red is the linear behavior observed with the original base model.

The behavior of eddy current spread decreasing with reduction in excitation coil size reported in [40] was observed in this simulation as well in the form of loss of linearity from 20 mm as opposed to 30 mm in the original base model. With the intention of increasing sensitivity for higher thicknesses, a second experiment was run by bringing the detector coil back to its original size (*i.e.*, inner radius = 30 mm). The detector coil does not affect the domain of influence impacted by the exciter. But making the detector coil larger enables it to capture more magnetic flux and in return, the induced voltages will be larger making the sensor more sensitive to higher thicknesses. Increased sensitivity in the higher thickness region achieved by making the detector coil larger is shown in Fig. 5.11 in maroon 'x'.

Since reduction of excitation coil size resulted in reducing the overall excitation coil resistance from 128 Ω to 67 Ω, the option of increasing the excitation current was considered as another mechanism to increase thickness sensitivity. Given that fusing currents of exciter and detector coil wire gages were in the ampere range, the excitation current was doubled by increasing to 100 mA from the original base model value of 50 mA. That resulted in further increasing thickness sensitivity as shown in black in Fig. 5.11. As can be seen from the figure, perfect linearity could not be achieved even after doubling the excitation current due to the effect of the reduced coil size. However in theory, it should be possible to achieve a linearity similar to the base model by increasing the excitation. Due to hardware limitations encountered in practice, increasing the excitation is not a practical solution. However, perfect linearity is not a necessity since a nonlinear thickness-feature function can be learned using GP as proposed in Chapter 4. Despite nonlinearity being prevalent, if β_{max} exhibits functional behavior with thickness, a GP approach is able to characterize the thickness-feature function. Therefore, slight increase in thickness sensitivity achieved in the higher thickness region through increasing detector coil size and excitation does suit the purpose since thickness discrimination is possible despite loss of linearity.

It was now necessary to check whether the lateral domain of influence had been reduced due to the reduction of excitation coil size. Since Subsection 5.4.2 showed that the lateral

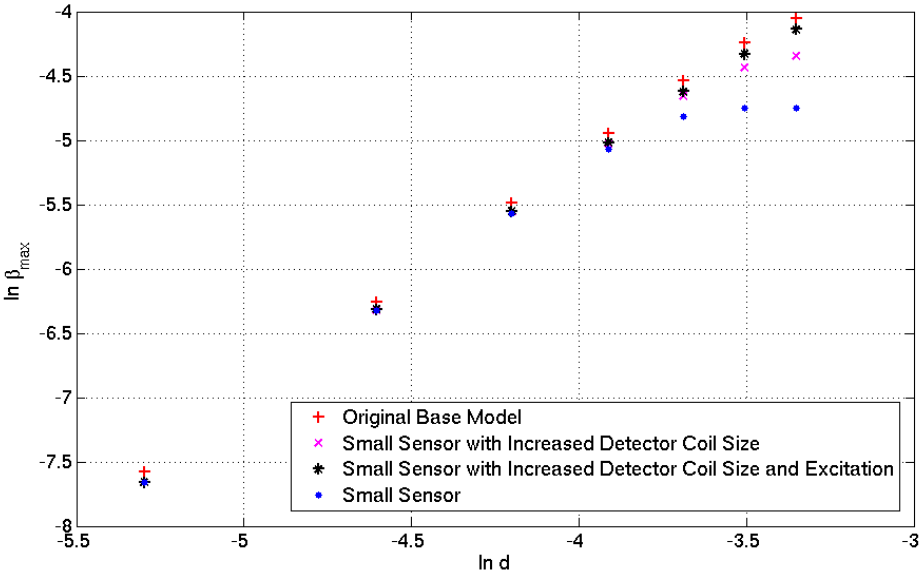

FIGURE 5.11: Results from experiments done to increase sensor resolution.

domain of influence is fairly uniform for all test piece thicknesses, the impact on lateral domain of influence was checked in this section using a 15 mm thick plate. The usual exercise of increasing w from 10 mm was carried out and the result is shown in Fig. 5.12. The test was run with the smaller sensor with the increased detector coil size and excitation current, despite the increase in excitation to 100 mA, a reduced domain of influence of about $w < 70$ mm was achieved. This is almost a 42% reduction of the domain of influence which was 120 mm in the original base model.

From the above observations, it can be concluded that the lateral domain of influence of a given sensor architecture can be reduced simply by reducing the size of the exciter coil. The disadvantage of losing thickness sensitivity for higher thicknesses will be experienced as a result. However, this loss of sensitivity can be counteracted by increasing detector coil size and excitation current. Linearity observed in the original base model was never reattained through the experiments done in this section, increase in thickness sensitivity was observed by increasing detector coil size and excitation current nevertheless. Since learning nonlinear thickness-feature functions through GP is possible, achieving increased sensitivity is sufficient although perfect linearity is nonexistent. Though it may be intuitively reasoned that increasing the excitation current may increase the lateral domain of

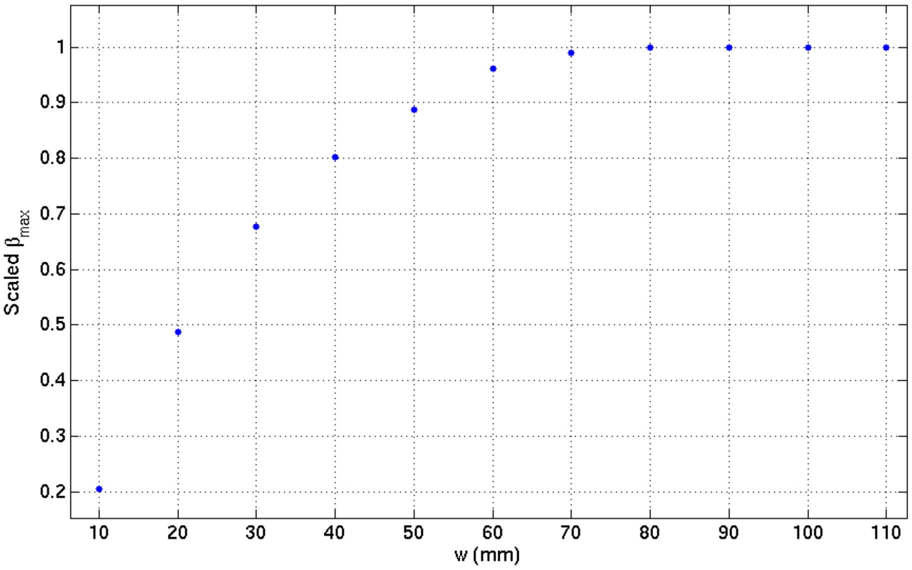

FIGURE 5.12: Domain of influence of the small sensor with larger detector coil and increased excitation.

influence, the observations suggest that reduction of sensor size is more dominantly impactive than the increase in excitation. Based on this knowledge, the sensor size may be reduced further to achieve any desired resolution. However, this will cause loss of sensitivity for higher thicknesses. Since low dependence of β_{max} on sensor shape was established, this knowledge generalizes to different sensor shapes.

Taking 100 mA as a design constraint for maximum allowable excitation current assuming hardware limitations, an optimum sensor size could be achieved by further reducing the exciter coil radius. The solution yielded a detector coil radius (r_{di}) of 30 mm and an exciter coil radius (r_{ei}) of 15 mm which is one fourth of the initial exciter coil radius of 60 mm found in the base model (Table 5.3). Other parameters remain the same as in Table 5.3. The thickness-feature function resulting from the optimized sensor is shown in Fig. 5.13.

5.6 Towards 3D Profiling

In contrast to the 2.5D representation of test piece condition completed in previous chapters, whereby the thickness of remaining ferromagnetic material is determined at discrete

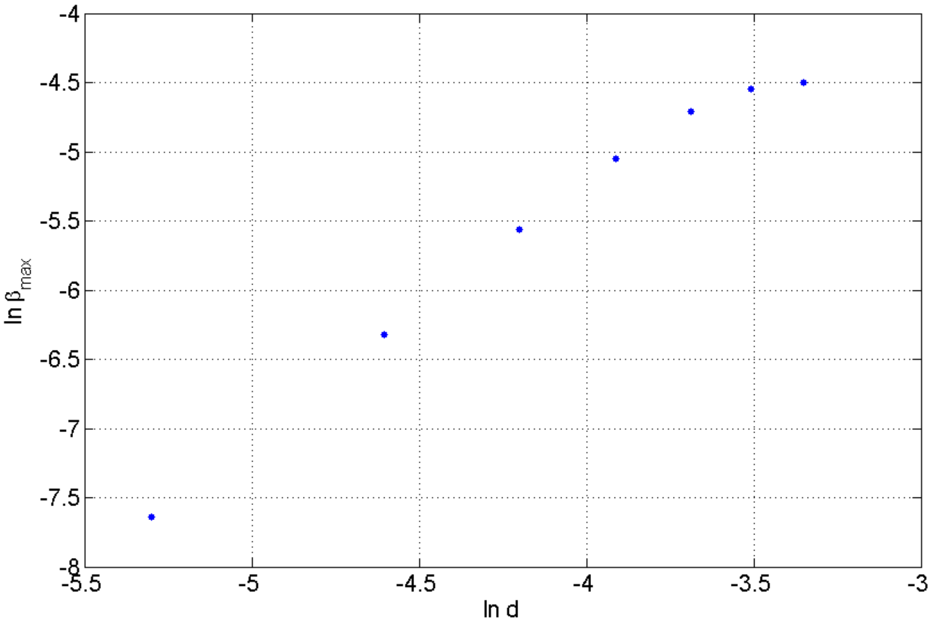

Figure 5.13: Thickness-feature function of the optimized sensor.

locations, this section proposes a framework to represent the pipe condition in 3D. The framework simultaneously estimates the thickness of the ferromagnetic material and the vertical distance between the PEC sensor and the top surface of the ferromagnetic substrate at discrete locations. The problems associated with 3D profiling are elaborated in the following subsection.

5.6.1 Effects of Corrosion and Graphitization Process on PEC NDE

A critical pipe wall at its original state is entirely composed of a ferromagnetic material (such as gray cast iron, ductile cast iron or mild steel) and with age, the pipe walls tend to corrode and graphitize [8, 11]. The usual pattern for corrosion or graphitization to develop, is for the phenomena to begin manifestation at the surface (both internal and external) and subsequently spread towards the center of the wall. As a result, the formed rust and graphite remain as layers close to the internal and external surfaces, and the remaining original ferromagnetic material exists as a layer trapped between them. Intention of condition assessment is to infer the thickness of the hence trapped healthy material layer.

If surface corrosion and graphitization exist, the sensor will not have physical contact with the healthy material layer. In previous chapters, only the thickness of the healthy material layer was inferred. Existence of layers of rust and graphite between the healthy material and the sensor did not pose a significant challenge due to the low dependence of the β_{max} feature on lift-off. If the ferromagnetic material thickness is solely inferred, the pipe condition can only be estimated in 2.5D. In contrast, if the thickness of the healthy material layer can be estimated in conjunction with the thickness of the rust or graphite layer remaining between the healthy layer and the sensor, the pipe condition can be presented as a 3D profile.

To investigate the capability of inferring thickness of both the healthy layer, and the layer between the sensor and the healthy layer, solving the problem of finding both l and d in the modified base model setup shown in Fig. 5.14 (r_{ei} = 30 mm, r_{di} = 30 mm and 100 mA excitation current) is attempted in the remainder of this chapter. μ_t and μ_b are the relative permeability of the top and bottom layer respectively, whereas σ_t and σ_b are corresponding electrical conductivities. Experiments done with strong magnets on chipped particles of graphite and rust layers present on critical pipes showed neutrality to magnets and therefore $\mu_t = \mu_b = 1$ was set when modelling. μ and σ have usual meanings associated with the base model.

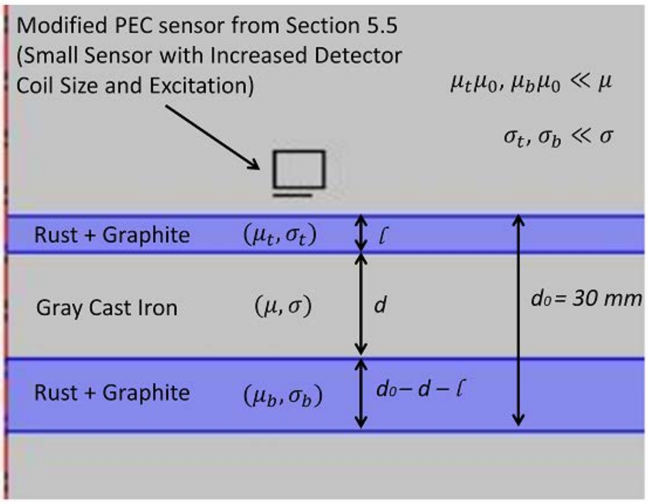

FIGURE 5.14: FEA model used for solving the problem of inferring thickness of both the healthy material layer and the top layer.

The electrical conductivity and magnetic nature of rust and graphite layers are significantly less than those of the ferromagnetic layer in the middle, as indicated in Fig. 5.14.

5.6.2 Effect of σ_t and σ_b on the PEC signal

Before attempting to solve the problem, it was important to identify the impact of σ_t and σ_b on the PEC signal. A model was parameterized with $d = 15$ mm, $l = 15$ mm, and simulations were run by varying σ_t from 0 to 10^5 S/m., the maximum possible value for both σ_t and σ_b given the conductivity of graphite is generally at most in the order of 10^4 (https://www.entegris.com/resources/assets/6205-7329-0513.pdf). Observed results presented in Fig. 5.15 suggested there is no significant impact on the signal (less that 1% variation in signal between 0 S/m and 10^5 S/m conductivity) and feature β_{max} (variation less than 1%) since $\mu_t\mu_0 << \mu$ as $\mu_t = 1$ and $\sigma_t < \sigma$. It should be noted that the signal shift from the reference observed in this case is attributed to the effect of lift-off observed in Chapter 3 since the healthy ferromagnetic layer is 15 mm away from the sensor. Thereafter, simulations validate that the impact caused by σ_t on the signal and its gradient is minimal.

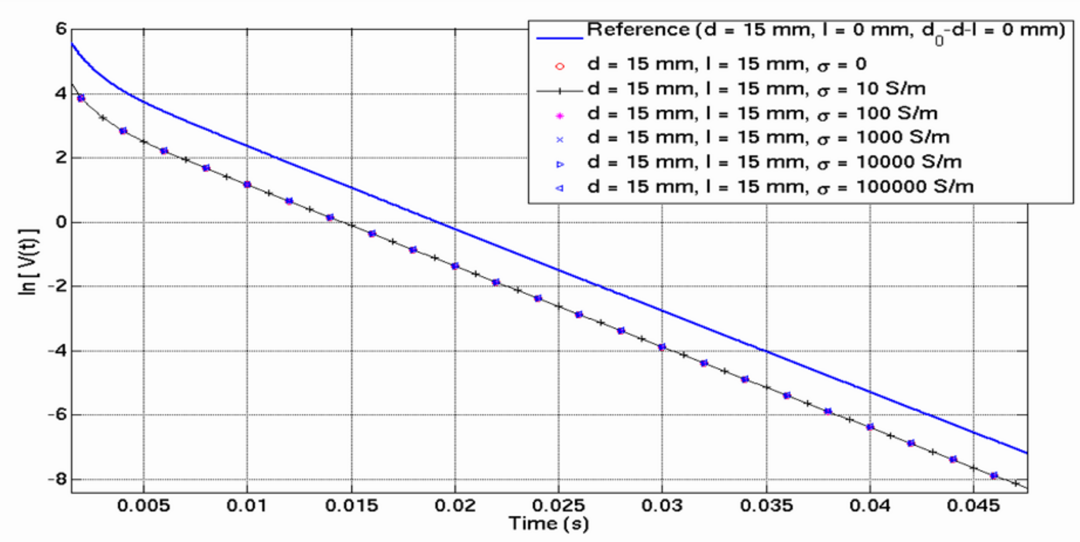

FIGURE 5.15: Influence on the signal caused by σ_t.

Similarly, to identify the influence of σ_b on the PEC signal, the model was parameterized as $d = 15$ mm and $d_0 - d - l = 15$ mm, and simulations undertaken with σ_b in the range

0 to 10^5 S/m. Results in Fig. 5.16 suggest there is no significant impact (less than 1% variation) on the signal and β_{maxx} since $\mu_b\mu_0 << \mu$ as $\mu_b = 1$ and $\sigma_b < \sigma$. For the sake of completeness, simulations were run for the two cases by making $\sigma_t = \sigma_b = 10^6$ S/m to verify the hypothesis that such high conductivity would invariably impact the signal, given the conductivity has reached the order of gray cast iron. A clear influence was observed as expected, but still in moderation since $\mu_t = \mu_b = 1$ held. Significantly higher values of μ_t and μ_b usually do not exist in graphitized and rusted layers [126].

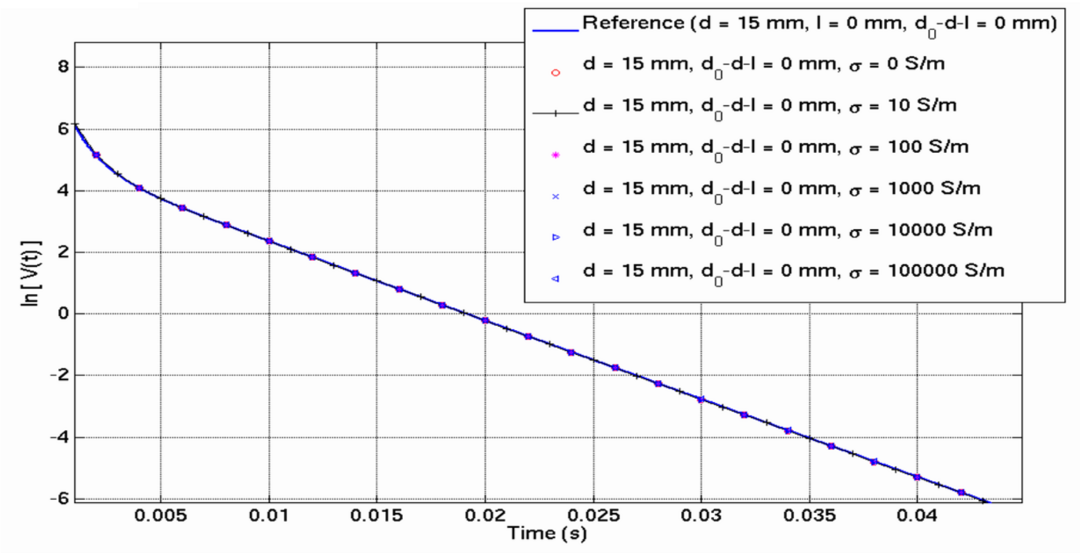

FIGURE 5.16: Influence on the signal caused by σ_b.

The observation of the impact on the signal being minimal for conductivities less than 10^5 S/m, typically maximum conductivity values of cast iron, validated the practicality of a framework for jointly inferring thickness of both the top and middle layers presented in the following section.

5.6.3 The 3D Profiling Framework

The fundamental of the framework is inferring thickness of the ferromagnetic layer using β_{max}, since β_{max} is not significantly influenced by lift-off caused by the top layer, the conductivity of the top layer within the considered range, and inferring the thickness of the top layer as liftoff using a threshold crossing time as a signal feature. Therefore, after the thickness-feature function has been learned, as done in Chapter 4, the procedure to infer both thickness and lift-off from a captured PEC signal can be summarized as:

1. Infer d using the learned thickness-feature function demonstrated in Chapter 4.
2. Given an inferred thickness d^* mm, using the model presented in Fig. 5.14, numerically simulate the cases where l takes the value $k(d_0 - d^*)$ mm, k takes the values 0, 0.25, 0.5, 0.75 and 1.0 with $\sigma_t = \sigma_b = 0$ S/m and $\mu_t = \mu_b = 1$. The intention behind selecting k values was generating five training data points corresponding to equally spaced lift-offs.
3. Extract feature t_{th} from the simulated signals, where $t = t_{th}$ is the time $\ln[V(t)]$ intersects a horizontal threshold h_{th}. For convenience, $h_{th} = 0$ is taken as the threshold in this chapter.
4. Learn the l-t_{th} function using GP as done in Chapter 4 with the aid of simulated values.
5. Infer l^* from the learned l-t_{th} function using the t_{th} feature extracted from the captured signal.

By following the above procedure, the thickness of both the ferromagnetic layer and the top layer can be inferred, enabling presentation of pipe wall condition in 3D.

5.6.4 Results

The learned thickness-feature function for the circular sensor ($r_{ei} = r_{di} = 30$ mm and 100 mA excitation current) is shown in Fig. 5.17. Training was purely based on simulation with no added experimental noise, as the focus of this chapter was on fundamental study, designing and fabricating a new sensor was not an objective of the project. No work was therefore carried out to design a circular sensor and experimentally characterize sensor noise to incorporate in the model at this stage. In the case of practical developments however, experimental noise can be characterized as done in Section 3.7 and added to the model.

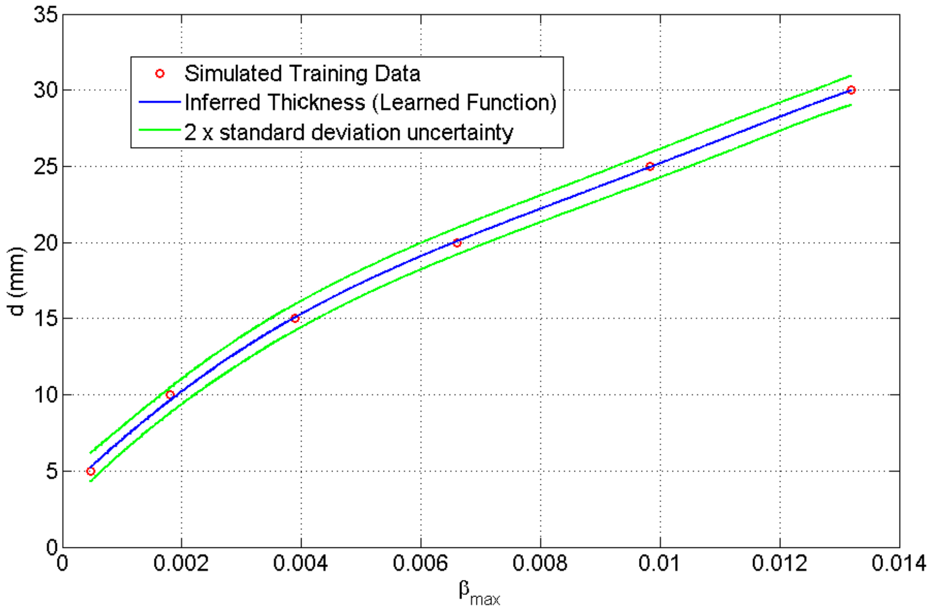

FIGURE 5.17: Thickness-feature function learned for the optimized circular sensor.

In the same way of the thickness-feature function was modeled, different lift-offs can be simulated for a known thickness and the l-t_{th} function can be learned by assuming $\sigma_t = \sigma_b = 0$ S/m and $\mu_t = \mu_b = 1$. A hence learned l-t_{th} function for $d = 10$ mm is shown in Fig. 5.18. Since the function between lift-off and threshold crossing time can be learned for any thickness, it is fundamentally possible to infer the thickness of the top layer when thickness of the ferromagnetic layer is known, enabling 3D profiling.

The 3D profiling capability on gray cast iron was tested for several cases and Table 5.5 shows results for 3D inferences for a test case where $\sigma_t = 1000$ S/m, $\sigma_b = 1500$ S/m, $\mu_t = \mu_b = 1$ and $d_0 = 30$ mm were assumed to generate testing data through simulation. Since thickness and lift-off are estimated using GP, the estimations in the table are provided with the two standard deviation uncertainty.

5.7 Conclusions

This chapter investigated via FEA simulation, the process for increasing the resolution of a detector coil based PEC sensor allowing 3D profiling of ferromagnetic materials by jointly inferring thickness of the remaining healthy material and the vertical separation

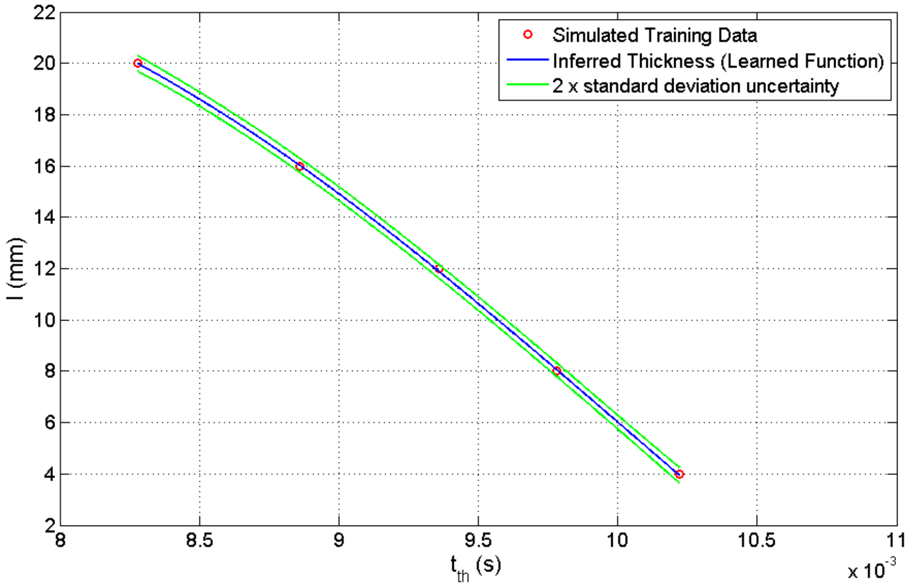

FIGURE 5.18: Learned function between lift-off and zero crossing time for $d = 10$ mm.

TABLE 5.5: 3D profiling capability on gray cast iron: Results.

Thickness (d)	Lift-off (l)	Estimated Thickness (d^*)	Estimated Lift-off (l^*)
7 mm	17 mm	6.66 (±0.856) mm	16.997 (±0.583) mm
12 mm	10 mm	11.7 (±0.852) mm	9.939 (±0.255) mm
17 mm	8 mm	17.1 (±0.863) mm	7.901 (±0.188) mm
22 mm	4 mm	21.8 (±0.879) mm	4.190 (±0.401) mm
27 mm	2 mm	26.1 (±0.952) mm	1.99993 (±0.0248) mm

between the sensor and the surface of the ferromagnetic material. In regard to increasing resolution, it was evident that reducing the sensor size indeed reduces the lateral domain of influence resulting in increase of resolution. However, vertical penetration depth also decreases with size reduction of the exciter coil and the effect can be mitigated by increasing excitation strength. Exciter coil size was observed to be the dominant factor affecting the lateral spread and not the excitation strength when the size was reduced to a half and the excitation was doubled. Based on the observed behavior, it could be concluded that the sensor resolution may be increased to a desired limit as long as available hardware has the capability of delivering and withstanding the required excitation strength. When considering thickness sensitivity, nonlinearities caused by loss of sensitivity resulting from increasing resolution is not a significant challenge as long as functional behavior is preserved in the thickness-feature function since nonlinearities can be learned using GP. Some other options that were not investigated in this chapter in relation to resolution increase were the number of coil turns and coil cross-section area. Both those parameters directly influence coil resistance, increasing the number of turns demands high excitation power and creates more magnetic field making the domain of influence larger. Increasing wire cross-section area makes the sensor physically larger, impacting the domain of influence, but reduces the demand for excitation power. When coming to practical developments through sensor design, incorporating those factors as well will be useful to produce an optimum and economical sensor.

The chapter also verified the large invariance to sensor shape property for the β_{max} feature. This further validates the theoretical approximation $\beta_{max} \approx \frac{\mu\sigma d^2}{\pi^2}$ at the core of this work.

Finally the chapter presented a framework which fundamentally enabled 3D representation of pipe wall. For this framework, the test piece in divided into three horizontal layers where the top and bottom layers represent rust/graphitization layers and the middle layer contains the ferromagnetic material. The rust graphite layers were found to be nonmagnetic through experimental validation of neutrality to magnets. However, there is no guarantee the rust graphite layers are non-conductive. Simulations suggested that the conductivity of top and bottom layers did not noticeably influence the signal until they became very large. Since it is known that rust and graphite layers cannot have high conductivities, and moderate conductivities do not significantly influence the signals, it was reasonable to model them as layers having a relative permeability of 1 and a conductivity of zero. Thus, it is possible to infer the thickness using β_{max} and infer the thickness of the top layer as lift-off. Inferring the thickness of the top layer was done by means of learning a function between a threshold crossing time and lift-off. Since the function between lift-off and threshold crossing time can be learned for any thickness, it is fundamentally possible to infer the thickness of the top layer when thickness of the ferromagnetic layer can be estimated, enabling 3D profiling.

Chapter 6

Conclusions

This thesis introduced a novel PEC signal feature based on the detector coil voltage decay rate and exploited it for estimating ferromagnetic material volume remaining in critical pipes via NDE. Behavior of the feature was analytically described and subsequently experimentally validated on a range of ferromagnetic materials. Two approaches; an analytical and a semi-parametric numerical approach were proposed to exploit the novel feature. The performance of the developed approaches was evaluated on in situ critical pipes managed by a commercial water utility. Both approaches predict pipe condition by means of a learned function which maps the signal feature to the average thickness of ferromagnetic material generalized to a region under the sensor. The analytical approach parametrically learned the function using measurements performed on calibration blocks. The numerical approach learned the function non-parametrically using GP with the aid of signal features numerically simulated by taking into account measured electrical and magnetic properties of pipe materials. The feature was found to exhibit significant invariance (low dependence) to lift-off, sensor shape and size. Low dependence on sensor shape and size were further numerically investigated to propose a method for achieving increased sensor resolution while maintaining a desired penetration capability. Finally, the significant invariance to lift-off was utilized to propose a framework which enables 3D inference of test piece condition.

6.1 Summary of Contributions

6.1.1 A Novel PEC Signal Feature for Thickness Quantification

Analyzing the detector coil based PEC signal in the form of the decay rate of the time domain signal's natural logarithm is unconventional and the introduced signal feature can be considered novel. Analytically describing the feature's behavior is possible by using the analytical model which represents the signal as a sum of exponentials. The feature exhibits clear functional relationship to ferromagnetic material thickness which makes the feature desirable for thickness quantification. Modeling this relationship forms the base of this thesis and the relationship can be modeled as a linear function as well as a nonlinear function. Due to practical limitations of the sensor, experimental data do not maintain linearity beyond certain thickness limits and such thicknesses cannot be modeled with the linear functional representation. However, theoretically existent nonlinearity as well as practically introduced nonlinearities can be modeled by probabilistically learning relationship as a nonlinear function. Further, a salience of the feature is its significant invariance on sensor shape, size and lift-off, which makes the feature immune to many practical challenges encountered during in situ applications. It was verified that the observed feature invariance enables advancements to the sensor such as increasing resolution and enabling 3D profiling.

6.1.2 An Analytical NDE Approach

The proposed analytical approach involved experimentally obtaining calibration signals and learning the linear form of the thickness-feature function by means of parameter estimation on linear regions of the sensor data. Despite removal of nonlinear regions, results showed that such an approach was able to estimate pipe wall thickness up to an accuracy of 90%. Since the linear function carries direct proportionality between the feature and the thickness, an alternative method of calibration based on ultrasounds was proposed to overcome the requirement of calibration blocks. That method involved qualitatively identifying high thickness regions of the pipe through values of the novel feature, and performing ultrasound measurements on those locations to obtain a reasonable corresponding thickness estimate. Due to the existence of proportionality, the rest of the thicknesses could be scaled with respect to the ultrasound measurement. This proved to be an effective method of scaling to support accurate PEC measurements without the requirement of calibration blocks. However, as long as the linear thickness-feature function was assumed for this approach, accounting for the nonlinearities introduced by limitations of the sensor was not possible.

6.1.3 A Numerical NDE Approach

The numerical approach proposed involved measuring electrical and magnetic properties of pipe materials and using them to simulate PEC sensor interaction with the material to produce signals using FEA. Subsequently the simulated signals were processed to extract feature values, and they were used to non-parametrically learn the nonlinear form of the thickness-feature function using GP. Precise electrical and magnetic properties of the material examined were measured by extracting samples and using them in a PPMS. Alternatively, XRF measurements and microscopic inspection can be done to broadly identify the material type to correlate approximate electrical and magnetic properties for material types available in literature. By using GP, theoretical nonlinearity existing in the nonlinear thickness-feature function as well as nonlinearities caused due to limitations of the sensor can be learned. Consequentially, an improvement of the accuracy of estimated wall thickness was observed over the analytical approach. In addition, the capability of providing uncertainty through GP is an added advantage to facilitate thickness estimates being used in sensor fusion applications.

6.1.4 A Numerical Study to Investigate the Possibility of Increasing PEC Sensor Resolution

The significant invariance of the signal feature to sensor shape and size were demonstrated in the thesis. These were exploited to numerically investigate increasing resolution of a circular sensor model. The interrelationship between sensor size and penetration capability was compensated by increasing excitation strength. It was demonstrated that despite an excitation increase, size was the dominant factor which influenced lateral domain of influence, thereby increased resolution could be achieved without significant loss of penetration capability.

Low dependence on lift-off was exploited to propose a framework to enable 3D profiling. The test piece was hypothetically divided into three horizontal layers of which the top and the bottom layers were considered to be rust/graphite layers and the middle layer was considered to be of healthy ferromagnetic material. Due to low dependence on lift-off, the feature still could be used to estimate thickness irrespective of foreign materials being present on top and bottom as long as they were nonmagnetic and considerably less conductive than the ferromagnetic layer. Since lift-off causes a signal attenuation which also appears on the time axis as a leftward signal shift, a horizontal threshold crossing time feature was used to infer the thickness of the top layer as a lift-off. Inferred thicknesses being lowly influenced by the top and bottom layers and the capability of learning a function which maps a threshold crossing time to lift-off for a given ferromagnetic material thickness suggests usability of the framework for 3D profiling.

6.2 Discussion of Limitations

The main limitation in the proposed NDE approaches is their calibration requiring either fabricating calibration blocks or following material property measurement procedures which cause minor destruction to pipes in the form of specimen extraction. Fabricating calibration blocks is time consuming and costly. Further, casting calibration blocks to have material properties matching those of critical pipes is extremely challenging. Current industry practice involves fabricating calibration blocks from standard materials and assuming their generalization over critical pipe materials; or else performing a measurement on a known thickness and estimating material properties. Though assuming generalization is reasonable in most cases, there are occasions where thickness interpretations are significantly divergent from the actuality due to material property mismatches.

An alternative mechanism of calibration was proposed in the thesis by using ultrasound measured thicknesses to scale PEC readings. The method though effective, requires cleaning the pipe surface to achieve a high degree of coupling required to perform an accurate ultrasound measurement.

Properties of pipe materials can be measured using a PPMS and incorporated to simulate PEC signals. This requires extracting small but solid samples and hence the procedure causes minor destruction to pipes. However, PEC signals can be used to qualitatively identify high thickness regions so that extracting samples from such regions will minimize impact on structural integrity. To reduce destruction even further, powder particles may be obtained to measure the magnetization curve, although not recommended as a best practice. The risk in doing so is the chance of powder particles being contaminated by foreign materials during the process of extraction. Furthermore, the powder particles may not optimally fit in the PPMS sample holder which may result in erroneous measurements. Measuring conductivity using powder particles is not recommended. Therefore, XRF measurements may be performed to broadly identify the type of material through composition, and approximate electrical properties, and even magnetic properties can be ascertained through literature studies. However, there is no guarantee that the published properties will satisfactorily match those of the particular test piece of interest. Therefore, directly measuring the properties precisely will yield optimal results and all other methods are ways of approximating.

Limitation in PEC sensor resolution is a challenge concerning quantification of isolated pitting. Detector coil based PEC sensors always predict an average which generalizes to a region under the sensor. The thesis therefore investigated the capability of increasing the resolution. Making the sensor smaller was observed to be an effective method; nevertheless the lateral domain of influence remains larger than the sensor footprint irrespective of sensor size. Theoretically, if the sensor is infinitesimally small, it will enable measuring fine defects. However, this is not practically possible as the required excitation energy will be infinitely large to achieve the desired penetration depth. Therefore in practice, resolution of a PEC sensor will be limited by the sensor size.

Though theory suggests perfect linearity in the linear thickness-feature function, in practice this is not achieved. Nonlinearity is observed in either side of the thickness estimation spectrum, very low and considerably high thicknesses, the exact ranges in question depend on the sensor configuration and the material being tested. In the low thickness region, signals enter the noise margin of the sampling circuitry before attaining constant gradient. Similarly, linearity is lost in the high thickness end due to the limitation of the sensor's penetration capability. Experiments done in the thesis suggested that linearity in the high thickness region can be reinstated by increasing excitation strength. That is a viable option to increase penetration capability and achieve linearity, however upgrading hardware to deliver and withstand required power is a challenge. A more economical option is to probabilistically model the nonlinear regions where functional behavior can be achieved with a prevailing excitation strength.

6.3 Future Work

Future work should extend towards simultaneous determination of material properties ($\mu\sigma$) and thickness without reliance on calibration measurements or measured material properties. Simultaneous measurement of $\mu\sigma$ and thickness has been accomplished on carbon steel by fitting an analytical model to measured data [35, 54]. However, the model has been specified for coaxial circular sensors and requires precise knowledge about lift-off and coil dimensions. Results have demonstrated some reasonable accuracy in general, however inaccuracies exist in estimating low thicknesses [35]. Despite limitations, a similar approach for solving the critical pipe condition assessment problem could be pursued.

To adopt such an approach to solve the specifics addressed in this thesis, either a similar analytical model has to be derived for rectangular sensors, or a model which is independent of sensor shape needs to be derived; or the rectangular architecture employed has to be replaced with the circular architecture to be able to use the already published model. Alternatively, since analytical and numerical modeling of PEC sensors is possible as attempted in this thesis, developing an optimization framework to simultaneously estimate properties and thickness by minimizing errors between experimental and modeled signals may prevail. That will be an effective method of solving the inverse eddy current problem, the challenge however is to define the problem to lead to a unique solution.

In terms of practical developments, increase of speed and efficiency of the measurement process was beyond the scope of this thesis. This thesis worked with an external condition assessment tool and therefore, exposing the wall exterior of buried pipes was necessary. Measurements were done manually as the current practice enforce it to be done so, thus the process was time consuming and inefficient. Therefore, there is space for developing accurate internal tools which can enter water pipes and autonomously perform measurements and record data. Research aimed towards such developments could be highly attractive for the future of the water industry.

Appendix A

Analytical Approach: Interpreted Pipe Wall Thickness Maps and Error Statistics

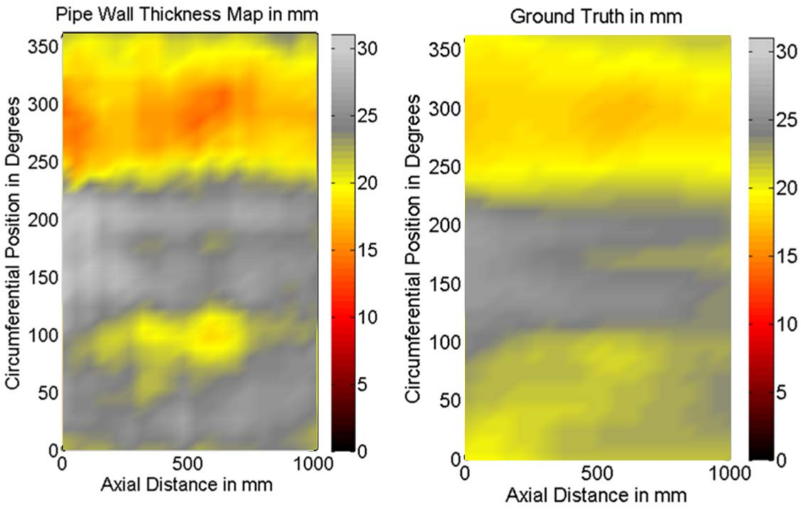

FIGURE A.1: Analytical approach; Section 1; interpreted thickness and GT maps.

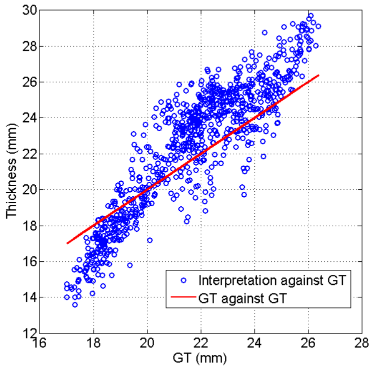

Figure A.2: Analytical approach; Section 1; variation of interpreted thickness along with GT.

Table A.1: Statistics of absolute error between interpreted pipe wall thickness and GT for Section 1.

Statistical Parameter	Value
RMS Error	1.92 mm
Mean Absolute Error	1.62 mm
Standard Deviation of Absolute Error	1.04 mm
Maximum Absolute Error	4.67 mm
Mean Percentage Accuracy	92.49%

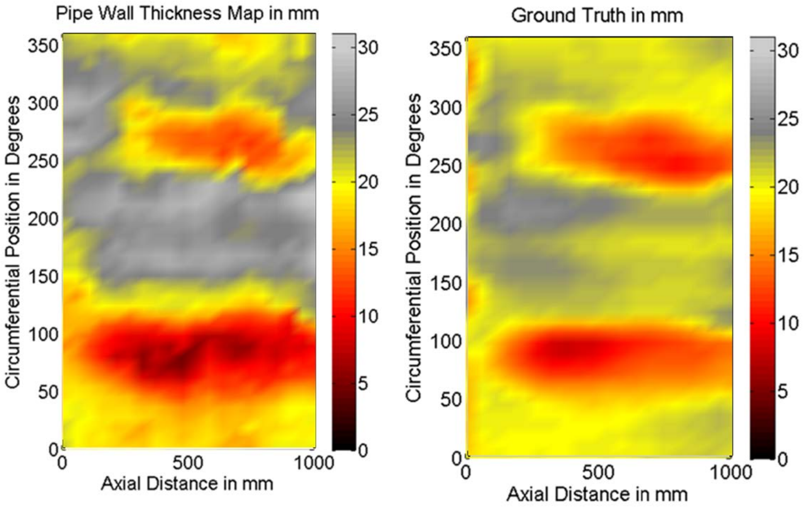

Figure A.3: Analytical approach; Section 2; interpreted thickness and GT maps.

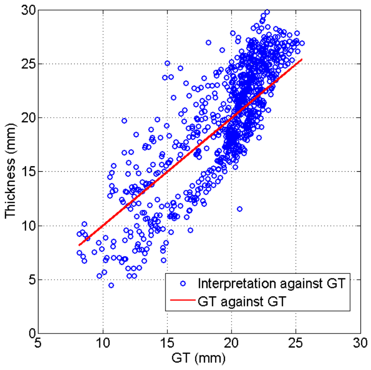

FIGURE A.4: Analytical approach; Section 2; variation of interpreted thickness along with GT.

TABLE A.2: Statistics of absolute error between interpreted pipe wall thickness and GT for Section 2.

Statistical Parameter	Value
RMS Error	3.16 mm
Mean Absolute Error	2.64 mm
Standard Deviation of Absolute Error	1.73 mm
Maximum Absolute Error	10.08 mm
Mean Percentage Accuracy	85.37%

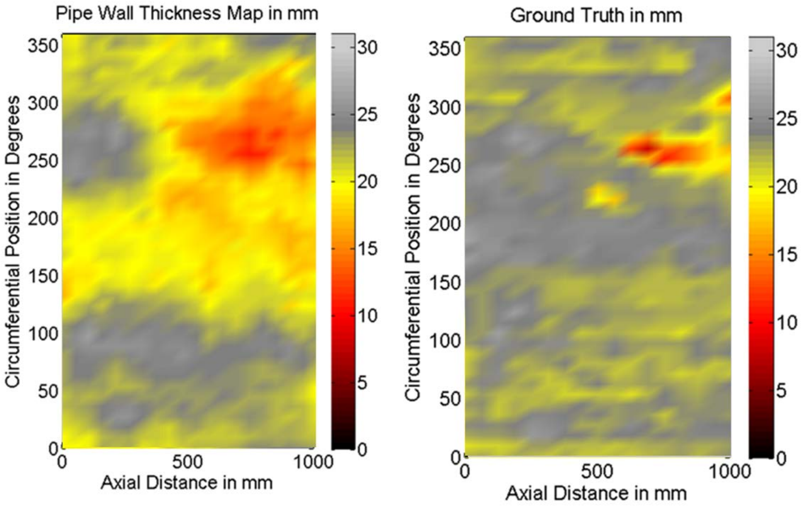

FIGURE A.5: Analytical approach; Section 3; interpreted thickness and GT maps.

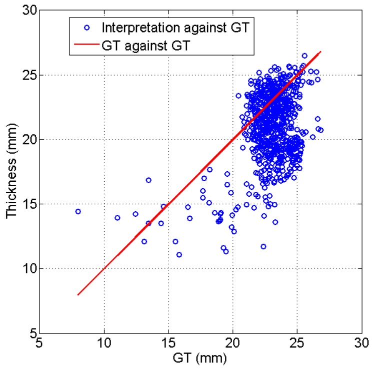

FIGURE A.6: Analytical approach; Section 3; variation of interpreted thickness along with GT.

TABLE A.3: Statistics of absolute error between interpreted pipe wall thickness and GT for Section 3.

Statistical Parameter	Value
RMS Error	3.24 mm
Mean Absolute Error	2.498 mm
Standard Deviation of Absolute Error	2.07 mm
Maximum Absolute Error	10.65 mm
Mean Percentage Accuracy	89.06%

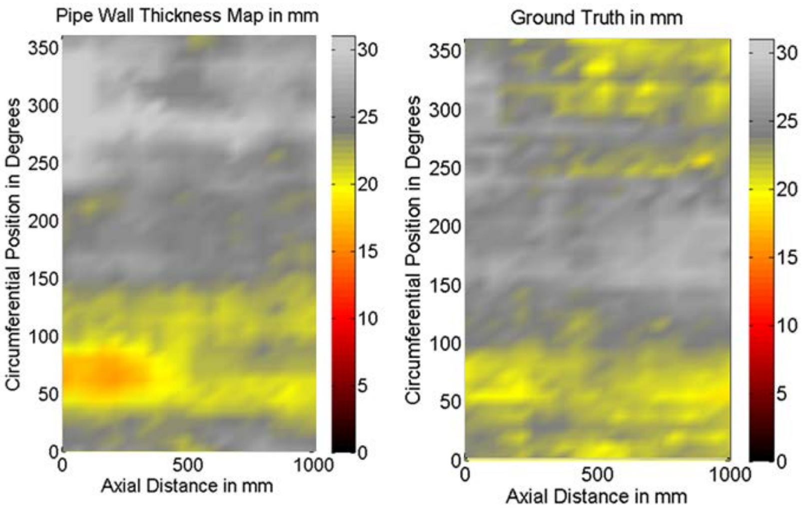

FIGURE A.7: Analytical approach; Section 4; interpreted thickness and GT maps.

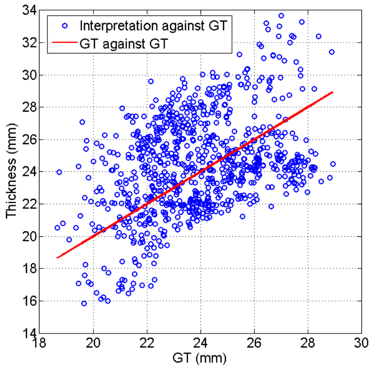

FIGURE A.8: Analytical approach; Section 4; variation of interpreted thickness along with GT.

TABLE A.4: Statistics of absolute error between interpreted pipe wall thickness and GT for Section 4.

Statistical Parameter	Value
RMS Error	2.93 mm
Mean Absolute Error	2.46 mm
Standard Deviation of Absolute Error	1.59 mm
Maximum Absolute Error	7.47 mm
Mean Percentage Accuracy	89.59%

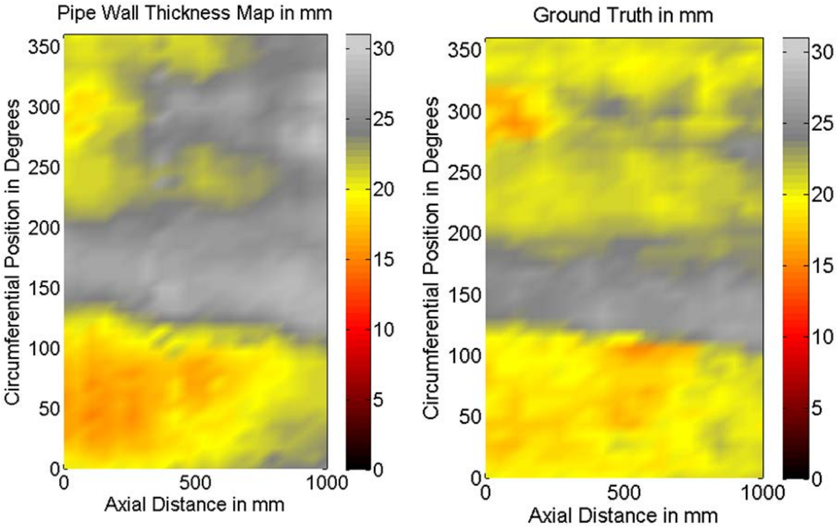

FIGURE A.9: Analytical approach; Section 5; interpreted thickness and GT maps.

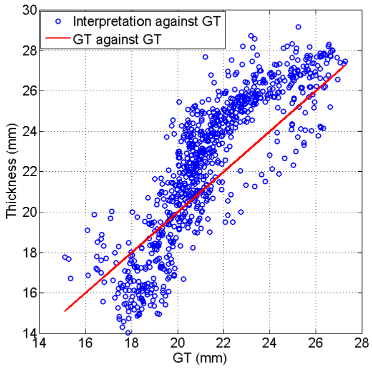

Figure A.10: Analytical approach; Section 5; variation of interpreted thickness along with GT.

Table A.5: Statistics of absolute error between interpreted pipe wall thickness and GT for Section 5.

Statistical Parameter	Value
RMS Error	2.21 mm
Mean Absolute Error	1.897 mm
Standard Deviation of Absolute Error	1.14 mm
Maximum Absolute Error	6.47 mm
Mean Percentage Accuracy	91.04%

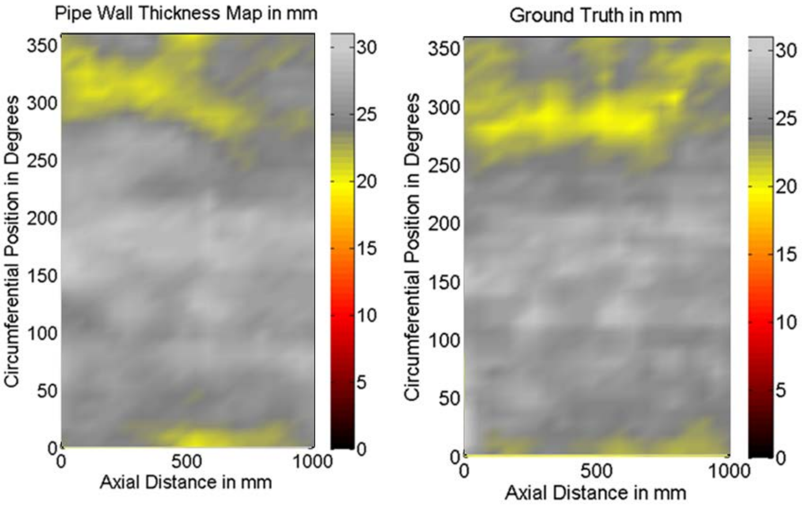

Figure A.11: Analytical approach; Section 6; interpreted thickness and GT maps.

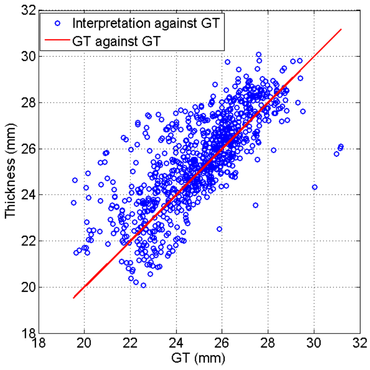

FIGURE A.12: Analytical approach; Section 6; variation of interpreted thickness along with GT.

TABLE A.6: Statistics of absolute error between interpreted pipe wall thickness and GT for Section 6.

Statistical Parameter	Value
RMS Error	1.48 mm
Mean Absolute Error	1.11 mm
Standard Deviation of Absolute Error	0.986 mm
Maximum Absolute Error	5.7093 mm
Mean Percentage Accuracy	95.42%

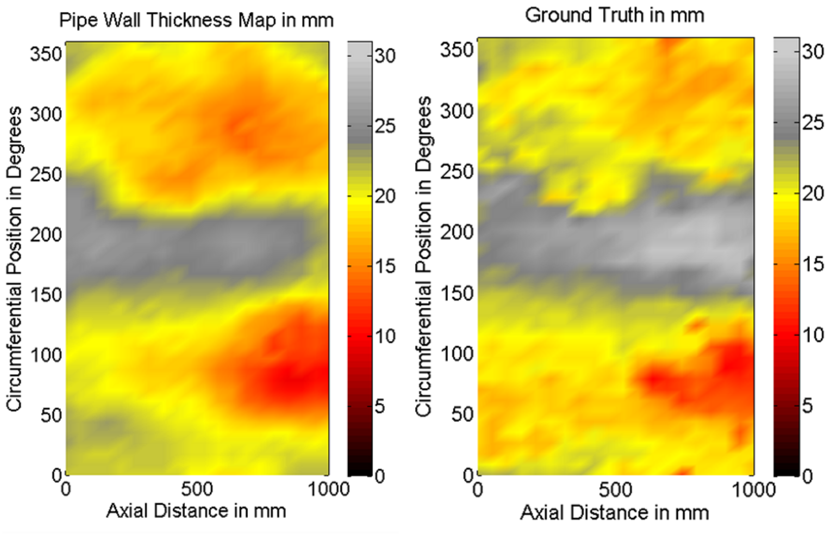

Figure A.13: Analytical approach; Section 7; interpreted thickness and GT maps.

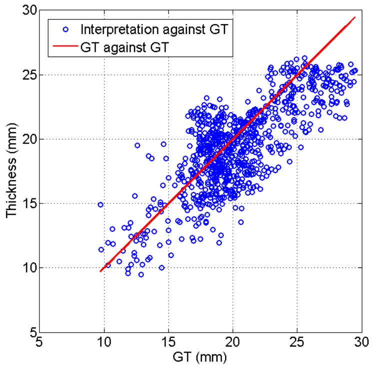

Figure A.14: Analytical approach; Section 7; variation of interpreted thickness along with GT.

Table A.7: Statistics of absolute error between interpreted pipe wall thickness and GT for Section 7.

Statistical Parameter	Value
RMS Error	2.62 mm
Mean Absolute Error	2.103 mm
Standard Deviation of Absolute Error	1.56 mm
Maximum Absolute Error	7.06 mm
Mean Percentage Accuracy	89.53%

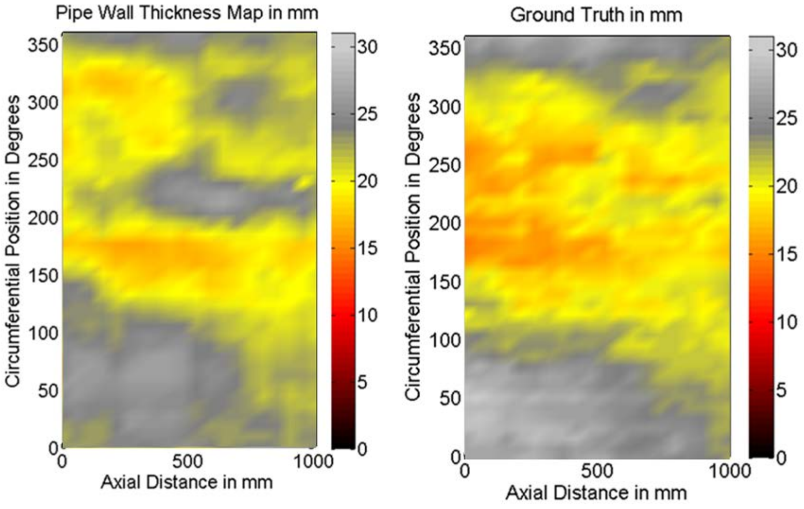

Figure A.15: Analytical approach; Section 8; interpreted thickness and GT maps.

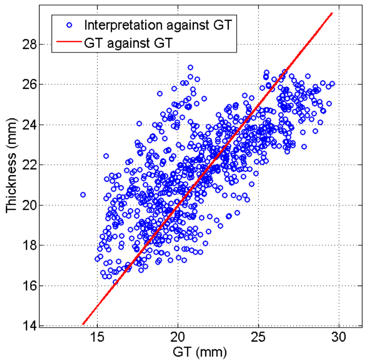

Figure A.16: Analytical approach; Section 8; variation of interpreted thickness along with GT.

Table A.8: Statistics of absolute error between interpreted pipe wall thickness and GT for Section 8.

Statistical Parameter	Value
RMS Error	2.38 mm
Mean Absolute Error	1.89 mm
Standard Deviation of Absolute Error	1.45 mm
Maximum Absolute Error	6.92 mm
Mean Percentage Accuracy	90.75%

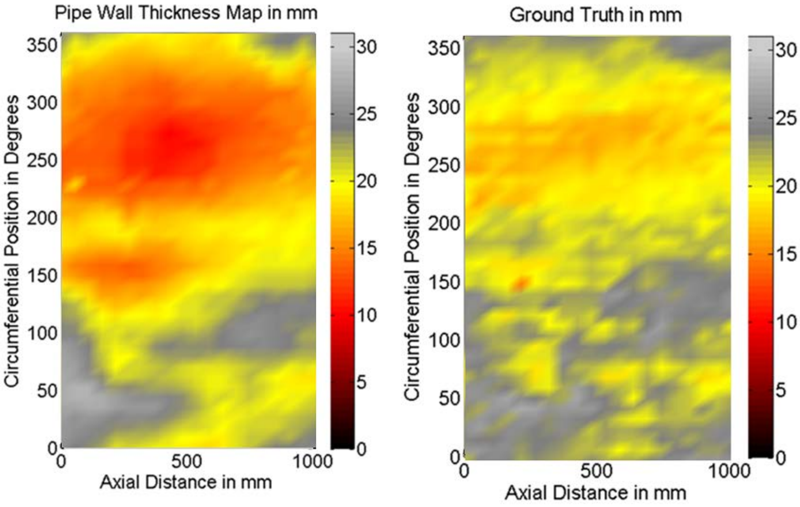

Figure A.17: Analytical approach; Section 9; interpreted thickness and GT maps.

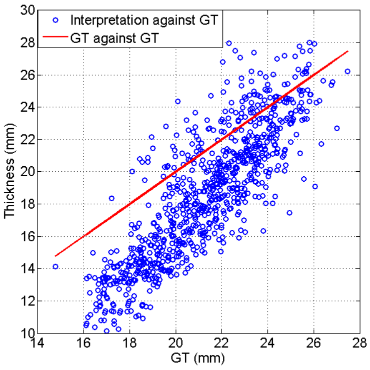

Figure A.18: Analytical approach; Section 9; variation of interpreted thickness along with GT.

TABLE A.9: Statistics of absolute error between interpreted pipe wall thickness and GT for Section 9.

Statistical Parameter	Value
RMS Error	3.546 mm
Mean Absolute Error	3.08 mm
Standard Deviation of Absolute Error	1.75 mm
Maximum Absolute Error	7.64 mm
Mean Percentage Accuracy	84.86%

Appendix B

Numerical and Probabilistic Approach: Interpreted Pipe Wall Thickness Maps and Error Statistics

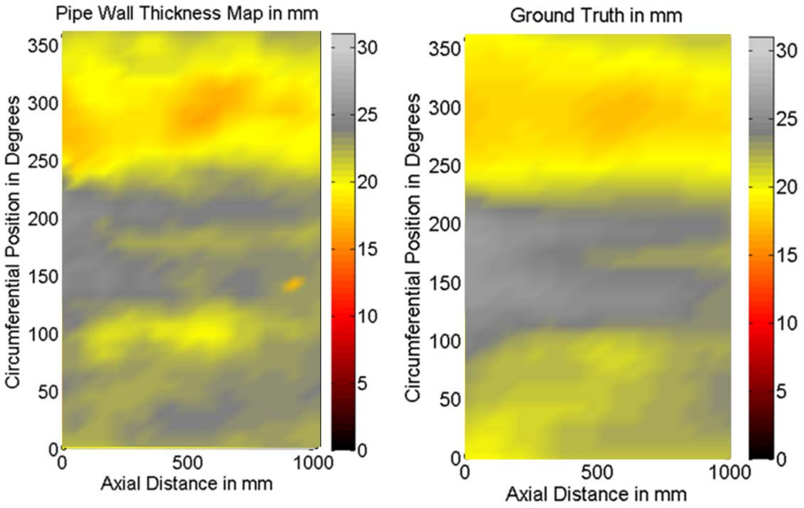

Figure B.1: Numerical and probabilistic approach; Section 1; interpreted thickness and GT maps.

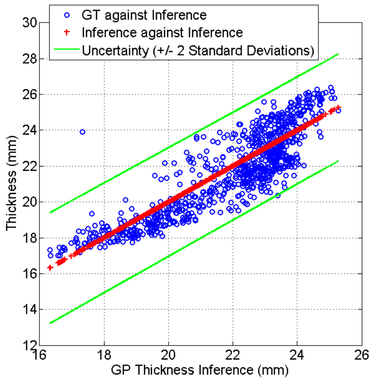

FIGURE B.2: Numerical and probabilistic approach; Section 1; variation of interpreted thickness along with GT.

TABLE B.1: Statistics of absolute error between interpreted pipe wall thickness and GT for Section 1.

Statistical Parameter	Value
RMS Error	1.11 mm
Mean Absolute Error	0.924 mm
Standard Deviation of Absolute Error	0.618 mm
Maximum Absolute Error	6.58 mm
Mean Percentage Accuracy	95.7%

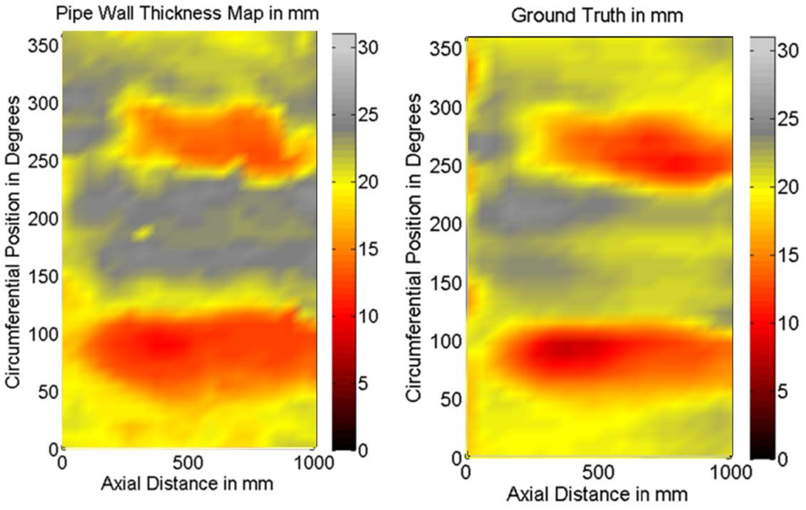

FIGURE B.3: Numerical and probabilistic approach; Section 2; interpreted thickness and GT maps.

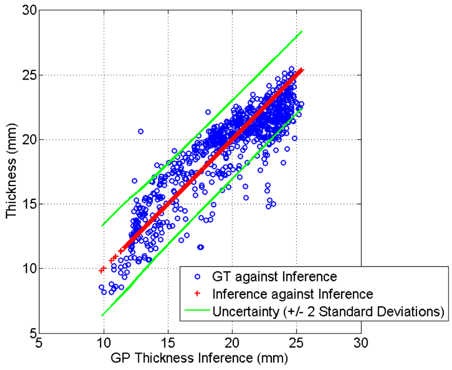

FIGURE B.4: Numerical and probabilistic approach; Section 2; variation of interpreted thickness along with GT.

TABLE B.2: Statistics of absolute error between interpreted pipe wall thickness and GT for Section 2.

Statistical Parameter	Value
RMS Error	1.796 mm
Mean Absolute Error	1.41 mm
Standard Deviation of Absolute Error	1.11 mm
Maximum Absolute Error	8.21 mm
Mean Percentage Accuracy	92.1%

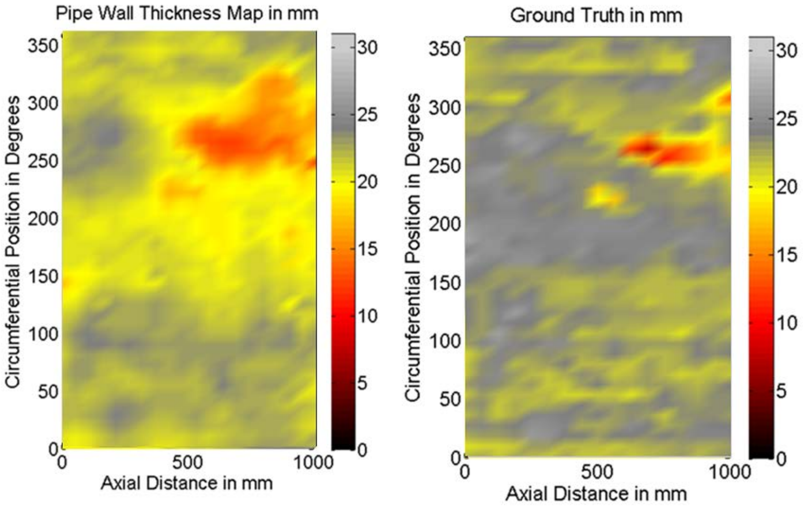

FIGURE B.5: Numerical and probabilistic approach; Section 3; interpreted thickness and GT maps.

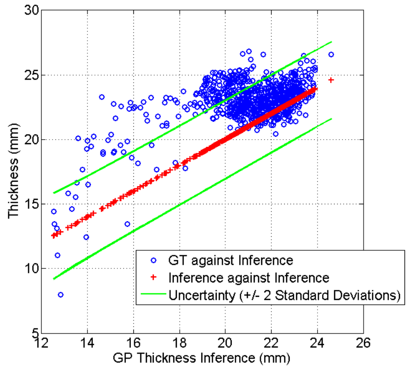

Figure B.6: Numerical and probabilistic approach; Section 3; variation of interpreted thickness along with GT.

Table B.3: Statistics of absolute error between interpreted pipe wall thickness and GT for Section 3.

Statistical Parameter	Value
RMS Error	2.64 mm
Mean Absolute Error	2.08 mm
Standard Deviation of Absolute Error	1.63 mm
Maximum Absolute Error	8.66 mm
Mean Percentage Accuracy	90.9%

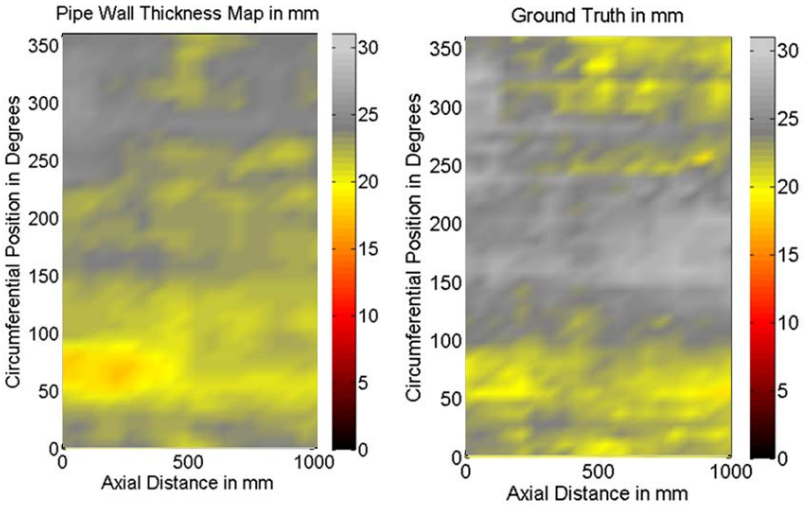

Figure B.7: Numerical and probabilistic approach; Section 4; interpreted thickness and GT maps.

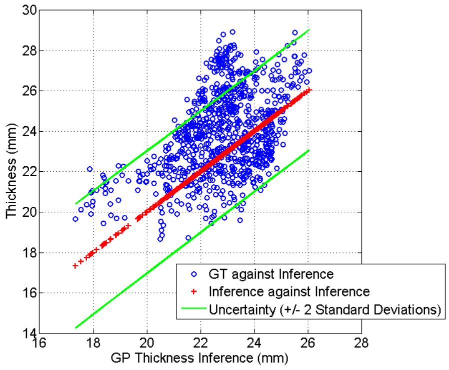

FIGURE B.8: Numerical and probabilistic approach; Section 4; variation of interpreted thickness along with GT.

TABLE B.4: Statistics of absolute error between interpreted pipe wall thickness and GT for Section 4.

Statistical Parameter	Value
RMS Error	2.25 mm
Mean Absolute Error	1.84 mm
Standard Deviation of Absolute Error	1.28 mm
Maximum Absolute Error	5.97 mm
Mean Percentage Accuracy	92.4%

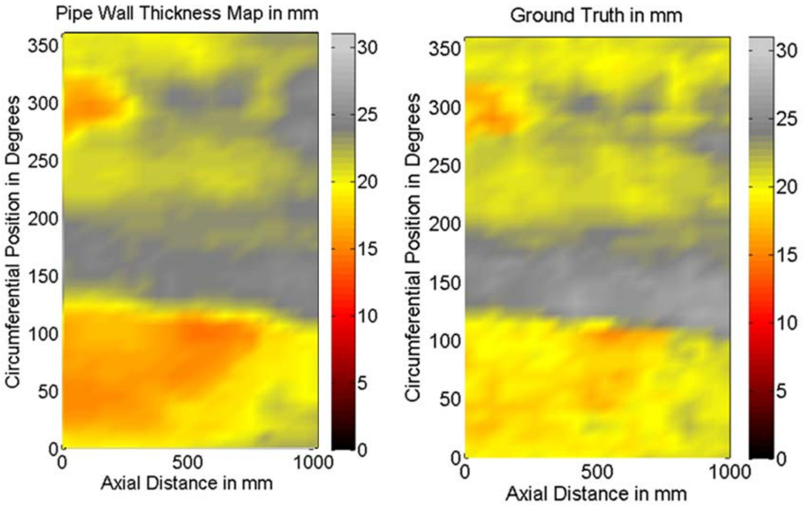

FIGURE B.9: Numerical and probabilistic approach; Section 5; interpreted thickness and GT maps.

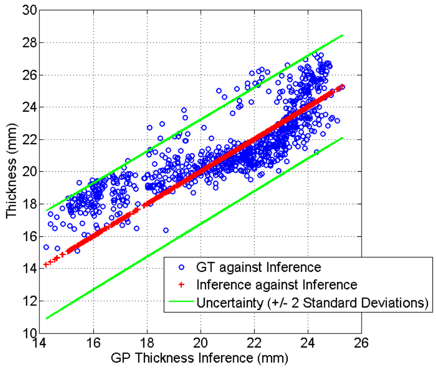

FIGURE B.10: Numerical and probabilistic approach; Section 5; variation of interpreted thickness along with GT.

TABLE B.5: Statistics of absolute error between interpreted pipe wall thickness and GT for Section 5.

Statistical Parameter	Value
RMS Error	1.59 mm
Mean Absolute Error	1.27 mm
Standard Deviation of Absolute Error	0.957 mm
Maximum Absolute Error	4.65 mm
Mean Percentage Accuracy	93.9%

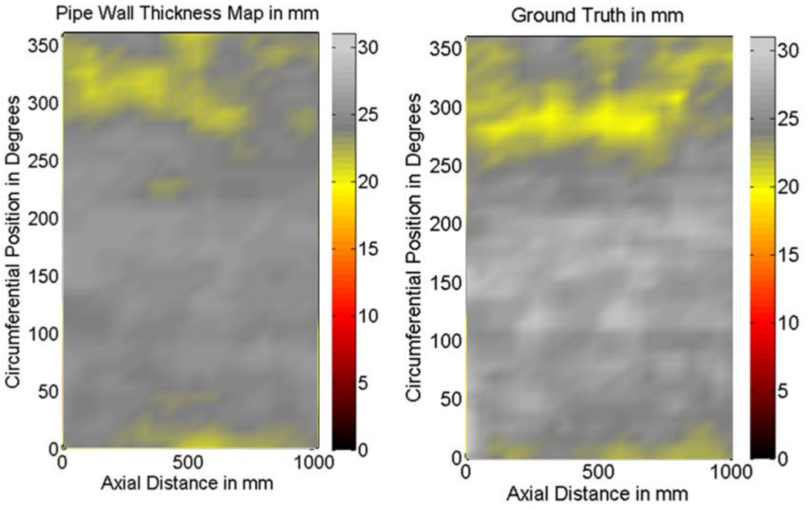

FIGURE B.11: Numerical and probabilistic approach; Section 6; interpreted thickness and GT maps.

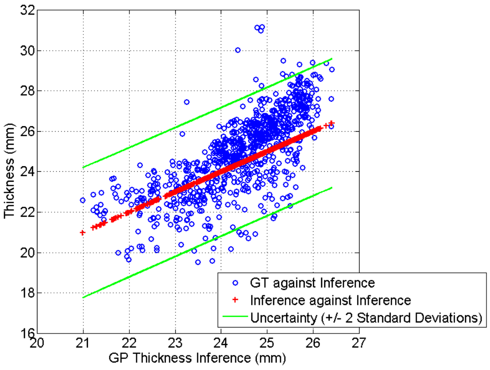

Figure B.12: Numerical and probabilistic approach; Section 6; variation of interpreted thickness along with GT.

Table B.6: Statistics of absolute error between interpreted pipe wall thickness and GT for Section 6.

Statistical Parameter	Value
RMS Error	1.51 mm
Mean Absolute Error	1.23 mm
Standard Deviation of Absolute Error	0.873 mm
Maximum Absolute Error	6.38 mm
Mean Percentage Accuracy	95.1%

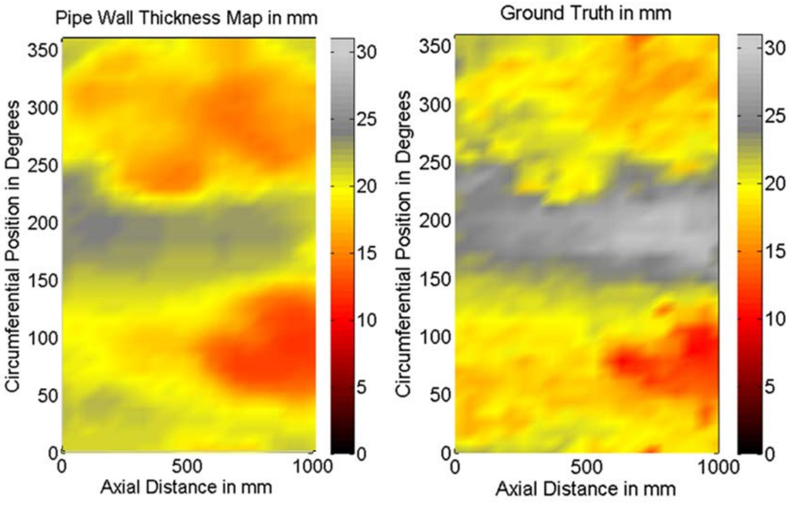

FIGURE B.13: Numerical and probabilistic approach; Section 7; interpreted thickness and GT maps.

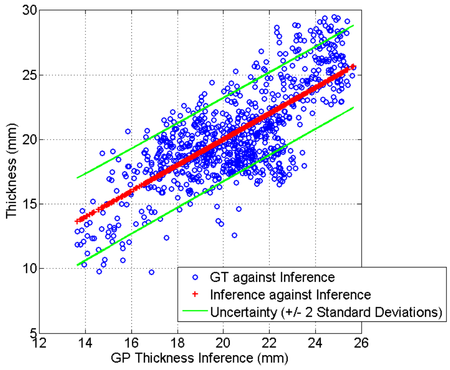

FIGURE B.14: Numerical and probabilistic approach; Section 7; variation of interpreted thickness along with GT.

Table B.7: Statistics of absolute error between interpreted pipe wall thickness and GT for Section 7.

Statistical Parameter	Value
RMS Error	2.42 mm
Mean Absolute Error	1.94 mm
Standard Deviation of Absolute Error	1.45 mm
Maximum Absolute Error	7.90 mm
Mean Percentage Accuracy	89.98%

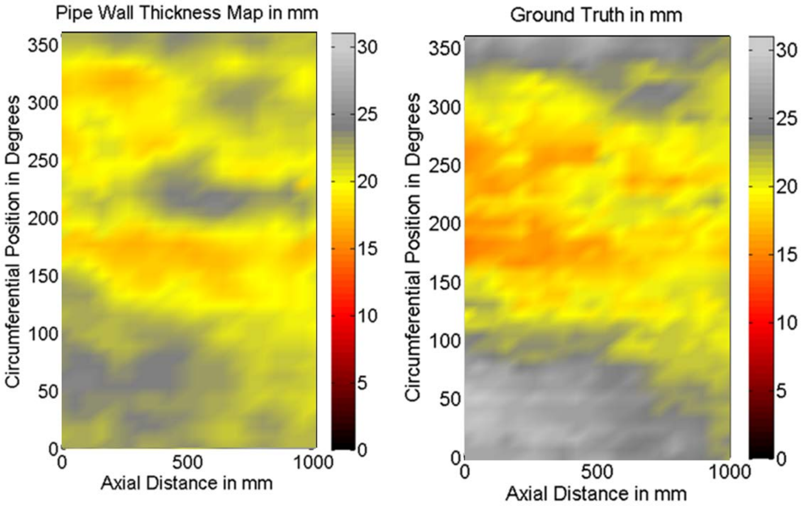

Figure B.15: Numerical and probabilistic approach; Section 8; interpreted thickness and GT maps.

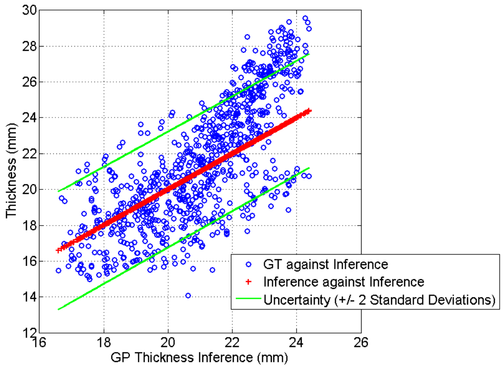

Figure B.16: Numerical and probabilistic approach; Section 8; variation of interpreted thickness along with GT.

Table B.8: Statistics of absolute error between interpreted pipe wall thickness and GT for Section 8.

Statistical Parameter	Value
RMS Error	2.42 mm
Mean Absolute Error	1.99 mm
Standard Deviation of Absolute Error	1.38 mm
Maximum Absolute Error	6.53 mm
Mean Percentage Accuracy	90.8%

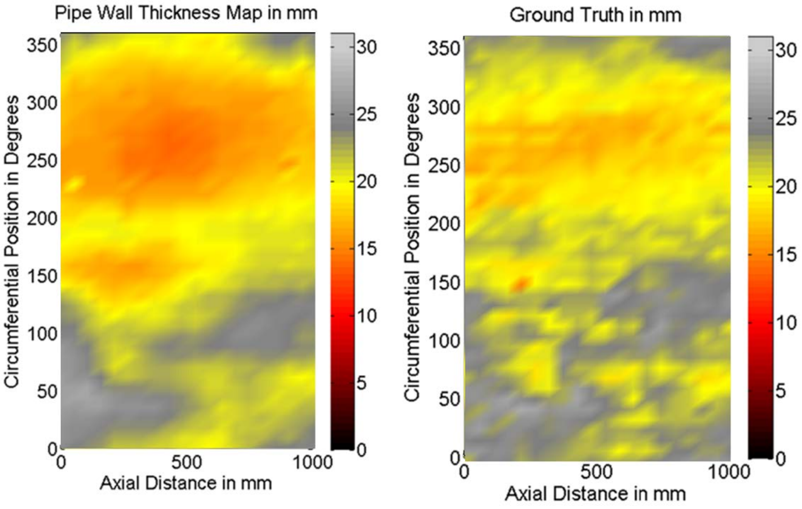

Figure B.17: Numerical and probabilistic approach; Section 9; interpreted thickness and GT maps.

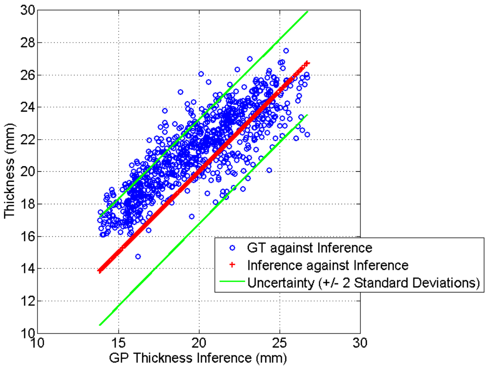

Figure B.18: Numerical and probabilistic approach; Section 9; variation of interpreted thickness along with GT.

Table B.9: Statistics of absolute error between interpreted pipe wall thickness and GT for Section 9.

Statistical Parameter	Value
RMS Error	2.22 mm
Mean Absolute Error	1.91 mm
Standard Deviation of Absolute Error	1.14 mm
Maximum Absolute Error	6.07 mm
Mean Percentage Accuracy	90.8%

Appendix C

On Site Pipe Scanning Protocol

Fig C.1 shows how the plastic grid is wrapped around the pipe and how the sensor is aligned. The grid is wrapped in such a way that the squares are aligned with the axis of the pipe and the sensor is placed in such a way that the long sides are parallel to the pipe axis.

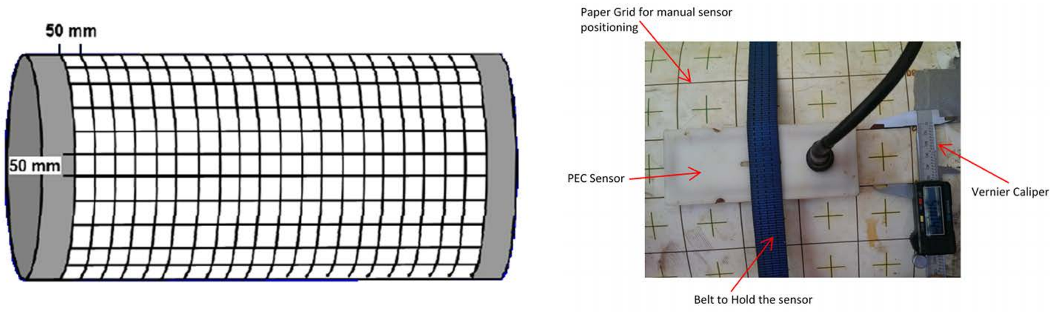

(a) (b)

Figure C.1: Placement of the grid and the sensor: (a) Grid wrapped around the pipe; (b) Sensor alignment.

Fig. C.2 shows how the axial (denoted as x-axis in Fig. C.2) and circumferential (denoted as y-axis in Fig. C.2) directions of 2.5D thickness maps are located on a pipe.

Scanning procedure: First the gird and the sensor are aligned on the pipe as shown in Fig. C.1. Scans are performed by coinciding the sensor's center with the centers of grid squares, *i.e.*, two adjacent scans are parted by a distance of 50 mm. Distance along the axial direction (x) is marked in mm on the 2.5D thickness map whereas the distance along

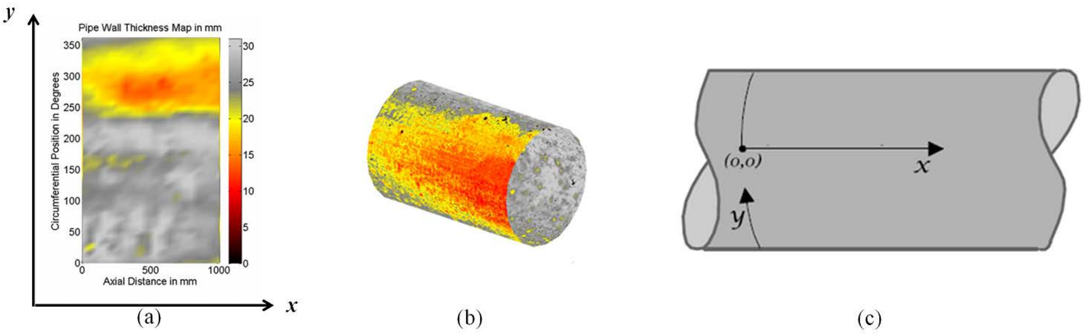

(a) (b) (c)

FIGURE C.2: How axial and circumferential directions of 2.5D thickness maps are located on a pipe: (a) Directions denoted on a 2.5D thickness map; (b) A rolled thickness map resembling a pipe; (c) How axial (x) and circumferential (y) directions appear on a pipe.

the circumferential direction (y) is marked as an angle θ in degrees given by $\theta = \dfrac{d_y}{\pi r} \times 180^0$ where d_y is a distance along the circumferential direction measured from a reference and r is the radius of the pipe. The units of both d_y and r should be the same.

Aligning PEC scans with the ground truth for validation was done with the aid of manually drilled calibration pits which have fixed dimensions, and relative locations with respect to the origin (0, 0).

Appendix D

Steps for Deriving the Eddy Current Diffusion Time Constant

Starting from Ampere's law for the quasi-static case we have

$$\nabla \times \vec{H} = \vec{J} \tag{D.1}$$

in usual notation. By performing the vector operation $\nabla \times (\nabla \times \vec{H}) = \nabla(\nabla.\vec{H}) - \nabla^2\vec{H}$ on Eq. D.1 and applying the Coulomb gauge $\nabla.\vec{H} = 0$ we get

$$\nabla^2\vec{H} = -\nabla \times \vec{J}. \tag{D.2}$$

By substituting the constitutive relationship $\vec{J} = \sigma\vec{E}$ and Faraday's law $\nabla \times \vec{E} = -\dfrac{\partial \vec{B}}{\partial t}$ in Eq. D.2; and subsequently substituting the constitutive relationship $\vec{B} = \mu\vec{H}$ in the resulting equation we get the Magnetic field Diffusion equation:

$$\nabla^2\vec{H} = \mu\sigma\frac{\partial \vec{H}}{\partial t}. \tag{D.3}$$

Solving Eq. D.3 withing a large flat conducting ferromagnetic plate associated with the PEC sensor setup dealt with in this thesis (excited with a step function, *i.e.*, pulsed excitation) yields $\vec{H}$ withing the plate and eddy currents can hence be calculated using Ampere's law.

After performing much work to solve Eq. D.3 for a conducting half-space and by extending the solution to a plate of finite thickness d as done in [127], the solution for $\vec{H}$ at any point within the plate becomes an infinite summation of exponential decays of time whose time constants τ_n are given by

$$\tau_n = \frac{\mu\sigma d^2}{n^2\pi^2} \tag{D.4}$$

where $n \in \mathbb{Z}^+$, n may take odd integer values only depending on boundary conditions. From Eq. D.4, we can easily understand that τ_n decreases with increasing n and the dominant time constant will therefore be τ_1 given by

$$\tau_1 = \frac{\mu\sigma d^2}{\pi^2}. \tag{D.5}$$

Therefore, c_1 in Chapter 3 is equal to $\dfrac{\pi^2}{\mu\sigma d^2}$ since $c_i = \dfrac{1}{\tau_1}$.

Bibliography

[1] J. García-Martín, J. Gómez-Gil, and E. Vázquez-Sánchez, "Non-destructive techniques based on eddy current testing," *Sensors*, vol. 11, no. 3, pp. 2525–2565, 2011.

[2] C. Huang, W. Xinjun, X. Zhiyuan, and Y. Kang, "Pulsed eddy current signal processing method for signal denoising in ferromagnetic plate testing," *NDT & E International*, vol. 43, no. 7, pp. 648–653, 2010.

[3] C. Huang and X. Wu, "An improved ferromagnetic material pulsed eddy current testing signal processing method based on numerical cumulative integration," *NDT & E International*, vol. 69, pp. 35–39, 2015.

[4] C. Huang, X. Wu, Z. Xu, and Y. Kang, "Ferromagnetic material pulsed eddy current testing signal modeling by equivalent multiple-coil-coupling approach," *NDT & E International*, vol. 44, no. 2, pp. 163–168, 2011.

[5] J. Rudd and M. Roubal, "Broadband electro-magnetic technique for advanced condition assessment and pipe failure prediction of water infrastructure," in *Ozwater Conference, 2014. http://www.awa.asn.au/htmlemails/Ozwater14/pdf/natozw14Final00366.pdf, last access date: 11/01/2015.*

[6] N. Ulapane, A. Alempijevic, T. Vidal-Calleja, J. V. Miro, J. Rudd, and M. Roubal, "Gaussian process for interpreting pulsed eddy current signals for ferromagnetic pipe profiling," in *Industrial Electronics and Applications (ICIEA), 2014 IEEE 9th Conference on*, pp. 1762–1767, IEEE, 2014.

[7] K. L. Rens, T. J. Wipf, and F. W. Klaiber, “Review of nondestructive evaluation techniques of civil infrastructure,” *Journal of performance of constructed facilities*, vol. 11, no. 4, pp. 152–160, 1997.

[8] R. B. Petersen and R. E. Melchers, “Long-term corrosion of cast iron cement lined pipes,” *Corrosion and Prevention*, pp. 11–14, 2012.

[9] J. V. Miro, J. Rajalingam, T. Vidal-Calleja, F. de Bruijn, R. Wood, D. Vitanage, N. Ulapane, B. Wijerathna, and D. Su, “A live test-bed for the advancement of condition assessment and failure prediction research on critical pipes,” *Water Asset Management International, ISSN Print: 1814-5434, ISSN Online: 1814-5442*, vol. 10, no. 2, pp. 03–08, 2014.

[10] D. Vitanage, J. Kodikara, and G. Allen, “Collaborative research on condition assessment and pipe failure prediction for critical water mains,” *Water Asset Management International*, vol. 10, pp. 15–18, 2014.

[11] R. Petersen, M. Dafter, and R. Melchers, “Long-term corrosion of buried cast iron water mains: field data collection and model calibration,” *Water Asset Management International*, vol. 9, pp. 13–17, 2013.

[12] Z. Liu and Y. Kleiner, “State of the art review of inspection technologies for condition assessment of water pipes,” *Measurement*, vol. 46, no. 1, pp. 1–15, 2013.

[13] W. Cheng, “Pulsed eddy current testing of carbon steel pipes wall-thinning through insulation and cladding,” *Journal of Nondestructive Evaluation*, vol. 31, no. 3, pp. 215–224, 2012.

[14] Z. Xu, X. Wu, J. Li, and Y. Kang, “Assessment of wall thinning in insulated ferromagnetic pipes using the time-to-peak of differential pulsed eddy-current testing signals,” *NDT & E International*, vol. 51, pp. 24–29, 2012.

[15] J. R. Davis, “ASM specialty handbook: cast irons,” *ASM International*, vol. 124, pp. 433–435, 1996.

[16] J.-M. Jin, *The finite element method in electromagnetics.* John Wiley & Sons, 2014.

[17] B. A. Szabo and I. Babuška, *Finite element analysis.* John Wiley & Sons, 1991.

[18] C. E. Rasmussen and C. K. I. Williams, "Gaussian processes for machine learning," *The MIT Press, 2006, ISBN: 0-262-18253-X*, 2006.

[19] N. Ulapane, A. Alempijevic, and V.-C. T. Miro, Jaime Valls, "Nondestructive evaluation of ferromagnetic material thickness using pulsed eddy current sensor detector coil voltage decay rate," *NDT & E International*, 2015. Under Review.

[20] D. Vasic, V. Bilas, and D. Ambrus, "Pulsed eddy-current nondestructive testing of ferromagnetic tubes," *Instrumentation and Measurement, IEEE Transactions on*, vol. 53, no. 4, pp. 1289–1294, 2004.

[21] H. Hashizume, Y. Yamada, K. Miya, S. Toda, K. Morimoto, Y. Araki, K. Satake, and N. Shimizu, "Numerical and experimental analysis of eddy current testing for a tube with cracks," *Magnetics, IEEE Transactions on*, vol. 28, no. 2, pp. 1469–1472, 1992.

[22] C. V. Dodd and W. E. Deeds, "Analytical solutions to eddy-current probe-coil problems," *Journal of applied physics*, vol. 39, no. 6, pp. 2829–2838, 1968.

[23] S. Sharma, "Application of finite element models to eddy current probe design for aircraft inspection," 1998. Doctoral Thesis, Digital Repository, Iowa State University, http://lib. dr. iastate. edu/.

[24] F. Thollon, B. Lebrun, N. Burais, and Y. Jayet, "Numerical and experimental study of eddy current probes in ndt of structures with deep flaws," *NDT & E International*, vol. 28, no. 2, pp. 97–102, 1995.

[25] J. R. Bowler, Y. Yoshida, and N. Harfield, "Vector-potential boundary-integral evaluation of eddy-current interaction with a crack," *Magnetics, IEEE Transactions on*, vol. 33, no. 5, pp. 4287–4294, 1997.

[26] J. H. Rose, E. Uzal, and J. C. Moulder, "Magnetic permeability and eddy-current measurements," in *Review of progress in quantitative nondestructive evaluation*, pp. 315–322, Springer, 1995.

[27] A. Pirani, M. Ricci, R. Specogna, A. Tamburrino, and F. Trevisan, “Multi-frequency identification of defects in conducting media,” *Inverse Problems*, vol. 24, no. 3, p. 035011, 2008.

[28] W. Yin and A. J. Peyton, “Thickness measurement of non-magnetic plates using multi-frequency eddy current sensors,” *NDT & E International*, vol. 40, no. 1, pp. 43–48, 2007.

[29] Y. Le Diraison, P.-Y. Joubert, and D. Placko, “Characterization of subsurface defects in aeronautical riveted lap-joints using multi-frequency eddy current imaging,” *NDT & E International*, vol. 42, no. 2, pp. 133–140, 2009.

[30] X. Chen and Y. Lei, “Excitation current waveform for eddy current testing on the thickness of ferromagnetic plates,” *NDT & E International*, vol. 66, pp. 28–33, 2014.

[31] X. Chen and Y. Lei, “Time-domain analytical solutions to pulsed eddy current field excited by a probe coil outside a conducting ferromagnetic pipe,” *NDT & E International, 2014*, 2014.

[32] A. Sophian, G. Y. Tian, D. Taylor, and J. Rudlin, “Flaw detection and quantification for ferromagnetic steels using pulsed eddy current techniques and magnetization,” *Transactions on Engineering Sciences*, vol. 44, pp. 381–390, 2003.

[33] D. G. Park, C. S. Angani, G. D. Kim, C. G. Kim, and Y. M. Cheong, “Evaluation of pulsed eddy current response and detection of the thickness variation in the stainless steel,” *Magnetics, IEEE Transactions on*, vol. 45, no. 10, pp. 3893–3896, 2009.

[34] C. Waters, “Rdt-incotest® for the detection of corrosion under insulation,” *NON DESTRUCTIVE TESTING AUSTRALIA*, vol. 36, no. 5, pp. 124–129, 1999.

[35] V. O. De Haan and P. J. de Jong, “Simultaneous measurement of material properties and thickness of carbon steel plates using pulsed eddy currents,” in *16th Word Conference on Non-Destructive Testing in Montreal*, 2004.

[36] Y. Li, G. Y. Tian, and A. Simm, “Fast analytical modelling for pulsed eddy current evaluation,” *NDT & E International*, vol. 41, no. 6, pp. 477–483, 2008.

[37] A. Sophian, G. Y. Tian, D. Taylor, and J. Rudlin, "Design of a pulsed eddy current sensor for detection of defects in aircraft lap-joints," *Sensors and Actuators A: Physical*, vol. 101, no. 1, pp. 92–98, 2002.

[38] G. Y. Tian and A. Sophian, "Reduction of lift-off effects for pulsed eddy current ndt," *NDT & E International*, vol. 38, no. 4, pp. 319–324, 2005.

[39] G. Y. Tian, Y. Li, and C. Mandache, "Study of lift-off invariance for pulsed eddy-current signals," *Magnetics, IEEE Transactions on*, vol. 45, no. 1, pp. 184–191, 2009.

[40] A. Sophian, "Characterisation of surface and sub-surface discontinuities in metals using pulsed eddy current sensors," 2003. Doctoral thesis, University of Huddersfield, http://eprints.hud.ac.uk/6916/.

[41] J. Huijsing, *Operational amplifiers: theory and design.* Springer Science & Business Media, 2011.

[42] T. Kugesstadt, "Active filter design techniques. texas instruments."

[43] S. Niewiadomski, *Filter handbook: a practical design guide.* Newnes, 1989.

[44] C. Kitchin and L. Counts, *A designer's guide to instrumentation amplifiers.* Analog Devices, 2006.

[45] T. Deliyannis, Y. Sun, and J. K. Fidler, *Continuous-time active filter design.* Crc Press, 2010.

[46] M. D. Lutovac, D. V. Tošić, and B. L. Evans, *Filter design for signal processing using MATLAB and Mathematica.* Miroslav Lutovac, 2001.

[47] F. Xuan, L. Cai, Y. Baojun, L. Zhe, Z. Fengqin, and L. Yang, "The impacts of median filter to the phases and shapes of signals," *GEOPHYSICAL PROSPECTING FOR PETROLEUM*, vol. 41, no. 1, pp. 37–41, 2002.

[48] C. S. Angani, D. G. Park, G. D. Kim, C. G. Kim, and Y. M. Cheong, "Differential pulsed eddy current sensor for the detection of wall thinning in an insulated stainless steel pipe," *Journal of Applied Physics*, vol. 107, no. 9, p. 09E720, 2010.

[49] Y. He, M. Pan, F. Luo, and G. Y. Tian, "Pulsed eddy current imaging and frequency spectrum analysis for hidden defect nondestructive testing and evaluation," *NDT & E International*, vol. 44, no. 4, pp. 344–352, 2011.

[50] A. Sophian, G. Y. Tian, D. Taylor, and J. Rudlin, "A feature extraction technique based on principal component analysis for pulsed eddy current ndt," *NDT & E International*, vol. 36, no. 1, pp. 37–41, 2003.

[51] G. Y. Tian, A. Sophian, D. Taylor, and J. Rudlin, "Multiple sensors on pulsed eddy-current detection for 3-d subsurface crack assessment," *IEEE Sensors Journal*, vol. 5, no. 1, pp. 90–96, 2005.

[52] D. Chen, Q. Ji, H. Zhang, and L. Zhao, "Application of pulsed eddy current in plate thickness evaluation," in *Proceedings of the 4th IEEE Conference on Industrial Electronics and Applications, IEEE ICIEA*, pp. 3286–3288, IEEE, 2009.

[53] M. Fan, P. Huang, B. Ye, D. Hou, G. Zhang, and Z. Zhou, "Analytical modeling for transient probe response in pulsed eddy current testing," *NDT & E International*, vol. 42, no. 5, pp. 376–383, 2009.

[54] V. O. De Haan and P. A. De Jong, "Analytical expressions for transient induction voltage in a receiving coil due to a coaxial transmitting coil over a conducting plate," *IEEE Transactions on Magnetics*, vol. 40, no. 2, pp. 371–378, 2004.

[55] S. Boyd and L. Vandenberghe, *Convex optimization.* Cambridge university press, 2004.

[56] A. W. Roberts and D. E. Varberg, *Convex functions.* Elsevier, 1973.

[57] R. R. Phelps, *Convex functions, monotone operators and differentiability.* Springer-Vlg, 1989.

[58] "Engineering information - cast iron pipe data." A data sheet from Mueller Co., REV 4-99.

[59] "Materials specification 1 for ductile iron pipe." Denver Water, Engineering Standards 14th Edition, March 2012.

[60] "Atlas tech note no. 12, pipe dimensions." Atlas Steels, January 2011.

[61] G. Golub, "Numerical methods for solving linear least squares problems," *Numerische Mathematik*, vol. 7, no. 3, pp. 206–216, 1965.

[62] C. Multiphysics, "Comsol multiphysics user guide (version 4.3 a)," *COMSOL, AB*, 2012.

[63] "Physical property measurement system." AC Measurement System (ACMS) Option Users Manual, Quantum Design, Part Number 1084-100 C-1.

[64] "Ppms, physical property measurement system." Quantum Design, 1070-002, Rev. A0.

[65] B. Skinner, J. Vidal-Calleja, Teresa amd Valls Miro, F. De Bruijn, and R. Falque, "3D point cloud upsampling for accurate reconstruction of dense 2.5D thickness maps," in *Proceedings of the Australasian Conference on Robotics and Automation 2014 (ACRA 2014)*, (Melbourne, Australia), pp. 1–7, Australian Robotics and Automation Association Inc., 2014.

[66] T. Vidal-Calleja, D. Su, F. De Bruijn, and J. V. Miro, "Learning spatial correlations for bayesian fusion in pipe thickness mapping," in *Robotics and Automation (ICRA), 2014 IEEE International Conference on*, pp. 683–690, IEEE, 2014.

[67] J. R. Bowler, "Eddy-current interaction with an ideal crack. i. the forward problem," *Journal of Applied Physics*, vol. 75, no. 12, pp. 8128–8137, 1994.

[68] A. L. Ribeiro, H. G. Ramos, and O. Postolache, "A simple forward direct problem solver for eddy current non-destructive inspection of aluminum plates using uniform field probes," *Measurement*, vol. 45, no. 2, pp. 213–217, 2012.

[69] Z. Chen and K. Miya, "Ect inversion using a knowledge-based forward solver," *Journal of nondestructive evaluation*, vol. 17, no. 3, pp. 167–175, 1998.

[70] S. J. Norton and J. R. Bowler, "Theory of eddy current inversion," *Journal of applied physics*, vol. 73, no. 2, pp. 501–512, 1993.

[71] J. R. Bowler, S. J. Norton, and D. J. Harrison, "Eddy-current interaction with an ideal crack. ii. the inverse problem," *Journal of applied physics*, vol. 75, no. 12, pp. 8138–8144, 1994.

[72] M. Soleimani, W. R. B. Lionheart, A. J. Peyton, X. Ma, and S. R. Higson, "A three-dimensional inverse finite-element method applied to experimental eddy-current imaging data," *Magnetics, IEEE Transactions on*, vol. 42, no. 5, pp. 1560–1567, 2006.

[73] Y. S. Tarng, S. C. Ma, and L. K. Chung, "Determination of optimal cutting parameters in wire electrical discharge machining," *International Journal of Machine Tools and Manufacture*, vol. 35, no. 12, pp. 1693–1701, 1995.

[74] D. F. Dauw, H. Sthioul, R. Delpretti, and C. Tricarico, "Wire analysis and control for precision edm cutting," *CIRP Annals-Manufacturing Technology*, vol. 38, no. 1, pp. 191–194, 1989.

[75] J. C. Lashley, M. F. Hundley, A. Migliori, J. L. Sarrao, P. G. Pagliuso, T. W. Darling, M. Jaime, J. C. Cooley, W. L. Hults, L. Morales, *et al.*, "Critical examination of heat capacity measurements made on a quantum design physical property measurement system," *Cryogenics*, vol. 43, no. 6, pp. 369–378, 2003.

[76] Q. Shi, C. L. Snow, J. Boerio-Goates, and B. F. Woodfield, "Accurate heat capacity measurements on powdered samples using a quantum design physical property measurement system," *The Journal of Chemical Thermodynamics*, vol. 42, no. 9, pp. 1107–1115, 2010.

[77] J. Olivier, B. Servet, M. Vergnolle, M. Mosca, and G. Garry, "Stability/instability of conductivity and work function changes of ito thin films, uv-irradiated in air or vacuum: Measurements by the four-probe method and by kelvin force microscopy," *Synthetic Metals*, vol. 122, no. 1, pp. 87–89, 2001.

[78] T. Kanagawa, R. Hobara, I. Matsuda, T. Tanikawa, A. Natori, and S. Hasegawa, "Anisotropy in conductance of a quasi-one-dimensional metallic surface state measured by a square micro-four-point probe method," *Physical review letters*, vol. 91, no. 3, p. 036805, 2003.

[79] V. Desnica, K. Škarić, D. Jembrih-Simbuerger, S. Fazinić, M. Jakšić, D. Mudronja, M. Pavličić, I. Peranić, and M. Schreiner, "Portable xrf as a valuable device for preliminary in situ pigment investigation of wooden inventory in the trski vrh church in croatia," *Applied Physics A*, vol. 92, no. 1, pp. 19–23, 2008.

[80] E. Frahm, "An evaluation of portable x-ray fluorescence for artifact sourcing in the field: can a handheld device differentiate anatolian obsidian sources," in *119th Annual Meeting of The Geological Society of America, Denver*, 2007.

[81] L. Solymar, D. Walsh, and R. R. A. Syms, *Electrical properties of materials.* Oxford University Press, 2014.

[82] G. Marom, S. Fischer, F. R. Tuler, and H. D. Wagner, "Hybrid effects in composites: conditions for positive or negative effects versus rule-of-mixtures behaviour," *Journal of Materials Science*, vol. 13, no. 7, pp. 1419–1426, 1978.

[83] H. S. Kim, "On the rule of mixtures for the hardness of particle reinforced composites," *Materials Science and Engineering: A*, vol. 289, no. 1, pp. 30–33, 2000.

[84] R. W. Pryor, *Multiphysics Modeling Using COMSOL: A First Principles Approach.* Jones & Bartlett Publishers, 2011.

[85] T. Morisue, "Magnetic vector potential and electric scalar potential in three-dimensional eddy current problem," *Magnetics, IEEE Transactions on*, vol. 18, no. 2, pp. 531–535, 1982.

[86] O. Biro and K. Preis, "On the use of the magnetic vector potential in the finite-element analysis of three-dimensional eddy currents," *Magnetics, IEEE Transactions on*, vol. 25, no. 4, pp. 3145–3159, 1989.

[87] P. Dular, J. Gyselinck, C. Geuzaine, N. Sadowski, and J. P. A. Bastos, "A 3-d magnetic vector potential formulation taking eddy currents in lamination stacks into account," *Magnetics, IEEE Transactions on*, vol. 39, no. 3, pp. 1424–1427, 2003.

[88] R. C. Degeneff, M. R. Gutierrez, S. J. Salon, D. W. Burow, and R. J. Nevins, "Kron's reduction method applied to the time stepping finite element analysis of induction

machines," *Energy Conversion, IEEE Transactions on*, vol. 10, no. 4, pp. 669–674, 1995.

[89] R.-f. Liu, D.-J. Yan, and M.-q. Hu, "Field circuit and movement coupled time stepping finite element analysis on permanent magnet brushless dc motors," in *Zhongguo Dianji Gongcheng Xuebao(Proceedings of the Chinese Society of Electrical Engineering)*, vol. 27, pp. 59–64, 2007.

[90] N. Ida, *Numerical modeling for electromagnetic non-destructive evaluation*, vol. 1. Springer Science & Business Media, 1995.

[91] P. Monk, *Finite element methods for Maxwell's equations.* Oxford University Press, 2003.

[92] A. Taflove and S. C. Hagness, *Computational electrodynamics.* Artech house, 2005.

[93] D. J. Griffiths and R. College, *Introduction to electrodynamics*, vol. 3. prentice Hall Upper Saddle River, NJ, 1999.

[94] C. A. Sawicki, "A dynamic demonstration of lenz's law," *The Physics Teacher*, vol. 35, no. 1, pp. 47–49, 1997.

[95] M. K. Roy, M. K. Harbola, and H. C. Verma, "Demonstration of lenz's law: Analysis of a magnet falling through a conducting tube," *American Journal of Physics*, vol. 75, no. 8, pp. 728–730, 2007.

[96] J. B. Bronzan, "The magnetic scalar potential," *American Journal of Physics*, vol. 39, pp. 1357–1359, 1971.

[97] R. D. Pillsbury Jr, "A three dimensional eddy current formulation using two potentials: The magnetic vector potential and total magnetic scalar potential," *Magnetics, IEEE Transactions on*, vol. 19, no. 6, pp. 2284–2287, 1983.

[98] O. Bíró, K. Preis, G. Buchgraber, and I. Ticar, "Voltage-driven coils in finite-element formulations using a current vector and a magnetic scalar potential," *IEEE transactions on magnetics*, vol. 40, no. 2, pp. 1286–1289, 2004.

[99] J. E. Marsden and A. Tromba, *Vector calculus.* Macmillan, 2003.

[100] H. Lass, *Vector and tensor analysis.* 1950.

[101] H. M. Schey, "Div, grad, curl, and all that: an informal text on vector calculus," *AMC*, vol. 10, p. 12, 1997.

[102] K.-J. Bathe and E. L. Wilson, "Numerical methods in finite element analysis," 1976.

[103] C. W. Steele, *Numerical computation of electric and magnetic fields.* Springer Science & Business Media, 2012.

[104] M. V. K. Chari, "Finite-element solution of the eddy-current problem in magnetic structures," *Power Apparatus and Systems, IEEE Transactions on*, no. 1, pp. 62–72, 1974.

[105] I. Z. Abidin, G. Y. Tian, J. Wilson, S. Yang, and D. Almond, "Quantitative evaluation of angular defects by pulsed eddy current thermography," *NDT & E International*, vol. 43, no. 7, pp. 537–546, 2010.

[106] S. Moaveni, *Finite element analysis: theory and application with ANSYS.* Pearson Education India, 2003.

[107] P. C. Rem, P. A. Leest, and A. J. Van den Akker, "A model for eddy current separation," *International journal of mineral processing*, vol. 49, no. 3, pp. 193–200, 1997.

[108] H. W. Liu, S. P. Zhan, Y. H. Du, and P. Zhang, "Study on pulsed eddy current nondestructive testing technology for pipeline corrosion defects based on finite element method," in *Applied Mechanics and Materials*, vol. 120, pp. 36–41, Trans Tech Publ, 2012.

[109] C. Gilles-Pascaud, G. Pichenot, D. Premel, C. Reboud, and A. Skarlatos, "Modelling of eddy current inspections with civa," in *proceedings of the 17th World Conference on Nondestructive Testing, Shanghai, edited on CD-ROM*, vol. 11, 2008.

[110] C. Reboud, G. Pichenot, D. Premel, and R. Raillon, "2008 ect benchmark results: Modeling with civa of 3d flaws responses in planar and cylindrical work pieces," *Proceedings of the 35th Annual Review of Progress in Quantitative Nondestructive Evaluation*, pp. 1915–1921, 2008.

[111] F. Vacher, F. Alves, and C. Gilles-Pascaud, "Eddy current nondestructive testing with giant magneto-impedance sensor," *NDT & E International*, vol. 40, no. 6, pp. 439–442, 2007.

[112] D. C. Giancoli, *Physics for scientists and engineers with modern physics.* Pearson Education, 2008.

[113] W. Steinhögl, G. Schindler, G. Steinlesberger, M. Traving, and M. Engelhardt, "Comprehensive study of the resistivity of copper wires with lateral dimensions of 100 nm and smaller," *Journal of Applied Physics*, vol. 97, no. 2, p. 023706, 2005.

[114] R. J. Allemang and D. L. Brown, "A correlation coefficient for modal vector analysis," in *Proceedings of the 1st international modal analysis conference*, vol. 1, pp. 110–116, SEM, Orlando, 1982.

[115] J. Lee Rodgers and W. A. Nicewander, "Thirteen ways to look at the correlation coefficient," *The American Statistician*, vol. 42, no. 1, pp. 59–66, 1988.

[116] R. Taylor, "Interpretation of the correlation coefficient: a basic review," *Journal of diagnostic medical sonography*, vol. 6, no. 1, pp. 35–39, 1990.

[117] C. E. Rasmussen, "Gaussian processes in machine learning," in *Advanced lectures on machine learning*, pp. 63–71, Springer, 2004.

[118] M. Seeger, "Gaussian processes for machine learning," *International Journal of Neural Systems*, vol. 14, no. 02, pp. 69–106, 2004.

[119] N. N. B. Ulapane and S. G. Abeyratne, "Gaussian process for learning solar panel maximum power point characteristics as functions of environmental conditions," in *Industrial Electronics and Applications (ICIEA), 2014 IEEE 9th Conference on*, pp. 1756–1761, IEEE, 2014.

[120] R. Fletcher and C. M. Reeves, "Function minimization by conjugate gradients," *The computer journal*, vol. 7, no. 2, pp. 149–154, 1964.

[121] M. R. Hestenes and E. Stiefel, "Methods of conjugate gradients for solving linear systems," 1952.

[122] D. S. Kershaw, “The incomplete cholesky-conjugate gradient method for the iterative solution of systems of linear equations,” *Journal of Computational Physics*, vol. 26, no. 1, pp. 43–65, 1978.

[123] J. H. Wilkinson, J. H. Wilkinson, and J. H. Wilkinson, *The algebraic eigenvalue problem*, vol. 87. Clarendon Press Oxford, 1965.

[124] N. J. Higham, “Analysis of the cholesky decomposition of a semi-definite matrix,” 1990.

[125] L. Sun, T. Vidal-Calleja, and J. V. Miro, “Bayesian fusion using conditionally independent submaps for high resolution 2.5 d mapping,” in *Robotics and Automation (ICRA), 2015 IEEE International Conference on*, pp. 3394–3400, IEEE, 2015.

[126] T. Ohtsuka and T. Komatsu, “Enhancement of electric conductivity of the rust layer by adsorption of water,” *Corrosion science*, vol. 47, no. 10, pp. 2571–2577, 2005.

[127] H. E. Knoepfel, *Magnetic fields: a comprehensive theoretical treatise for practical use*. John Wiley & Sons, 2008.